University of Dublin
Trinity College
Department of Civil, Structural & Environmental Engineering

The Effect of Prestress Force Magnitude and Eccentricity on the Natural Bending Frequencies of Prestressed Concrete Structures

Darragh Noble

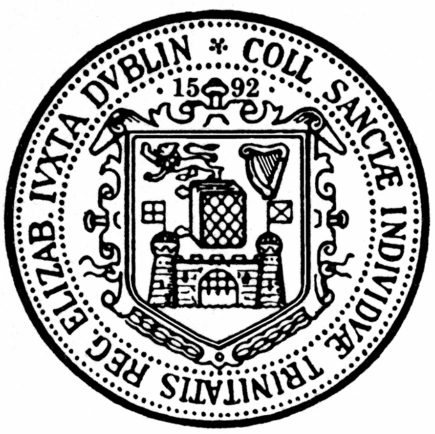

Supervised by
Assoc. Prof. Alan O'Connor

29^{th} April 2016

A Thesis submitted to the University of Dublin for the degree of
Doctor of Philosophy

Declaration

The author hereby declares that this thesis, in whole or in part, has not been submitted to any other university as an exercise for a degree. Except where reference has been provided in the text, this thesis is entirely the author's own work.

The author agrees to deposit this thesis in the University's open access institutional repository or allow the library to do so on my behalf, subject to Irish Copyright Legislation and Trinity College Library conditions of use and acknowledgement and that the library may, for academic purposes, lend or copy this thesis upon request.

Darragh Noble

April 2016

Executive Summary

The effect of prestress force magnitude on the natural bending frequencies of prestressed concrete structures is something widely debated in literature to date. It has major implications for the dynamic design and accurate analysis of such structures, as accurate knowledge of the modal properties of structures is a vital part of accurate prediction modelling and safe dynamic design.

This Ph.D. thesis outlines the work carried out between September 2012 and August 2015 on a research project investigating how the application of a prestress force affects the dynamic properties of prestressed concrete structures. Steel and concrete test specimens have been tested both statically and dynamically to determine the change in their flexural/bending stiffness according to the application of both external axial loads and post-tensioning loads to the sections. A new simple linear mathematical model predicting changes in natural frequency with increasing post-tensioning load magnitude has also been proposed.

Dynamic impact testing has been conducted on four rectangular steel hollow sections. Two sections with different slenderness ratios have been externally axially loaded by jacking them against abutments in a large load frame. Dynamic impact tests were conducted at incremental values of external axial load, and the natural frequencies and damping ratios were determined by analysing the response signals obtained from an accelerometer affixed to the beams during vibration. As such, the migration of the modal properties with increasing external axial load could be determined. Similar testing was repeated on two identical rectangular hollow sections that instead of being externally axially loaded by jacking them against external abutments, were post-tensioned by threading a post-tensioning strand through their hollow. The migration of the fundamental frequencies with increasing post-tensioning load was determined and compared with the results for the externally axially loaded sections. The purpose of this research

was to determine under what conditions the "compression-softening" effect is valid.

A new simple linear mathematical model predicting changes in natural frequency with increasing post-tensioning force for post-tensioned concrete beams has been proposed. The model predicts linear changes in Young's Modulus, second moment of area, span length and mass per unit length with increasing post-tensioning load magnitude, and subsequently calculates the resulting changes in the natural frequency as a result of the changes in the aforementioned parameters affecting natural frequency.

Static and dynamic testing was also conducted on nine different reinforced, post-tensioned concrete beams. Each beam had a different straight-profiled post-tensioning strand eccentricity. The magnitude of the post-tensioning force was increased incrementally and accelerometer impact response signals were obtained at different post-tensioning load levels, from which the natural frequency and damping ratios were obtained. A signal processing algorithm was applied to each of the signals in order to eliminate noise and isolate the correct bending frequency. The Fast Fourier Transform (FFT) was used to convert the obtained response signals from the time domain to the frequency domain, from which the natural frequencies were determined by a peak-peaking algorithm, and the damping ratios were calculated via the half-power bandwidth method. Static three-point bending testing was also conducted at incremental values of post-tensioning force. The mid-span deflection was measured for a given applied force, at each value of post-tensioning load, and subsequently the flexural rigidity of the section at different post-tensioning load levels could be determined.

The beams were then cracked by loading them in four-point bending. Following cracking of each of the beam sections the dynamic impact tests were repeated, determining the fundamental bending frequency and damping ratio at different post-tensioning load levels. The migration of the bending frequency with increasing post-tensioning force magnitude was compared for the cracked and uncracked cases. Conclusions are subsequently drawn as to the effect of post-tensioning force magnitude on the natural frequencies of post-tensioned concrete structures and the implication any effect may have on design and analysis of these structures.

Dedication

Firstly, I'd like to thank my parents, Brian and Dolores, and my sister Ciara for their love and unwavering support over the years. Without you I would not be where I am today.

To the Little Granny, uncles, aunts and cousins - thank you for all your love and support over the years.

To my supervisor, Prof. Alan O'Connor, I owe a huge debt of gratitude. Thank you for all your hard work and dedication over the last number of years, your generosity, your patience and your constant support.

I'd like to express my deepest thanks to Dr. Maria Nogal. Thank you for your friendship, support, expertise, advice, patience and generosity over the last 18 months.

To Dr. Vikram Pakrashi, thank you for your constant insight, engaging thoughts and phone calls. Thank you for spending time philosophising about the nuances of the project, at any and every time of day and night!

To the academic staff in the Dept. of Civil, Structural and Environmental Engineering at Trinity College Dublin, especially to Dr. Francesco Pilla, Profs. Biswajit Basu, Dermot O'Dwyer, Brian Broderick and Roger West for their constant encouragement and inspiring lectures over the years.

To the technical staff in the Dept. Thank you for your hard work, expertise, dedication and generous accommodation in helping to deliver this project. A special thank you to Dr. Kevin Ryan, Michael Grimes, Dave McAuley, Mick Harris and Eoin Dunne.

To the administrative staff in the Dept. A massive thank you to Patricia Tutty, Linda McHugh, Mary Curley and all of the administrative staff who helped in organising conference visits, trips away, and in processing all of my teaching claim forms over the years!

I would like to gratefully acknowledge the financial support donated by the Irish Research Council (IRC) under its Embark initiative. I would also like to sincerely thank Banagher Concrete, Heitons Steel, Roadstone Ireland, Fairyhouse Steel, and Freyssinet Ireland for their support in supplying testing materials throughout the duration of the project.

To my fellow PhD students in the department throughout the years - Maria B, Mairéad, Tara, Aidan, Ronan, Hisham, Bea and the many others, thank you for your friendship and companionship, and the occasional sympathetic ear!

To my friends who have provided me with plenty of fun, encouragement and respite from study over the last three years. To Conor O'L, Conor D, Paul, John, Rosie, Ben, Conor C, Tony D, Dan Mc, Seán, Michael, John, Paddy, Gary Q, Kev, and the many others. Thanks for the 5-a-side, the sports, the nights out, the dinners, the weekends away, the live music, the pints, the barstool rants and the craic. Your friendship is greatly valued, appreciated and cherished.

Finally, to Michelle, thank you for becoming my best friend over the past few months. Thank you for keeping me company while nerding together, and pushing me through my corrections. Most of all, thank you for your inspiration, support and encouragement - it's deeply cherished.

Contents

List of Tables

List of Figures

1. Introduction

This thesis presents a study of the effect of post-tensioning force magnitude and eccentricity on the modal properties, specifically fundamental bending frequency and damping ratio, of straight-profiled post-tensioned concrete beams. The purpose of the thesis is to determine if a statistically significant relationship exists between post-tensioning force magnitude and the natural frequency and damping ratios. The thesis presents the results of dynamic testing and modelling of cracked and uncracked post-tensioned concrete beam sections, as well as dynamic testing of some rectangular hollow steel sections.

Chapter 1 introduces the thesis, presenting the background and motivation behind the body of work undertaken, a statement of the key objectives of the studies conducted, and a thorough outline of the contents of each chapter. Chapter 2 presents the state of the art of the topic to date, and presents the mathematical prediction models for the change in fundamental frequency with increasing prestress force magnitude, and presents the results of laboratory testing conducted in this field previously. Chapter 3 presents the main theory, techniques and tools behind modal analysis, in order to provide the reader with a grounding in the main theory behind modal analysis as a prerequisite for reading Chapters 4, 6 and 7. Chapter 4 describes the test set-up, and presents the results of dynamic testing conducted on steel rectangular hollow sections. Chapter 5 presents a linear mathematical model predicting changes in fundamental bending frequency with increasing post-tensioning force magnitude through predicting changes in Young's Modulus, axial length, second moment of area and mass per unit length with post-tensioning force magnitude. Chapter 6 presents the results of static and dynamic testing on 9 uncracked post-tensioned concrete beam sections with different straight-profiled post-tensioning strand eccentricities. Chapter 7 presents the results of dynamic testing on the same 9 post-tensioned concrete beam sections with different straight-profiled post-tensioning strand

eccentricities, following cracking by four-point bending testing. Chapter 8 presents the main conclusions from the studies conducted and described throughout the thesis in Chapters 2-7, describes some of the limitations of the studies conducted, and provides some suggestions for future research in the field.

1.1. Background

The effect of prestress force magnitude on the natural frequency of pre- and post-tensioned concrete structures is something that has been widely debated in literature to date (Quilligan et al., 2012), as discussed further and in detail in Chapter 2. This has implications for the dynamic design and analysis of all types of post-tensioned concrete structures. With the increased use of pre- and post-tensioning, which helps engineers to span greater distances while minimising the cross sectional dimensions of their sections, the dynamic response of these structures becomes of greater importance. Structures such as pre-cast post-tensioned concrete wind turbine towers, pre- and post-tensioned concrete bridge girders, and pre- and post-tensioned concrete floor slabs are just some such structures. These structures can be susceptible to extreme dynamic loading throughout their design life. For example, offshore post-tensioned concrete wind turbine towers are dynamic structures that are constantly subjected to a dynamic thrust induced from the turbine, the gust of the wind on the turbine tower, and the dynamic loading of the sea waves on the submerged section of the superstructure. Furthermore, bridge girders are susceptible to constant dynamic loading from the periodic passing of cars and heavy vehicles such as truck freight and construction vehicles. The effect of dynamic wind loading on bridge structures is also an important factor that must always be taken into consideration, as outlined by incidents such as the dynamic (resonant) excitation and subsequent collapse of the Tacoma Narrows Bridge, in Tacoma, Washington in 1940. Furthermore, all types of structures, when built in certain high risk locations, can be susceptible to extreme loading through seismic ground motions caused by earthquakes. Strength is not the only consideration in dynamic design, and often slender structures are susceptible to significant vibration serviceability problems, the most high-profile of such cases being the closure, retrofit and re-opening of the Millennium

pedestrian footbridge over the Thames River in London in 2002. Such vibration serviceability problems are reported to be common in the case of slender post-tensioned floor slabs (Pavic et al., 2001), and as such accurate and precise knowledge of the modal parameters of such post-tensioned floor slabs are of great importance to their design. In addition, there are many analysis techniques that require accurate knowledge of the modal parameters of the structure to be analysed. For example, in the Lagrangian approach, accurate knowledge of the modal parameters, i.e. natural frequency, ω_n, damping ratio, ξ_n, and mode shape, Φ_n, is required, as the dynamic deflection model is based upon a linear combination of a series of pre-determined mode shapes. Quilligan et al. (2012) applied this Lagrangian approach to a pre-cast post-tensioned concrete wind turbine tower. The assumption was made that the modal properties were unaffected by the magnitude of the post-tensioning force, in accordance with the work conducted by Hamed and Frostig (2006), and hence a linear elastic beam model was applied to the post-tensioned concrete wind turbine tower. This highlights the importance of the problem at hand. If a relationship does exist between post-tensioning force and the modal properties then it must be taken into account in the Lagrangian model in order to model the dynamic deflection of such post-tensioned wind turbine towers accurately. As such, structural engineers should be able to monitor and estimate changes in the natural bending frequency of prestressed concrete structures over the course of their design life to ensure their safety and serviceability and as a result, the prediction of the change in natural frequency of prestressed concrete structures over time is of great importance.

Furthermore, if a correlation between prestress force and natural frequency is found, it allows for the determination of the prestress loss over the design life of a prestressed concrete structure through non-destructive testing.

1.2. Motivation

Prestress force decreases over time due to concrete creep, steel relaxation, anchorage pull in and other factors. If this decrease in prestress force magnitude is accompanied by a correlated change in modal properties, i.e. natural frequency, damping ratio and mode shape, then this will have implications

in the dynamic design and analysis of pre- and post-tensioned concrete structures and also as mentioned in Section 1.1 previously, in the field of System Identification. Significant changes in fundamental frequency due to decreasing post-tensioning load would allow the post-tensioning force to be determined from non-destructive dynamic testing.

Furthermore, as outlined in Section 1.1, accurate knowledge of the modal parameters is required in order to accurately estimate dynamic behaviour through the Lagrangian approach. If the modal parameters are significantly affected by post-tensioning force magnitude, then this needs to be taken into account to accurately simulate the dynamic behaviour of dynamic structures such as post-tensioned concrete wind turbine towers.

1.3. Objectives

The main research objective of this project is to determine if there is a relationship between the magnitude of the prestressing force in pre- and post- tensioned concrete structures, and the dynamic characteristics of those structures, primarily the natural bending frequencies, (ω_n) and the damping ratios (ξ_n). This will be determined through operational modal analysis conducted in the laboratory on both post-tensioned steel rectangular hollow sections (RHSs), and on both cracked and uncracked post-tensioned reinforced concrete beams.

The main research objective has been subsequently broken down into a number of specific research objectives, outlined below;

1. **Determine the validity of the *"compression-softening"* effect.** The "compression-softening" effect states that the natural frequency will decrease for an externally axially loaded slender section, as the section begins to soften. It is based on Euler buckling theory and it has been argued that this effect can be applied to pre- and post-tensioned concrete sections. The validity of this theory is put to the test, through dynamic testing of steel RHS sections.

2. **Determine whether *"compression-softening"* holds only for 'slender' members.** To determine the validity of the "compression-softening" effect for both slender and stocky sections, and to compare

the dynamic response of the slender/stocky rectangular hollow sections.

3. **Determine how the dynamic properties of steel sections change with increasing axial force.** To determine the effect of both external axial load and post-tensioning force magnitude on the modal properties of rectangular steel hollow sections, and to compare both cases.

4. **To create a model to predict changes in natural frequency with increasing post-tensioning force magnitude.** To create a simple mathematical model that predicts changes in fundamental bending frequency with increasing post-tensioning force magnitude and varying post-tensioning strand eccentricity.

5. **Investigate how the dynamic properties of uncracked post-tensioned reinforced concrete sections change with increasing axial force.** To investigate how the modal properties, specifically damping ratio and fundamental frequency, of 9 uncracked post-tensioned concrete beams are affected by different post-tensioning load levels.

6. **Determine how the dynamic properties of uncracked post-tensioned reinforced concrete sections change with varying prestress force eccentricity.** To determine how the modal properties of the post-tensioned concrete beams are affected by different straight-profiled post-tensioning strand eccentricities.

7. **Investigate how the dynamic properties of cracked post tensioned reinforced concrete sections change with increasing axial force.** To investigate how the modal properties of 9 cracked post-tensioned concrete beams are affected by different post-tensioning load levels.

8. **To compare the effect of changing post-tensioning force magnitude on the dynamic properties of cracked and uncracked post-tensioned concrete sections.** To compare the effect of post-tensioning force magnitude on both cracked and uncracked concrete beam sections and to compare the response of both type of sections.

9. **To compare the results of the generated model to the results obtained from dynamic testing.** A comparison of the simple mathematical model to the obtained experimental results in order to test the accuracy of the model.

1.4. Organisation of Thesis

This thesis is made up of eight chapters, outlined as follows;

Chapter 1 provides an introduction to the topic of the effect of post-tensioning force on the modal properties of pre- and post-tensioned concrete structures. The objectives of this work and an outline of this thesis are also presented.

Chapter 2 presents a state of the art review of current research in the area of the effect of post-tensioning force on the modal properties of pre- and post-tensioned concrete structures. The literature review outlines the relevant models used in literature to date to predict changes in fundamental frequency with increasing pre- and post-tensioning force magnitude, the differences, and their limitations. It also tracks the methodology and results of experimental studies that have already been conducted in the field.

Chapter 3 provides an introduction to some of the basic theory, concepts and tools of modal analysis/modal testing. It provides necessary background in the theory, tools and techniques behind experimental dynamic testing and provides the reader with a concise introduction, background and basis of these important aspects, which become relevant in later chapters. It outlines the theoretical basis behind experimental modal analysis and some of the specific tools and techniques used to conduct the analysis. It outlines the measurement techniques behind collecting good dynamic data, and outlines some specific techniques behind digital signal processing, providing sufficient theoretical basis for further chapters.

Chapter 4 describes the testing procedure and results for the dynamic testing of externally axially loaded and post-tensioned steel rectangular hollow sections. The fundamental natural bending frequency of the beam sections

and the corresponding damping ratios have been calculated from the measured dynamic response of the beam to a series of impact hammer strikes at a series of increasing axial load levels.

Chapter 5 outlines a linear mathematical model developed in MATLAB to predict changes in natural frequency with increasing post-tensioning load magnitude for post-tensioned concrete beams. The model predicts changes in the parameters affecting natural frequency with increasing post-tensioning load level, such as changes in span length, changes in second moment of area, changes in mass per unit length, and changes in Young's Modulus.

Chapter 6 describes the static and dynamic testing of 9 different straight-profiled uncracked post-tensioned concrete beams, with different post tensioning strand eccentricities. The results of the changes in fundamental frequency and damping ratio with increasing post-tensioning load level are presented. The predictions of the model outlined in **Chapter 5** are compared to the results obtained from testing.

Chapter 7 presents the results of dynamic testing conducted on the same 9 straight-profiled concrete sections in a cracked (damaged) state. The changes in fundamental frequency and damping ratio of the cracked post-tensioned concrete beams with increasing post-tensioning force are presented, and the results are compared to that for the uncracked beam sections. The cracking procedure of the 9 post-tensioned beams via four-point bending tests is also outlined.

Chapter 8 concludes the thesis by outlining how the objectives detailed in Chapter 1 have been achieved. In addition, recommendations are made for future work to further develop an understanding of the potential changes in modal properties of post-tensioned concrete structures with increasing post-tensioning load magnitude.

Appendices present the results of all statistical significance testing, for the steel sections, the concrete sections and the cracked concrete sections in table format, along with the Nomenclature for the mathematical terms

presented throughout the thesis.

2. Literature Review

The correct estimation of the modal parameters (natural frequency, damping ratio and mode shapes) of all structures is a requirement of sound structural design. In recent years, there have been significant advances in the fields of pre- and post-tensioning, allowing structural engineers to make use of longer spans. Prestressed concrete is a technology primarily used to reduce design serviceability problems in structures. In recent years, more and more concrete structures are designed as prestressed sections, for example, most recently in the field of post-tensioned concrete offshore wind turbine towers. This is in addition to the pre-existing practice of pre- and post-tensioned concrete bridge girders and pre- and post-tensioned concrete floors. Offshore wind turbines are dynamic machines that can be susceptible to extreme site-specific dynamic loads, due to the effect of the wind, waves, and also potentially, to seismic loads. Bridge girders tend to span long distances and are susceptible to repetitive dynamic loading from traffic, and may also be susceptible to other dynamic environmental effects. The correct estimation of the modal parameters enables potential negative vibration serviceability problems or even extreme structural resonance conditions to be identified and subsequently avoided. The effect of prestress force magnitude on the modal properties of such structures is not currently well established.

The effect of prestress force magnitude on the natural frequency of prestressed concrete structures has many implications, specifically in the prestressed concrete bridge industry and for post-tensioned concrete wind turbine towers. Prestress force decreases over time due to concrete creep, steel relaxation, anchorage pull in and other factors. Structural engineers should thus be able to monitor or estimate changes in the natural bending frequency of prestressed concrete structures over the course of their design life to ensure their safety and serviceability. Additionally, the correct estimation of the effect that prestress loss has on the natural bending frequencies of such

structures is directly related to the adequacy and accuracy of estimating the extreme dynamics of these structures. As a result, the prediction of the change in natural frequency of prestressed concrete structures over time is of great importance. However, there is currently widespread disagreement and confusion over the effect that prestress force magnitude has on natural bending frequency.

This chapter aims to present the individual prediction models that have been suggested for use to date, to compare and contrast them, and to comment on their validity. Currently there are three distinct arguments among researchers; the natural vibration frequency of prestressed concrete structures decreases as the magnitude of the prestressing force is increased, the natural vibration frequency of prestressed concrete structures is unchanged by prestress force magnitude, the natural vibration frequency of prestressed concrete structures increases as the magnitude of the prestressing force is increased. A variety of different models have been formulated to date in favour or in critique of these viewpoints. The majority of experimental modal analysis on dynamic test results suggest that there is an increase in natural bending frequency with increasing prestressing force. On the other hand, (external) axial loads in combination with bending loads on beams theoretically predicts a decrease in natural bending frequency with increasing axial loading. However, a non-linear kinematic model, accounting for large deflections and moderate rotations will show that the final equation of motion of a pre- or post- tensioned concrete structure is independent of the magnitude of the prestressing force.

2.1. Introduction

This chapter presents the current state of the art of predicting the possible change in natural vibration frequencies with varying prestress force magnitude for prestressed concrete structures. This is a problem that has implications for all types of prestressed concrete structures, but particularly in the field of prestressed concrete bridges and more recently for post-tensioned concrete wind turbine towers. The effect that the applied prestressing force has on the dynamic behaviour of a prestressed concrete beam is a topic that has been widely debated amongst researchers in the field of civil and structural engineering for many years (Quilligan et al., 2012). The arguments

can be organised into the following 3 categories;

1. The natural vibration frequency of prestressed concrete structures tends to decrease as the magnitude of the prestressing force is increased. This is known as the *"compression-softening"* effect and is based on classical Euler-Bernoulli beam theory of an externally axially loaded homogeneous beam (Chan and Yung, 2000; Dai and Chen, 2007; Dall'Asta and Leoni, 1999; Law and Lu, 2005; Miyamoto et al., 2000; Raju and Rao, 1986; Tse et al., 1978). It is based on the assumption that a prestressing force is equivalent to an external axial load, and is modelled as a percentage of the critical Euler buckling load.

2. The natural vibration frequency of prestressed concrete structures is unaffected by prestress force magnitude. This argument has been taken to the fore by Hamed and Frostig (2006), who present a nonlinear kinematic model and conclude that the final equation of motion for the vibrating beam system is independent of the prestress force magnitude, and consequently that the natural vibration frequency of prestressed concrete structures is not affected by the magnitude of the prestressing force.

3. The natural vibration frequency of prestressed concrete structures tends to increase as the magnitude of the prestressing force is increased. This has found to be the case in numerous empirical studies conducted (Hop, 1991; Saiidi et al., 1994; Zhang and Li, 2007), however, a satisfactory mathematical model predicting the increase in natural frequency with increasing prestressing force has yet to be formulated, despite some attempts (Kim et al., 2004; Zhang and Li, 2007).

2.1.1. Frequency decreases with increasing prestressing force

Many authors have argued that the natural vibration frequency of prestressed concrete structures tends to decrease as the magnitude of the prestressing force increases (Chan and Yung, 2000; Dall'Asta and Leoni, 1999; Miyamoto et al., 2000; Raju and Rao, 1986; Tse et al., 1978). Various mathematical models have been formulated, based on a linear kinematic

framework (*"Kirchhoff's kinematic model"*) highlighting this. It considers small deflection theory only and does not take into account large displacements and moderate rotations about the axis of bending. The *"compression-softening"* equation, as first outlined by Tse et al. (1978) is given as;

$$\omega_n = \sqrt{\left(\frac{n\pi}{\ell}\right)^4 \frac{EI}{m} - \left(\frac{n\pi}{\ell}\right)^2 \frac{N}{m}} \tag{2.1}$$

where ω_n is the natural frequency of the beam in radians per unit time, n is the mode number, ℓ is the span length, N is the axial compressive force (positive), m is the beam mass per unit length, E is Young's modulus of elasticity and I is the second moment of area, with respect to the centroid of the cross section.

There are arguments suggesting that this *"compression-softening"* effect, as first set out by Tse et al. (1978) is not valid for prestressed concrete structures. Firstly, the main assumptions made by Chan and Yung (2000); Dall'Asta and Leoni (1999); Raju and Rao (1986); Miyamoto et al. (2000); Tse et al. (1978) take into account an external axial load being applied to a homogeneous section. In the case of prestressed concrete, neither of these assumptions are valid. According to some authors (Bažant and Cedolin, 1987; Deák, 1996; Jain and Goel, 1996), *"compression-softening"* is only applicable to external axial loads and the prestressing force cannot be considered as such as it is internal to the structure. Bourne (2013) also presents a similar argument, summarised in Figure 2.1.

Furthermore, as pointed out by Saiidi et al., concrete is not a homogeneous material and is susceptible to cracks. Saiidi et al. (1994) showed experimentally that the application of Equation 2.1 to prestressed concrete beams is erroneous. This is discussed at length in Section 2.5.1. Equation 2.1 is based on Euler buckling theory, which is only applicable to homogeneous externally axially loaded beams, such as steel beams. The main assumption of applying the *"compression-softening"* effect is that the prestressing force in the strand is equivalent to an external axial load of equal magnitude applied to the beam ends. This has been refuted by many authors who state that the prestressing force is not equivalent to an externally applied axial load as it is internal to the structure and as a result cannot cause Euler buckling to occur (Bartlett, 1987; Bourne, 2013; Dall'Asta and Leoni, 1999; Deák, 1996; Jain and Goel, 1996).

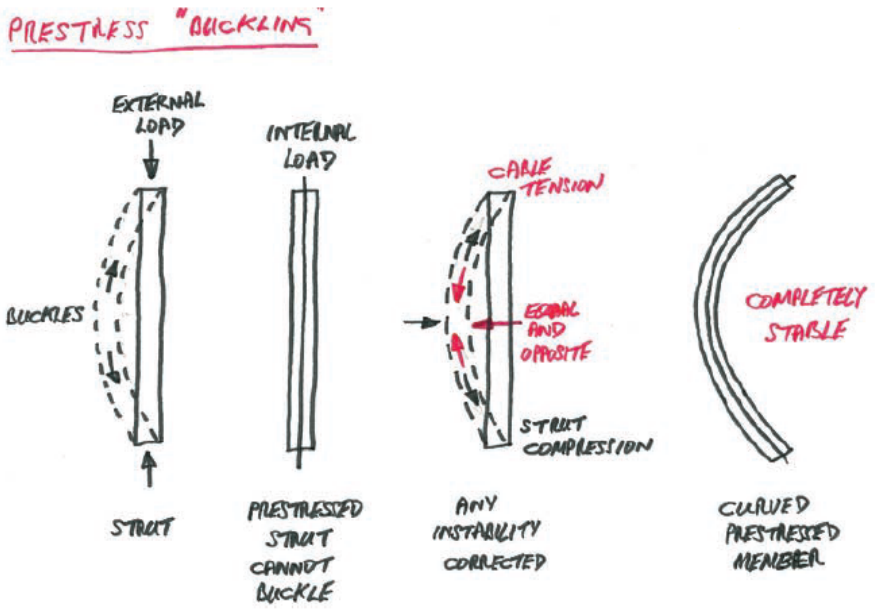

Figure 2.1.: Prestressing cannot cause buckling to occur (Bourne, 2013)

2.1.2. No change in frequency with increasing prestressing force

Hamed and Frostig (2006) presented a rigorous mathematical proof indicating that the magnitude of the prestressing force does not affect the natural frequencies of prestressed concrete beams. A non-linear kinematic framework was adopted, in comparison with the aforementioned linear kinematic framework presented in other studies (Chan and Yung, 2000; Dall'Asta and Leoni, 1999; Miyamoto et al., 2000; Tse et al., 1978). This enabled large displacements and moderate rotations to be accounted for. It was subsequently mathematically demonstrated that the governing equation of motion (vibration equation) for the beam is independent of axial force, for bonded and unbonded prestressing tendons. Dall'Asta and Dezi (1996) through mathematical modelling, Kerr (1976), through mathematical modelling, backed up by experimental testing and Dai and Chen (2007), through a finite element analysis, all concluded that there was a change in natural frequency with varying prestressing force, however, they suggested that the magnitude of the change is negligible and subsequently concur with Hamed and Frostig (2006) in stating that the magnitude of the prestress force has no effect on the natural vibration frequency of prestressed concrete structures, within

practical ranges of prestressing force. Other authors (Bartlett, 1987; Deák, 1996) also concur with this, however, their respective discussions are not backed up by any form of mathematical or experimental proof.

2.2. Frequency increases with increasing prestressing force

Experimental evidence is relatively abundant to suggest that the natural frequency of prestressed concrete structures actually increases with increasing magnitude of prestressing force (Ho et al., 2012; Hop, 1991; Lu and Law, 2006; Saiidi et al., 1994; Williams and Falati, 1999; Zhang and Li, 2007; Zhang et al., 2012). Experimental modal analysis has been conducted on a series of vibration tests, both in-situ and in the lab indicating that natural frequency increases with increasing prestressing force. Saiidi et al. (1994), who initially assumed the *"compression-softening"* argument to hold true for prestressed concrete beams, suggest the reason behind this is due to the effect of the prestressing force on the closure of micro-cracks that have been induced in the prestressed concrete section, and the subsequent increase in stiffness in the section as a result. However, this has not been proven conclusively, either experimentally or theoretically. Mathematical models have also been formulated indicating the increase in natural frequency with increasing prestressing force (Kim et al., 2004; Zhang and Li, 2007).

Furthermore, there is significant evidence to suggest that the natural frequency of prestress concrete structures is not only sensitive to the magnitude of the prestressing force but is also sensitive to the tendon profile within the section and the tendon eccentricity (Dall'Asta and Leoni, 1999; Hop, 1991; Miyamoto et al., 2000). The tendon profile and eccentricity alters the net second moment of area of the cross section, thus directly affecting the bending stiffness and hence natural frequency of the beam section. The models tracking an increase in natural frequency with increasing prestressing force tend to focus on stiffness alteration, or the increase in flexural rigidity, EI, of the section with increasing prestressing force.

2.3. Objective

The objective of this chapter is to present the reader with the variety of different approaches that have been suggested by researchers to date to predict the change in natural bending frequency of prestressed concrete structures with varying prestress force magnitude. It is clear that currently there is a great deal of ambiguity as to which of the three arguments holds true. Experimental methods tend to show an increase in natural frequency with increasing prestressing force. Albeit, this increase tends to be small for practical ranges of prestressing force and it has been argued that the increase is negligible (Dall'Asta and Dezi, 1996; Kerr, 1976). Classical mechanics tends to point in the direction of the *"compression-softening"* effect (Miyamoto et al., 2000; Tse et al., 1978), but the validity of the assumption that an internal prestressing force in the tendon is equivalent to an external axial load has been refuted (Bartlett, 1987; Bourne, 2013; Dall'Asta and Leoni, 1999; Deák, 1996; Jain and Goel, 1996).

The different models predicting the change in natural bending frequencies with magnitude of prestressing force for simply supported prestressed concrete beams are outlined in the following sections. The models are categorised into three distinct groups. Firstly, there is the derivation from classical mechanics of the aforementioned *"compression-softening"* effect by Tse et al. (1978) and the subsequent improvements to the model by firstly the inclusion of shear and rotary inertia in the formulation (Raju and Rao, 1986), and secondly the addition of geometric effects for external tendons in the *"queen-post"* arrangement (Miyamoto et al., 2000). These models predict a decrease in natural bending frequency with increasing prestressing force.

Secondly, the bending stiffness (flexural rigidity, EI) alteration models are presented. Numerous models based on both empirical findings and analytical modelling from first principles have focused on the change in flexural rigidity, EI, of the section with varying prestress force. Some authors track changes in stiffness empirically and present empirical predictions based on linear regression analysis of the results obtained (Saiidi et al., 1994; Zhang et al., 2012), Williams and Falati (1999) take an ACI code-based approach, tracking the change in effective second moment of area, I_e, with applied moment (Williams and Falati, 1999; Kong and Evans, 1987; ACI Committee

318, 2008). Other studies focus on the change in flexural rigidity from first principles (Dall'Asta and Dezi, 1996; Kim et al., 2004), in which Kim et al. (2004) present a *"tension-strength"* model, adding the flexural rigidity of a taut string to that of the concrete section and calculating the axial shortening of the concrete section due to the axial prestressing force. Finally, Zhang and Li (2007) present a model similar to Kim et al. (2004) in that the flexural rigidity of a taut string is added to that of the concrete section, but include the effect of shear inertia.

2.4. "Compression-softening" (Tse et al., 1978)

The *"compression-softening"* argument was put forward by Tse et al. (1978). It is valid for externally axially loaded Euler-Bernoulli beams that are susceptible to buckling failure. The theory is based on Euler buckling theory and states that the closer a beam gets to its Euler buckling load, P_{cr}, the less stiff the beam becomes in bending, and thus the natural bending frequencies of the beam are decreased. Through the assumption of undamped simply harmonic motion, the appropriate boundary conditions for a simply supported beam and the appropriate mode shapes of vibration for a simply supported beam, it can be shown that the n^{th} natural bending frequency of a simply supported beam under axial tension is given by Tse et al. (1978);

$$\omega_n = \sqrt{\left(\frac{n\pi}{\ell}\right)^2 \frac{T}{m} + \left(\frac{n\pi}{\ell}\right)^4 \frac{EI}{m}} \tag{2.2}$$

where T is the axial tensile force. If $T = 0$, the natural frequency is that of a simply supported beam;

$$\omega_n = \left(\frac{n\pi}{\ell}\right)^2 \sqrt{\frac{EI}{m}} \tag{2.3}$$

If $EI = 0$, the equation is that of a flexible taut string where the tension will act as to stiffen the beam, thereby increasing its natural frequency;

$$\omega_n = \left(\frac{n\pi}{\ell}\right) \sqrt{\frac{T}{m}} \tag{2.4}$$

By making the substitution $T = -N$, and introducing an axial compressive load in place of the axial tensile load, Equation 2.1 is obtained, and is referred to in the literature as the *"compression-softening"* effect. In the

case of axial tension it is known as the *"tension-stiffening"* effect, and is analogous to the so-called *"centrifugal-stiffening"* effect seen with rotating wind turbine blades. The free-body diagram as considered by Tse et al. (1978) is outlined in Figure 2.2.

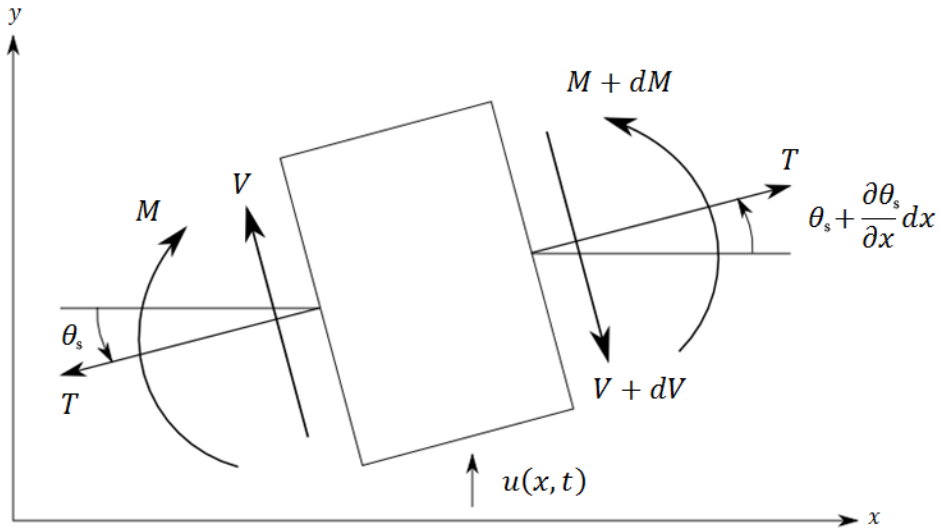

Figure 2.2.: Free Body Diagram; Lateral vibration of beam with axial tension (Tse et al., 1978)

The tension, T, is assumed constant for small deflections of the beam and the other effects are negligible. m is the mass per unit length, the slope, $\theta_s = \frac{\partial u}{\partial x}$, V is the shear force and the deflection, $u = u(x,t)$, which is a function of both position along the beam and time. From Newton's second law, which simply states and the sum of the external forces acting on a body must equal the rate change of momentum, i.e $\Sigma(external forces) = mass \times acceleration$, the dynamic force equation can be written as;

$$m\frac{\partial^2 u}{\partial t^2}dx = -\left(V + \frac{\partial V}{\partial x}dx\right) + V + T\left(\theta_s + \frac{\partial \theta_s}{\partial x}dx\right) - T\theta_s \tag{2.5}$$

which can be reduced to;

$$m\frac{\partial^2 u}{\partial t^2}dx = -\frac{\partial V}{\partial x} + T\frac{\partial^2 u}{\partial x^2} \tag{2.6}$$

by making the substitution $\theta_s = \frac{\partial u}{\partial x}$. Furthermore, by acknowledging Euler-

Bernoulli beam theory, the relationship between moment and shear can be described as;

$$V = \frac{\partial M}{\partial x} \tag{2.7}$$

beam curvature and moment are related by;

$$M = EI\frac{\partial^2 u}{\partial x^2} \tag{2.8}$$

therefore Equation 2.6 becomes;

$$m\frac{\partial^2 u}{\partial t^2} = -\frac{\partial^2}{\partial x^2}\left(EI\frac{\partial^2 u}{\partial x^2}\right) + T\frac{\partial^2 u}{\partial x^2} \tag{2.9}$$

Equation 2.9 is the beam equation under the effect of axial tension. The sign of T is reversed if the beam is under compression. Considering an undamped system, it is assumed that a mode of vibration is harmonic, as for discrete systems, therefore the solution must be of the form;

$$u(x,t) = \phi(x)\sin(\omega t + \psi) \tag{2.10}$$

where ω_n is the n^{th} natural frequency of vibration of the beam, and $\phi(x)$ is the eigenfunction describing the modeshape of the beam at the frequency ω. By substituting Equation 2.10 into Equation 2.9 and simplifying, the following is obtained;

$$EI\frac{d^4\phi}{dx^4} - T\frac{d^2\phi}{dx^2} - m\omega^2\phi = 0 \tag{2.11}$$

By letting the solution of the problem take the form: $\phi = Ce^{sx}$, where C and s are arbitrary constants, it can be shown that the corresponding characteristic equation of the differential equation in Equation 2.11 is;

$$EIs^4 - Ts^2 - m\omega^2 = 0 \tag{2.12}$$

The quadratic roots of Equation 2.12 are;

$$s_{1,2}^2 = \frac{T}{2EI}\left[1 \pm \left(1 + \frac{4m\omega^2 EI}{T^2}\right)^{\frac{1}{2}}\right] \tag{2.13}$$

The quadratic roots must be real and of opposite sign. By letting $s_1 = \pm a$

and $s_2 = \pm jb$ where $j = \sqrt{-1}$, the following solution to Equation 2.11 is obtained;

$$\phi = C_1 \sinh ax + C_2 \cosh ax + C_3 \sin bx + C_4 \cos bx \tag{2.14}$$

The boundary conditions of a simply supported beam are;

$$\phi|_{x=0} = \left.\frac{d^2\phi}{dx^2}\right|_{x=0} = \phi|_{x=\ell} = \left.\frac{d^2\phi}{dx^2}\right|_{x=\ell} = 0 \tag{2.15}$$

Tse et al. (1978) states that it can be shown from these conditions that $C_1 = C_2 = C_4 = 0$ and that $C_3 \sin b\ell = 0$ i.e. $b\ell = n\pi$ for $n = 1, 2, 3, ...$ The natural frequency is obtained by equating;

$$b^2 = \left(\frac{n\pi}{\ell}\right)^2 = -\frac{T}{2EI}\left[1 \pm \left(1 + \frac{4m\omega^2 EI}{T^2}\right)^{\frac{1}{2}}\right] \tag{2.16}$$

after some simplifications the following is obtained;

$$\omega_n^2 = \left(\frac{n\pi}{\ell}\right)^2 \frac{T}{m} + \left(\frac{n\pi}{\ell}\right)^4 \frac{EI}{m} \tag{2.17}$$

As stated previously, if $T = 0$, the natural frequency is that of a simply supported beam. If $EI = 0$, the equation is that of a flexible taut string, the tension will act as to stiffen the beam, thereby increasing its natural frequency. The sign of T is reversed if the beam is under compression, obtaining Equation 2.1. This is referred to in the discussed literature as the *"compression-softening"* effect.

Figure 2.3 shows the results of applying Equation 2.1 to a simply supported prestressed concrete beam whose properties are outlined in Table 2.1. In Figure 2.3c the magnitude of the externally applied axial force is increased in values of 10% of its Euler buckling load, P_{cr}, up to P_{cr}, for the first three natural bending modes (n) of the beam. A decrease in natural bending frequencies is observed. In the case where $n = 1$ and $N = P_{cr}$, the natural frequency drops to zero. This is a special case of Equation 2.1, i.e. $\omega_n = 0$ for $n = 1$ and $N = P_{cr} = \frac{\pi^2 EI}{\ell^2}$. The beam is deemed to have already buckled in it's first mode shape and therefore mathematically, according to Equation 2.1 is already deemed to be *'vibrating'* in its first mode at a frequency of $0Hz$. At that axial load level, it is considered to be able to vibrate in its second or third mode at $260Hz$ and $638Hz$ respectively.

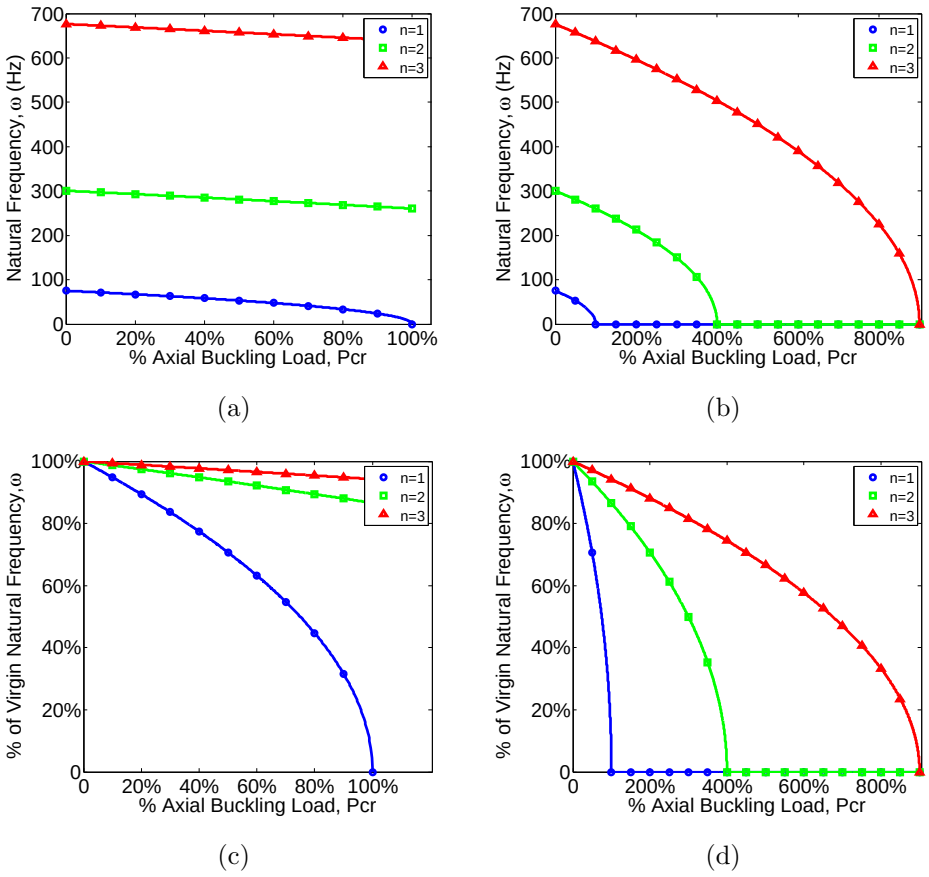

Figure 2.3.: Change in bending freq. with increasing axial compressive force.

Table 2.1.: Parameters for simply supported beam used to calculate natural bending frequency of beams in Figure 2.3 using Equation 2.1

Property	**Value**	**Unit**
Breadth, b	150	mm
Height, h	200	mm
Cross Sectional Area, A	0.03	m^2
Span, ℓ	2.0	m
Young's Modulus, E	26.88	GPa
Second Moment of Area, I	1×10^{-4}	m^4
Density of reinforced concrete, ρ	24	kN/m^3
Mass per unit length, $m = \rho \times A$	73.39	kg/m

Figures 2.3c and 2.3d represent the same data, however on the y-axis, the natural frequency is normalised as a percentage of its *'virgin'* natural frequency. Figure 2.3a and Figure 2.3b also represent the same data, however the x-axis is extended to include the buckling conditions for the second and third bending modes of vibration, which reach $0Hz$ at $n = 2$, $N = 4P_{cr}$ and $n = 3$, $N = 9P_{cr}$ respectively. The individual buckling mode shapes for the first three modes of vibration of a simply supported beam are represented in Figure 2.4.

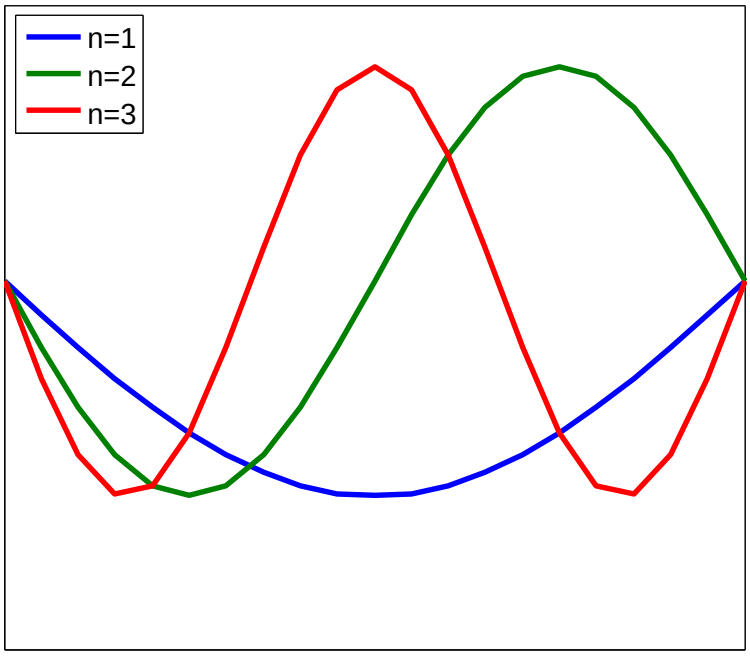

Figure 2.4.: Modeshapes for the first three bending vibration modes.

As pointed out by Saiidi et al. (1994), Equation 2.1 can be written in a dimensionless form;

$$Z = 1 - \frac{1}{n^2}X \tag{2.18}$$

where Z is an index showing the sensitivity of the square of the frequency

to changes in the axial load index;

$$Z = Y/Y_o \tag{2.19}$$

where;

$$Y = \frac{\omega_n^2}{(EI/mL^4)} \tag{2.20}$$

and;

$$Y_o = (n\pi)^4 \tag{2.21}$$

The parameter X is the ratio of the axial load to the buckling load and is given by;

$$X = \frac{N}{(\pi^2 EI/L_e^2)} \tag{2.22}$$

This indicates that the sensitivity of the change in frequency with axial load decreases significantly for higher modes of vibration (Saiidi et al., 1994), which is represented graphically in Figure 2.5.

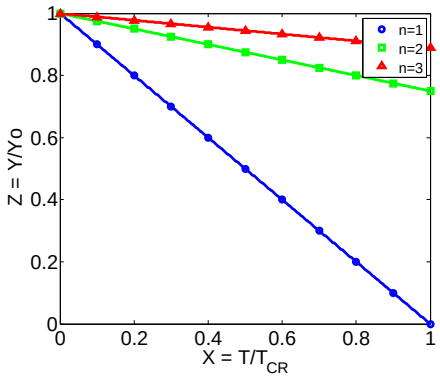

Figure 2.5.: Sensitivity of change in square of frequency to increasing axial load index (Saiidi et al., 1994)

Many authors (Bartlett, 1987; Bourne, 2013; Dall'Asta and Leoni, 1999; Deák, 1996; Jain and Goel, 1996) argue that the application of the *"compression softening"* effect to a prestressed concrete beam is erroneous from the outset, for a number of different reasons. It has been argued that a prestressing force should be considered as an internal force within the sys-

tem and is not equivalent to an externally applied axial load (Dall'Asta and Leoni, 1999). Deák (1996) argues Equation 2.1 is applicable only to an *"external axial compressive force that maintains its original line of action during the vibration of the member, thus being converted into an eccentric force with respect to the axis of the beam."* In essence, the arguments seem to point in the direction that a prestressing force should not be considered to cause the beam to buckle in accordance with Euler buckling theory and therefore Equation 2.1 is not applicable.

2.4.1. Miyamoto et al. (2000) model

From the outset, it should be stated that in this study, the intention is to include only prestressed concrete beams with internal tendons, however Miyamoto et al. (2000) present a study on the behaviour of a composite (steel-concrete) prestressed girder strengthened with external tendons, in a so-called *"queen-post"* arrangement, as shown in Figure 2.6a. The model is fundamentally different from the others from the beginning as it considers a composite girder with external tendons. Other research focuses primarily on single material beams (steel or concrete) that are prestressed internally (i.e. the tendon lies within the confines of the beam cross section). On closer inspection it should be noted that the mathematical formulation by Miyamoto et al. (2000) is identical to Tse et al. (1978) save for the inclusion of the geometric terms relating to the external prestressing strand layout. Miyamoto et al. (2000) acknowledges the *"compression-softening"* effect and states that in *"...theory, prestressing lowers the natural frequency of the girder; thus using external prestressing tendons the vibration characteristics, which include the natural frequency of the existing structural system are affected."*

The analytical distributed mass model derived by Miyamoto et al. (2000) consists of the *"compression-softening"* effect, as outlined by Tse et al. (1978), in addition to geometric terms accounting for the profile of the external prestressing tendons, such as the angle of the tendons, θ, the distance from the support to the deviator, a, and the starting eccentricity of the tendon from the centroid of the cross section, e.

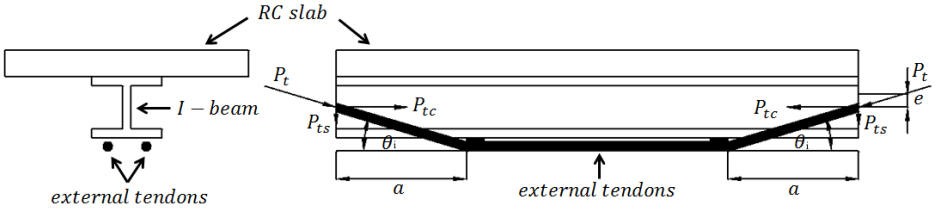

(a)

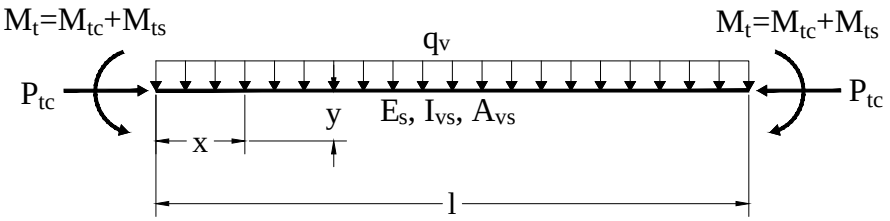

(b)

Figure 2.6.: (a) Composite steel-concrete beam studied by Miyamoto et al. (2000); (b) Distibuted mass model as suggested by Miyamoto et al. (2000)

Miyamoto et al. (2000) Analytical Model

According to Miyamoto et al. (2000), the flexural vibration of a girder subjected to a prestressing force exerted by external tendons is expressed as;

$$\frac{\partial^2}{\partial x^2}\left(E_s I_{vs}\frac{\partial^2 y}{\partial x^2}\right)+\frac{\partial^2}{\partial x^2}\left(P_t y\right)-\frac{\partial^2}{\partial x^2}\left(M_p\right)=-\frac{\Sigma\gamma_i A_i}{g}\frac{\partial^2 y}{\partial t^2} \tag{2.23}$$

where $E_s I_{vs}$ is the flexural rigidity of the girder, γ_i is the unit weight of the girder and A_i is the cross-sectional area of the girder. P_t is the magnitude of the prestressing force and M_p is the bending moment due to the prestressing force. P_t and M_p can be expressed as;

$$P_{tc}=P_{tc}^0+\Delta P_{tc} \tag{2.24}$$

$$M_p=\left(P_{tc}^0+\Delta P_{tc}\right)e+\left(P_{ts}^0+\Delta P_{ts}\right)a \tag{2.25}$$

P_{tc} is the component of horizontal direction of prestressing force, P_{ts} is the vertical component of the prestressing force, ΔP_{tc} is the horizontal com-

ponent of the increase in prestressing force due to flexural vibration, ΔP_{ts} is the vertical component of the increase in the prestressing force due to flexural vibration. e is the eccentricity of the prestressing tendons (i.e. the distance of the prestressing tendon from the neutral axis of the composite section), a is the distance of the deviators from each end of the beam in the queen-post arrangement, as shown in Figure 2.6a (Miyamoto et al., 2000).

$$\begin{aligned}&\frac{\partial^2}{\partial x^2}\left(E_s I_{vs}\frac{\partial^2 y}{\partial x^2}\right)+\frac{\partial^2}{\partial x^2}\left(P_{tc}^0+\Delta P_{tc}\right)y\\&\quad-\frac{\partial^2}{\partial x^2}\left[\left(P_{tc}^0+\Delta P_{tc}\right)e+\left(P_{ts}^0+\Delta P_{ts}\right)a\right]=-\frac{\Sigma\gamma_i A_i}{g}\frac{\partial^2 y}{\partial t^2}\end{aligned} \tag{2.26}$$

Miyamoto et al. argue that since $y_{max} << e$ and therefore $\Delta P_{tc}.y << \Delta P_{tc}.e$, the value of $\Delta P_{tc}.y$ is negligibly small and therefore (2.26) can be written as;

$$E_s I_{vs}\frac{\partial^4 y}{\partial x^4}+P_{tc}^0\frac{\partial^2 y}{\partial x^2}-\left[e\frac{\partial^2}{\partial x^2}\left(\Delta P_{tc}\right)+a\frac{\partial^2}{\partial x^2}\left(\Delta P_{ts}\right)\right]=-\frac{\Sigma\gamma_i A_i}{g}\frac{\partial^2 y}{\partial t^2} \tag{2.27}$$

where ΔP_t is the amount of change in the tendon tension due to flexural vibration, which varies with vibrational displacement. Therefore, Miyamoto et al. (2000) assume that ΔP_t is proportional to the maximum value of vibrational displacement, y, and assume that it is infinitesimal and can hence calculate ΔP_t from the elasticity equation $\delta_0+\left(\Delta P_t\cos\theta\right)\delta_1=0$, where;

$$\Delta P_t\cos\theta_i=\frac{\int\left(\frac{mM}{E_s I_{vs}}\right)\mathrm{dx}}{\int\left(\frac{m^2}{E_s I_{vs}}\right)\mathrm{dx}+\frac{\ell}{E_s A_{vs}}+\frac{\ell_t}{E_t A_t}} \tag{2.28}$$

$$\Delta P_t\cos\theta_i=\frac{\frac{P\ell^2}{8E_s I_{vs}}\left(e.\cos\theta_i+a.\sin\theta_i\right)}{\frac{\ell}{E_s I_{vs}}\left(e.\cos\theta_i+a.\sin\theta_i\right)^2+\frac{\ell}{E_s A_{vs}}+\frac{\ell_t}{E_t A_t}} \tag{2.29}$$

P is the applied prestressing load, E_t is the Young's Modulus of the tendon, A_t is the cross sectional area of the tendon and ℓ_t is the tendon length. The authors disregard the shear force as it is assumed that it is negligibly small.

Rearranging (2.28), ΔP_t can be expressed as;

$$\Delta P_t = \frac{\ell \left(e.\cos\theta_i + a.\sin\theta_i\right)}{8\cos\theta_i \left[\left(e.\cos\theta_i + a.\sin\theta_i\right)^2 + \lambda\right]} P \tag{2.30}$$

where;

$$\lambda = \frac{I_{vs}}{A_{vs}} + \frac{E_s I_{vs}}{E_t A_t} \frac{\ell_t}{\ell} \tag{2.31}$$

ℓ is the span of the composite steel-concrete section and ℓ_t is the length of the external prestressing tendon, A_{vs} is the area of the composite girder, I_{vs} is the second moment of area of the composite girder. The static midspan deflection of the composite girder is calculated using the following formula (Miyamoto et al., 2000);

$$y_p = \frac{\ell^3}{48 E_s I_{vs}} P \tag{2.32}$$

Substituting (2.32) into (2.31), Miyamoto et al. (2000) obtains an expression for the displacement as a function of the change in prestressing force, ΔP_t;

$$y_p = \frac{\ell^2 \cos\theta_i \left[\left(e.\cos\theta_i + a.\sin\theta_i\right)^2 + \lambda\right]}{6 E_s I_{vs} \left(e.\cos\theta_i + a.\sin\theta_i\right)} \Delta P_t \tag{2.33}$$

where y_p is the static midspan deflection of the composite girder under the applied load P. The authors then produce an expression for the upward movement of the girder ($y_{\Delta P_t}$) due to the change in force in the prestressing tendon, ΔP_t;

$$\begin{aligned} y_{\Delta P_t} &= \frac{M_{\Delta P_t}}{8 E_s I_{vs}} \ell^2 \\ &= \frac{e.\cos\theta_i + a.\sin\theta_i}{8 E_s I_{vs}} \ell^2 \Delta P_t \end{aligned} \tag{2.34}$$

The vibration displacement, y can then be calculated from the relationship $y = y_p - y_{\Delta P_t}$, giving;

$$y = \frac{\left(4\cos\theta_i - 3\right)\left(e\cos\theta_i + a\sin\theta_i\right)^2 + 4\lambda\cos\theta_i}{24 E_s I_{vs} \left(e\cos\theta_i + a\sin\theta_i\right)} \ell^2 \Delta P_t \tag{2.35}$$

Rearranging, Miyamoto et al. (2000) express ΔP_t as a function of y;

$$\Delta P_t = \frac{24E_s I_{vs}\left(e\cos\theta_i + a\sin\theta_i\right)}{\ell^2\left(\mu + 4\lambda\cos\theta_i\right)} y \tag{2.36}$$

where;

$$\mu = \left(4\cos\theta_i - 3\right)\left(e\cos\theta_i + a\sin\theta_i\right) \tag{2.37}$$

Subbing (2.36) into (2.27) and rearranging, Miyamoto et al. (2000) obtain;

$$E_s I_{vs}\frac{\partial^4 y}{\partial x^4} + \left(P_{tc}^0 - \frac{24E_s I_{vs}}{\ell^2}\frac{v}{\mu + 4\lambda\cos\theta_i}\right)\frac{\partial^2 y}{\partial x^2} = -\frac{\Sigma\gamma_i A_i}{g}\frac{\partial^2 y}{\partial t^2} \tag{2.38}$$

where;

$$v = \left(e\cos\theta_i + a\sin\theta_i\right)^2 \tag{2.39}$$

The solution to (2.38) is of the form;

$$y = X(x)e^{i\omega_n t} \tag{2.40}$$

Since the composite girder is simply supported, the mode shape, $X(x)$ takes the form;

$$X(x) = D\sin\frac{n\pi}{\ell}x \tag{2.41}$$

for n=(1,2,3...), where D is an arbitrary constant. Substituting (2.40) and (2.41) into (2.38) and rearranging, Miyamoto et al. (2000) obtain the following;

$$E_s I_{vs}\left(\frac{n\pi}{\ell}\right)^4 - \left(P_{tc}^0 - \frac{24E_s Ivs}{\ell^2}\frac{v}{\mu + 4\lambda\cos\theta_i}\right)\left(\frac{n\pi}{\ell}\right)^2 = \frac{\Sigma\gamma_i A_i}{g}\omega_n^2 \tag{2.42}$$

Solving for ω_n, the following is obtained;

$$\omega_n = a_v\left(\frac{n\pi}{\ell}\right)^2\xi \tag{2.43}$$

ξ is given by;

$$\xi = \sqrt{\left[1 - \left(\frac{\ell}{n\pi}\right)^2 \frac{P_{tc}^0}{E_s I_{vs}} + \frac{24}{(n\pi)^2} \frac{v}{\mu + 4\lambda \cos\theta_i}\right]} \tag{2.44}$$

$$a_v = \sqrt{\frac{E_s I_{vs}}{m}} \tag{2.45}$$

m is the mass per unit length of the beam. ξ is a term containing the *"compression-softening"* formula in addition to geometric terms describing the path of the prestressing tendons. By setting $\xi = 1$, Equation 2.43 becomes the natural bending frequency equation for a simply supported beam with zero prestressing force. According to the authors, if $\xi > 1$, the influence of the tendon arrangement is said to be greater than the horizontal component of the initial prestressing force , the strengthening with external tendons increases the natural frequency. For values of ξ in the range $0 < \xi < 1$, the influence of the horizontal component of the prestressing force is large and the strengthening decreases natural frequency. By setting $\theta_i = 0$, $a = 0$ and $e = 0$, Equation 2.43 reduces to Equation 2.1, as obtained in Tse et al. (1978), as ξ becomes;

$$\xi = \sqrt{\left[1 - \left(\frac{\ell}{n\pi}\right)^2 \frac{P_{tc}^0}{E_s I_{vs}}\right]} \tag{2.46}$$

by setting $\theta = 0$, $a = 0$, ξ becomes;

$$\xi = \sqrt{\left[1 - \left(\frac{\ell}{n\pi}\right)^2 \frac{P_{tc}^0}{E_s I_{vs}} + \frac{24}{(n\pi)^2} \frac{e^2}{e + 4\lambda}\right]} \tag{2.47}$$

Equation 2.47 indicates that when the geometric effect of the increasing eccentricity is greater than the effect of the *"compression-softening"* term, an increase in natural frequency can be predicted. This was also found to be the case experimentally (Miyamoto et al., 2000). Impact hammer tests were carried out on a composite steel-concrete girder in the *"queen-post"* arrangement. It was found that for the less eccentric tendons ($e/y_{sl} = 0.1$) the natural vibration frequencies tended to decrease as the magnitude of the prestressing force was increased, in accordance with the *"compression-softening"* effect. For the configuration with the more eccentric tendons

($e/y_{sl} = 1.0$) it was found that the natural vibration frequencies tended to increase as the magnitude of the prestressing force was increased (Miyamoto et al., 2000). This is discussed further in Section 2.12.1.

Figure 2.7 displays the results of applying Equations 2.43, 2.45 and 2.47 to the simply supported beam outlined in Table 2.1 with varying prestress force eccentricity, e. It can be seen from Figure 2.7 that Equations 2.43, 2.45 and 2.47 predict that increasing the prestress force eccentricity acts as to increase the natural frequency of the beam with respect to zero prestress force eccentricity. This can be attributed to the geometric effect of increasing the second moment of area, I, and subsequently the flexural rigidity, EI of the beam. Figure 2.8 charts the aforementioned *"compression-softening"* effect for a range of different prestress force eccentricities. As before, the more eccentric the tendon, the higher the first natural bending frequency for a given level of prestress force, as the second moment of area of the section is increased in accordance with the parallel axis theorem.

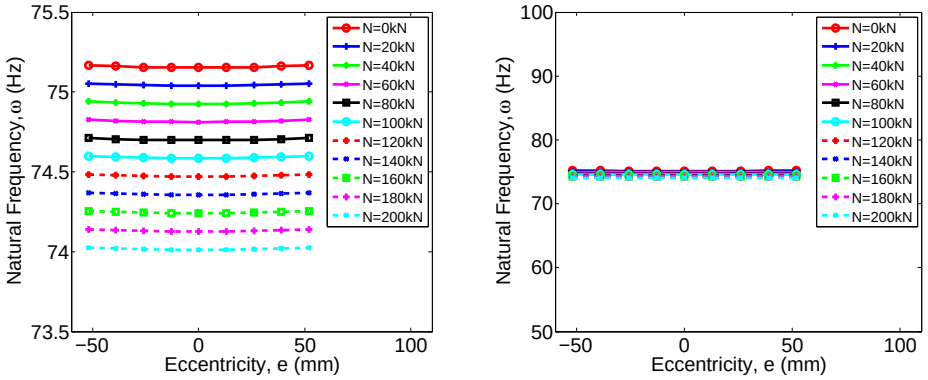

Figure 2.7.: Change in NF with varying eccentricity of prestress force for various prestress force magnitudes

2.4.2. Raju and Rao (1986) model

Raju and Rao (1986) present a paper in which the effect of the magnitude of the prestress force on the free vibration behaviour of a simply supported prestressed concrete beam is studied, accompanied by the effects of rotary and shear inertia through a Rayleigh-Ritz formulation. The effect of rotary and shear inertia has been ignored by Tse et al. (1978) and Miyamoto et al.

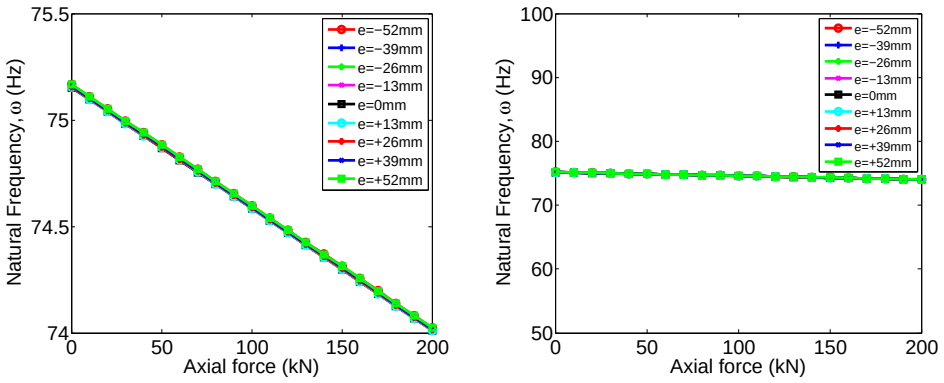

Figure 2.8.: Change in NF with varying prestress force for various eccentricities of prestressing strand

(2000). The kinematic relations have been altered from Tse et al. (1978) to include the effect of rotary and shear inertia. Beam curvature is given as (Raju and Rao, 1986);

$$\psi_x = -\left(\frac{\partial^2 w}{\partial x^2} + \frac{\partial \gamma}{\partial x}\right) \tag{2.48}$$

as opposed to an Euler-Bernoulli beam, in which the curvature is considered to be a function of the transverse displacement only, and independent of shear inertia, such that (Tse et al., 1978);

$$\psi_x = -\left(\frac{\partial^2 w}{\partial x^2}\right) \tag{2.49}$$

ψ_x is the beam curvature, w is the transverse displacement, γ_{ss} is the shear rotation and x is the axial coordinate. The strain energy, U, and the kinetic energy, T_{KE}, for a beam of length ℓ is given as (Raju and Rao, 1986);

$$U = \frac{EI}{2}\int_0^\ell \left[\left(\frac{\partial^2 w}{\partial x^2} + \frac{\partial \gamma_{ss}}{\partial x}\right)^2 + \frac{5}{12\left(1+\nu\right)r^2}\gamma_{ss}^2\right] \mathrm{dx} \tag{2.50}$$

$$T_{KE} = \frac{m\omega^2}{2}\int_0^\ell \left[w^2 + r^2\left(\frac{\partial w}{\partial x} + \gamma_{ss}\right)^2\right] \mathrm{dx} \tag{2.51}$$

where E is the Young's Modulus of elasticity, I is the second moment of area, r is the radius of gyration, m is the mass per unit length, ν is Poisson's

ratio for concrete ($\approxeq 0.3$), γ_{ss} is the shear strain and ω is the natural circular frequency. Raju and Rao also point out that a shear factor of 5/6 has been assumed in Equation 2.50. The work done by the external axial load, P_{ext}, is given by;

$$W = \frac{P_{ext}}{2} \int_0^{\ell} \left(\frac{\partial w}{\partial x} \right)^2 \mathrm{dx} \tag{2.52}$$

For a simply supported beam, the assumed mode of vibration is;

$$w = a \sin \left(\frac{n\pi x}{\ell} \right) \tag{2.53}$$

The deformation mode for shear rotation, γ_{ss} is assumed from the similarity between $\frac{\partial w}{\partial x}$ and γ_{ss} and is given as;

$$\gamma_{ss} = b \cos \left(\frac{n\pi x}{\ell} \right) \tag{2.54}$$

where n is the mode number and a and b are the unknown coefficients for the amplitude of vibration. The authors apply the Rayleigh-Ritz method, in which the total potential energy is minimised with respect to a and b;

$$\frac{\partial}{\partial a} \left(U - W - T_{KE} \right) = 0 \tag{2.55}$$

$$\frac{\partial}{\partial b} \left(U - W - T_{KE} \right) = 0 \tag{2.56}$$

Following the implementation of the Rayleigh-Ritz method, which is a energy minimisation technique, tracking total energy as the superposition of strain energy, kinetic energy, and work done by an external axial load acting on the system, expressions are obtained for the critical load parameter;

$$\lambda_b = \frac{P_{ext} \ell^2}{EI} \tag{2.57}$$

and the frequency parameter;

$$\lambda_f = \frac{m\omega^2 \ell^4}{EI} \tag{2.58}$$

The solution is identical to that by Tse et al. (1978) but that it includes the effect of shear and rotary inertia. The critical load parameter is found

to be;

$$\lambda_b = \frac{\pi^2}{\frac{12(1+\nu)\pi^2}{5\beta^2} + 1} \tag{2.59}$$

rearranging, and simplifying, the following critical buckling load is obtained Raju and Rao (1986);

$$P_{CR} = \frac{5\beta^2}{12\left(1+\nu\right)\pi^2 + 5\beta^2} \frac{\pi^2 EI}{\ell^2} \tag{2.60}$$

where $\beta = \ell/r$ is the slenderness ratio and ν is the Poisson's ratio for the material. The frequency parameter, λ_f is given as a function of the critical load parameter, λ_b;

$$\lambda_f = \frac{B - \sqrt{B^2 - 4C}}{2} \tag{2.61}$$

where B and C are functions of mode number, n, slenderness ratio, β, Poisson's ratio, ν and the critical load parameter, λ_b;

$$B = \left(n\pi\beta\right)^2 + \frac{5}{12\left(1+\nu\right)}\left(\beta^4 + \left(n\pi\beta\right)^2\right) - \left(n\pi\right)^2 \lambda_b \tag{2.62}$$

$$C = \frac{5}{12\left(1+\nu\right)}\left(n\pi\beta\right)^4 - \left(n\pi\beta\right)^2 \left[\left(n\pi\right)^2 + \frac{5\beta^2}{12\left(1+\nu\right)}\right] \lambda_b \tag{2.63}$$

rearranging Equation 2.50, the n^{th} natural frequency, ω_n is given as;

$$\omega_n^2 = \frac{EI}{m\ell^4}\left[\frac{B - \sqrt{B^2 - 4C}}{2}\right] \tag{2.64}$$

It was found that the natural frequency of these beams decreased with increasing prestressing force and for a given prestressing force that the natural frequencies of the prestressed concrete beams increased for increasing slenderness ratios, β at a given axial load value. It was concluded that the effect of shear deformation and rotary inertia is significant for higher modes of vibration, even for slender beams and that the effect of an axial compressive load is significant for the lower modes of vibration (Raju and Rao, 1986).

Table 2.2 shows the numerical difference between predictions for the first

Table 2.2.: Comparison of including (Raju and Rao, 1986) against excluding (Miyamoto et al., 2000) the effect of rotary and shear inertia on the *"compression-softening"* effect

Axial force (kN)	Miyamoto et al. (2000) [Hz]	Raju and Rao (1986) [Hz]	% Diff. (%)
0	83.27	81.98	1.56%
10	83.22	81.93	1.56%
20	83.17	81.88	1.56%
30	83.12	81.82	1.57%
40	83.06	81.77	1.57%
50	83.01	81.72	1.57%
60	82.96	81.67	1.57%
70	82.91	81.62	1.57%
80	82.86	81.57	1.57%
90	82.81	81.51	1.57%
100	82.76	81.46	1.58%
110	82.70	81.41	1.58%
120	82.65	81.36	1.58%
130	82.60	81.31	1.58%
150	82.50	81.20	1.58%
160	82.45	81.15	1.59%
170	82.40	81.10	1.59%
180	82.34	81.05	1.59%
190	82.29	80.99	1.59%
200	82.24	80.94	1.59%

natural bending frequency of the simply supported beam described in Table 2.1 using Equation 2.1, including the effect of rotary and shear inertia (Raju and Rao, 1986) and excluding the effect of rotary and shear inertia (Miyamoto et al., 2000; Tse et al., 1978). The fourth column shows the average percentage difference between the two values and indicates that the inclusion of the rotary and shear inertia causes the predicted values for the natural frequency to decrease somewhere in the region of $1.56 - 1.59\%$ for the range of prestressing force shown in column 1.

Figure 2.9 shows the linear increase in average percentage difference in natural bending frequency prediction with increasing axial force magnitude. As can be seen from the graph, the magnitude is significant in relation to the change in natural bending frequency over the given range of axial forces and therefore, the effect of rotary and shear inertia ought to be included in any

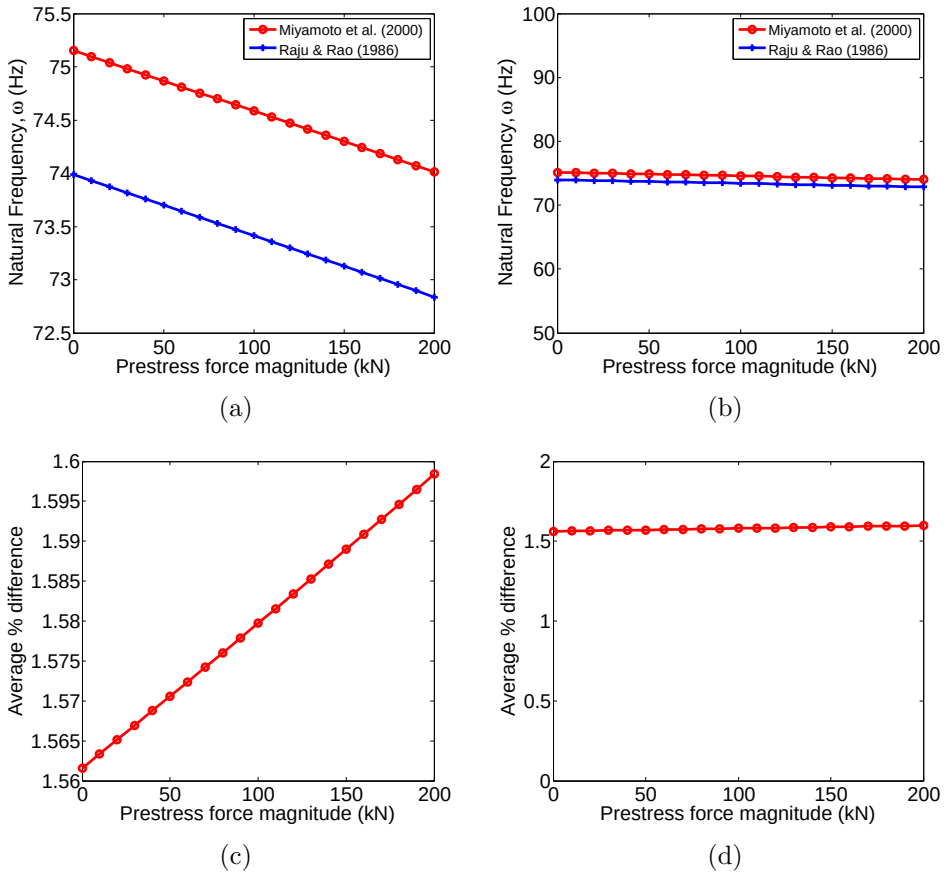

Figure 2.9.: (a) & (b) Effect of Including Shear and Rotary Inertia in the Natural Bending Frequency prediction of Simply Supported Beams using Equation 2.1; (c) & (d) Ave. % diff. in NF prediction using Equation 2.1 between including and excluding Shear and Rotary Inertia with increasing axial force magnitude

frequency prediction, as pointed out by Raju and Rao (1986). Figure 2.9 indicates that the inclusion of shear and rotary inertia is relatively more important than the change in prestressing force in the calculation of natural bending frequencies of prestressed concrete beams.

Bartlett (1987) and Bažant and Cedolin (1987), like many (Dall'Asta and Leoni, 1999; Deák, 1996; Jain and Goel, 1996) before them consider that it is erroneous to treat a prestress load as an external axial load, and that it may only be valid in cases where the beam has been jacked against permanent abutments or in some cases when the prestressing force is induced by high-

strength steel wires which are anchored to the end faces of the beam with extremely large internal voids compared to the area of the beam cross section (Bartlett, 1987). According to Bartlett (1987) *"this assumption is wrong for all cases of pretensioned and post-tensioned grouted beams"* and is also not valid for post-tensioned, ungrouted beams where *"the duct dimensions are small compared to the vibration deflection amplitudes."*

A more generic solution to the one formulated by Raju and Rao (1986) is suggested by Bert (1987). It is pointed out that the solution proposed by Raju and Rao (1986) is only valid for a simply supported beam with Poisson's ratio, $\nu = 0.3$ and for rectangular cross sections, as a shear factor, $k = 5/6$ is assumed. The following modifications to the model suggested by Raju and Rao (1986) are proposed by Bert (1987):

$$\lambda_b = \frac{\pi^2}{\frac{E_x \pi^2}{kG_{xz}} + 1} \tag{2.65}$$

$$B = (n\pi\beta)^2 + \frac{kG_{xz}}{E_x}\left(\beta^4 + (n\pi\beta)^2\right) - (n\pi)^2 \lambda_b \tag{2.66}$$

$$C = \frac{kG_{xz}}{E_x}(n\pi\beta)^4 - (n\pi\beta)^2\left[(n\pi)^2 + \frac{kG_{xz}}{E_x}\right]\lambda_b \tag{2.67}$$

where E_x is the Young's modulus in the axial direction, G_{xz} is the transverse shear modulus in the plane of vibration and k is the shear factor for the given cross section. As a result, Bert (1987) claims that *"it is clear that the effect of the axial load and transverse shear deformation is much more pronounced for composite beams that for isotropic ones."*

2.5. Stiffness Alteration Models

Many authors (Saiidi et al., 1994; Williams and Falati, 1999; Zhang et al., 2012) produce empirical based stiffness alteration models to track the increase in natural frequency with increasing prestress force. Through empirical studies and subsequent experimental modal analysis of prestressed concrete beams with varying prestress force magnitude it has been found experimentally, that there is an increase in natural frequency with increasing prestressing force (Ho et al., 2012; Hop, 1991; Lu and Law, 2006; Saiidi et al., 1994; Williams and Falati, 1999; Zhang and Li, 2007; Zhang et al.,

2012). Other authors have produced mathematical and finite element models based on the *"tension-strength"* model, tracking an increase in natural frequency with increasing prestress force (Kim et al., 2004; Zhang and Li, 2007).

2.5.1. Saiidi et al. (1994) model

Saiidi et al. (1994) conducted experimental modal analysis on both a prestressed concrete bridge in service and simply supported prestressed concrete beams. It was found in both cases that the natural frequencies increased with increasing prestress force magnitude. Since the data obtained through both field and laboratory testing contradicted predictions made in accordance with the *"compression-softening"* effect, Saiidi et al. calculated the equivalent flexural rigidity, EI_{eff}, for each experimentally measured value of prestressing force at each prestressing load level, using the modified version of Equation 2.1 (Saiidi et al., 1994);

$$(EI)_{eff} = m\left(\frac{\ell}{n\pi}\right)^4\left[\omega_n^2 + \left(\frac{n\pi}{\ell}\right)^2\frac{N}{m}\right] \tag{2.68}$$

The authors attributed the conflict between the measured and predicted data to initial microcracking that had occurred in the beam section, primarily due to shrinkage. It was suggested that the effect of the prestressing force was therefore to close the cracks, thereby enhancing the stiffness of the section (Saiidi et al., 1994). No work has been conducted to prove that the increase in stiffness can be attributed to the closure of microcracks. Linear regression analysis was then applied to develop an empirical relationship between applied prestressing force and equivalent flexural rigidity. The data for prestressing forces of $18kN$ or less was excluded as it was considered to be affected by the crack at midspan that is not normally expected in prestressed members and because the average prestress force for these points was small. In place of the omitted data an artificial data point, E_cI_g was added for the case of zero prestress. A least-square regression best-fit line was then forced to pass through this point. An empirical relationship was hence obtained and is outlined in Equation 2.69 (Saiidi et al., 1994);

$$(EI)_{eff} = \left(1 + 1.75\frac{N}{f_c'}\right)EI_g \tag{2.69}$$

N is the magnitude of the prestressing force measured in Newtons, N and f'_c is the concrete strength in units of N/mm^2. Equation 2.69 represents the empirical relationship between effective flexural rigidity and the magnitude of the prestressing force for a simply supported beam with a straight prestressing tendon passing through the centroid of the section. It shows that there is a gain in equivalent flexural rigidity for increasing magnitude of prestressing force. This empirical relationship was then applied to the Golden Valley bridge to estimate the effective flexural rigidity according to the magnitude of prestressing force (Saiidi et al., 1994). Once $(EI)_{eff}$ had been obtained, then Equation 2.68 was used to calculate the first natural frequencies. The calculated first natural frequencies of the Golden Valley bridge using the revised effective flexural rigidities calculated using Equation 2.69 were found to be within 6% of the measured data. Furthermore, the calculated results were found to decrease at the same rate as the measured data (Saiidi et al., 1994).

It was found through field testing of a simply supported post-tensioned bridge and laboratory testing of a simply-supported post-tensioned concrete beam that the measured first natural frequencies for both bridge and beam followed the opposite trend to that predicted by the *"compression-softening"* effect (Saiidi et al., 1994). The theoretical prediction for homogeneous members is that as the prestress force decreases the frequency increases as a reduction of axial load should stiffen the element (Tse et al., 1978). It was in fact found that as the prestress force increased, the natural bending frequencies of both the bridge and beam increased. As pointed out previously, it was suggested that as the prestress force decreases, e.g. over time due to steel relaxation, concrete creep etc. more microcracks open up in the concrete and the member softens (Saiidi et al., 1994). No cracked analysis was conducted to verify this. It should also be pointed out that Equation 2.69 is based on empirical evidence only and also includes the dimensional parameter, N/f'_c. As a result, the left hand side of Equation 2.69 has units of Nmm^2, whereas the right hand side of the equation contains a multiple of the dimensional term, N/f'_c added to a dimensionless constant. As a result, Equation 2.69 is not dimensionally consistent. The authors also state that since the data for the Golden Valley bridge showed, for practical ranges of prestress force, the change in natural frequencies for prestressed concrete members is very small even for the fundamental mode, and since

changes in structural parameters such as degree of fixity at supports, mass, section properties etc. can affect frequency and introduce variation of the order of the measured changes in frequency, it is not feasible to use vibration data to determine prestress losses (Saiidi et al., 1994).

2.5.2. Zhang et al. (2012) model

Dynamic testing on two unbonded fully prestressed concrete beams was conducted by Zhang et al. (2012). It was found that the natural frequency of the beams increased with increasing prestressing force magnitude. The authors explore the change in frequencies in terms of the change in elastic modulus, and a modified formula is presented;

$$(EI)_n = \left(1 + \frac{2000000N}{nE_{conc}I_{conc}}\right) E_{conc}I_{conc} \tag{2.70}$$

where N is in kN. The authors consider fully prestressed concrete beams only that have been guaranteed not to crack or buckle under service loading. As a result the second moment of area of the beams are deemed to remain constant. Hence the changes in the Young's Modulus, E, has been investigated. The following formula is obtained as the variation in E with prestressing force magnitude (Zhang et al., 2012);

$$E = E_0 \left(1 + \frac{mN\ell^2}{250E_0I_0}\right) \tag{2.71}$$

The authors consider that there are limitations to the models put forward by Saiidi et al. (1994) and Kim et al. (2004). They point out that Saiidi et al. assume that stiffness is related to concrete strength only, and the so-called *"tension-strength"* model as put forward by Kim et al. considers only the effect on the prestressing steel and neglects the effect of concrete compaction. The model put forward by Kim et al. is outlined in Section 2.8.

2.5.3. Williams and Falati (1999) model

Williams and Falati (1999) describe an extensive programme of modal testing on a post-tensioned concrete one-way spanning slab strip at 50% of full scale. The slab itself was prestressed in one direction only, and was treated and analysed in the same manner as a vibrating beam, using the formula for a vibrating beam to predict vibration frequency. The slab was constructed

with high slenderness and therefore low natural frequency, giving a high likelihood of vibration serviceability problems (Williams and Falati, 1999). It was found experimentally that the natural frequencies of prestressed concrete structures increase with increasing prestressing force, and that the damping decreases. No discernible effects on the mode shapes was reported (Williams and Falati, 1999). The authors also point out that the level of cracking of the concrete is an important factor in determining the stiffness and damping of the floor. They attempted to estimate the effective second moment of area of the cross section at each level of prestressing force. According to the authors; *"the effective second moment of area of a cracked section, averaged over it's length, depends on the loss of effective depth due to cracking"* (Williams and Falati, 1999). This is a code-based approach (ACI Committee 318, 2008);

$$I_e = \left(\frac{M_{cr}}{M_a}\right)^3 I_u + \left[1 - \left(\frac{M_{cr}}{M_a}\right)^3\right] I_{cr} \tag{2.72}$$

where M_a is the maximum gross moment and M_{cr} and the cracking moment. The level of cracking in the slab depends on the design tensile stress, f_t, where for a reinforced beam;

$$f_t = \frac{M_{cr} y_t}{I} \tag{2.73}$$

However, when prestressing is present, the stress is reduced to;

$$f_t = \frac{M_{cr} y_t}{I} - \frac{P}{A} - \frac{P e y_t}{y} \tag{2.74}$$

This indicates that increasing the prestressing force increases the magnitude of the cracking moment, or if the section is already cracked, has the effect of reducing the level of cracking. This leads to overall stiffening of the system and subsequent increase in the natural frequency. Williams and Falati also consider that fewer cracks also reduce sources of energy dissipation and lead to lower damping.

The authors found that by applying the equation for natural frequency of a simply supported beam in conjunction with Equation 2.72, there was an acceptable agreement with experimental values, indicating that the changes in natural frequency with level of prestressing force are due mainly to changes in the amount of cracking. These discrepancies have been at-

tributed to the difference between ideal and experimental boundary conditions (Williams and Falati, 1999).

2.6. Dall'Asta and Dezi (1996) model

Dall'Asta and Dezi (1996) in response to Saiidi et al. (1994) produced a model stating that the increase reported in natural frequency with increasing prestressing force by Saiidi et al. was theoretically predictable and produced a model based on Kirchhoff's kinematic relations. Applying Kirchhoff's kinematic model;

$$\epsilon_{xx}(x,z) = \frac{du_o}{dx} - z\frac{d^2w}{dx^2} \tag{2.75}$$

to a prestressed concrete beam with constant cross section and length, and solving leads to the following;

$$\omega_n^2 = \frac{n^4\pi^4}{m\ell^4}\left[\left(E_b - \frac{N}{A_b}\right)I_b + \left(E_{cab} + \frac{N}{A_{cab}}\right)I_{cab}\right] \tag{2.76}$$

where m is the mass per unit length of the beam. According to the authors, for practical ranges of prestressing force the N/A_b term is negligible compared to the E_b term. Furthermore, it is also pointed out that the magnitude of the I_c term is negligible compared to the magnitude of the I_b term. As a result, the authors conclude, from mathematical modelling that the effect of the prestress force on the beam bending frequencies is negligible (Dall'Asta and Dezi, 1996);

$$\omega_n^2 \approx \frac{n^4\pi^4}{mL^4}E_bI_b \tag{2.77}$$

2.7. Jain and Goel (1996) model

Jain and Goel (1996), in their discussion in response to the paper presented by Saiidi et al. (1994), state, as both Deák (1996) and Dall'Asta and Dezi (1996) suggested, that an externally applied compressive axial force softens a beam laterally and the natural vibration frequencies decrease. Jain and Goel also state, like Deák and Dall'Asta and Dezi before, that this cannot be applied to the situation where the axial force is applied by prestressing cables that are themselves anchored to the end faces of the beam, making

the axial force an internal force of the system. The authors illustrate this by deriving the first natural vibration frequency of a simply supported beam by energy methods. Since the fundamental mode shape of a simply-supported uniform beam with and without axial force is sinusoidal, the exact value of fundamental frequency can be obtained by equating the maximum kinetic energy of the system to the maximum potential energy of the system. The beam deflection, $v(x,t)$, under the first mode may be expressed as (Jain and Goel, 1996);

$$v(x,t) = A \sin\left(\frac{\pi x}{\ell}\right) \sin \omega t \tag{2.78}$$

where A in the amplitude of vibration at midspan. The kinetic energy during vibration is described as;

$$\begin{aligned} KE &= \int_0^\ell \frac{1}{2} m \left(\frac{\partial^2 v}{\partial x^2}\right) \mathrm{dx} \\ &= \frac{1}{4} m \omega^2 A^2 \ell \cos^2 \omega t \end{aligned} \tag{2.79}$$

The potential energy in the beam is defined as the flexural deformation minus the work done by externally applied force due to movement of two ends of the beam;

$$\begin{aligned} PE &= \int_0^\ell \frac{1}{2} EI \left(\frac{\partial^2 v}{\partial t^2}\right) \mathrm{dx} - N \int_0^\ell \frac{1}{2} \left(\frac{\partial v}{\partial x}\right)^2 \mathrm{dx} \\ &= \left(\frac{\pi^4 EIA^2}{4\ell^3} - \frac{\pi^2 NA^2}{4\ell}\right) \sin^2 \omega t \end{aligned} \tag{2.80}$$

Equating Equations 2.79 and 2.80 Jain and Goel obtained the following, concurring with Equation 2.1 obtained by Tse et al. (1978);

$$\omega_1^2 = \frac{\pi^4 EI}{m\ell^4} - \frac{\pi^2 N}{m\ell^2} \tag{2.81}$$

Jain and Goel argue that for the case where the axial force is applied by the use of prestressing tendons, there is no externally applied axial load and as a result, the second term in Equation 2.81 does not appear and therefore

the equation reduces to the following;

$$\omega_1^2 = \frac{\pi^4 EI}{m\ell^4} \tag{2.82}$$

Equation 2.82 is the equation for the natural frequency of a simply supported beam, and therefore Jain and Goel conclude that the natural frequency of a simply supported prestressed beam is independent of the magnitude of the prestressing force.

2.8. Tension-Strength model, (Kim et al., 2004)

Kim et al. (2004) report on a non-destructive method to detect prestress loss in beam-type prestressed concrete bridge structures. An analytical model is formulated to estimate changes in the natural frequency of prestressed concrete bridges according to changes in the magnitude of the prestressing force. In addition, an inverse solution algorithm is presented in order to predict prestress loss based on measured changes in natural frequency. This section sets out to explore the utilisation of tracking changes in the dynamic modal properties of a structure as a non-destructive means of damage detection. Kim et al. point out that prestressing force is introduced in order to control crack initiation, reduce deflection and to add strength to prestressed members. Prestress loss occurs due to elastic shortening and bending of concrete, creep and shrinkage of concrete, steel relaxation, anchorage pull-in and frictional loss between the tendon and surrounding materials (Kim et al., 2004). The authors point out that unless a prestressed structure, such as a prestressed bridge, is instrumented at the time of construction, the prestress force cannot be directly monitored and therefore alternative methods must be sought. According to Kim et al., the non-destructive evaluation methods from previous works such as Saiidi et al. (1994), Miyamoto et al. (2000), Saiidi et al. (1996) is based on the following considerations;

1. the loss of prestress force in the structure is related to the change in structural stiffness,

2. the loss of prestress force changes the vibration characteristics of the structure, and,

3. the change in structural stiffness can be estimated by monitoring changes in vibration characteristics of the structure.

2.8.1. Prestressed beam model

Kim et al. (2004) presents an alternative tension-strength model with straight concentric tendons, in which the change in length of the prestressed concrete beam due to prestressing force is modelled. The model is outlined in Figures 2.10, 2.11 and 2.12 (Kim et al., 2004). The axial shortening of the PSC beam due to prestressing force is modelled, resulting in a decrease of span length;

$$\delta L = L - L_r \tag{2.83}$$

There is also an expansion of the cross section due to Poisson's effect. The composite flexural rigidity of the prestressed beam is given as the sum of the flexural rigidity of the tendon plus the flexural rigidity of the concrete beam section such that;

$$E_r I_r = E_{conc} I_{conc} + E_s I_s \tag{2.84}$$

The governing differential equation, as presented by Kim et al. (2004) is given by;

$$\frac{\partial^2}{\partial x^2}\left(E_r I_r \frac{\partial^2 y}{\partial x^2}\right) + m_r \frac{\partial^2 y}{\partial t^2} = 0 \tag{2.85}$$

m_r is the mass per unit length of the prestressed beam in kg/m and is given as the sum of the mass per unit length of the prestressing tendon plus the mass per unit length of the concrete beam section;

$$m_r = \rho_c A_{conc} + \rho_s A_s \tag{2.86}$$

The authors derive the equivalent flexural rigidity of the tendon by analysing the flexural vibration of a cable under uniform tension, and produce the governing differential equation;

$$-N\frac{\partial^2 y}{\partial x^2} + \rho_s A_s \frac{\partial^2 y}{\partial t^2} = 0 \tag{2.87}$$

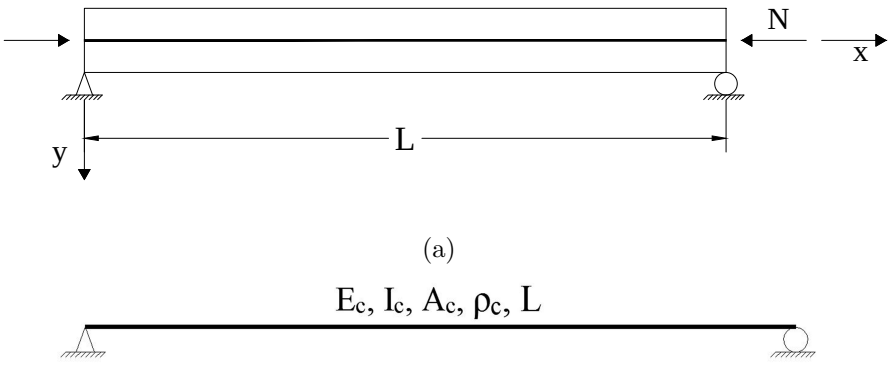

(a)

(b)

Figure 2.10.: (a) PSC beam under axial force (Kim et al., 2004); (b) Euler-Bernoulli beam under axial force (Kim et al., 2004)

Many authors (Kim et al., 2004; Miyamoto et al., 2000; Saiidi et al., 1994) consider that no successful attempt has yet been made to determine the relationship between prestress loss and the change in modal parameters. The equivalent flexural rigidity of the tendon is derived by analysing the flexural vibration of a cable under uniform tension (Kim et al., 2004);

$$\omega_{n_c}^2 = \left(\frac{n\pi}{L_r}\right)^2 \frac{N}{\rho_s A_s} \tag{2.88}$$

It is then assumed that there is a beam equivalent to the cable under tension with the same modal properties and the n^{th} natural frequency is given as;

$$\omega_{n_c}^2 = \left(\frac{n\pi}{L_r}\right)^4 \frac{E_s I_s}{\rho_s A_s} \tag{2.89}$$

Through equating Equation 2.88 and 2.89, the equivalent flexural rigidity of the tendon is obtained as a function of the prestressing force, N;

$$E_s I_s = \left(\frac{L_r}{n\pi}\right)^2 N \tag{2.90}$$

the following is therefore obtained (Kim et al., 2004);

$$E_r I_r = E_{conc} I_{conc} + \left(\frac{L_r}{n\pi}\right)^2 N \tag{2.91}$$

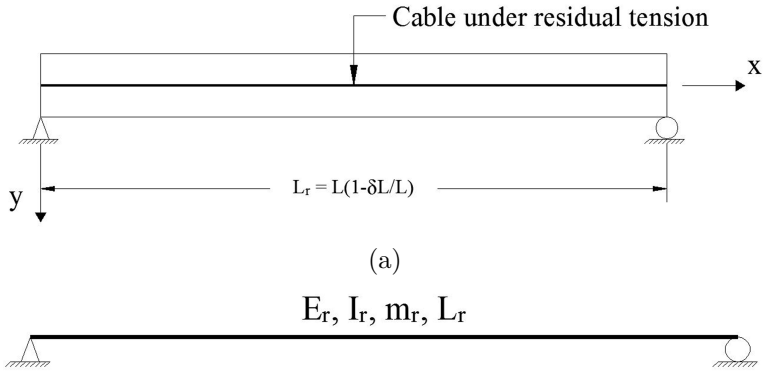

(a)

(b)

Figure 2.11.: (a) PSC beam under initial deformation (Kim et al., 2004); (b) Beam of equivalent flexural rigidity (Kim et al., 2004)

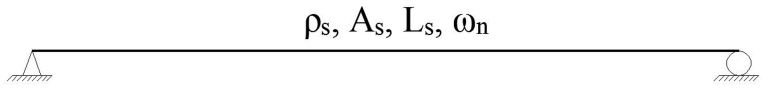

(a)

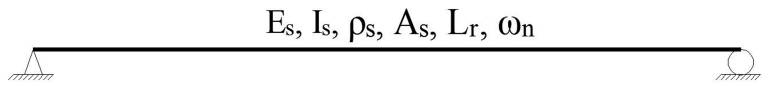

(b)

Figure 2.12.: (a) Cable under tension load (Kim et al., 2004); (b) Beam with equivalent flexural rigidity (Kim et al., 2004)

$E_r I_r$ is assumed to be constant along the entire length of the beam. Applying appropriate boundary conditions to the governing differential equation and substituting for $E_r I_r$, the following equation is obtained for the change in natural frequency of a simply supported prestressed beam with magnitude of prestressing force, according to the *"tension-strength"* model as proposed by Kim et al. (2004);

$$\omega_n^2 = \left(\frac{n\pi}{L_r}\right)^4 \frac{1}{m_r} \left(E_{conc} I_{conc} + \left(\frac{L_r}{n\pi}\right)^2 N \right) \tag{2.92}$$

where L_r is the length of the prestressed beam following elastic shortening,

in accordance with normal strain, given as;

$$\begin{aligned} L_r &= L\left(1 - \frac{\delta L}{L}\right) \\ &= L\left(1 - \frac{N}{A_{conc}E_{conc}}\right) \end{aligned} \tag{2.93}$$

Kim et al. (2004) state that when $A_{conc}/L_r^2 << 1$, the axial compression effect is negligible if the prestressing force, N, is less than the yielding condition. Furthermore, it is pointed out that in the *"residual-tension"* model outlined, the effective flexural rigidity of the beam is written in terms of the deformed beam span length and the magnitude of the prestressing force, and hence the natural frequency of the beam can be inferred.

2.8.2. Inverse Solution

The inverse solution to Equation 2.92 is presented by Kim et al. (2004) as a means of monitoring the structural health of the beam;

$$(N)_n = \omega_n^2 m_r \left(\frac{L_r}{n\pi}\right)^2 - E_{conc}I_{conc}\left(\frac{n\pi}{L_r}\right)^2 \tag{2.94}$$

Having calculated N from Equation 2.94, it can be substituted back into Equation 2.91 to obtain the equivalent flexural rigidity of the beam section and hence monitor the structural health of the prestressed beam. By assuming no change in the beam's geometry and material properties occur due to changes in the prestressing force, the authors obtain the first variation of the prestress force;

$$(\delta N)_n = \delta\omega_n^2 m_r \left(\frac{L_r}{n\pi}\right)^2 \tag{2.95}$$

where $(\delta N)_n$ is the change in the prestressing force that can be identified by the n^{th} mode and $\delta\omega_n^2$ is the change in the square of the n^{th} natural frequency due to prestress loss (Kim et al., 2004). Kim et al. express the relative change in prestress force that can be identified by the n^{th} mode as;

$$\left(\frac{\delta N}{N}\right)_n = \frac{\delta\omega_n^2 m_r \left(\frac{L_r}{n\pi}\right)^2}{\omega_n^2 m_r \left(\frac{L_r}{n\pi}\right)^2 - E_{conc}I_{conc}\left(\frac{n\pi}{L_r}\right)^2} \tag{2.96}$$

rearranging, the following is obtained;

$$\left(\frac{\delta N}{N}\right)_n = \frac{\delta\omega_n^2}{\omega_n^2 - \bar{\omega_n}^2} \tag{2.97}$$

where $\bar{\omega_n}$ is the virgin natural frequency (i.e. the natural frequency of a simply supported beam with zero prestressing force) and is given as;

$$\bar{\omega_n}^2 = \left(\frac{n\pi}{L_r}\right)^4 \frac{E_{conc}I_{conc}}{m_r} \tag{2.98}$$

2.8.3. Verification of Model vs. Saiidi et al. (1994)

Kim et al. (2004) applied the analytical *"tension-strength"* model outlined in Equation 2.92 to a beam with identical properties to that tested by Saiidi et al. (1994) and compared the results. It was found that for the first mode, the analytical model over-predicted the natural frequencies by an average of 4.4%. For the second mode, it was found that the analytical *"tension-strength"* model under-predicted the natural frequencies by an average of 4.8%. The results obtained by Kim et al. (2004) are outlined in Table 2.3.

2.8.4. Detection of prestress loss

Prestress loss is detected from an inverse solution of the prestressed concrete beam models. The authors measure the relative change in prestressing force using the formula:

$$\frac{\delta N}{N_f} = \frac{\delta\omega_n^2}{\omega_{nf}^2 - \bar{\omega_n^2}} = \frac{\omega_{nf}^2 - \omega_{nd}^2}{\omega_{nf}^2 - \bar{\omega_n^2}} \tag{2.99}$$

where $\bar{\omega_n}$ is the theoretical natural frequency with prestress force, $N = 0$. It was found that for prestress loss prediction, the analytical model provided a better approximation than the FE model.

2.8.5. Conclusions

A methodology to non-destructively detect prestress loss in PSC structures has been presented by Kim et al. (2004). An analytical model to estimate natural frequencies of prestressed concrete bridges under various prestress forces was developed, the so-called *"tension-strength"* model. Finally, Kim et al. produced an inverse-solution algorithm to predict prestress-loss in

Table 2.3.: Results obtained by Kim et al. (2004)

Case	PS (kN)	Exp. Freq. (Hz) (Saiidi et al., 1994)		Kim et al. (2004) Model Pred. Freq. (Hz)				Kim et al. (2004) FE Pred. Freq. (Hz)			
		f_1	f_2	f_1	f_2	f_1 % d.	f_2 % d.	f_1	f_2	f_1 % d.	f_2 % d.
(1)	(2)	(3)	(4)	(5)	(6)	(7)	(8)	(9)	(10)	(11)	(12)
1	0.00	11.41	43.99	11.41	45.64	0.0%	-3.7%	11.20	44.05	1.9%	-0.1%
2	15.71	12.09	44.11	11.83	46.06	2.1%	-4.4%	11.69	44.55	3.3%	-1.0%
3	27.05	13.47	44.89	12.13	46.37	10.0%	-3.3%	12.03	44.89	10.7%	0.0%
4	36.49	12.89	44.69	12.37	46.63	4.0%	-4.3%	12.31	45.16	4.5%	-1.1%
5	57.25	13.63	45.62	12.89	47.18	5.5%	-3.4%	12.90	45.74	5.3%	-0.3%
6	81.81	14.49	45.57	13.47	47.83	7.1%	-5.0%	13.57	46.40	6.4%	-1.8%
7	91.26	14.72	46.32	13.69	48.07	7.0%	-3.8%	13.82	46.65	6.1%	-0.7%
8	121.46	14.72	45.86	14.36	48.85	2.4%	-6.5%	14.58	47.40	1.0%	-3.4%
9	130.91	14.97	46.10	14.57	49.10	2.7%	-6.5%	14.81	47.62	1.1%	-3.3%
10	132.80	15.07	45.87	14.61	49.15	3.1%	-7.1%	14.86	47.67	1.4%	-3.9%

PSC structures. Kim et al. (2004) produced an analytical model showing that the natural vibration frequencies of a prestressed concrete structure increase with increasing prestressing force, in accordance with the test results obtained by Saiidi et al. (1994).

2.9. Zhang and Li (2007) model

Zhang and Li (2007) conducted dynamic testing on three bonded and two unbonded fully prestressed concrete beams. The results of the testing indicate that the frequency of PSC beams increase with increasing prestressing force magnitude, in line with the findings of other authors (Hop, 1991; Kim et al., 2004; Saiidi et al., 1994). The authors state that the results differ from the *"compression-softening"* theory as a prestressed concrete beam cannot be considered to be an isotropic, homogeneous, linear elastic material, nor can it be considered to be externally axially loaded, therefore *"compression-softening"* theory is not valid. Rather an orthotropic linear-elastic model has been formulated to analyse the relationship between prestress force magnitude and natural bending frequency of prestressed concrete beams (Zhang and Li, 2007). In the mathematical model presented, the prestressing tendon is considered to carry an axial tension, N_T, whereas the concrete and the ordinary reinforcing steel are considered to carry an axial compression, N_T. Since the cross sectional area and second moment of area of the prestressing strand is much smaller than the concrete beam and the diameter is much smaller than it's length, the authors neglect the effect of moment inertia and shear deformation of the prestressing strand, and include only the effect of bending deformation stiffness in analysing beam vibration. The equivalent stiffness of the prestressing tendon, $E_s I_s$, is given by Kim and Stubbs (2002) and Kim et al. (2004) as;

$$E_s I_s = \frac{\ell^2 N_T}{(n\pi)^2} \tag{2.100}$$

As a result, Zhang and Li (2007) give the bending stiffness of the prestressed concrete beam as;

$$EI_{eff} = E_c I_c + \left(\frac{\ell}{n\pi}\right)^2 N \tag{2.101}$$

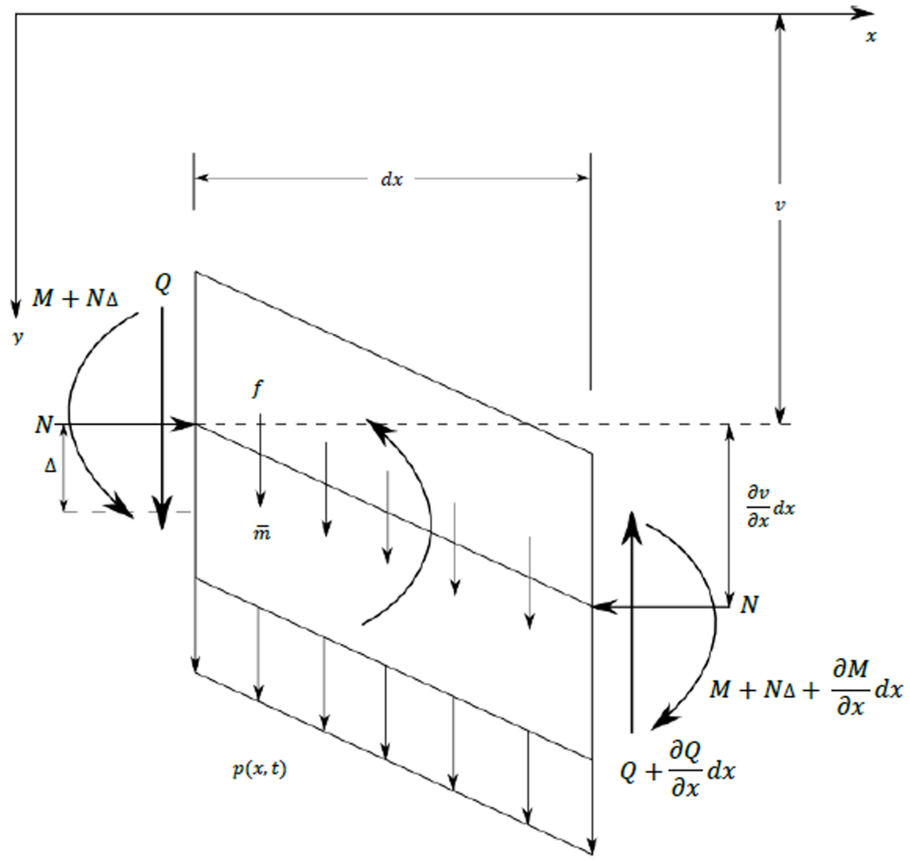

Figure 2.13.: Free Body Diagram; Zhang and Li (2007) model

Figure 2.13 shows the free-body diagram derived by Zhang and Li (2007) to derive their final equation of motion of a prestressed concrete beam. Letting the X axis lie through the centroid of the beam cross section, with right corresponding with the positive X direction, and the Y axis is positive vertically downwards, then the positive Z axis agrees with the right-hand rule. Zhang and Li express the displacement components of the beam as;

$$\begin{cases} U(x,y,z,t) = u(x,t) + y\varphi(x,t) \\ V(x,y,z,t) \cong v(x,t) \end{cases} \tag{2.102}$$

$u(x,t)$ is the plane displacement along the X axis and $\varphi(x,t)$ is the angular displacement of the cross section along the abscissa, x. $v(x,t)$ is the sectional

displacement along the Y axis. The normal and shear strain is given as;

$$\begin{cases} \epsilon_x = \dfrac{\mathrm{dU}}{\mathrm{dx}} = \dfrac{\mathrm{du}}{\mathrm{dx}} + y\dfrac{\mathrm{d}\varphi}{\mathrm{dx}} \\ \gamma_{xy} = \dfrac{\mathrm{dU}}{\mathrm{dy}} + \dfrac{\mathrm{dV}}{\mathrm{dx}} = \varphi(x,t) + \dfrac{\mathrm{dv}}{\mathrm{dx}} \end{cases} \tag{2.103}$$

Hooke's Law states;

$$\begin{Bmatrix} \epsilon_x \\ \gamma_{xy} \end{Bmatrix} = \begin{bmatrix} s_{11} & s_{16} \\ s_{61} & s_{66} \end{bmatrix} \begin{Bmatrix} \sigma_x \\ \tau_{xy} \end{Bmatrix} \tag{2.104}$$

where s_{11}, s_{16}, s_{61} and s_{66} are *'softness factors'*. Zhang and Li then substitute Equation 2.103 into Equation 2.104 and take the surface integral. The authors then multiply y to both sides of the equation and take the surface integral again, obtaining the following;

$$\begin{cases} \varphi + \dfrac{\mathrm{dv}}{\mathrm{dx}} = s_{16}\dfrac{T_x}{A_c} + s_{66}\dfrac{Q_y}{A_c} \\ I_c\dfrac{\mathrm{d}\varphi}{\mathrm{dx}} = s_{11}M_z + s_{16}\displaystyle\iint_A \tau_{xy} y \mathrm{dA_c} \end{cases} \tag{2.105}$$

T_x is the tensile stress along the X axis, Q_y is the shear stress along the Y axis, M_z is the bending moment about the Z axis, I_c is the second moment of area of the beam cross section about the Z axis, and A_c is the cross sectional area of the concrete beam. When the equivalent stiffness of the prestressed tendon is added to the flexural stiffness of the prestressed concrete beam, Equation 2.105 becomes (Zhang and Li, 2007);

$$\begin{cases} Q_y = k\dfrac{A_c}{s_{66}}\left(\varphi + \dfrac{\mathrm{dv}}{\mathrm{dx}}\right) \\ M_z = \left(\dfrac{I_c}{s_{11}} + \left(\dfrac{\ell}{n\pi}\right)^2 N\right)\dfrac{\mathrm{d}\varphi}{\mathrm{dx}} \end{cases} \tag{2.106}$$

k is the effective shear factor. The relationship between Q_y and M_z is;

$$\begin{cases} M_z + N\Delta + Q_y\mathrm{dx} - N\dfrac{\partial v}{\partial x} + \rho I_c\dfrac{\partial^2\varphi}{\partial t^2}\mathrm{dx} - \left(M_z + N\Delta + \dfrac{\partial M_z}{\partial x}\mathrm{dx}\right) = 0 \\ Q_y + \rho A_c\dfrac{\partial^2 v}{\partial t^2}\mathrm{dx} + p(x,t) - \left(Q_y + \dfrac{\partial Q_y}{\partial x}\right) = 0 \end{cases} \tag{2.107}$$

where $\rho I_c \frac{\partial^2 \varphi}{\partial t^2}$ is the *"inertia force of inertia moment"*. $N\Delta$ is the moment due to eccentricity. The inertial force per unit length, $\rho A_c \frac{\partial^2 v}{\partial t^2}$, is considered to be negligible by Zhang and Li (2007). The self-weight of the beams are also ignored. Equation 2.104 is further simplified as;

$$\begin{cases} \dfrac{\partial M_z}{\partial x} + N\dfrac{\partial v}{\partial x} - Q_y = \rho I_c \dfrac{\partial^2 \varphi}{\partial t^2} \\ \dfrac{\partial Q_y}{\partial x} = \rho A_c \dfrac{\partial^2 v}{\partial t^2} \end{cases} \tag{2.108}$$

Substituting Equation 2.106 into Equation 2.108 the following is obtained;

$$\begin{cases} \left(\dfrac{I_c}{s_{11}} + \left(\dfrac{l}{n\pi} \right)^2 N \right) \dfrac{\partial^2 \varphi}{\partial x^2} + N\dfrac{\partial v}{\partial x} - \dfrac{kA_c}{s_{66}} \left(\varphi + \dfrac{\partial v}{\partial x} \right) - \rho I_c \dfrac{\partial^2 \varphi}{\partial t^2} = 0 \\ \dfrac{kA_c}{s_{66}} \left(\dfrac{\partial \varphi}{\partial x} + \dfrac{\partial^2 v}{\partial x^2} \right) - \rho A_c \dfrac{\partial^2 v}{\partial t^2} = 0 \end{cases} \tag{2.109}$$

Following the application of kinematic relations and Hooke's law, Zhang and Li obtain expressions for shear force and bending moment as a function of distance along the horizontal axis of the beam (x). Furthermore, following a force balance on an infinitesimal segment of the prestressed concrete beam, and substituting for flexural rigidity and the assumed mode shapes of vibration, the governing equations of motion for the beam are obtained (Zhang and Li, 2007);

$$\begin{aligned} \rho^2 I_c \frac{s_{66}}{k} \omega^4 - \left(\rho A_c + \rho I_c \left(\frac{n\pi}{\ell} \right)^2 \left(\frac{s_{66}}{k s_{11}} + 1 \right) \right) \omega^2 + \\ \left(\frac{I_c}{s_{11}} + \left(\frac{\ell}{n\pi} \right)^2 N \right) \left(\frac{n\pi}{\ell} \right)^4 + \left(\frac{n\pi}{\ell} \right)^2 N = 0 \end{aligned} \tag{2.110}$$

The softness factors are given as $s_{11} = 1/E$, $s_{66} = 2(1+\nu)/E$, $I_z = I_c$ Zhang and Li (2007). Poisson's ratio is given as $\nu = 0.2$, and the effective shear factor as $k = 1.2$. Equation 2.110 then becomes;

$$\begin{aligned} \rho^2 I_c \frac{2}{E} \omega^4 - \left(\rho A_c + 3\rho I_c \left(\frac{n\pi}{\ell} \right)^2 \right) \omega^2 + \\ \left(E_c I_c + \left(\frac{\ell}{n\pi} \right)^2 N \right) \left(\frac{n\pi}{\ell} \right)^4 + \left(\frac{n\pi}{\ell} \right)^2 N = 0 \end{aligned} \tag{2.111}$$

ω is calculated from Equation 2.111 by deleting two imaginary numbers and one irrational item. The results indicated an increase in natural frequency with increasing prestress force and the analytical prediction for the first bending mode agree well with the experimental results (Zhang and Li, 2007). It should be pointed out however that solution of Equation 2.111 in it's current guise does not lend itself to the conclusion that an increase in the magnitude of the prestressing force, N, leads to an increase in the natural bending frequency of prestressed concrete beams. By making the substitutions;

$$\begin{aligned} A &= \rho^2 I_c \frac{2}{E} \\ B &= -\left(\rho A_c + 3\rho I_c \left(\frac{n\pi}{\ell}\right)^2\right) \\ C &= \left(E_c I_c + \left(\frac{\ell}{n\pi}\right)^2 N\right)\left(\frac{n\pi}{\ell}\right)^4 + \left(\frac{n\pi}{\ell}\right)^2 N \\ \lambda &= \omega^2 \end{aligned} \tag{2.112}$$

Equation 2.111 becomes;

$$A\lambda^2 + B\lambda + C = 0 \tag{2.113}$$

The real solution of Equation 2.111 is therefore given by;

$$\omega = \sqrt{\frac{-B + \sqrt{B^2 - 4AC}}{2A}} \tag{2.114}$$

The C term increases linearly with increasing magnitude of prestressing force, N, therefore, the determinant $\left(B^2 - 4AC\right)$ must decrease with increasing C. As a result, it must be concluded from this model that the natural frequency of prestressed concrete structures must decrease with increasing prestress force magnitude, N, contrary to what has been reported by Zhang and Li (2007).

2.10. Non-linear kinematic modelling, (Hamed and Frostig, 2006)

Hamed and Frostig produce a non-linear kinematic model presenting the

effect that the magnitude of the prestressing force has on the natural frequency of prestressed concrete beams with both bonded and unbonded tendons. The equations of motion for the prestressed beam and associated boundary and continuity conditions are rigorously derived using the variational principle of virtual work following Hamilton's principle (Hamed and Frostig, 2006);

$$\int_{t_1}^{t_2} \delta \left(T - (U + V)\right) \mathrm{dt} = 0 \tag{2.115}$$

where T is the kinetic energy, U is the internal potential energy, V is the external potential energy and δ is the variational operator. The authors state that the mathematical model derived is rigorous and general, and valid for any type of boundary and continuity conditions, as well as tendon profile. The kinematic assumptions made by Hamed and Frostig (2006) are those of large displacements and moderate rotations, in order to take into account the compressive force effect caused by the prestress force. It should be noted that for the case of free vibration, $V = 0$. The non-linear kinematic model contains the $\left(\frac{dw}{dx}\right)^2$ term, which is omitted by Dall'Asta and Dezi (1996) when using Kirchhoff's kinematic model of small displacements. u_o is the longitudinal deformation of the beam at the centroid, w is the vertical deformation of the concrete beam, u is the longitudinal deformation of the concrete beam. w_{cab} and u_{cab} are the vertical and longitudinal deformations of the cable respectively (Hamed and Frostig, 2006);

$$\epsilon_{xx}(x, z) = \frac{du_o}{dx} + \frac{1}{2}\left(\frac{dw}{dx}\right)^2 - z\frac{d^2w}{dx^2} \tag{2.116}$$

The prestressing tendon is also subject to the same kinematic relations of large displacements and moderate rotations;

$$\epsilon_{xx,cab}(x, z_{cab}) = \frac{du_{cab}}{dx} + \frac{1}{2}\left(\frac{dw_{cab}}{dx}\right)^2 - \left(\frac{dz_{cab}}{dx}\right)\left(\frac{dw_{cab}}{dx}\right) \tag{2.117}$$

Comparing Equation 2.116 with the kinematic relations derived by Dall'Asta and Dezi, it can be seen that Dall'Asta and Dezi have ignored the non-linear $\left(\frac{dw}{dx}\right)^2$ term. They have used Kirchhoff's kinematic model, which considers only small deformations and rotations, whereas the kinematic model used

by Hamed and Frostig (2006) considers large displacements and moderate rotations.

Hamed and Frostig point out the shortcomings of previous similar studies conducted on the effect that the prestress force has on the natural vibration frequencies of prestressed concrete beams. Firstly, Hamed and Frostig point out that Saiidi et al. (1994) have not considered the perturbed cable tension and eccentricity due to beam vibrations, and therefore the use of Equation 2.1 is erroneous. The authors argue that Dall'Asta and Dezi (1996) produce a linear kinematic model only and therefore the non-linear effects associated with the non-linear change in eccentricity of the compressive force in the concrete beam and the tension force in the tendon are beyond the capabilities of the proposed model. This is outlined in Equation 2.118;

$$\epsilon_{xx}(x,z) = \frac{du_o}{dx} - z\frac{d^2w}{dx^2} \tag{2.118}$$

Hamed and Frostig also claim that despite Deák (1996) stating that the prestress force does not reduce the natural frequency of prestressed concrete beams, it is not supported by any analytical or mathematical proof. Similarly, it is argued that despite Jain and Goel (1996) arguing that the prestress force is internal to the beam section and therefore cannot act as to reduce the natural frequency of prestressed concrete beams, it lacks an appropriate mathematical model to verify the argument. Hamed and Frostig state that Raju and Rao (1986) show that the prestress force reduces the natural frequencies of lower modes based on a Rayleigh-Ritz formulation that describes the prestress force as an external axial force only. Miyamoto et al. (2000) produced an incremental formulation of the equations of motion of a prestressed composite girder and have included the change in tendon force along with compressive force along the girder. They calculated that the natural frequencies decrease as the amount of prestressing force increases, however, Hamed and Frostig argues that this is due to the fact that the change in tendon eccentricity has been ignored. Dall'Asta and Leoni (1999) have presented a general formulation for the vibration of beams prestressed with internal frictionless cables. As highlighted by Hamed and Frostig, again the model is based on kinematic relations of small displacements and the formulation for the beam does not include the effect of the compressive force and therefore yields erroneous results. Despite not considering

the compressive force effects, Dall'Asta and Leoni (1999) indicate that the natural frequency decreases as the prestress force increases. Finally, Hamed and Frostig offers a critique on Kerr (1976). Kerr (1976) uses a linear formulation for the study of the dynamic response of a prestressed beam. It is argued by Hamed and Frostig that this simple linear analysis is not able to determine the change in cable force and eccentricity during vibration of the beam and it is limited to straight cables that pass directly through the centroid of the beam.

Mathematical Model - Bonded Tendons

The following is the mathematical model as derived by Hamed and Frostig (2006) for the case of a prestressed concrete beam with bonded tendons. Hamilton's principle, as set out in Equation 2.115 requires that;

$$\delta L = \int_{t_1}^{t_2} \delta \left(T - (U + V) \right) = 0 \tag{2.119}$$

The first variation of kinetic energy is given by;

$$\delta T = \int_{V_{beam}} \rho \dot{w} \delta \dot{w} \mathrm{dv} \tag{2.120}$$

ρ is the mass density of the concrete. The mass of the cable is neglected. w is the displacement of the beam in the vertical direction, therefore $\dot{w}$ as the first time derivative of the displacement, is the velocity of the beam in the vertical direction. V_{beam} is the volume of the concrete beam. The first variation of the internal potential energy is;

$$\begin{aligned} \delta U = & \int_{V_{beam}} \sigma_{xx} \delta \epsilon_{xx} \mathrm{dv} + \int_{V_{cab}} \sigma_{xx,cab} \delta \epsilon_{xx,cab} \mathrm{dv} \\ & + \int_0^{\ell} \delta \left[\lambda_1(x)(w - w_{cab}) \right] \mathrm{dx} + \int_0^{\ell} \delta \left[\lambda_2(x)(u - u_{cab}) \right] \mathrm{dx} \end{aligned} \tag{2.121}$$

where σ_{xx} is the longitudinal normal stress in the concrete beam, $\sigma_{xx,cab}$ is the stress in the cable, ϵ_{xx} is the longitudinal normal strain in the concrete beam, $\epsilon_{xx,cab}$ is the strain in the cable, V_{cab} is the volume of the cable and $\lambda_1(x)$ and $\lambda_2(x)$ are Lagrange multipliers. The Lagrange multipliers are actually the vertical and longitudinal components of the force that the

prestress cable exerts on the concrete beam, and they impose identical deformations on the concrete beam and the cable (Hamed and Frostig, 2006). w_{cab} and u_{cab} are the vertical and longitudinal deformations of the cable respectively. w is the vertical deformation of the concrete beam and u is the longitudinal deformation so that;

$$u = u_0 - z_{cab}\frac{dw}{dx} \tag{2.122}$$

u_0 is the longitudinal deformation of the concrete beam at its centroid and z_{cab} is the cable eccentricity measured downwards from the centre of gravity of the concrete beam. The governing equations of motion and associated boundary and continuity conditions are derived by Hamed and Frostig (2006) using Equations 2.119, 2.120, 2.121, 2.122 along with the kinematic relations of large displacements and moderate rotations as outlined in Equations 2.116 and 2.117. After significant algebraic manipulations, integration by parts, and acknowledging that the unknown deformations will take the following form in the case of free vibrations;

$$w(x,t) = w(x)sin(\omega t + \phi) \tag{2.123}$$

The equations of motion are reduced to two non-linear governing equations as follows;

$$\begin{aligned} m\omega^2 w + \frac{d^2 M_{xx}}{dx^2} + \frac{d}{dx}\left((N_{xx,cab} + N_{xx})\frac{dw}{dx}\right) \\ + \frac{d}{dx}\left(N_{xx,cab}\frac{dz_{cab}}{dx}\right) - \frac{d}{dx}\left(\frac{dN_{xx}}{dx}z_{cab}\right) = 0 \end{aligned} \tag{2.124}$$

$$\frac{dN_{xx}}{dx} + \frac{dN_{xx,cab}}{dx} = 0 \tag{2.125}$$

where;

$$N_{xx,cab} = EA_{cab}\left[\frac{N_{xx}}{EA} - z_{cab}\frac{d^2 w}{dx^2}\right] \tag{2.126}$$

Hamed and Frostig outline that in general the equations are non-linear with variable coefficients and are solved using the Multiple Shooting Method, which is a numerical algorithm for the solution of an ordinary differential equation (ODE) boundary value problem (Stoer and Bulirsch, 2010). The

authors have shown that one of the boundary conditions is given by;

$$N_{xx} + N_{xx,cab} = 0 \tag{2.127}$$

Hamed and Frostig state that hence the global axial force in the prestressed beam is null throughout the length of the beam, changing Equation 2.124 to a linear differential equation;

$$m\omega^2 w + \frac{d^2 M_{xx}}{dx^2} + \frac{d}{dx}\left(N_{xx,cab}\frac{dz_{cab}}{dx}\right) - \frac{d}{dx}\left(\frac{dN_{xx}}{dx}z_{cab}\right) = 0 \tag{2.128}$$

It is argued that despite the last two terms surviving, they are linear terms with variable coefficients as the eccentricity of the cable, z_{cab} is a known function. The authors go on to state that as a result, the principle of superposition may be applied for all solution steps and the solution of the free vibration problem of a prestressed beam does not require considering the stresses that exist in the beam prior to vibration. As a result, Hamed and Frostig (2006) conclude that the magnitude of the prestress force does not effect the natural frequencies of bonded pre-stressed beams.

Hamed and Frostig (2006) then go on to formulate the above result incrementally and hence compare the formulation to the mathematical models created by Saiidi et al. (1994), Raju and Rao (1986), Miyamoto et al. (2000), Chan and Yung (2000) and Dall'Asta and Dezi (1996). After applying Hamilton's principle for an incremental formulation and neglecting the second order terms (Δ^2), the equations of motion change into the following two governing differential equations;

$$m\omega^2 \Delta w + \Delta\frac{d^2 M}{dx^2} + \frac{d}{dx}\left(\Delta N_{xx,cab}\frac{dz_{cab}}{dx}\right) - \frac{d}{dx}\left(\Delta\frac{dN_{xx}}{dx}z_{cab}\right) \tag{2.129}$$

$$\Delta\frac{dN_{xx}}{dx} + \Delta\frac{dN_{xx,cab}}{dx} = 0 \tag{2.130}$$

where;

$$\Delta N_{xx,cab} = EA_{cab}\left[\frac{\Delta N_{xx}}{EA} - z_{cab}\Delta\frac{d^2 w}{dx^2}\right] \tag{2.131}$$

As before, the authors state that these equations reveal that the effect of the static axial force disappears and therefore the magnitude of the prestress force does not affect the natural frequencies of prestressed concrete beams. Hamed and Frostig then proceed to compare the above model to others formulated in the literature. The authors categorise the models into two distinct types; the *"compressed beam"* model, as in Saiidi et al. (1994), Raju and Rao (1986), Miyamoto et al. (2000) and Chan and Yung (2000), and the *"small displacement"* kinematic model (Dall'Asta and Dezi, 1996). It is stated that the compressed beam model does not consider the prestressing cable at all, and thus the equations of motion for the compressed beam model are formulated by omitting the equations of motion for the cable, yielding;

$$-m\Delta\ddot{w} + \frac{d}{dx}\left(N_{xx}\Delta\frac{dw}{dx}\right) + \frac{d}{dx}\left(\Delta N_{xx}\frac{dw}{dx}\right) + \Delta\frac{d^2M}{dx^2} = 0 \tag{2.132}$$

$$\Delta\frac{dN_{xx}}{dx} = 0 \tag{2.133}$$

The second category is the *"small displacement"* kinematic model, as formulated by Dall'Asta and Dezi (1996). Hamed and Frostig point out that kinematic relations of small displacements are used for the concrete beam model, referred to as *"Kirchhoff's kinematic model"* by Dall'Asta and Dezi (1996). The kinematic relation is described by Equation 2.134;

$$\epsilon_{xx}(x,z) = \frac{du_0}{dx} - z\frac{d^2w}{dx^2} \tag{2.134}$$

As pointed out by Hamed and Frostig, the use of this kinematic relation cancels the non-linear terms in the governing equation of the concrete beam leading to the following equations of motion;

$$-m\Delta\ddot{w} + \Delta\frac{d^2M}{dx^2} - \Delta\lambda_1 - \frac{d}{dx}\left(\Delta\lambda_2 z_{cab}\right) = 0 \tag{2.135}$$

$$\Delta\frac{dN_{xx}}{dx} - \Delta\lambda_2 = 0 \tag{2.136}$$

$$\Delta\frac{dN_{xx,cab}}{dx} + \Delta\lambda_2 = 0 \tag{2.137}$$

$$\frac{d}{dx}\left(N_{xx,cab}\Delta\frac{dw_{cab}}{dx}\right)+\frac{d}{dx}\left(\Delta N_{xx,cab}\left(\frac{dz_{cab}}{dx}+\frac{dw_{cab}}{dx}\right)\right)+\Delta\lambda_1=0 \tag{2.138}$$

$$-\Delta w+\Delta w_{cab}=0 \tag{2.139}$$

$$-\Delta u_0+z_{cab}\Delta\frac{dw}{dx}+\Delta u_{cab}=0 \tag{2.140}$$

The authors point out that the magnitude of the static axial force in the cable prior to the vibration stage ($N_{xx,cab}$) affects the dynamic behaviour of the beam in this model. They suggest that although the beam vibrates in small displacements in service, a non-linear approach that accounts for large displacements and moderate rotations ought to be used in order to describe the effect of the axial forces in the tendons and the overall behaviour of the prestressed concrete beam.

Mathematical Model - Unbonded Tendons

A similar mathematical model is hence formulated by Hamed and Frostig (2006) for the case of unbonded tendons, using Hamilton's principle, however, a term is introduced in the first variation of internal potential energy taking into account the change in prestress force of the unbonded tendon, through a constraint stating that the change in length of the concrete fibre adjacent to the cable is equal to the change in length of the unbonded tendon as per Equation 2.141;

$$\delta U=\int_{V_{beam}}\sigma_{xx}\delta\epsilon_{xx}\mathrm{dv}+\int_{V_{cab}}\sigma_{xx,cab}\delta\epsilon_{xx,cab}\mathrm{dv}+\int_0^\ell\delta\left[\lambda_1(x)(w-w_{cab})\right]\mathrm{dx}+\delta\left[\lambda\left(\int_0^\ell\epsilon_{xx}(z=z_{cab})\mathrm{dx}-\int_0^\ell\epsilon_{xx,cab}\mathrm{dx}\right)\right] \tag{2.141}$$

where λ is the Lagrange multiplier representing the increase in the prestressing force. According to Hamed and Frostig, the increase is assumed to be uniform along the beam since there is no friction between the tendon and the concrete beam for unbonded tendons. The same kinematic relations of large displacements and moderate rotations have been used. Having ap-

plied Hamilton's principle as before and after a series of integration by parts, algebraic manipulations and application of the appropriate boundary conditions, the equations of motion are reduced to three non-linear governing equations as follows (Hamed and Frostig, 2006);

$$m\omega^2 w + \frac{d^2M}{dx^2} + \frac{d}{dx}\left((N_{xx,cab} + N_{xx})\frac{dw}{dx}\right) + N\frac{d}{dx}\left(N_{xx,cab}\frac{dz_{cab}}{dx}\right) = 0 \tag{2.142}$$

$$\frac{dN_{xx}}{dx} = 0 \tag{2.143}$$

$$\frac{dN_{xx,cab}}{dx} = 0 \tag{2.144}$$

As with the bonded case, Equation 2.143 and Equation 2.144 coupled with the boundary conditions;

$$N_{xx,cab} - \lambda = 0 \tag{2.145}$$

$$N_{xx} + \lambda = 0 \tag{2.146}$$

yields;

$$N_{xx}(x) + N_{xx,cab}(x) = 0 \tag{2.147}$$

As a result, like for the bonded case, the global axial force in the prestressed beam is null throughout its length, changing Equation 2.142 to a linear differential equation;

$$m\omega^2 w + \frac{d^2M}{dx^2} + N\frac{d}{dx}\left(N_{xx,cab}\frac{dz_{cab}}{dx}\right) = 0 \tag{2.148}$$

Hamed and Frostig (2006) conclude again that the solution of the free vibration problem of a prestressed beam with unbonded tendons does not require considering the stresses that exist in the beam prior to vibration, as the equations of motion are linear. This leads again to the conclusion that the magnitude of the prestress force does not affect the natural frequencies of prestressed beams with unbonded tendons also. As before, it is observed that the magnitude of the prestress force prior to vibration affects the natu-

ral vibration behaviour when small deflection theory is used, but as pointed out for the bonded case, the approach does not account for the non-linear effects of the compressed force (Hamed and Frostig, 2006).

Summary

Hamed and Frostig, in their dynamic analysis of vertical free vibration of prestressed concrete beams take into account compressive force effects and changes in prestress force and in cable eccentricity. The concrete beam model follows Euler-Bernoulli assumptions and moderate deformations, namely large displacements and moderate rotations. The constitutive relationships of the concrete and the prestressed concrete follow Hooke's law, and the effect of longitudinal vibrations and rotary inertia are considered negligible.

Having developed a non-linear kinematic, analytical model for the dynamic behaviour of uncracked prestressed concrete beams with bonded and unbonded tendons, and having rigorously derived the equations of motion and subsequent boundary and continuity conditions using the variational principle of virtual work following Hamilton's principle, it has been mathematically rigorously proven that the magnitude of the prestress force does not affect the natural frequencies of bonded or unbonded prestressed beams (Hamed and Frostig, 2006). As a result, it is proposed that the natural frequencies of bonded prestressed beams can be determined through linear elastic beam theory with an equivalent moment of inertia of the composite section, while the natural frequency of unbonded beams can be determined by the proposed model (Hamed and Frostig, 2006). It should be noted however, that no analysis has been conducted on the effect that the magnitude of the prestressing force has on crack closing and subsequent increase in stiffness of the beam section. Furthermore, the additional joint stiffness induced by the prestressing force for precast, post-tensioned concrete wind turbine towers cannot be captured by this model. Finally, the mathematical model is in disagreement with the dynamic testing carried out by Saiidi et al. (1994) and Hop (1991) to name but a few.

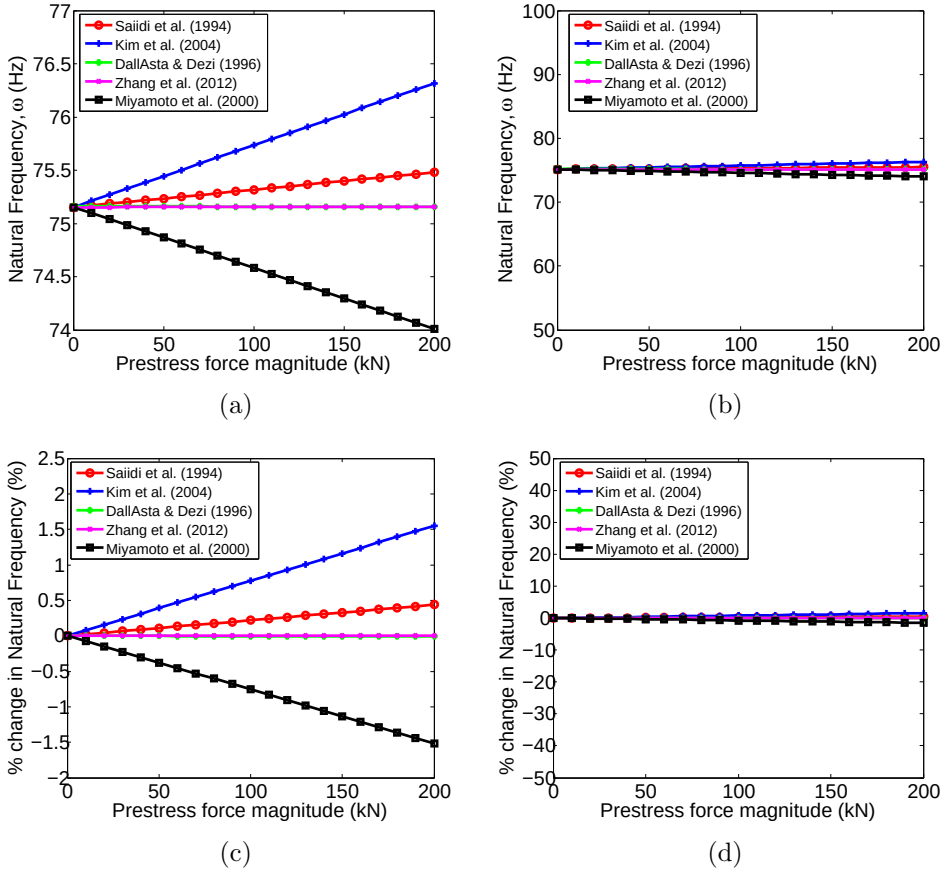

Figure 2.14.: (a)&(b) First Natural Frequency (Hz) with increasing PS force (kN) for different models; (c)&(d) % change in first Natural Frequency (Hz) with increasing PS force (kN) for different models

2.11. Summary of models

Figure 2.14 shows a graphical representation of the difference between the main models present in the literature (Dall'Asta and Dezi, 1996; Miyamoto et al., 2000; Kim et al., 2004; Saiidi et al., 1994; Zhang et al., 2012). Figures 2.14c and 2.14d indicate that the % change in natural frequency for the given (practical) prestress force levels of $0kN$ - $200kN$ is very small. The models predict a change in first natural bending frequency of the beam specified in Table 2.1 within the range of -1.5% to $+1.5\%$. It has been argued previously that the magnitude of the observed change in natural frequency is negligible (Dai and Chen, 2007; Dall'Asta and Dezi, 1996; Kerr, 1976).

Figure 2.9 indicates that including the effect of shear and rotary inertia can have a difference of 1.56%, which indicates that the inclusion of shear and rotary inertia is relatively just as important as prestress force effects in this practical range. Furthermore, the accuracy that structural engineers can predict the natural bending frequency of prestressed concrete beams is governed by boundary condition assumptions, and assumptions of the material properties that have a much greater uncertainty than the ±1.5% reported for this beam under the current range of prestress force magnitude.

Table 2.4.: Summary of the mathematical models presented in Figure 2.14

Author	Prediction Model
Kim et al. (2004)	$\omega_n^2 = \left(\frac{n\pi}{L_r}\right)^4 \frac{1}{m_r}\left(E_c I_c + \left(\frac{L_r}{n\pi}\right)^2 N\right)$
Saiidi et al. (1994)	$\omega_n^2 = (\frac{n\pi}{\ell})^4 \frac{\left(1+1.75\frac{N}{f'_c}\right)EI_g}{m}$
Zhang et al. (2012)	$\omega_n^2 = (\frac{n\pi}{\ell})^4 \frac{E_0\left(1+\frac{mN\ell^2}{250E_0I_0}\right)I}{m}$
Dall'Asta and Dezi (1996)	$\omega_n^2 = \frac{n^4\pi^4}{m\ell^4}\left[\left(E_b - \frac{N}{A_b}\right)I_b + \left(E_c + \frac{N}{A_c}\right)I_c\right]$
"Compression Softening" Chan and Yung (2000); Law and Lu (2005); Miyamoto et al. (2000); Tse et al. (1978)	$\omega_n^2 = \left(\frac{n\pi}{\ell}\right)^4 \frac{EI}{m} - \left(\frac{n\pi}{\ell}\right)^2 \frac{N}{m}$

Figure 2.14 shows that three models, namely Saiidi et al., Kim et al. and Zhang et al., predict that there is an increase in the first natural bending frequency with increasing prestress force magnitude. Kim et al. predict the greatest rate of increase, whereas Zhang et al. predict the lowest rate of increase. This is observed from the relative slopes of the lines. The other two models, namely Dall'Asta and Dezi and Miyamoto et al. predict a decrease in the first natural bending frequency with increasing prestress force magnitude. Miyamoto et al. agree with the *"compression-softening"* and predict a greater rate of decrease than Dall'Asta and Dezi. Differentiation of the prediction models in Table 2.4 with respect to N indicates the relative rates of increase/decrease of the predicted first natural bending frequency.

2.12. Experimental Works

Table 2.5.: Summary of experimental approaches

Author (Year)	Type of testing	No. accelerometers	No. excitation points	Conclusion
Saiidi et al. (1994)	Field Testing	8No.; equally spaced	1No. @$\frac{1}{4}$ span	$\omega_n \downarrow$ with $\downarrow$ N.
	Lab Testing	7No.; equally spaced	2No. @ $\frac{1}{4}$ span; 2No. @$\frac{1}{2}$ span	$\omega_n \uparrow$ with $\uparrow$ N.
Miyamoto et al. (2000)	Field Testing	9No.; 3No. @ midspan of each of 3 girders	15No. @ various locations on bridge deck	$\omega_n \downarrow$ with $\uparrow$ N.
	Lab Testing	5No.; equally spaced	1No. @ $\frac{1}{4}$ span; 1No. @$\frac{1}{2}$ span	$\omega_n \uparrow$ with $\uparrow$ N for $e/y_{sl} = 1.0$; $\omega_n \downarrow$ with $\uparrow$ N for $e/y_{sl} = 0.1$.
Ho et al. (2012)	Lab Testing	7No.; equally spaced	1No. @$\frac{1}{4}$ span	$\omega_n \uparrow$ with $\uparrow$ N.
Lu and Law (2006)	Lab Testing	7No.; equally spaced	1No. @$\frac{1}{4}$ span; 1No. @$\frac{3}{8}$ span	$\omega_n \uparrow$ with $\uparrow$ N.

Many empirical studies have been conducted into how prestress force magnitude affects natural bending frequencies of prestressed concrete beams (Ho et al., 2012; Hop, 1991; Kerr, 1976; Lu and Law, 2006; Miyamoto et al., 2000; Saiidi et al., 1994; Williams and Falati, 1999; Zhang and Li, 2007; Zhang et al., 2012). The majority of these studies have reported the general trend that natural bending frequencies tend to increase with increasing prestress force magnitude (Ho et al., 2012; Hop, 1991; Lu and Law, 2006; Saiidi et al., 1994; Williams and Falati, 1999; Zhang and Li, 2007; Zhang et al., 2012). The exception are the experimental studies conducted by Miyamoto et al.

(2000) and Kerr (1976).

2.12.1. Miyamoto et al. (2000)

Miyamoto et al. conducted field impact tests on a composite steel girder bridge, strengthened with external tendons and laboratory impact hammer testing on composite steel-concrete girder strengthened with external tendons. This study is fundamentally different from the other studies conducted in the literature in two ways, firstly the tendons are external to the beam section and secondly, the girder tested is a steel I-beam with composite concrete deck. Other research focuses on single material beams (steel or concrete) that are prestressed internally, i.e. the tendon lies within the confines of the cross section. The composite girder with external tendons was set up in the Queen-post arrangement as shown in Figure 2.6a. The ratio of the eccentricity, e to the distance from the neutral axis of the composite section to the bottom flange, y_{sl} was varied. The tendon material was also varied to examine the effect of change in EA on natural bending frequency. Two impact points for the impact hammer were located at $\ell/4$ and $\ell/2$ with response points located at $\ell = 0$, $\ell/4$, $\ell/2$, $3\ell/4$ and ℓ. In order to minimise experimental error, Miyamoto et al. recorded 10 waveform patterns for each set of test conditions and for each impact point. A mean transfer function was then obtained by averaging 8 of the 10 Fast Fourier Transform (FFT) results. For the girder configuration with the less eccentric tendons (i.e. $e/y_{sl} = 0.1$), it was found that the natural vibration frequencies tend to decrease as the magnitude of the prestressing force is increased. For the configuration with the more eccentric tendons ($e/y_{sl} = 1.0$), it was found that the natural vibration frequencies tend to increase as the magnitude of the prestressing force is increased. It should be noted that no constant increase or decrease in natural vibration frequency is observed in either case. There is an overall decreasing trend for the less eccentric tendons and an overall increasing trend for the more eccentric tendons, but there is some variation within the data. The authors conclude that for a less eccentric tendon arrangement ($e/y_{sl} = 0.1$) the introduction of a prestressing force makes the axial compressive component of the prestressing force acting on the girder dominant and thereby decreasing the natural vibration frequency. It is concluded for the more eccentric arrangement ($e/y_{sl} = 1.0$) that since

the larger eccentricity increases the transformed second moment of area of the composite section significantly and therefore increases the apparent flexural rigidity (bending stiffness) of the composite section, and because the axial compressive component of the prestressing force is smaller than in the less eccentric case, an increase in the natural vibration frequency is therefore observed.

2.12.2. Kerr (1976)

Kerr (1976) conducted experimental modal analysis on a steel cantilever beam. The beam, which consisted of two spring steel strips, connected together by aluminium cross bars, was mounted on a shake table. A prestressing rod was threaded through the centroid of the beam cross-section and the prestress force was induced using a weight and pulley. Kerr considered that the effect of the inertia of the weight on the end of the pulley upon the lateral response of the beam was negligible (Kerr, 1976). The natural frequency of the system was obtained by increasing the frequency of the shake table during testing until the resonance condition was reached. A stroboscopic light was used to maintain high accuracy. Kerr concluded that the obtained test results coincide with the analytical findings that the centrally placed prestressing force, P has no effect on the natural frequencies (Kerr, 1976).

2.12.3. Saiidi et al. (1994)

Saiidi et al. (1994) conducted field testing on the Golden Valley bridge, near Reno, Nevada. The bridge tendons were instrumented from the time of stressing meaning a direct estimate of the magnitude of the actual prestressing force in the bridge was available at any time. From field testing on the Golden Valley bridge it was found that there was a reduction in the first mode frequencies with decreasing magnitude of prestressing force, i.e. with increasing prestressing loss. No consistent trend in second mode frequencies was observed. Subsequently, laboratory tests were conducted. A 12' (3.66 m) simply supported beam was jacked at one end with a grade 250 seven-wire straight concentric strand placed in a 25 mm diameter duct that was ungrouted. The beam had a breadth of 4" (101.6 mm) and depth of 5" (127 mm) and the duct was placed in the centre. It was reinforced both

longitudinally and in the transverse direction with grade 60 bars. Saiidi et al. (1994) reported the specimen developed a small crack at midspan under self-weight during handling. The beam was instrumented with 7 equally spaced accelerometers that measured the vertical acceleration response of the beam, and a mechanical gauge was mounted at midpoint to measure vertical deflection. Both impact hammer tests and three-point static bending tests were conducted with different prestressing forces. It should be noted that the jack was disconnected from the beam during vibration testing to avoid the effect of the jack's mass on the beam's vibration response. The prestressing force was varied from zero up to a maximum of 131.5 kN and back down to zero again. Four sets of free vibration data were collected for each axial force, two of which the beam was excited by impact at midspan and the other two the impact was applied at quarter span. Like with the field testing described, the Fast Fourier Transform method was used to analyse the frequencies and modal amplitudes. The data obtained for the free vibration testing indicated that the first natural frequency increased as the prestressing force was increased. This coincides with the findings from the field testing on the Golden Valley bridge. The second mode frequencies were also found to increase generally but were found not to be as sensitive.

2.12.4. Hop (1991)

Hop (1991) conducted dynamic testing on 19No. prestressed concrete beams. It was found that for the majority of prestressed beams the natural frequencies increased with increasing prestressing force. The frequencies increased by a maximum value of 10% at a stress level of 150 daN/cm^2. However, for the eccentrically prestressed beam it was found that the frequencies increased up to a threshold value and then began to decrease again back to the "virgin frequency" (i.e. the natural vibration frequency of a non-prestressed beam) at a stress level of 150 daN/cm^2. The beams were then retested twenty years later, and it was found that the virgin natural frequency of 13 out of the 15 beams retained for testing had increased over time, by an average amount of 5%. This was attributed to the gain in concrete strength over time due to the continuation of the hydration reaction, which continues indefinitely in the presence of moisture. The Young's modulus of the concrete was estimated to be 14% greater in 1980 than it had

been twenty years previously, attributing to the increase in frequency.

2.12.5. Zhang and Li (2007)

Zhang and Li (2007) conducted dynamic testing on three bonded and two unbonded fully prestressed concrete beams. The results of the testing indicate that the frequency of PSC beams increase with increasing prestressing force magnitude, in line with the findings of Saiidi et al. (1994) and Hop (1991). Linear and curved prestressing tendons were both used. It was found that the measured frequencies of the beams with the linear tendon profile for the first two modes of vibration increased with a steady trend as the magnitude of the prestressing force increased. For the curved tendon profile, a general increase in natural frequency was observed, but the trend does not follow a steady pattern and varies widely as the prestressing force is increased, for both modes of vibration. For all modes of vibration, the measured increase in natural frequency is of the order of 5% of the experimentally determined virgin natural frequency. Zhang et al. conducted further dynamic testing on two unbonded fully prestressed concrete beams (Zhang et al., 2012). It was again found that the natural frequency of the beams increased with increasing prestressing force magnitude. 2 No. simply supported, unbonded prestressed beams, each spanning 3m in length were tested. A straight concentric strand was used as the prestressing steel with a standard tensile strength of 1860 MPa. 5No. accelerometers were laid out along the length of the beam. According to Zhang et al., in order to guarantee the accuracy, the sampling frequency for the first natural frequency was 100 Hz. The sampling frequency for the second and third modes was taken to be 500 Hz and 1000 Hz respectively. It was found that the natural frequency of prestressed concrete beams increase with the increase in prestressing force.

2.12.6. Williams and Falati (1999)

A paper by Williams and Falati describes an extensive programme of modal testing on a post-tensioned concrete one-way spanning slab strip at 50% of full scale (Williams and Falati, 1999). The slab was constructed with high slenderness and therefore low natural frequency, giving a high likelihood of vibration serviceability problems. The slab was designed as a one-way span-

ning, simply supported slab with a span length of 5.1m, breadth, $b = 1.0m$, and depth, $d = 135mm$. The prestress was introduced by 4No. 15.7mm diameter unbonded Freyssinet super strands, with a characteristic breaking load of 265kN. When fully stressed, they provided a prestressing force of 175kN. The slab was also reinforced with 10mm diameter high yield steel bars at 125mm centres, giving a reinforcement ratio of $A_s/bh = 0.5\%$. According to the authors, this amount of reinforcement was sufficient to allow the slab to carry its own self-weight in the absence of the prestressing force, which, was necessary in order to enable the effect of prestress level to be investigated (Williams and Falati, 1999). Two methods of slab excitation were used - instrumented hammer and electro-magnetic shaker. The natural frequencies and mode shapes were extracted from the frequency response functions (FRFs) in the usual way. Damping was determined in two ways: firstly by curve fitting the FRF peaks and using the half-power bandwidth method, and secondly by exciting the slab in a particular mode and then switching off the shaker and calculating the logarithmic decrement of the subsequent decaying vibrations (Williams and Falati, 1999). The slabs were tested at zero prestress, each tendon stressed to 100kN (57% of its design prestress), and with each tendon stressed to 175kN (full design prestress). It was found experimentally that the natural frequencies of the prestressed concrete one-way spanning slab increased with increasing prestressing force, and that the damping decreased. No discernible effects on the mode shapes were reported (Williams and Falati, 1999).

2.12.7. Ho et al. (2012)

Ho et al. (2012) conducted dynamic tests on a lab-scaled post-tensioned concrete T-beam, 6m in length, to determine the experimental modal parameters for a set of prestress cases. 7No. accelerometers were placed along the length of the girder at 1m intervals. The impact was applied in the vertical direction by an electromagnetic shaker 0.75m from the right hand support of the beam. 7No. accelerometers were used to measure the dynamic responses at a sampling frequency of 1 kHz (Ho et al., 2012). The axial prestress forces were introduced into the tendon by stressing the tendon with a jack at one end and anchoring the tendon at the other face of the beam. A load cell was installed at the left end in order to measure the

applied prestress force. It should be noted that during the measurement, the stressing jack was removed from the girder to avoid the influence of the jack weight on the dynamic characteristics of the test structures (Ho et al., 2012). It was found that the first and second natural frequencies decreased as the magnitude of the prestressing force decreased. The frequency domain decomposition (FDD) technique was used to extract the natural frequencies and corresponding mode shapes from the acceleration signals (Ho et al., 2012). It was reported that the mode shapes were not changed significantly due to change in prestressing force (Ho et al., 2012).

2.12.8. Lu and Law (2006)

Lu and Law (2006) carried out experimental work on a prestressed concrete beam in the laboratory. The beam tested was $4.0m$ in length, with a 200mm $\times$ 150mm uniform cross section, with a clear span of $3.8m$. A 7 wire strand was placed in a 57mm ungrouted duct at the beam centroid. The beam was instrumented with 7 equally spaced accelerometers, measuring the vertical acceleration. The sampling rate was 2000Hz. The equivalent flexural rigidity of the prestressed concrete beam was found to increase with prestressing. The equivalent mass per unit length of the beam was also found to have been increased, due to axial shortening under prestressing force and the additional mass of the prestressing strand. Subsequently, it was found that the first three natural frequencies increased after prestressing.

2.13. Cracked Prestressed Concrete Sections

The effect of prestress force magnitude on the modal properties (frequency, damping and mode-shape) of uncracked prestressed concrete structures is something that has been widely debated among researchers to date, as outlined in previous sections.

The effect of pre- and post-tensioning force magnitude on the natural bending frequencies of cracked prestressed concrete structures is something that is more established, and widely agreed upon. Saiidi et al. (1994) report an increase in natural frequency with increasing post-tensioning force. As pointed out by Bruggi et al. (2008) the tests carried out by Saiidi et al. (1994) were conducted on cracked beam sections only. Uncracked sections

were not tested. Williams and Falati (1999) present a formula to calculate the average effective second moment of area of a cracked concrete cross section. The effect of crack closure in accordance to this method is that it increases the effective second moment of area of the cross section, and subsequently the natural bending frequencies. Hop (1991) agrees, reporting a decrease in natural bending frequencies with increased cracking, and states that increasing the prestressing force acts as to close the cracks, stiffen the section and increase the natural bending frequencies of the beam sections. Grace and Ross (1996) also report a decrease in girder stiffness leading to a decrease in natural frequency also attributing it to cracking in the cross section. Unger et al. (2006) state that a loss in post-tensioning increases the appearance of cracks which reduces the bending stiffness and subsequent natural frequencies of the system. De Roeck (2003) concurs, stating that *"a loss of pre-stress will result in a measurable change in eigenfrequencies only if it is accompanied by originating cracks."* Hamed and Frostig (2004) also report that large cracking damage yields drastic reduction in the natural frequencies of cracked prestressed concrete beams.

Pavic et al. (2001) agree that *"concrete cracking and excessive static deflection in a prestressed post-tensioned slab can be overcome to a large extent by the careful choice of the amount and location of the prestress"* but argue that *"no amount of prestressing, however, will significantly improve the floor dynamic behaviour since this is governed largely by slab stiffness, mass and damping on which different levels of prestressing do not have major influence."* Dall'Asta and Dezi (1996) consider it is possible to determine the prestressing force by measuring the natural frequency of a PSC structure in its cracked state only. Rodríguez et al. (2010) acknowledges this fact in relation to post-tensioned concrete wind turbine towers, stating that uncracked towers *"maintain their original stiffness and frequency of oscillation"* but once the towers are cracked and the cracks have been decompressed, *"any perturbations of the tower will only mobilise a smaller stiffness, an effect that will be shown by the vibration frequencies."*

There is however, disagreement when it comes to the effect of prestress force on the damping ratios for cracked prestressed concrete structures. Kato and Shimada (1986) state that there are hardly any changes in damping values, whereas Blakeley et al. (1970) report damping of PSC structures to be lower than that of RC structures, quoting damping ratios of 1-2%

before cracking of the member and 3-6% after cracking.

2.14. Conclusions

It is clear from this discussion that there is a lack of agreement between researchers in the field as to the effect that prestress force magnitude has on the natural bending frequency of uncraked prestressed concrete beams. There are currently three distinct arguments;

1. The natural vibration frequency of prestressed concrete structures tends to decrease as the magnitude of the prestressing force is increased (Chan and Yung, 2000; Dai and Chen, 2007; Dall'Asta and Leoni, 1999; Law and Lu, 2005; Miyamoto et al., 2000; Raju and Rao, 1986; Tse et al., 1978).

2. The natural vibration frequency of prestressed concrete structures is unaffected by prestress force magnitude (Hamed and Frostig, 2006).

3. The natural vibration frequency of prestressed concrete structures tends to increase as the magnitude of the prestressing force is increased (Hop, 1991; Kim et al., 2004; Saiidi et al., 1994; Zhang and Li, 2007).

A satisfactory mathematical model is yet to be formulated predicting the change in natural frequency with increasing prestressing force, however, the model suggested by Kim et al. (2004) has the best agreement with experimental results. It should be noted that the magnitude of the predicted change in natural frequency is very small for practical ranges of prestressing force, and could be considered to be negligible. Furthermore, as highlighted by Ho et al. (2012), recently the interest on variability of dynamic properties of bridges (i.e. natural frequency, mode shape, damping ratio) caused by environmental effects such as temperature, humidity, wind and other factors is increasing. Studies such as those conducted by Cornwell et al. (1999) and Peeters and De Roeck (2001) report frequency differences in the ranges of 6% and 14-18% respectively due to normal environmental changes. The change in natural frequency due to prestress loss may be negligible as a result. Furthermore, no statistical significance tests have yet been conducted on the data to determine whether the observed changes in natural frequency

with prestress force magnitude is simply due to random variation or whether it is systematic. The majority of experimental studies conducted indicate that the natural frequency of prestressed concrete structures increases with increasing prestressing force magnitude (Ho et al., 2012; Hop, 1991; Lu and Law, 2006; Saiidi et al., 1994; Williams and Falati, 1999; Zhang and Li, 2007; Zhang et al., 2012).

The effect of prestress force magnitude on the natural frequency of cracked prestressed concrete structures is something that is more widely established and agreed upon. Authors agree that for cracked pre- and post-tensioned concrete structures the effect of the post-tensioning force is to close cracks, stiffen the section and therefore increase the natural bending frequencies of the cracked pre- and post-tensioned concrete structures (Saiidi et al., 1994; Bruggi et al., 2008; Williams and Falati, 1999; Hop, 1991; Grace and Ross, 1996; Unger et al., 2006; De Roeck, 2003; Hamed and Frostig, 2004; Pavic et al., 2001; Rodríguez et al., 2010).

The problem of the effect of prestress force magnitude on the natural bending frequency of prestressed concrete beams has implications in many fields, such as in prestressed bridge design, post-tensioned floor slabs, and even post-tensioned concrete wind turbine tower design. Prestress force magnitude decreases over time due to concrete creep, steel relaxation, anchorage pull-in and other effects. The natural bending frequency of prestressed concrete bridges and post-tensioned concrete wind turbine towers may change over time according to the effect of prestress loss. It is important for structural engineers to be able to account for any subsequent change in natural frequency over time due to prestress loss, as it may become a critical design parameter affecting the long term performance of the structure. Furthermore, if the change in natural frequency with prestress force magnitude can be determined, this can be related to the well established Eurocode 2 (British Standards Institute, 2004) formula for predicting prestress loss with time, and subsequently a model for the variation in natural frequency over time due to prestress loss could be formulated.

3. Modal Testing - Basics

This chapter presents the main theory, techniques and tools behind modal analysis. The purpose of this chapter is to provide the reader with a grounding in the main theory behind modal analysis as a prerequisite for reading Chapters 4, 6 and 7.

3.1. Introduction

This thesis describes and outlines the mathematical modelling and subsequent experimental modal testing of post-tensioned steel and concrete beams in the lab. The purpose of modal testing is to determine empirically the dynamic (modal) properties of the tested specimens. The modal properties of interest are the natural frequencies, ω_n, the corresponding damping ratios, ξ, and the corresponding mode shapes of vibration, Φ_n. This thesis aims to establish if any relationship exists between the modal properties, primarily the fundamental bending frequency, ω_1, and the magnitude of the post-tensioning force, N, for post-tensioned concrete structures. The results of the experimental work conducted is outlined in Chapters 4, 6 and 7. The purpose of this chapter is to introduce the reader to some of the basic theory, concepts and tools of experimental modal analysis/modal testing.

The chapter is organised as follows; Section 3.2 outlines the theoretical basis behind experimental modal analysis and some of the specific tools and techniques used to conduct the analysis. Section 3.3 outlines the measurement techniques behind collecting good dynamic data, including outlining the basic steps behind conducting modal analysis. Section 3.4 outlines some specific techniques behind digital signal processing, in order to prepare the dynamic signals for analysis when they are collected. This chapter provides necessary background in the theory, tools and techniques behind experimental dynamic testing and provides the reader with a concise introduction, background and basis of these aspects prior to reading Chapters 4, 6 and 7.

3.2. Experimental Modal Analysis

The following sections describe the method behind experimental modal analysis and present the basic theory of the test method described in the latter parts of this thesis, specifically, Chapters 4, 6 and 7. The following description draws heavily upon the work of Ewins (2000), Avitabile (2001b) and Biloŝová (2011) who are considered leaders in the field of modal testing and analysis. According to Ewins (2000) 'Modal Testing' is defined as the *"processes involved in testing components or structures with the objective of obtaining a mathematical description of their dynamic or vibration behaviour."* Avitabile (2001a) considers modal testing as a process in which a structure is described in terms of its natural characteristics or dynamic properties, namely frequency, ω_n, damping, ξ, and mode shape, Φ_n.

Why is modal analysis conducted, and what is it used for? The primary reason is to identify the modal parameters (natural frequency, damping & mode shapes) of real structures. In doing so, the resonant frequencies and the excited mode shape can be determined (Ewins, 2000; Biloŝová, 2011). This is important, as, in structural dynamics, the response of the systems amplifies as the frequency of the applied dynamic force gets closer and closer to the natural frequency of the structure. The response reaches a maximum when the rate of oscillation of the dynamic force exciting the structure matches the natural frequency of the structure. This is know as ***'structural resonance'*** and can cause significant vibration problems in real structures, most famously with the collapse of the Tacoma Narrows Bridge in Tacoma, Washington, as a result of extreme structural resonance. Experimentally obtained values of the modal parameters can be used as model validation for a theoretical model such as a Finite Element (FE) analysis. However, as pointed out by Ewins (2000); Biloŝová (2011), this requires precise determination of the natural frequencies and an accurate measurement of the experimental mode shapes of vibration. Modal testing may also be used to generate a mathematical model for a component part of a complex structure that may be included in the overall model for the structure (Ewins, 2000; Biloŝová, 2011). Finally, it may also be used as a determination technique for dynamic excitation forces.

In the context of this thesis, modal testing has been used solely as a tool to determine the structural vibration properties of a variety of simple

steel and concrete structures. Specifically, modal testing has been used as a tool to determine if a relationship exists between post-tensioning force magnitude, N, and the natural bending frequencies, ω_n, for a variety of pre- and post-tensioned steel and concrete structures tested in the lab.

3.2.1. Theoretical Basis of Modal Testing

Modal testing enables the characteristic dynamic properties of a structural system to be identified empirically. According to Ewins (2000), such a dynamic structural system is best described by three different types of model, as outlined in Figure 3.1, namely;

1. **Spatial Model.** The spatial model is the description of the physical characteristics of the structure, namely its mass, stiffness and damping characteristics that are described by matrices $[M]$, $[K]$ and $[C]$ respectively.

2. **Modal Model.** The modal model describes the structures natural vibration characteristics in terms of a set of natural frequencies (eigenvalues, λ^2) modal damping factors, and vibration mode shapes (Φ).

3. **Response Model.** The response model describes exactly how the given structure will respond under certain excitation conditions. This is dependent on the properties of the structure, but also on the nature and magnitude of the excitation. A set of Frequency Response Functions (FRFs) are generated describing the response of the structure to a given excitation (Ewins, 2000).

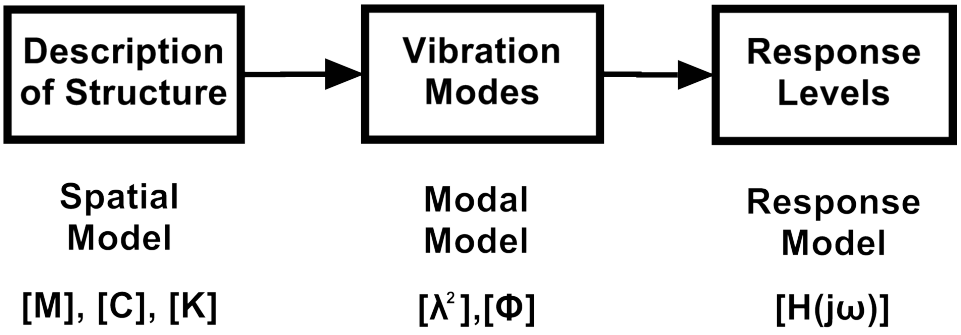

Figure 3.1.: Theoretical Modal Analysis (Ewins, 2000)

The generalised equation of motion for an MDOF (multi degree of freedom) structure is given by;

$$[M]\{\ddot{x}(t)\} + [C]\{\dot{x}(t)\} + [K]\{x(t)\} = \{F(t)\} \tag{3.1}$$

where $[M]$ is the mass matrix of the structure, $[C]$ is the damping matrix, $[K]$ is the stiffness matrix, $\{x(t)\}$ is a time dependent vector of displacements of the structure and $\{F(t)\}$ is a time dependent force vector exciting the structure. An eigensolution is then performed and a modal transformation equation is used to convert these coupled equations into a set of uncoupled single DOF systems in a new coordinate system, known as the *"Modal Space"*;

$$\left[\overline{M}\right]\{\ddot{p}\} + \left[\overline{C}\right]\{\dot{p}\} + \left[\overline{K}\right]\{p\} = [U]^T\{F\} \tag{3.2}$$

where $\overline{M}$, $\overline{C}$ and $\overline{K}$ are the modal mass, modal damping and modal stiffness matrices. The transformation from the physical space to the modal space is a process where a complicated set of coupled physical equations are reduced to a simple set of uncoupled single DOF systems (Avitabile, 2001a). Figure 3.2 schematically shows the reduction of the spatial model into the modal model, and this is defined as *"Experimental Modal Analysis"*, where a complicated set of coupled physical equations are reduced to a simple set of uncoupled SDOF systems, i.e. Equation 3.1 is reduced to Equation 3.2.

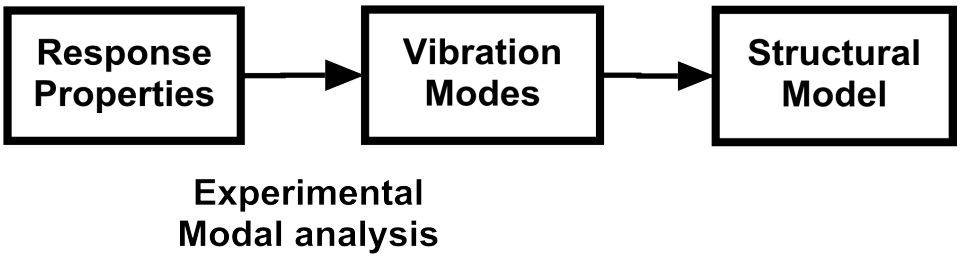

Figure 3.2.: Experimental Modal Analysis (Ewins, 2000)

3.2.2. Frequency Response Function (FRF)

The Frequency Response Function (FRF) is defined as the ratio of the output response of a structure due to an applied force. By taking the Fourier Transform (FT) of both the input signal and the output signal, they are

converted from the time domain into the frequency domain. The ratio of the output signal to the input signal in the frequency domain is defined as the FRF. Due to the nature of the Fourier Transform, the functions are complex, with real and imaginary terms, and can be described in terms of magnitude and phase (Avitabile, 2001a).

$$FRF = H\left(j\omega\right) = \frac{\hat{O}\left(j\omega\right)}{\hat{I}\left(j\omega\right)} \tag{3.3}$$

where $\hat{O}\left(j\omega\right)$ and $\hat{I}\left(j\omega\right)$ are defined as the Fourier Transform of the output and input signals in the time domain respectively. They are given mathematically as;

$$\hat{O}\left(j\omega\right) = \left(\frac{1}{2\pi}\right)\int_{-\infty}^{+\infty} o\left(t\right)e^{-j\omega t}\mathrm{dt} \tag{3.4}$$

$$\hat{I}\left(j\omega\right) = \left(\frac{1}{2\pi}\right)\int_{-\infty}^{+\infty} i\left(t\right)e^{-j\omega t}\mathrm{dt} \tag{3.5}$$

Figure 3.3 shows a schematic of the modal analysis outlining the definition of the Frequency Response Function (FRF) as the system transfer function in the frequency domain. Both the input and output signals are converted from the time domain to the frequency domain by means of the Fourier Transform. The FRF is then defined as the ratio of the output signal in the frequency domain to the input signal in the frequency domain. The coherence function is defined as the cross-correlation of the output and input signals, and measures the causality of the signals, i.e. the amount of correlation between the input and output signal. Analysis of the FRF gives information about the modal properties of the structural system. Specifically, the peaks in the FRF are used to identify the experimental natural bending frequencies of the structural system, through peak-picking algorithms.

The experimental modal testing carried out and described in Chapters 4, 6 and 7 describe the results of output-only modal analysis. The output signal only was measured. No measurement signal was taken of the dynamic impacts used to excite the respective structural systems tested, i.e. of the dynamic input signals. In this way, the experiments conducted are considered as output-only dynamic tests. These tests are becoming increasingly

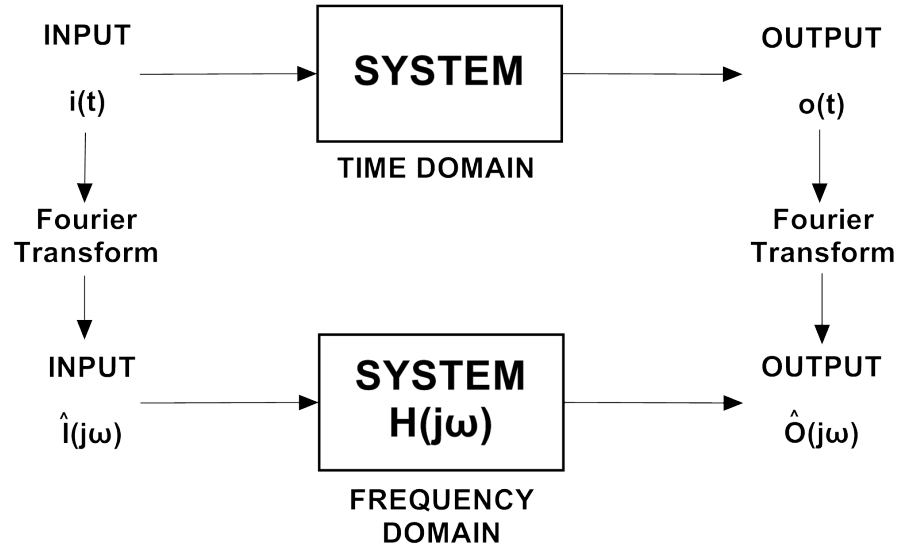

Figure 3.3.: Modal Analysis; determination of system transfer function (FRF)

common, especially in the field of Operational Modal Analysis (OMA), in which the modal parameters of a structure are determined from the structures response to ambient vibration conditions. Consequently, in the testing conducted and described later in the thesis, determination of the FRF and coherence functions is not possible. The modal properties are instead extracted from the Fourier Transform representations of the system output signals.

3.2.3. Fourier Series

The main assumption underlying all forms of modal analysis is that any dynamic response signal may be represented, in the time domain, as an infinite series of sinusoids, each with their own unique amplitude and frequency. The amplitudes are considered as the modal contribution of each mode of vibration to the overall dynamic signal, whereas the frequencies are defined as the natural vibration frequencies of the structural system, for the corresponding mode shape of vibration. All other seemingly random portions of the vibration response are considered as a noise components of the system, and as such, asystematic. As such, it is important to represent each dynamic signal as an infinite series of sinusoids.

The Fourier Series is a mathematical technique to represent any periodic time (T) signal, $x(t)$ as an infinite series of sinusoids;

$$x\left(t\right) = \frac{1}{2}a_0 + \sum_{n=1}^{\infty}\left(a_n cos\omega_n t + b_n sin\omega_n t\right) \tag{3.6}$$

where;

$$\omega_n = \frac{2\pi n}{T} \tag{3.7}$$

where T is the natural period of the periodic signal to be represented in seconds. The coefficients are given by;

$$\begin{aligned} a_0 &= \frac{2}{T}\int_0^T x\left(t\right)\mathrm{dt} \\ a_n &= \frac{2}{T}\int_0^T x\left(t\right) cos\omega_n t\mathrm{dt} \\ b_n &= \frac{2}{T}\int_0^T x\left(t\right) sin\omega_n t\mathrm{dt} \end{aligned} \tag{3.8}$$

Alternatively, the Fourier Series can also be written in terms of magnitude and phase information;

$$x\left(t\right) = c_0 + \sum_{n=1}^{\infty} c_n cos(\omega_n t + \phi_n) \tag{3.9}$$

where the magnitude, c_n and phase, ϕ_n are given by;

$$\begin{aligned} c_n &= \sqrt{a_n^2 + b_n^2} \\ \phi_n &= tan^{-1}\left(-\frac{b_n}{a_n}\right) \end{aligned} \tag{3.10}$$

Alternatively, making use of Euler's Formula, $e^{j\theta} = cos\theta + jsin\theta$, the Fourier Series may also be expressed in the form (Ewins, 2000);

$$x\left(t\right) = \sum_{-\infty}^{+\infty} X_n e^{j\omega t} \tag{3.11}$$

where;

$$X_n = \frac{1}{T}\int_0^T x\left(t\right) e^{-j\omega_n t}\mathrm{dt} \tag{3.12}$$

3.2.4. Fourier Transform

In signal processing, dynamic signals are often thought of in the time domain, i.e. as functions of time. Often, to engineers and analysts, it is more beneficial to represent the signals in the frequency domain. Despite the frequency domain being less intuitive than the time domain, it is often easier to manipulate and subsequently interpret the signals in the frequency domain. For example, the identification of the natural frequencies of the structural system becomes trivial in the frequency domain by invoking peak-picking algorithms. The Fourier Transform is used to convert the impact response signals obtained during dynamic testing described in Chapters 4, 6 and 7 from the time domain into the frequency domain.

The Fourier Transform is a mathematical technique that converts signals from their time domain representation, and describes them in terms of their frequency content. The time signal is decomposed into its individual frequency components in the frequency domain. Some mathematical operations are easier to perform in the frequency domain rather than in the time domain. Engineers make use of this by converting to the frequency domain, applying the desired operations and then transforming back into the time domain. The Fourier transform is defined mathematically as;

$$\hat{f}\left(\omega\right) = \left(\frac{1}{2\pi}\right)\int_{-\infty}^{+\infty} f\left(t\right) e^{-j\omega t}\mathrm{dt} \tag{3.13}$$

where t is the variable in the time domain and ω is the variable in the frequency domain. The inverse transform is defined as;

$$f\left(t\right) = \frac{1}{2\pi}\int_{-\infty}^{+\infty} \hat{f}\left(\omega\right) e^{j\omega t}\mathrm{d}\omega \tag{3.14}$$

3.2.5. Discrete Fourier Transform

The Fourier Transform, as described in Section 3.2.4, is only applicable to continuous functions, i.e. analogue signals. However, often in signal processing and Fourier Analysis, there is a requirement to compute the

Fourier Transform of a discrete time signal, i.e. a signal that is described only at discrete time intervals. For example, in computing, and data logging, an analogue signal is discretised into a digital signal, and is only defined by a discrete number of points. The number of points that define a digital signal is determined by the sampling rate of the analogue to digital converter (ADC) of the data logger.

The above form of the Fourier Transform, as outlined in Equation 3.13, is incompatible with such signals, and requires a numerical integration technique. The Discrete Fourier Transform, or DFT, of a function defined only at N discrete points is defined mathematically as (Ewins, 2000);

$$x\left(t_k\right) = \sum_{n=0}^{N-1} X_n e^{2\pi jnk/N} \tag{3.15}$$

where;

$$X_n = \frac{1}{2}\sum_{k=1}^{N} x_k e^{-2\pi jnk/N} \tag{3.16}$$

Alternatively, this can be expressed in series form;

$$x\left(t_k\right) = \frac{1}{2}a_0 + \sum_{n=1}^{N/2}\left(a_n cos\frac{2\pi nk}{N} + b_n sin\frac{2\pi nk}{N}\right) \tag{3.17}$$

where;

$$\begin{aligned} a_0 &= \frac{2}{N}\sum_{k=1}^{N} x_k \\ a_n &= \frac{1}{N}\sum_{k=1}^{N} x_k cos\frac{2\pi nk}{N} \\ b_n &= \frac{1}{N}\sum_{k=1}^{N} x_k sin\frac{2\pi nk}{N} \end{aligned} \tag{3.18}$$

The DFT assumes that the function, $x(t)$ is periodic. The DFT representation is only valid for the specific values x_k used in the discretised description of $x(t)$ (Ewins, 2000).

3.2.6. Fast Fourier Transform (FFT)

The DFT is a computationally expensive algorithm, of the order of $O\left(N^2\right)$. Cooley and Tukey (1965) proposed the Fast Fourier Transform (FFT), which is an algorithm to perform a DFT of the order of $O\left(N \log N\right)$, with significant computational savings as a result. The FFT is used extensively throughout the course of this thesis as a means of converting the structural response signals, obtained from the dynamic testing conducted and outlined and described fully later, in Chapters 4, 6 and 7, from the time domain to the frequency domain via the signal processing toolbox in MATLAB (MATLAB, 2014).

3.2.7. Single Degree of Freedom (SDOF) System

Figure 3.4 shows the basic model for single degree of freedom dynamic systems, characterised by their mass, m, stiffness, k, and critical viscous damping parameter, c, or hysteretic damping parameter, d. SDOF systems are the simplest vibratory systems that can be described. $x(t)$ is the time-variant displacement of the SDOF system and f(t) is the applied time variant force.

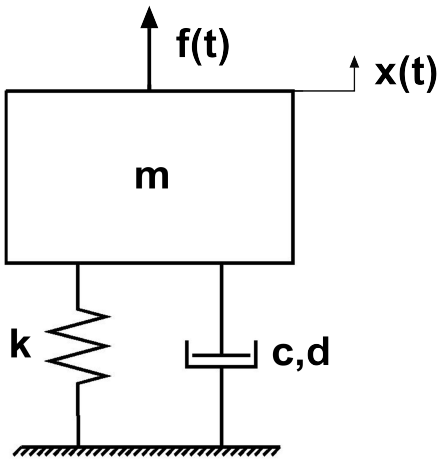

Figure 3.4.: Single Degree of Freedom (SDOF) Oscillator (Ewins, 2000)

Undamped systems

Damping is defined as *"an influence within or upon an oscillatory system that has the effect of reducing, restricting or preventing oscillation."* Exam-

ples include viscous drag in mechanical systems (Wikipedia, 2015b). Consider the idealised case of undamped simple harmonic motion (SHM), i.e. when $f(t) = 0$. The governing (homogeneous) equation of motion is given as;

$$m\ddot{x} + kx = 0 \tag{3.19}$$

The solution $x(t) = Xe^{j\omega t}$ requires that;

$$Xe^{j\omega t}\left(k - \omega^2 m\right) = 0 \tag{3.20}$$

The non-trivial solution gives;

$$\omega = \sqrt{\frac{k}{m}} \tag{3.21}$$

Therefore the modal model consists of a single mode of vibration, at a single characteristic natural frequency, ω, as expected for SDOF systems. In a frequency response analysis, consider excitation of the form (Ewins, 2000);

$$f(t) = Fe^{j\omega t} \tag{3.22}$$

where X and F are complex, containing both frequency and phase information. The equation of motion is now;

$$\left(k - \omega^2 m\right) Xe^{j\omega t} = Fe^{j\omega t} \tag{3.23}$$

The response model, or the Frequency Response Function (FRF), $H(j\omega)$ is given as;

$$H(j\omega) = \frac{X}{F} = \frac{1}{k - \omega^2 m} \tag{3.24}$$

There are different types of FRF, depending on the response parameter in question. The response parameters that can be measured are the displacement, X, the velocity, V, and the acceleration, A. The generic FRF is known by different terms, depending on the response parameter used to calculate it, as outlined in Table 3.1. They are represented generically by the mathematical term $H(j\omega)$.

Table 3.1.: Different Frequency Response Functions

Response Parameter	**Symbol**	**Name**	**Inverse**
Frequency Response Function, FRF	$H(j\omega)$		
Displacement, X	$\alpha(j\omega)$	Receptance Admittance Dynamic compliance Dynamic flexibility	Dynamic stiffness
Velocity, V	$Y(j\omega)$	Mobility	Mechanical impedance
Acceleration, A	$A(j\omega)$	Inertance Accelerance	Apparent mass

3.2.8. Viscous Damping

Adding a viscous damper, and considering free vibration, as shown in Figure 3.4 (when $f(t) = 0$), Equation 3.19 becomes;

$$m\ddot{x} + c\dot{x} + kx = 0 \tag{3.25}$$

The general solution is in the form $x(t) = Xe^{st}$, where s is complex as opposed to imaginary (Ewins, 2000). This requires that;

$$Xe^{st}\left(ms^2 + cs + k\right) = 0 \tag{3.26}$$

The non-trivial solution is given as;

$$\begin{aligned} s_{1,2} &= -\frac{c}{2m} \pm \frac{\sqrt{c^2 - 4km}}{2m} \\ &= -\xi\omega \pm j\omega_D \end{aligned} \tag{3.27}$$

where;

$$\begin{aligned} \omega &= \sqrt{\frac{k}{m}} \\ \xi &= \frac{c}{2\sqrt{km}} \\ \omega_D &= \omega\sqrt{1-\xi^2} \end{aligned} \tag{3.28}$$

This implies a modal solution of the form (Ewins, 2000);

$$\begin{aligned} x(t) &= Xe^{-\xi\omega t}e^{j\omega_D t} \\ &= Xe^{j\omega_D t - \xi\omega t} \end{aligned} \tag{3.29}$$

This is a single vibration mode with a complex natural frequency containing an imaginary (oscillatory) part ($\omega_D = \omega\sqrt{1-\xi^2}$) and a real (decay) part (damping rate of $\xi\omega$). The physical significance of this can be seen in Figure 3.5, which has been reproduced from Ewins (2000).

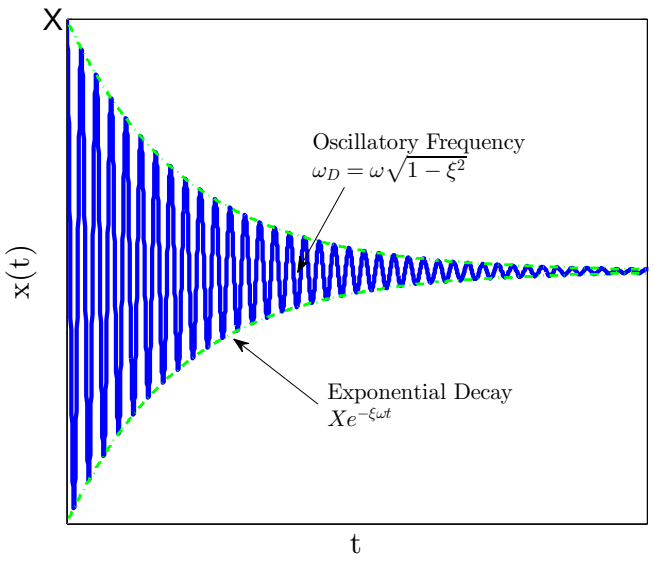

Figure 3.5.: Free vibration characteristics of a damped SDOF system (Ewins, 2000)

Finally, as for the undamped case, considering the forced response when $f(t) = Fe^{j\omega t}$, the equation of motion becomes;

$$\left(-\omega^2 m + j\omega c + k\right) Xe^{j\omega t} = Fe^{j\omega t} \tag{3.30}$$

yields a FRF of the form;

$$H(j\omega) = \frac{1}{(k - \omega^2 m) + j(\omega c)} \tag{3.31}$$

which is complex and contains both magnitude and phase information. As pointed out by Ewins (2000), viscous damping is a poor representation of the damping that occurs in real structures. There is evidence to suggest that structural damping is actually itself frequency dependent. Structural damping is comprised of hysteretic damping due to the material properties from which they are made and friction damping that exists between joints in the structure. As a result, Ewins (2000) suggests a modified equation which satisfies the requirement that the energy lost per cycle is independent of frequency, $d = \omega c$.

3.2.9. Representation of FRF data

A Bode plot is a plot of the modulus of the FRF versus frequency with phase versus frequency, i.e. Figure 3.6a and Figure 3.6d represented with one another in the same graph. Figure 3.6 shows the magnitude, phase, real and imaginary plots of an SDOF system as a function of frequency. The SDOF system in question is an idealised system for the purposes of representation. The system has a resonant frequency defined at $\omega_1 = 78Hz$, which is concurrent with the peaks in Figures 3.6a, 3.6b and 3.6c, and the phase change evident in Figure 3.6d. The synthesised response signal had a peak amplitude arbitrarily defined as unity, $A = 1$. The viscous damping ratio, xi, was given as 2%, $\xi = 0.02$. The input signal itself was defined as an idealised dirac-delta function with amplitude $A = 1$. The impulse response, $o(t)$, of the system was defined as;

$$o(t) = Ae^{\omega t(j-\xi)} \tag{3.32}$$

It can be seen from Figure 3.6d that at resonance condition, the phase angle shifts by 180^o. Due to the large frequency range over which these

plots are defined, the plots are sometimes defined on a logarithmic scale, as in Figure 3.7. When plotted on a log scale, there are some patterns that can be recognised (Ewins, 2000), namely;

- straight line in low frequency range;
- peak in the resonant region, and;
- straight line in high frequency range.

The maximum frequency that can be plotted is known as the Nyquist Frequency, and is defined as half of the sampling rate of a discrete time signal. For example, if a signal has been sampled at a rate of 10,000Hz in the time domain, then the frequency content up to 5,000Hz can be captured.

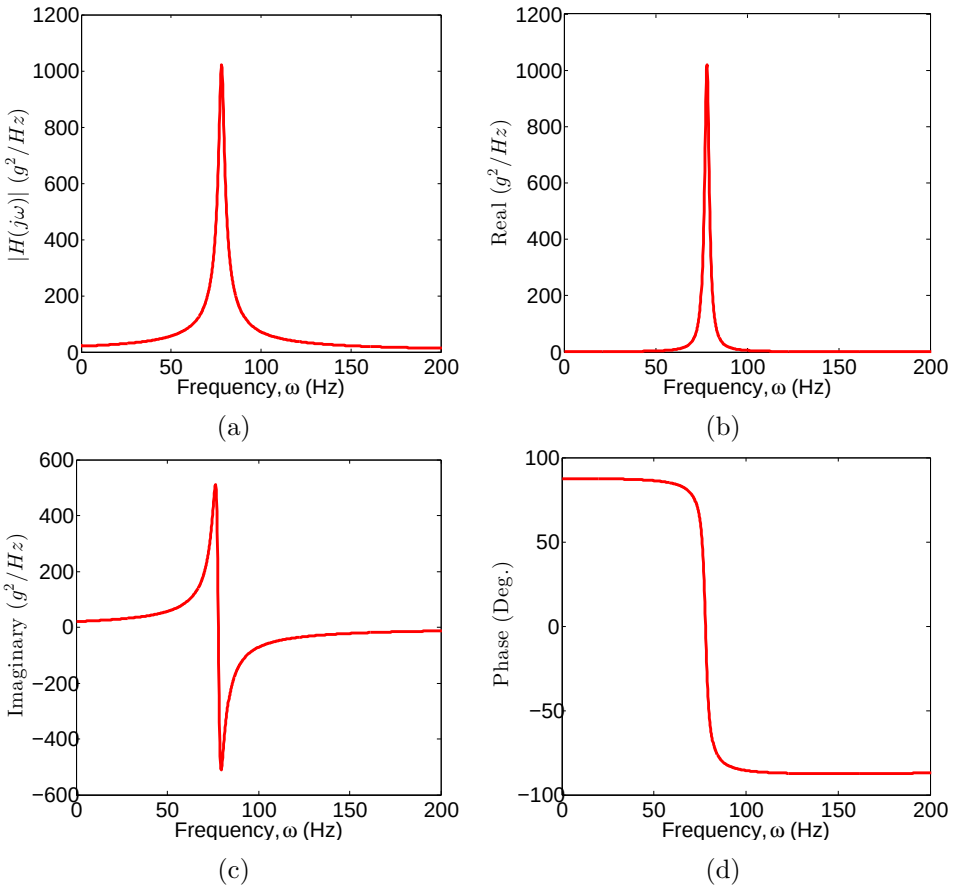

Figure 3.6.: (a) Magnitude; (b) Real; (c) Imaginary, and; (d) Phase information plotted as a function of frequency, ω, for a simple idealised SDOF oscillator response

Plots of the real part of the FRF vs. frequency and the imaginary part of the FRF vs. frequency are shown (Figures 3.6b and 3.6c.) Here, it can be seen that the phase change through the resonant region is characterised by a sign change in the imaginary part. Log scales are not useful here, as there is a need for negative values (Ewins, 2000). Figure 3.8a shows the Nyquist or Argand plane plot of real part vs. imaginary part of FRF. When analysed in conjunction with the 3D plot of real part vs. imaginary part vs. frequency (Figure 3.8b), it is clear that the resonant frequencies in the Argand plane are those that are furthest away from the rest, as all other frequencies are very closely spaced (Ewins, 2000).

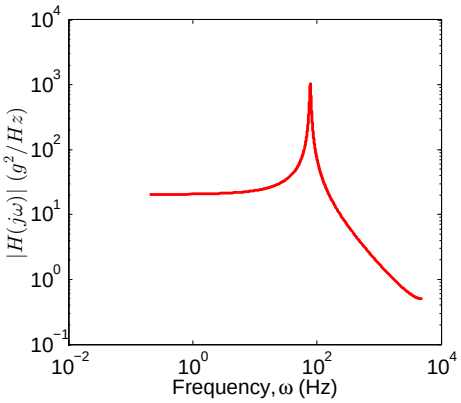

Figure 3.7.: Magnitude of FRF vs. Frequency on Log scale

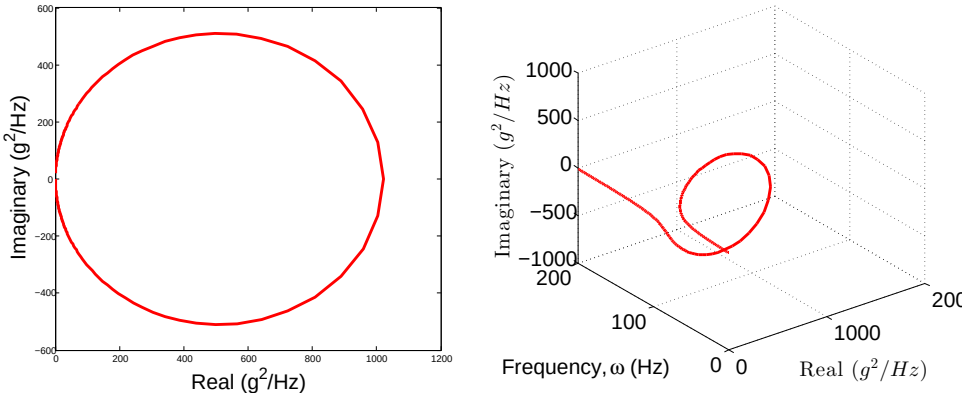

(a) (b)

Figure 3.8.: Plots of; (a) Real vs. Imaginary data (b) 3D plot of Imaginary vs. Frequency vs. Real data

3.2.10. Multi Degree of Freedom (MDOF) System

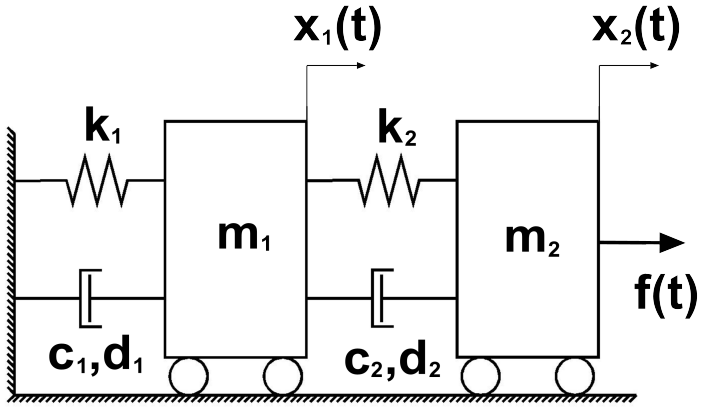

Figure 3.9.: 2 DOF Oscillator

Figure 3.9 shows a generalised two degree of freedom system. For an undamped MDOF system with N degrees of freedom, the governing equation of motion is written in matrix form as;

$$[M]\{\ddot{x}(t)\} + [K]\{x(t)\} = \{f(t)\} \tag{3.33}$$

where $[M]$ and $[K]$ are $N \times N$ mass and stiffness matrices respectively, and $\{x(t)\}$ and $\{f(t)\}$ are $N \times 1$ vectors of time varying displacements and forces (Ewins, 2000). Under free vibration conditions, $\{f(t)\} = 0$, the solution takes the following form;

$$\{x(t)\} = \{X\}e^{j\omega t} \tag{3.34}$$

where $\{X\}$ is an $N \times 1$ vector of time-independent amplitudes (Ewins, 2000). Substitution into Equation 3.33 leads to the following;

$$\left([K] - \omega^2[M]\right)\{X\}e^{j\omega t} = \{0\} \tag{3.35}$$

The non-trivial solution yields;

$$\|[K] - \omega^2[M]\| = 0 \tag{3.36}$$

Solving for $\{\omega^2\}$ gives a $N \times 1$ vector of natural frequencies, $\{\omega_1, ..., \omega_r, ..., \omega_N\}$. Substitution of these values back into Equation 3.34 yields a corresponding

set of relative values for $\{X\}$, i.e. $\{\psi\}_r$, which is the corresponding mode shape to the r^{th} natural frequency. The complete solution is expressed in two $N \times N$ eigenmatrices;

$$[\ddots \omega_r^2 \ddots][\psi] = \{0\} \tag{3.37}$$

The spatial model is defined by $[M]$ and $[K]$, while the modal model is defined by the two eigenmatrices $[\omega_r^2]$, $[\psi]$. The eigenvalue vector, i.e. natural frequencies, are unique, but the eigenvector matrix, i.e. mode shapes is not (Ewins, 2000).

3.2.11. Orthogonality

The modal model possesses the property of orthogonality;

$$\begin{aligned} [\psi]^T [M] [\psi] &= [m_r] \\ [\psi]^T [K] [\psi] &= [k_r] \end{aligned} \tag{3.38}$$

from which; $[\omega_r^2] = [m_r]^{-1}[k_r]$, where m_r and k_r are the modal mass and modal stiffness of mode r respectively. These values are scaled arbitrarily and are therefore mass normalised. The mass-normalised eigenvectors, $[\Phi]$ have the property Ewins (2000);

$$\begin{aligned} [\psi]^T [M] [\psi] &= [m_r] \\ [\psi]^T [K] [\psi] &= [k_r] \end{aligned} \tag{3.39}$$

The relationship between the mass-normalised mode shape for mode r, $\{\Phi\}_r$ and its general form $\{\psi\}_r$ is;

$$\{\Phi\}_r = \frac{1}{\sqrt{m_r}}\{\psi\}_r \tag{3.40}$$

where; $m_r = \{\psi\}_r^T[M]\{\psi\}_r$. Proof of the orthogonality properties given by Ewins (2000); for a particular mode, the equation of motion for free

vibration is given as;

$$\left([K] - \omega_r^2 [M]\right) \{\psi\}_r = \{0\} \tag{3.41}$$

Premultiplying by the transpose of a different eigenvector;

$$\{\psi\}_s^T \left([K] - \omega_r^2 [M]\right) \{\psi\}_r = 0 \tag{3.42}$$

The same goes for other eigenvectors;

$$\left([K] - \omega_s^2 [M]\right) \{\psi\}_s = \{0\} \tag{3.43}$$

If this is transposed and postmultiplied by $\{\psi\}_r$, it gives;

$$\{\psi\}_s^T \left([K]^T - \omega_s^2 [M]^T\right) \{\psi\}_r = 0 \tag{3.44}$$

Since $[M]$ and $[K]$ are generally symmetric, they are identical to their transposes and Equation 3.41 and Equation 3.44 are combined to give;

$$\left(\omega_r^2 - \omega_s^2\right) \{\psi\}_s^T [M] \{\psi\}_r = 0 \tag{3.45}$$

which if $\omega_r \neq \omega_s$ can only be satisfied if;

$$\{\psi\}_s^T [M] \{\psi\}_r = 0; r \neq s \tag{3.46}$$

also;

$$\{\psi\}_s^T [K] \{\psi\}_r = 0; r \neq s \tag{3.47}$$

For the special case where $r = s$, or if $\omega_r = \omega_s$, Equations 3.46 and 3.47 do not apply, but from Equation 3.42;

$$\left(\{\psi\}_r^T [K] \{\psi\}_r\right) = \omega_r^2 \left(\{\psi\}_r^T [M] \{\psi\}_r\right) \tag{3.48}$$

so that;

$$\begin{gathered} \{\psi\}_r^T [M] \{\psi\}_r = m_r \\ \\ \{\psi\}_r^T [K] \{\psi\}_r = k_r \end{gathered} \tag{3.49}$$

and;

$$\omega_r^2 = \frac{k_r}{m_r} \tag{3.50}$$

3.2.12. Forced Response Solution - FRF Characteristics

Consider a MDOF structure that is excited sinusoidally, where the excitation force, $f(t)$ is given as;

$$\{f(t)\} = \{F\}e^{j\omega t} \tag{3.51}$$

assuming that the solution takes the form; $\{x(t)\} = \{X\}e^{j\omega t}$, where $\{F\}$ and $\{X\}$ are $N \times 1$ vectors of time-independent complex amplitudes, the equation of motion becomes;

$$\left([K] - \omega^2 [M]\right) \{X\}e^{j\omega t} = \{F\}e^{j\omega t} \tag{3.52}$$

rearranging to solve for unknown responses;

$$\{X\} = \left([K] - \omega^2 [M]\right)^{-1} \{F\} \tag{3.53}$$

which is written as;

$$\{X\} = [H(j\omega)] \{F\} \tag{3.54}$$

where $[H(j\omega)]$ is the $N \times N$ FRF matrix, or response model. The general element in the FRF matrix is given as;

$$H_{jk}(j\omega) = \left(\frac{X_j}{F_k}\right); \quad F_m = 0; \quad m = 1; \quad N \neq k \tag{3.55}$$

from Equation 3.53;

$$\left([K] - \omega^2 [M]\right) = [H(j\omega)]^{-1} \tag{3.56}$$

Premultiplying both sides by $[\Phi]^T$ and postmultiplying both sides by $[\Phi]$ to obtain;

$$[\Phi]^T \left([K] - \omega^2 [M]\right) [\Phi] = [\Phi]^T [H(j\omega)]^{-1} [\Phi] \tag{3.57}$$

or;

$$\left[\left(\omega_r^2 - \omega^2\right)\right] = [\Phi]^T \left[H\left(j\omega\right)\right]^{-1} [\Phi] \tag{3.58}$$

which lead to;

$$\left[H\left(j\omega\right)\right] = [\Phi] \left[\left(\omega_r^2 - \omega^2\right)\right]^{-1} [\Phi]^T \tag{3.59}$$

Therefore, the FRF matrix, $[H(j\omega)]$ is symmetric (Ewins, 2000);

$$H_{jk}\left(j\omega\right) = \left(X_j/F_k\right) = H_{kj}\left(j\omega\right) = \left(X_k/F_j\right) \tag{3.60}$$

where;

$$H_{jk}\left(j\omega\right) = \sum_{r=1}^{N} \frac{\left(\Phi_{jr}\right)\left(\Phi_{kr}\right)}{\omega_r^2 - \omega^2} = \sum_{r=1}^{N} \frac{\left(\psi_{jr}\right)\left(\psi_{kr}\right)}{m_r\left(\omega_r^2 - \omega^2\right)} \tag{3.61}$$

or;

$$H_{jk}\left(j\omega\right) = \sum_{r=1}^{N} \frac{{}_rA_{jk}}{\omega_r^2 - \omega^2} \tag{3.62}$$

where ${}_rA_{jk}$ is known as a modal constant for mode r. This solution can be rolled out for various types and levels of damping, as outlined by Bilôšová (2011) and presented in Table 3.2.

Table 3.2.: FRF Formulae and Natural Frequencies for all types of damping (Bilôšová, 2011)

MDOF System	**FRF Equation**
Undamped	$H(j\omega) = \sum_{r=1}^{N} \frac{(\Phi_{jr})(\Phi_{kr})}{\omega_r^2 - \omega^2}$
Proportional hysteretic	$H(j\omega) = \sum_{r=1}^{N} \frac{(\Phi_{jr})(\Phi_{kr})}{\omega_r^2 - \omega^2 + j\eta_r\omega_r^2}$
Proportional viscous	$H(j\omega) = \sum_{r=1}^{N} \frac{(\Phi_{jr})(\Phi_{kr})}{\omega_r'^2 - \omega^2 + 2j\omega\omega_r'\xi_r}$
General hysteretic	$H(j\omega) = \sum_{r=1}^{N} \frac{(\Phi_{jr})(\Phi_{kr})}{\omega_r^2 - \omega^2 + j\eta_r\omega_r^2}$
General viscous	$H(j\omega) = \sum_{r=1}^{N} \frac{\left({}_rR_{jk} + j\frac{\omega}{\omega_r'}\right)_r S_{jk}}{\omega_r'^2 - \omega^2 + 2j\omega\omega_r'\xi_r}$

where $\omega_r^{'2} = \omega_r\sqrt{1-\xi_r^2}$ and;

$$\begin{aligned} \{_rR_k\} &= 2\left(\xi_r Re\{_rG_k\} - Im\{_rG_k\}\sqrt{1-\xi_r^2}\right) \\ \{_rS_k\} &= 2Re\{\{_rG_k\}\} \\ \{_rG_k\} &= (\theta_{kr}/a_r)\,\{\theta\}_r \end{aligned} \tag{3.63}$$

where $\{\theta\}_r$ is the r^{th} mode shape for a viscously damped system, and a_r is given by the orthogonality properties of a viscously damped system;

$$[\Theta]^T \begin{bmatrix} C & M \\ M & 0 \end{bmatrix} [\Theta] = [a_r] \tag{3.64}$$

where $[C]$ and $[M]$ are the damping and mass matrices for the given viscously damped MDOF system.

3.3. Measurement Techniques

Section 3.2 outlines the theoretical background and basic mathematical techniques required to conduct a full experimental modal analysis. It outlines the mathematical techniques required to represent the dynamic signals obtained appropriately in the time and frequency domain, such as outlining the main concepts and theory behind Fourier Analysis in Sections 3.2.3, 3.2.4, 3.2.5 and 3.2.6. Furthermore, the single degree of freedom (SDOF) and multiple degree of freedom (MDOF) concepts are introduced, alongside concept of the frequency response function, which is defined as the transfer function for a dynamic system.

The following section will focus primarily on the practical implementation of experimental modal analysis and how the various dynamic testing techniques are applied in the laboratory. The quality of the signal collected is of utmost importance, and highlighted in Section 3.3.1. The choice of test specimen support conditions is dealt with in Section 3.3.2, the type of dynamic excitation is then referred to in Section 3.3.3. Throughout the course of the testing conducted and described in this thesis, impact strikes were used to dynamically excite the test specimens in all cases. Section 3.3.4 outlines the importance of choosing the correct sensory equipment, specifically, an accelerometer. Section 3.3.5 details the difference between analysing op-

erating data and modal data. The basic steps for impact testing are laid out in Section 3.3.6. The implications of multiple input, multiple output dynamic testing are highlighted in Section 3.3.7. Finally, Experimental Modal Analysis (EMA) requires knowledge of both the input force and the output force. In output-only studies, the technique is most accurately referred to as Operational Modal Analysis (OMA), which is discussed further in Section 3.3.9. The aim of the following section is to focus on the practical implementation of modal analysis in the laboratory.

3.3.1. Signal quality

The first thing that should be ensured when conducting modal testing in a laboratory is that the quality of the signals obtained is of the highest quality. Quality assurance of the measured dynamic data is of utmost importance. Firstly the signals obtained should be of sufficient strength and clarity and free of excessive noise (Ewins, 2000). Ewins (2000) reports that it's often the case that there's a very large component of the signal in one frequency range and it dictates the gain settings on amplifiers and analysers such that the low level signal components are difficult to determine. This error has been identified throughout the course of this thesis. The extent of the noise issue is highlighted by some real data obtained from the experimental testing conducted in the laboratory. Figure 3.10 shows both the time domain and frequency domain output response of the tested structure, due to an impact excitation. The peaks in the frequency domain are identified as the natural frequencies of the structure. As evident in Figure 3.10b, the fundamental bending frequency is evident at a frequency of approximately 69Hz, and the 2^{nd} and 3^{rd} harmonic frequencies are evident at frequencies of approximately 246Hz and 630Hz respectively. However, what is also evident is significant noise - unwanted frequency components in the signal that are corrupting it. This unwanted frequency content is attenuated by appropriate use of signal processing and signal filtering that is outlined in detail in Chapters 4 and 6.

Another error identified is that sometimes, the component of vibration out of the plane of measurement contaminates the output, giving misleading information regarding the vibration of the structure (Ewins, 2000). This is due to misalignment of the accelerometer due to tolerance errors in the laboratory.

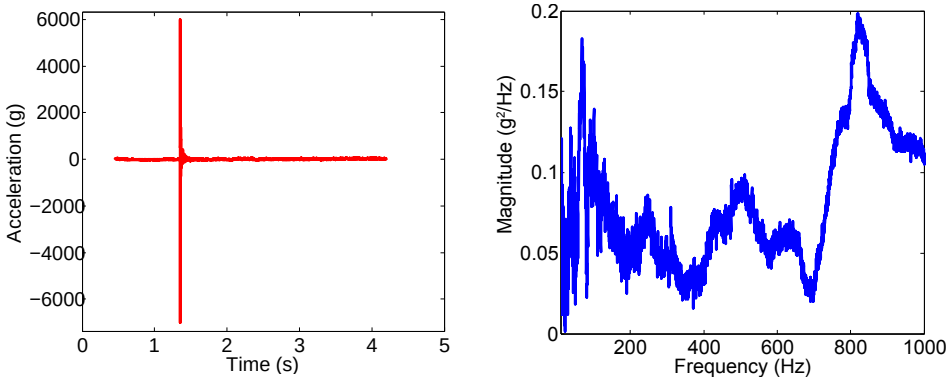

(a) (b)

Figure 3.10.: Unfiltered impact response signal (a) time domain; (b) frequency domain

The following sections, Section 3.3.2- 3.3.9 deal with the modal test set-up and implementation in the lab.

3.3.2. Support conditions

Having established that the quality of the dynamic data obtained is of utmost importance to the successful outcome of modal testing, it is now important to highlight the importance of setting up the test correctly in the laboratory, and how the test set-up can affect the results. Firstly, the support conditions of the structure to be tested must be decided upon.

Throughout the course of this thesis, the description of dynamic testing on a variety of test specimens is outlined. All test specimens have been *'grounded'*. Specifically, each specimen has been designed to be simply supported, i.e. rotation is allowed, but horizontal and vertical motion is restricted. As pointed out by Ewins (2000), it is very difficult to provide idealised support conditions in practice as all structures have their own stiffness and cannot be regarded as truly rigid.

The support conditions are directly linked to the boundary conditions of the differential equation of motion of the structure, and subsequently affect the frequency of vibration of the structure. Since it is almost impossible to *'idealise'* these conditions in the laboratory, assumptions are generally made, and in all cases described in this thesis, the tested structures are assumed to be simply supported.

3.3.3. Impact Excitation

Once the support conditions of the test specimen have been decided upon, the next important decision to be addressed is how the structure is to be excited under dynamic testing. There are different kinds of dynamic excitation techniques. The most common tests include impact testing, sine sweep testing, white noise testing, and even ambient vibration testing.

In the case of the testing conducted and described throughout the course of this thesis, impact excitation was used to dynamically excite the specimens. The impactor is usually fitted with a force transducer so that a measurement of the dynamic impact force can be obtained. A measurement of the input force is required in order to determine the frequency response function (FRF), coherence function etc... However, throughout the course of the tests conducted, the impactor was not fitted with a force transducer. In this manner, the FRFs for the specimens were not determined. As a result, the project is an output-only response study. The natural frequencies were determined from transforming the time domain signals into the frequency domain via the Fast Fourier Transform (FFT), and identifying the peaks in the data. In this manner, the study should not be referred to as an Experimental Modal Analysis (EMA), as by definition, it requires knowledge of the input force, but rather must be referred to as an Operational Modal Analysis (OMA), in that output-only data is analysed.

Another important consideration in impact testing is the choice of the impactor head material. Shrewd choice of the impactor head is of vital importance to the outcome of the study, and the quality of the data obtained. The tip material of the impactor determines the frequency range of the data, as does the impact time. The frequency range of excitation is determined by the stiffness of the contacting surfaces and the mass of the impactor, and system resonance occurs at a frequency given by; (contact stiffness/impactor mass)$^{\frac{1}{2}}$. Above this frequency, it is very difficult to transfer energy into the structure (Ewins, 2000). An infinitesimal impact hammer response time has a completely flat frequency response and therefore all frequencies are excited in such case, as shown in Figures 3.11a and 3.11b. Avitabile (2001b) points out that the input spectrum should be *"reasonably flat"* over the frequency range of concern. The input power spectrum is controlled by the length of the time of the impact pulse, as

shown in Figure 3.11. A long pulse in the time domain results in a short or narrow frequency spectrum, whereas a short pulse in the time domain results in a wide frequency spectrum (Avitabile, 2001b). The hammer tip is responsible for the frequency spectrum excited, and in general, the harder the tip, the wider the frequency range excited (i.e. the wider the Bandwidth of the input signal) (Avitabile, 2001b). It is also possible to choose too hard a hammer tip causing too much excitation at higher frequencies, causing all of the modes of the structure to respond. However, practically, this is not possible to achieve. The effect of increasing the impact time is shown in Figure 3.11. Impact hammer pulses have frequency content that is essentially flat up to a certain frequency and then diminished from then on. There is a direct relationship between the cutoff frequency and the pulse duration. The shorter the length, the greater the frequency range (Ewins, 2000). This is illustrated in Figure 3.11. This is also related to the stiffness of the contacting surfaces and the mass of the impactor head. The stiffer the surfaces, the shorter the pulse and therefore the greater the frequency range. In general, as soft a tip as possible is used to inject all the input energy into the frequency range of interest. If a stiffer tip is used, energy is being input into vibrations outside the range of interest, at the expense of those inside that range (Ewins, 2000). It is possible that the choice of a hard steel impactor tip throughout the testing conducted, contributed significantly to the high levels of noise reported in Figure 3.10, Section 3.3.1.

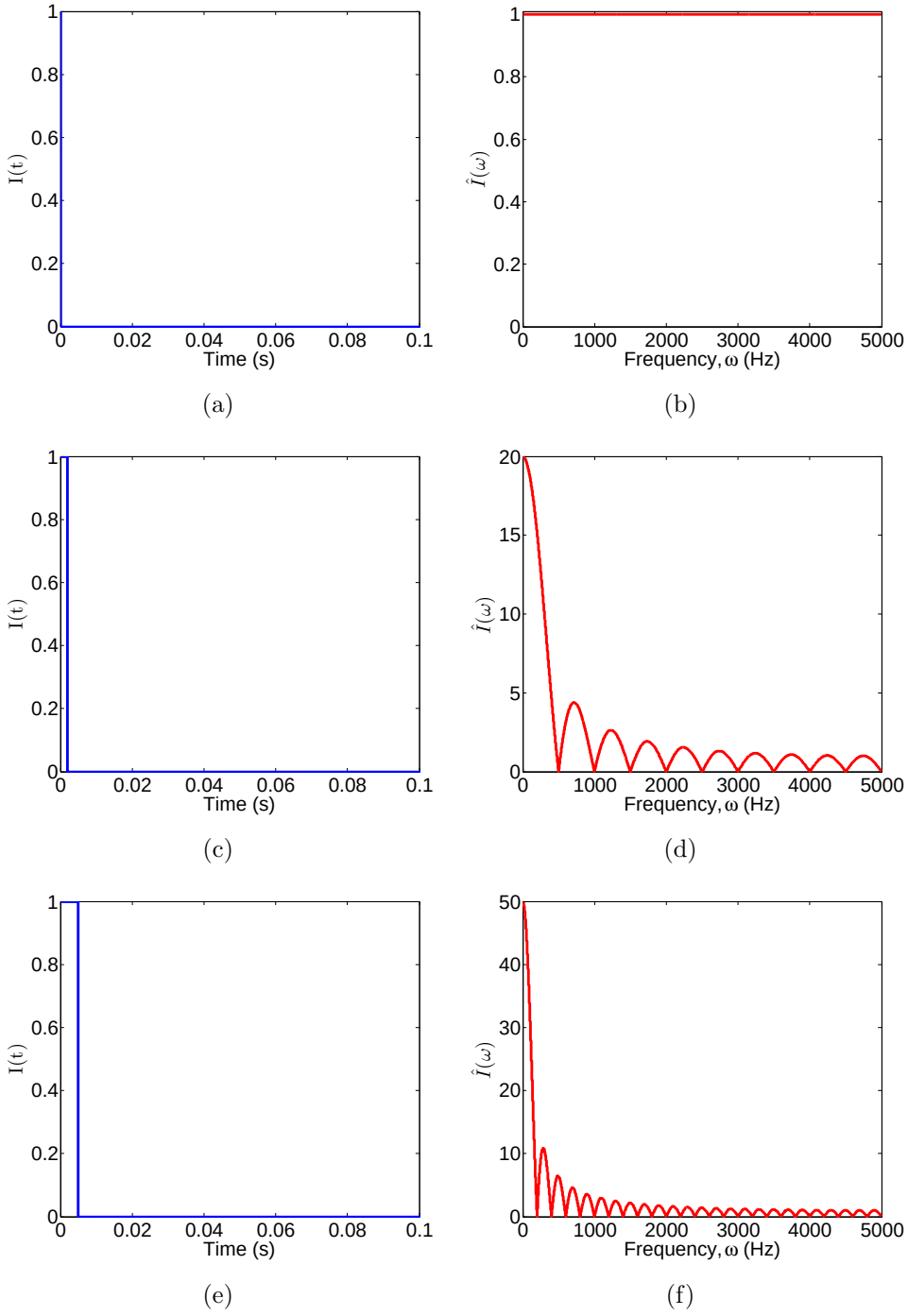

Figure 3.11.: The effect of impact contact time on the input frequency spectrum; (a) 0.0001s time domain (b) 0.0001s frequency domain; (c) 0.002s time domain (d) 0.002s frequency domain; (e) 0.005s time domain (f) 0.005s frequency domain

Another practical difficulty, and common problem experienced during modal testing with impact excitation, as outlined by both Ewins (2000) and Avitabile (2001b,a) is the *'double-hit'*, in which the structure rebounds and strikes the hammer before the hammer can be pulled away. In these cases, the frequency response is seen to have *'holes'* at certain frequencies, which can lead to erroneous results. A double impact causes a non-uniform, non-flat input force spectrum, and as such, should be avoided at all costs, as it invokes the possibility of missing critical frequency content due to the destructive interference of the second hit on the original signal.

3.3.4. Choice of accelerometer

The choice of sensory equipment also affects the outcome of the tests significantly. There are many types of dynamic sensors, such as force transducers, velocity transducers, dynamic strain gauges, dynamic LVDTs etc... however the most common type of dynamic sensors are accelerometers, which also was chosen as the dynamic sensor used throughout the modal testing conducted.

Accelerometer sensitivities range between 1-10,000pC/g. In general, it is better to choose an accelerometer with as high a sensitivity as possible. However, the greater the sensitivity, the heavier the accelerometer, and the lower the resonant frequency of the accelerometer itself, and hence the lower the maximum working frequency (Ewins, 2000). In addition, the addition of an accelerometer adds mass to a structure and subsequently alters the natural frequency. However, the mass of the accelerometer in this case is negligible compared to the mass of the relatively large-scale specimens tested. Other issues with the choice of accelerometer include how it is attached to the structure. In all tests conducted and described throughout the course of this thesis, the accelerometer was affixed to the steel and concrete specimens by means of a threaded stud. Evidently, this requires modification of the structure, as holes need to be drilled in the structure to accommodate affixing the measurement device. Again, this was considered insignificant to the overall structural stiffness of the tested specimen(s). The screwed stud has a particularly high frequency capability, but this may only be obtained if the accelerometer is affixed exactly normal to the structure surface. Misalignment will result in a corresponding loss of stiffness and

therefore a lower cutoff frequency (Ewins, 2000).

The placement of the accelerometer on the structure is also of utmost importance. If the accelerometer is placed close to the node of a mode of vibration then it is very difficult to make an effective measurement of that particular mode. As a result, during concrete testing the accelerometer was placed $800mm$ from the support, between midspan and the support, in order to clearly capture all of the first three natural bending modes of vibration, as shown in Figure 3.12.

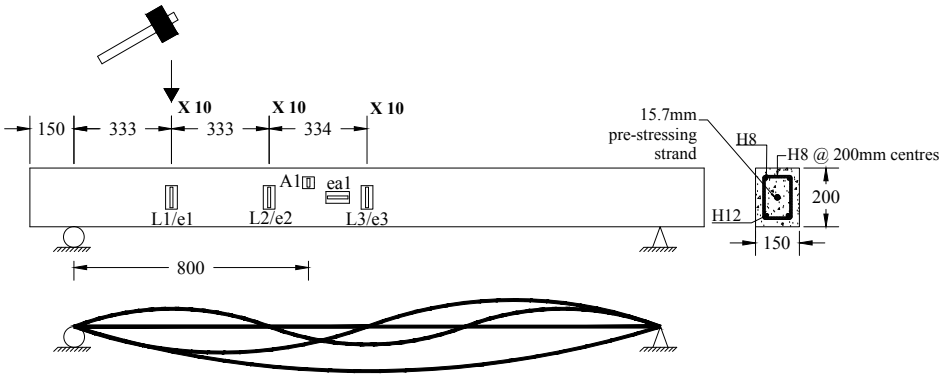

Figure 3.12.: Positioning of accelerometer to capture first 3 modes of vibration

Ultimately the accelerometer used in the modal testing of the structures was a Dytran model 3200b4 10,000g range accelerometer.

3.3.5. Operating data vs. Modal data

The difference between operating data and modal data is important. To obtain modal data, knowledge of the input force characteristics is required, and this must be compared to the output force characteristics in order to obtain the FRFs, however, with operating data, the input force is not measured, and the analysis is conducted on the output response of the structure only. This is the fundamental difference between Experimental Modal Analysis (EMA) and Operational Modal Analysis (OMA).

Recalling how a structure responds to any dynamic excitation;

$$\hat{O}(j\omega) = H(j\omega)\,\hat{I}(j\omega) \tag{3.65}$$

The response is computed by multiplying the frequency response function (FRF) by the input forcing function. It is important to note that the FRF acts as a filter on the input force which results in some output response. The excitation causes all modes of vibration to be activated and therefore the response is the linear superposition of all the modes activated by the input excitation (Avitabile, 2001b). With operating data, the input force or the FRF is never measured, the output response only is measured. Therefore, the measured deformations are the actual response of the structure due to input excitation. The operating data itself is usually primarily some combination of the first and second modes of vibration. Note that when operating data is collected, instead of measuring FRFs, output spectra are measured. The Modal data is contained in the FRFs whereas the Operating data is contained in the output spectra. The natural frequencies of the structure may still be extracted form the peaks in the output spectra, as discussed later in this thesis.

3.3.6. Basic steps for impact testing

The following section outlines in detail the basic steps in conducting a modal impact test in the laboratory. These steps were followed throughout the modal testing conducted and described in Chapters 4, 6, and 7.

The excitation is initially applied to the structure using a hammer. If the force transmitted to the structure is measured using an in-built force transducer, then the test is referred to as an Experimental Modal Analysis (EMA). If the input force is not measured, then the test is referred to as an Operational Modal Analysis (OMA). The response of the structure is measured using an accelerometer, or various accelerometers, distributed at response points of the structure. In many data acquisition systems, a pre-trigger delay is specified to capture the entire transient of the impact device (Avitabile, 2001b). The data is then collected and a low-pass filter is applied to filter out uninteresting high-frequencies and to prevent aliasing from occurring (see Section 3.4.1). The data is then passed to an analogue to digital converter (ADC) where the data is sampled and converted into digital form. It is important that the data is sampled at a rate that captures the frequency bandwidth of interest. The Nyquist frequency (ω_{Nyq}) is given as half of the sampling rate of the data (ω_s), i.e. $\omega_{Nyq} = \omega_s/2$. This

means that if the data is sampled at $\omega_s = 10,000Hz$, then the maximum bandwidth is $\omega_{Nyq} = 5,000Hz$.

Leakage (Section 3.4.3) will occur if the entire signal is not captured during the acquired data sample (Avitabile, 2001b). Some form of windowing (Section 3.4.4) may be required to minimise the effects of leakage on the signal. For example, if the response signal does not decay to zero by the end of the sample interval, an exponential window may be required to avoid signal distortion following the Fourier Transform process (Avitabile, 2001b). Following sufficient windowing and signal filtering in order to remove noise and all other unwanted frequency components, the input signal and the output signal in the time domain are converted into the frequency domain using the Fast Fourier Transform technique. Following this, the Frequency Response Function (FRF) is computed, as given in Equation 3.3, and outlined in Figure 3.3. Having determined the FRF, single degree of freedom (SDOF) curve-fitting techniques are used to identify the natural frequencies of the structural system through some sort of peak-picking algorithm. The mode shapes are extracted from the data by measuring the relative amplitude of each peak response at a specified frequency at the different locations in the structure at which they are measured.

3.3.7. MIMO Testing

MIMO testing stands for multiple-input multiple-output testing, in which the structure is excited at multiple input points, and its response is measured at multiple output points. The careful choice of the input and output points lead to the determination of the experimental mode shapes of the structure. The following explanation will closely follow that described by Avitabile (2001b). Consider the 3DOF cantilever structure shown in Figure 3.13.

Here, there are multiple dynamic input/excitation points, i, and multiple dynamic output/response points, j. Since there are 3 input points and 3 response points, there are 9 possible complex-valued Frequency Response Functions (FRFs) that may be computed. Let $h_{i,j}$ denote the complex-valued FRF at response point j due to excitation at input point i. These FRFs are organised in the form of a 3×3 matrix of FRF data. Let $H(j\omega)$

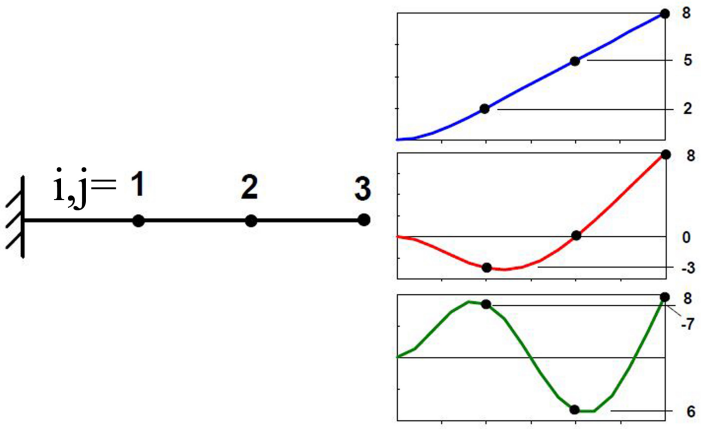

Figure 3.13.: 3DOF cantilever model with corresponding mode shapes (Avitabile, 2001b)

denote such a matrix, and therefore is given as;

$$H(j\omega) = \begin{bmatrix} h_{1,1} & h_{1,2} & h_{1,3} \\ h_{2,1} & h_{2,2} & h_{2,3} \\ h_{3,1} & h_{3,2} & h_{3,3} \end{bmatrix} \tag{3.66}$$

Note that frequency response is a complex number and therefore may be described in terms of magnitude and phase, or in terms of real and imaginary values. The data is shown in Figure 3.14.

Figure 3.14a shows the Magnitude of the FRF functions, Figure 3.14b shows the Phase data, Figure 3.14c shows the Real data, and Figure 3.14d shows the Imaginary data. From Figure 3.14, it is clear that the FRF matrix is symmetric. This is due to the fact that the mass, damping and stiffness matrices that describe the system are also symmetric (Avitabile, 2001a). This property is known as ***reciprocity***; $h_{i,j} = h_{j,i}$. This effectively means that the same measurement may be taken by exciting the structure at point 1 and measuring the response at point 3, as exciting the structure at point 3 and measuring the response at point 1. This leads to the conclusion that in order to accurately describe the modal properties of a structural system, it is possible to measure the response at multiple locations, and keep the excitation point constant, or to measure the response at one location and change the excitation point. In the studies conducted and described in Chapters 4, 6, and 7, the latter was chosen, in that the response of the

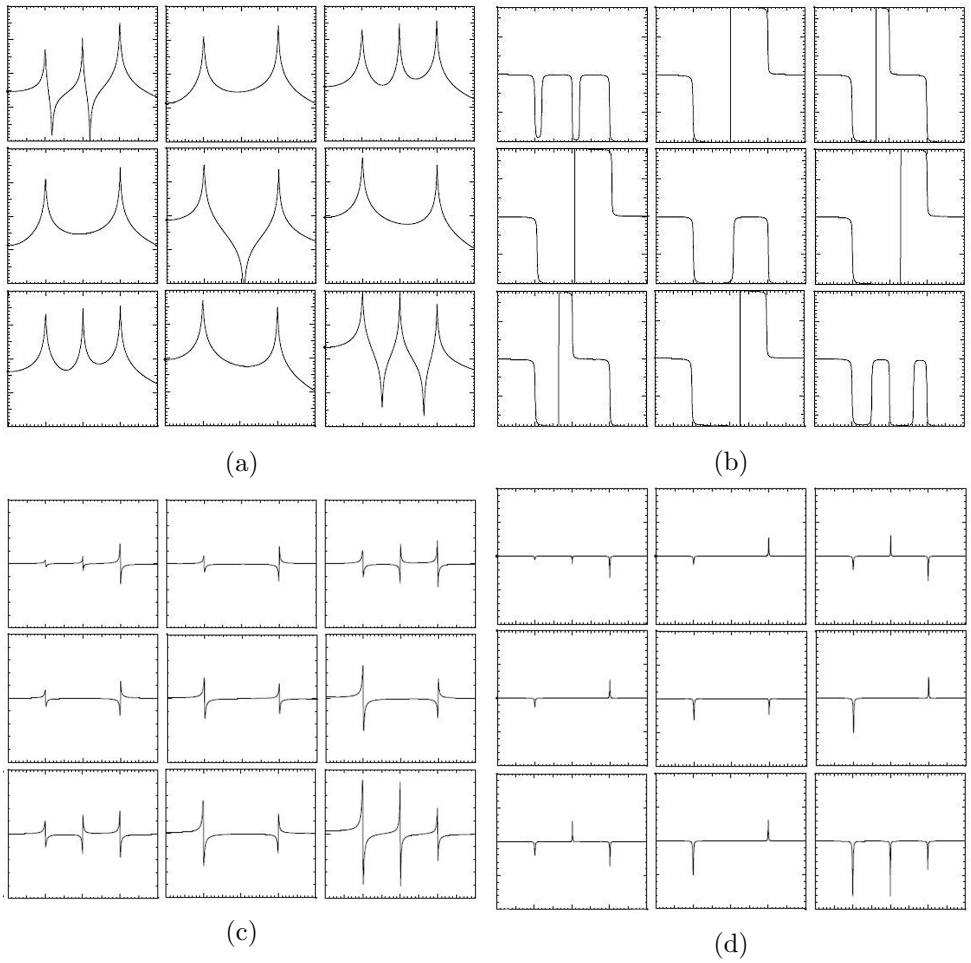

Figure 3.14.: FRF data for 3DOF cantilever model; (a) Magnitude; (b) Phase; (c) Real; (d) Imaginary. (Avitabile, 2001a)

structure was measured at one location only, but the input location was changed.

The mode shapes are extracted from the imaginary part of the frequency response function, as outlined by Avitabile (2001a). By taking the amplitude of the imaginary response at the corresponding first modal frequency, ω_1, the first bending mode of vibration may be obtained as shown in Figure 3.15. The first bending mode of vibration may be obtained from all 3 rows and all 3 columns of the FRF matrix. Figure 3.15a shows the extraction of the first bending mode from the 2^{nd} row of the FRF matrix, and Figure 3.15b shows the extraction of the first bending mode from the 3^{rd}

row of the FRF matrix.

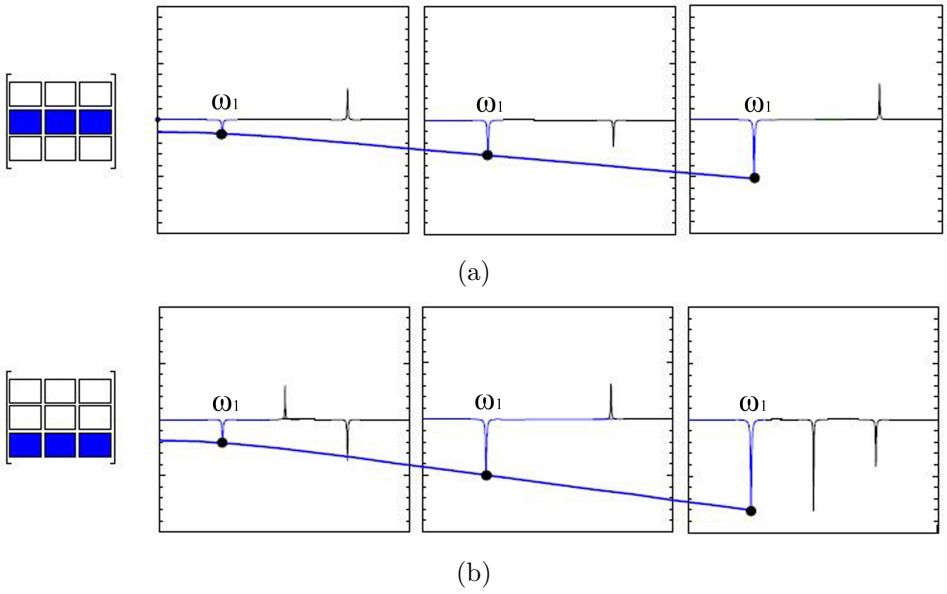

Figure 3.15.: Extraction of first bending mode shape from FRF matrix; (a) Row 2; (b) Row 3. (Avitabile, 2001a)

Consider now the extraction of the second mode shape of vibration from the given data. Figure 3.16a shows the second row of the FRF matrix. However, there is no amplitude for the second mode of vibration. This highlights an important aspect of modal testing - the reference point cannot be located at the node of a mode as the mode does not show up in the FRF measurements and therefore the mode cannot be obtained. Similarly, the mode is unattainable from the second column of the FRF matrix. Figure 3.16b shows the third row of the FRF matrix, where the second mode shape of vibration can be extracted from the peak amplitude of vibration of the imaginary part of the FRF (Avitabile, 2001a).

Finally, by adding more input-output measurement locations, then the mode shapes may be represented more accurately as shown in the waterfall plot in Figure 3.15 (Avitabile, 2001a).

3.3.8. Coherence function

The coherence function is a function used to assess the quality of the obtained data. It gives an indication of how much of the output signal is

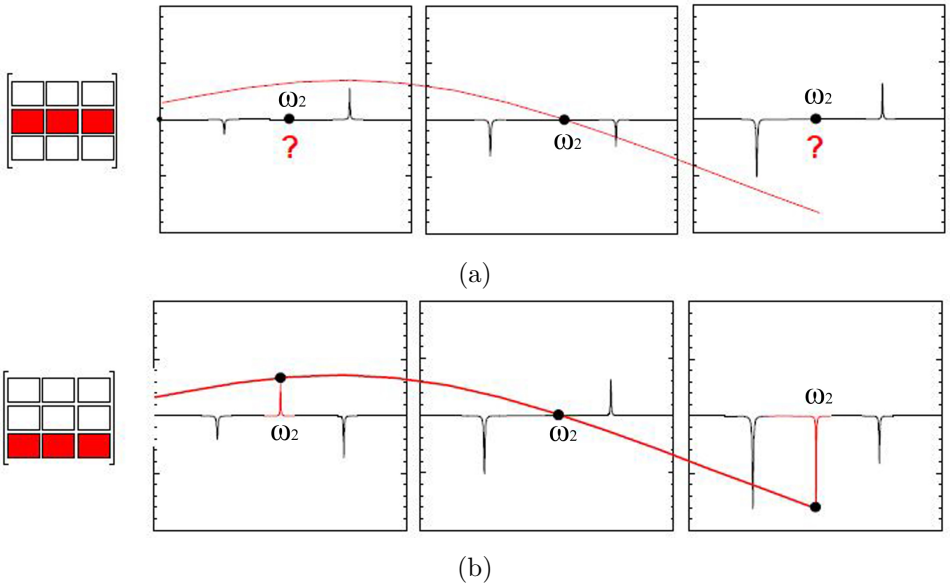

Figure 3.16.: Extraction of second bending mode shape from FRF matrix; (a) Row 2; (b) Row 3. (Avitabile, 2001a)

actually related to the input signal - i.e. a measurement of causality. Coherence can only be evaluated for averaged measurements. If there is only one average, there can be no variation relative to the one measurement made, therefore the coherence must be 1.0. However, this is not an indication of quality data. The coherence function may only be used to evaluate variation on a set of averaged functions, therefore averaging is required (Avitabile, 2001b). Coherence is measured to ensure that there is a relatively good casual relationship between the input and output signals, ensuring a good measurement is made.

Since coherence measurements, by definition, require measurement of both the input and output force, they have not been obtained in the testing described throughout this thesis. An output-only study has been conducted and described throughout the course of this thesis. Coherence is effectively a measure of the correlation between the input and the output signals.

3.3.9. Operational Modal Analysis

Operational Modal Analysis (OMA) is the measurement of the modal properties of a structure based on ambient vibration data (i.e. vibration data

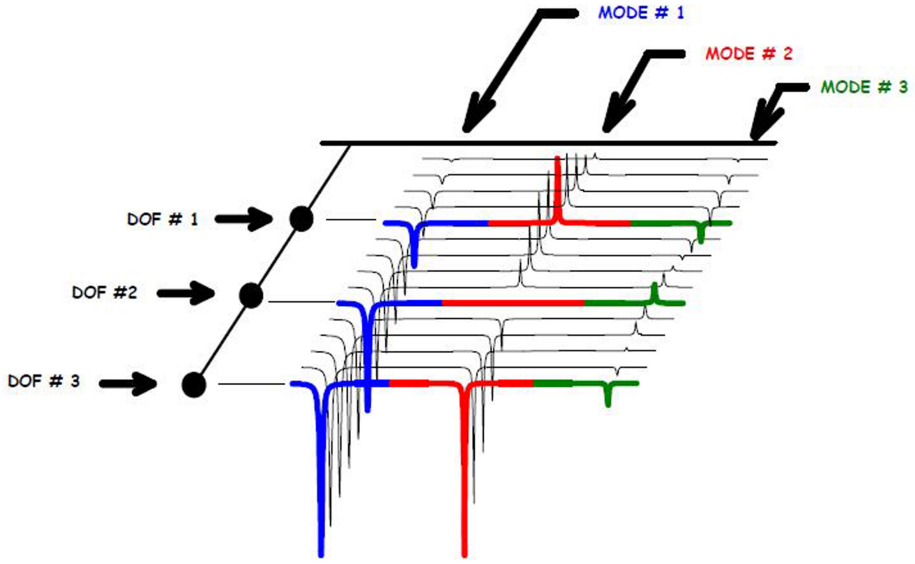

Figure 3.17.: Waterfall plot of first 3 bending mode shapes of vibration (Avitabile, 2001a)

collected from the structure under its normal operating conditions). These structural systems are known as *"output-only systems"*. One of the main features of this type of analysis is that the input forces do not need to be measured. As pointed out by Avitabile (2001b), this is the biggest benefit and greatest downfall of the method, as there is no guarantee that the excitation will cause response of all of the desired system characteristics.

In output-only systems, the input force is not measured, but it is assumed that it is generally broadband and excites a frequency band that defines the operating characteristics of the system (Avitabile, 2001b). In the case of impact testing, it is desirable to minimise the contact time of the impact in order to maximise the range of frequencies excited. In theory, an infinitesimal contact time will excite all frequencies, however, this is unattainable in practice. Avitabile (2001b) also reports that in general, output-only systems tend to predict much higher damping than exists in reality.

3.4. Digital Signal Processing

The Fourier Transform, as described in Section 3.2.4, is only applicable to continuous functions, however, there is a requirement to conduct Fourier

Analysis on a discrete time signal. An analogue signal is discretised into a digital signal through data sampling. The number of points that define a digital signal is determined by the sampling rate of the analogue to digital converter (ADC) of the data logger.

The Fourier transform, in it's simplest form states that a function $x(t)$, periodic in time, T, can be written in the form (Ewins, 2000);

$$x\left(t\right) = \frac{a_0}{2} + \sum_{n=1}^{\infty}\left(a_n \cos\frac{2\pi nt}{T} + b_n \sin\frac{2\pi nt}{T}\right) \tag{3.67}$$

where a_n and b_n are given by;

$$\begin{aligned} a_n &= \left(\frac{2}{T}\right)\int_0^T x\left(t\right)\cos\left(\frac{2\pi nt}{T}\right)\mathrm{dt} \\ b_n &= \left(\frac{2}{T}\right)\int_0^T x\left(t\right)\sin\left(\frac{2\pi nt}{T}\right)\mathrm{dt} \end{aligned} \tag{3.68}$$

When $x(t)$ is discretised and of finite duration, so is fully defined by N particular values of time $(t_k; k = 1, N)$, a finite Fourier series is written;

$$x_k\left(= x\left(t_k\right)\right) = \frac{a_0}{2} + \sum_{n=1}^{\infty}\left(a_n \cos\left(\frac{2\pi nt_k}{T}\right) + b_n \sin\left(\frac{2\pi nt_k}{T}\right)\right); k = 1, N \tag{3.69}$$

The coefficients a_n or b_n are the Fourier (spectral) coefficients for $x(t)$ and are often displayed in modulus and phase form; $c_n(= X_n) = \sqrt{a_n^2 + b_n^2}$ and $\phi_n = tan^{-1}\left(-b_n/a_n\right)$ (Ewins, 2000). The input signal is digitised by an A-D converter and recorded as a set of N discrete values, evenly spaced in the period T. In impact testing, this is wholly defined by the sampling rate. In the testing described throughout the course of this thesis, the signals were sampled at a rate of 10,000Hz, i.e. the signal was sampled at a rate of 10,000 times per second. There is a relationship between the sampling rate, ω_s and the range and resolution of the frequency spectrum (ω_{Nyq}, $\Delta\omega$). The range of the spectrum is $0 - \omega_{Nyq}$, where ω_{Nyq} is known as the Nyquist frequency and is given by;

$$\omega_{Nyq} = \frac{\omega_s}{2} = \frac{1}{2}\left(\frac{2\pi N}{T}\right) \tag{3.70}$$

the resolution of the lines in the spectrum, $\Delta\omega$, is given by (Ewins, 2000);

$$\Delta\omega = \frac{\omega_s}{N} = \frac{2\pi}{T} \tag{3.71}$$

3.4.1. Aliasing

Aliasing is an error associated with digital signal processing (DSP) in which the existence of very high frequency components in the signal are missed as the sampling rate is not large enough. It is not possible to determine any frequency greater than the Nyquist frequency, which is, by definition, half the sampling rate. A signal of frequency ω and one of $(\omega_s - \omega)$ are indistinguishable when represented as a discretised time history, causing a distortion in the spectrum measured by the DFT (Ewins, 2000). Figure 3.18 illustrates the issue with signal aliasing. There are two signals - a low frequency signal and a high frequency signal. The sampling rate is such that the low frequency signal is captured however, the sampling rate is too slow to capture the high frequency signal, and therefore the signal has been 'aliased'.

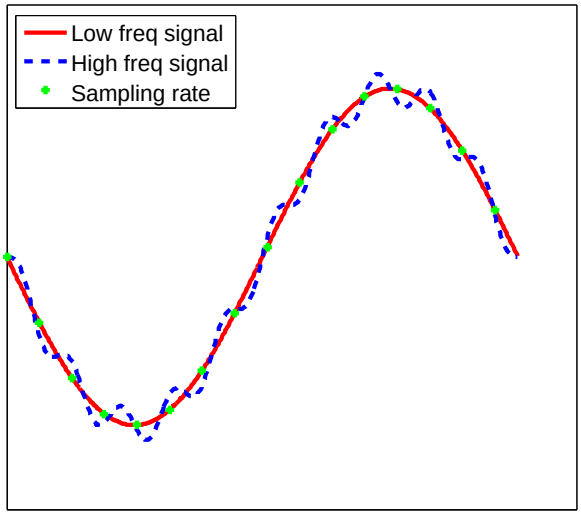

Figure 3.18.: Aliasing (reproduced from Ewins (2000))

Figure 3.19 shows the effect of aliasing on the signals in the frequency

domain. The highest frequency which can be included is the Nyquist frequency, i.e. half the sampling rate. In the case of aliasing, as shown in Figure 3.19, where the frequency components greater than the Nyquist frequency are reflected or 'aliased' in the range $0 - (\omega_s/2)$ (Ewins, 2000). The solution to this is to use an anti-aliasing filter. The anti-aliasing filter is a low pass, sharp cut-off filter, as shown in Figure 3.20b. The type of filter implemented is usually a high order low pass Butterworth filter (Butterworth, 1930). Anti-aliasing filters are not automatically built-in to signal analysers and data collectors. The reduced aliasing due to an anti-aliasing filter can be seen in Figure 3.20c.

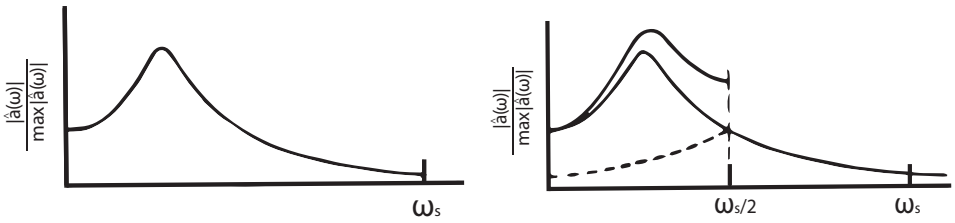

Figure 3.19.: Effect of aliasing on a signal (Adapted from Ewins (2000))

3.4.2. Butterworth Filter

The Butterworth filter is a type of signal processing filter that is designed to have as flat a frequency response as possible in the passband and was first described by Butterworth (1930). The higher order the Butterworth filter, the closer to ideal 'brick wall' response. However, a high order filter leads to excessive passband ripple that will corrupt the original signal. Figure 3.21, obtained from Wikipedia (2015a) shows the benefit of the Butterworth filter over its rivals. The main benefit is in the smoothness of the frequency response of the filter in both the passband and the stopband region, therefore minimising signal corruption in both the stopband and passband of the frequency domain. The passband region is the region in which the frequency content is passed, whereas the stopband region is the region in which the frequency content is attenuated by the filter.

The Butterworth filter is defined by Oppenheim et al. (1999) by their property that the magnitude response is maximally flat in the passband.

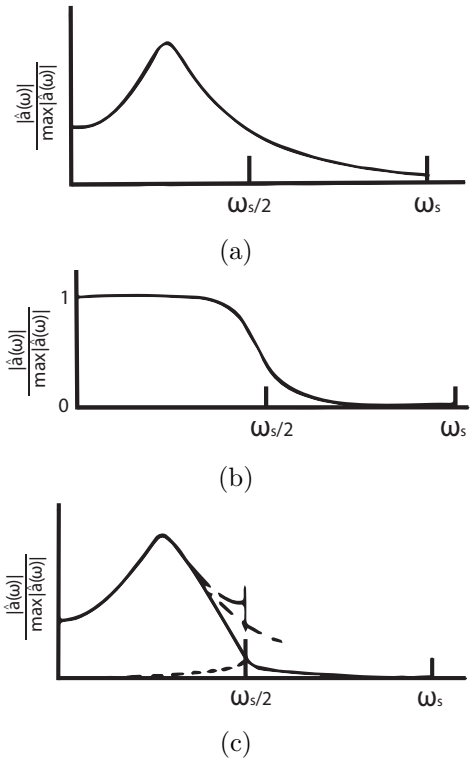

Figure 3.20.: Anti-aliasing filter process - adapted from Ewins (2000)

For an N^{th} order lowpass filter, this means that the first $(2N-1)$ of the magnitude squared function are zero at $\omega = 0$. Furthermore, the magnitude squared response is monotonic in both the passband and the stopband. The magnitude-squared response of the continuous Butterworth lowpass filter is given by;

$$|H_c(j\omega)|^2 = \frac{1}{1 + (j\omega/j\omega_c)^{2N}} \tag{3.72}$$

Figure 3.22 shows superimposed Butterworth lowpass filters with differing orders in the frequency domain. The Fast Fourier Transform (FFT) is used to convert signals from the time domain into the frequency domain, as often, signal processing techniques are more intuitive to understand and to implement in the frequency domain as opposed to the time domain. The filter is then multiplied with the FFT of the signal in the frequency domain to obtain the filtered signal. An idealised filter will eliminate all frequency components in the stopband and pass all frequency components in the pass-

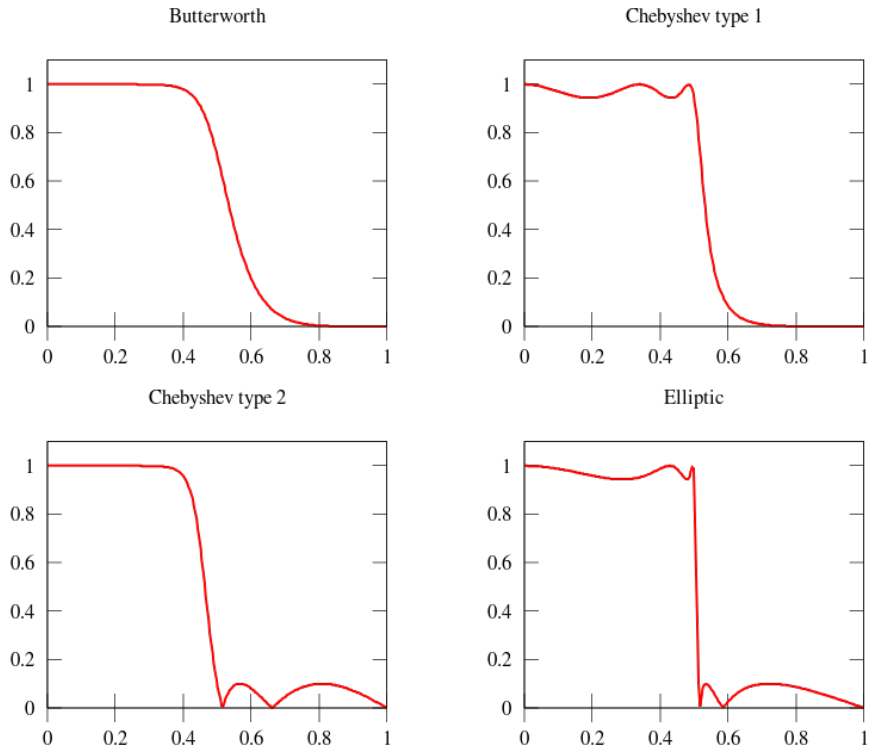

Figure 3.21.: Comparison of different types of filters (Wikipedia, 2015a)

band, however, as shown in Figure 3.22, the cut-off is not absolute and the frequency data is attenuated on either side of the cut-off frequency, ω_c. High order filters are preferable, however, the order must not be excessive as this can cause significant passband and stopband ripple which corrupts the signal and counteracts the benefit of using the Butterworth filter to begin with.

3.4.3. Leakage

Leakage is a signal processing problem related to discrete signals and the definition of the Fourier Transform. The Fourier Transform is defined in Equation 3.13, and the integral is defined over the range of $(-\infty, +\infty)$. Leakage occurs due to the need to take only a finite length of time-history, coupled with the assumption of periodicity (Ewins, 2000). The effect of leakage is displayed in Figure 3.23, adapted from Ewins (2000). Figures 3.23a and 3.23b show the same perfectly periodic signal in both time and fre-

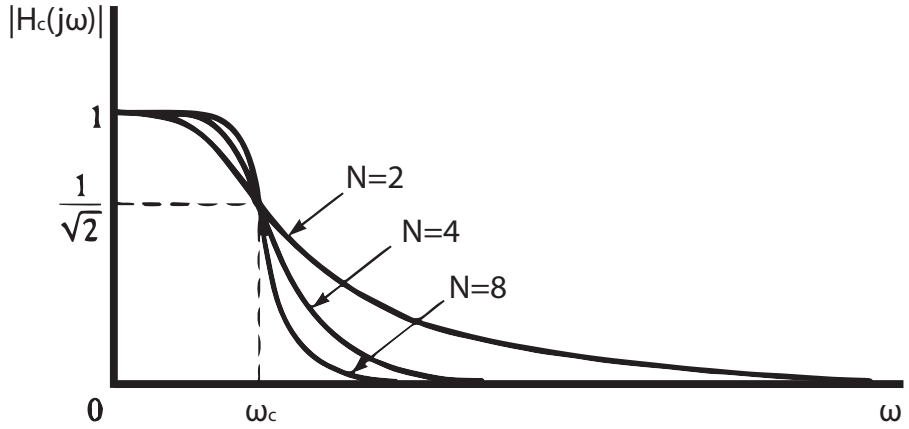

Figure 3.22.: Butterworth filter, with various orders, N (Oppenheim et al., 1999)

quency domain. Due to this perfect periodicity, the frequency domain representation is a single line at the frequency of the sine wave (Ewins, 2000). However, when the periodicity assumption is not valid and there is a discontinuity at the beginning or the end of the signal in the time domain, the resulting frequency spectrum does not indicate the original frequency. This frequency is actually not represented. Energy has *'leaked'* into a number of the spectral lines close to the true frequency and the spectrum is spread over several lines (Ewins, 2000). Ewins (2000) suggests the following to minimise the effects of leakage;

- changing duration of signal to match periodicity. This can only be done if underlying signal is periodic.
- Increasing duration of measurement period. This results in finer frequency resolution by reducing the separation between spectral lines.
- ***'Zero padding'***; adding zeros before and after signal, which artificially removes the periodicity requirement. In the same manner, impact signals experience minimal distortion due to leakage once the signal is analysed over the appropriate region.
- ***'Windowing'***; the original signal is modified in the time domain in order to reduce the effect of leakage.

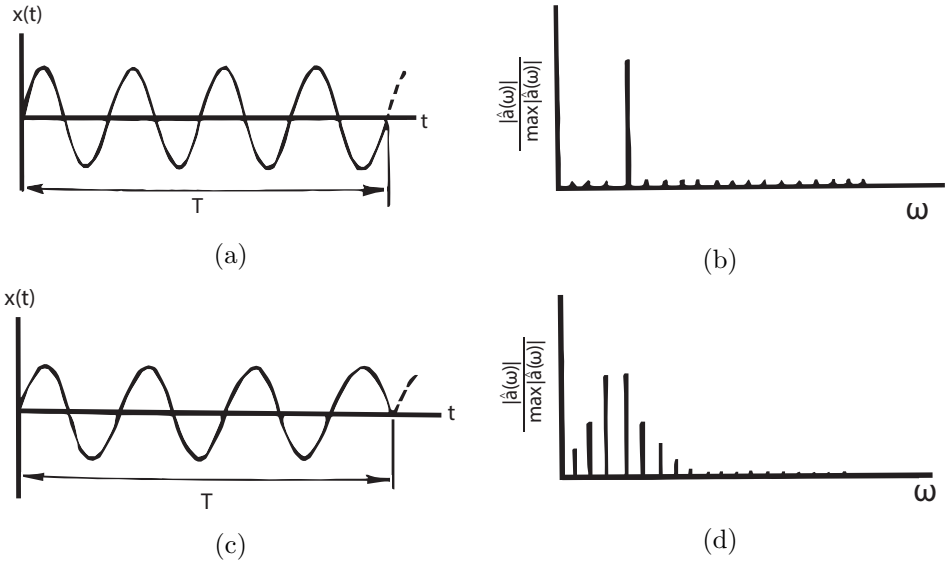

Figure 3.23.: Effect of leakage. Adapted from Ewins (2000)

3.4.4. Windowing

Windowing involves the modification of the signal in the time domain in order to suppress the effects of unwanted frequency content and minimise the effects of leakage, which as discussed in Section 3.4.3, corrupts the signal in the frequency domain. The original signal is given as $x(t)$, the windowed signal, $w(t)$ and the modified signal as $x'(t)$, such that; $x'(t) = x(t).w(t)$. This operation can also be conducted in the frequency domain, however it is given by; $X'(\omega) = W(\omega) * X(\omega)$, where $*$ is the convolution operator. Figure 3.24, which has been adapted from Ewins (2000), shows different types of windows and the resulting modified signals. Figure 3.24b shows the Boxcar window, Figure 3.24e shows the Hanning window, Figure 3.24h shows the Cosine-taper window and Figure 3.24k shows the Exponential window.

Avitabile (2001b) point out that when conducting a modal test, the type of input excitation can be selected such that the use of windows can be eliminated. Recall that the Fourier Transform is defined in the range $(-\infty, +\infty)$, however, the data is only acquired over a very short space of time. Provided that the signal acquired may be reconstructed periodically for all time, then there is no leakage effect (Avitabile, 2001b). Weighted window functions are used to minimise the effect of leakage by minimising the effect of discontinu-

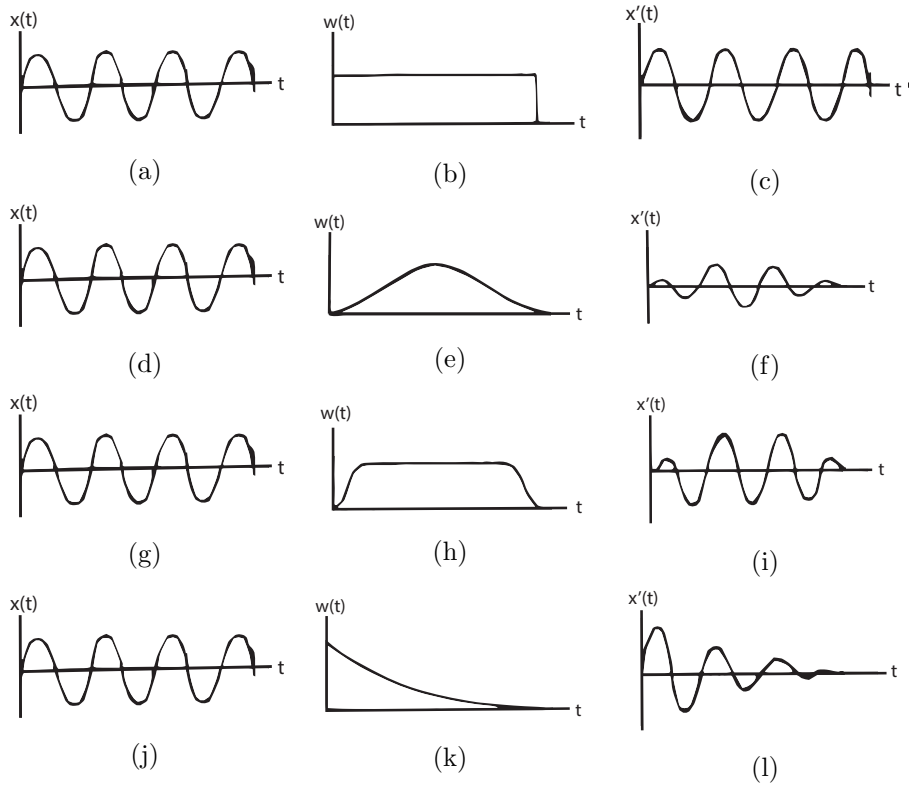

Figure 3.24.: Different types of windows; (a) Boxcar; (b) Hanning; (c) Cosine taper; (d) Exponential. Adapted from Ewins (2000)

ity when performing the FFT. Avitabile (2001b) warns that **all windows distort data**, as they distort the peak amplitude and appear to indicate more damping than actually exists. Avitabile (2001b) suggests in order to avoid the use of windows to continuously sample a periodic repetition of the data, or to completely observe the signal in one data sample. The latter is obtained by choosing impulse/impact excitation as the type of dynamic excitation.

3.4.5. Filtering

Filtering is the process of modifying the signal in the frequency domain to remove unwanted frequency components from the signal, i.e. to filter them out. It is a frequency domain process. As outlined by Ewins (2000), there are five main filter types, namely;

- low-pass (see Section 3.4.1)
- high-pass
- band-limited
- narrow-band
- notch

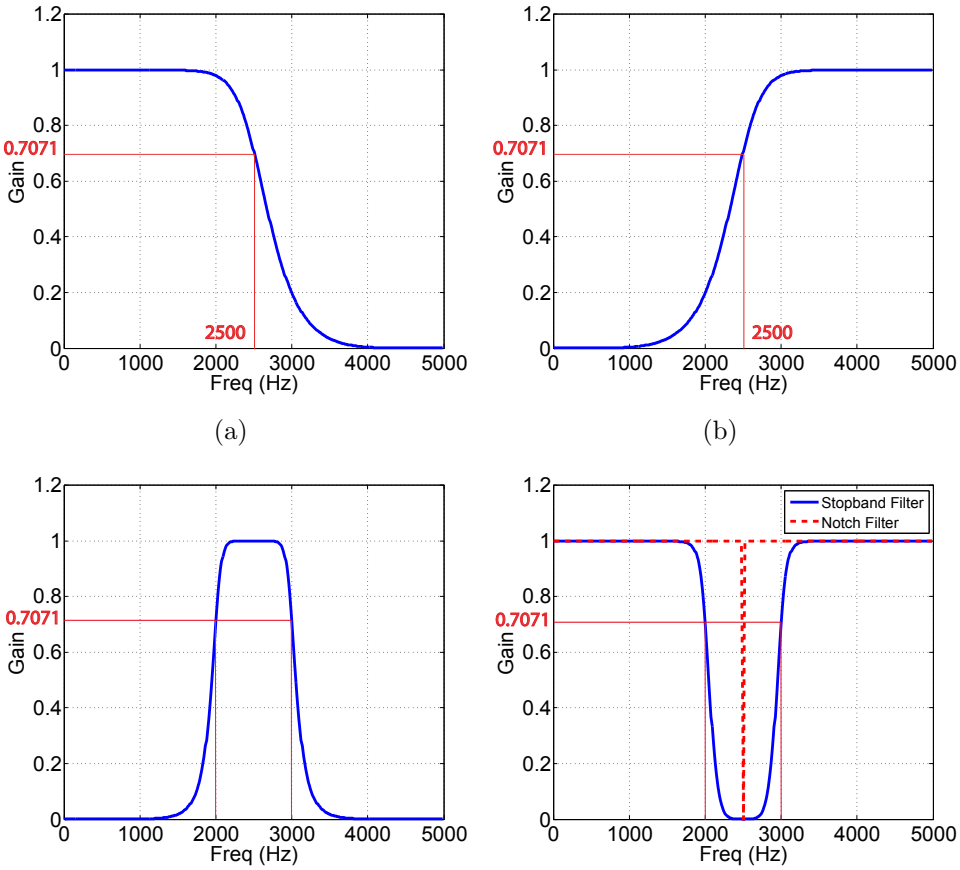

Figure 3.25.: Different type of frequency filters; (a) Low-pass Butterworth filter (b) High-pass Butterworth filter (c) Band-pass Butterworth filter (d) Stopband Butterworth filter

Figure 3.25 shows 5 different types of filters. Figure 3.25a shows a low-pass Butterworth filter, passing all frequencies lower than the cut-off frequency, $\omega_c = 2500Hz$ and stopping all frequencies $> \omega_c$. Figure 3.25b shows a high-pass Butterworth filter, passing all frequencies $> \omega_c$, and stopping

all frequencies $< \omega_c$. Figure 3.25c shows a passband filter, passing the frequencies $2000 < \omega < 3000Hz$ and attenuating all frequencies outside of this range. Figure 3.25d shows a Stopband filter and a specific type of Stopband filter, known as a *'Notch'* filter. Stopband filters attenuate all filters within a certain range, known as the 'stopband'. When this range is very small/specific, it is known as a *'Notch'* filter. All the filters shown are 5^{th} order. In practice, all filters have a finite frequency range over which they function and exhibit roll-off features near critical frequency regions. For example, Figure 3.25a shows a low-pass Butterworth filter with cut-off of $2500Hz$. The amplitude response of the filter at cut-off is equal to $1/\sqrt{2}$. This is equivalent to $-3dB$ as $dB = 10log_{10}(A^2)$, where A is the Amplitude, or *'Gain'* of the filter.

Filtering is a technique best conducted in the frequency domain such that $X'(\omega) = X(\omega).F(\omega)$ where $F(\omega)$ is the frequency domain representation of the filter, $X(\omega)$ is the frequency domain representation of the original signal and $X'(\omega)$ is the frequency domain representation of the filtered signal. This is the opposite to windowing, which is best performed in the time domain. Inverse Fourier Transforms (IFTs) may be performed on these signals to convert them back into the time domain. Filtering may also be performed in the time domain in the same way that windowing may be performed in the frequency domain, such that $x'(t) = x(t) * f(t)$, where $f(t)$ is the IFT of the frequency filter, $x(t)$ is the original signal in the time domain and $x'(t)$ is the filtered signal in the time domain.

3.4.6. Zoom

Zooming in on the frequency range of interest in the frequency domain representation of a signal is a common solution for the need for finer frequency resolution. However, it is important that a bandpass filter is applied to the signal to avoid the aliasing effects referred to previously in Section 3.4.1. When using zoom to observe a narrow frequency range, it's important to ensure that as little vibration energy as possible is outside the frequency range of interest (Ewins, 2000).

3.4.7. Averaging

It is necessary to perform an averaging process involving several samples before a result is obtained that can be used with confidence. The two major considerations which determine the number of averages required are (Ewins, 2000);

- statistical reliability
- removal of spurious random noise from the signals

3.5. Summary

In this chapter, the reader has been presented with the main tools, techniques and theory of the principles behind dynamic testing and specifically modal analysis of structures. Some of these techniques have been used at length through the experimental testing conducted throughout the course of this project and described in detail in Chapters 4, 6 and 7. In all cases, output-only testing has been conducted and the fundamental modal frequencies have been extracted from a set of simple structural systems in the lab. The structures tested were both in steel and in post-tensioned concrete.

Section 3.2 outlined the theoretical basis behind experimental modal analysis and some of the specific tools and techniques used to conduct the analysis. Section 3.3 outlined the measurement techniques behind collecting good dynamic data, including outlining the basic steps behind conducting modal analysis. Section 3.4 presented some specific techniques behind digital signal processing, in order to prepare the dynamic signals for analysis. This chapter provided necessary background in the theory, tools and techniques behind experimental dynamic testing and serves as to provide the reader with a concise introduction, background and basis of these aspects prior to reading Chapters 4, 6 and 7.

4. Dynamic impact testing of post-tensioned steel rectangular hollow sections; an investigation into the "compression softening" effect

This chapter describes the results of dynamic impact testing on externally axially loaded steel rectangular hollow sections (RHSs) and compares the response to that of post-tensioned steel RHSs. Both the fundamental natural bending frequency of the beam sections and the corresponding damping ratios have been calculated from the measured dynamic response of the beam to a series of impact hammer strikes. The validity of the *"compression-softening"* effect for post-tensioned sections is tested. The implications of the research are vast, as currently, there is significant disagreement among researchers about the effect of pre- and post-tensioning loads on the dynamic characteristics of structures. The fundamental bending frequencies have been calculated and corresponding damping ratios have been calculated from dynamic test results for each axial load level. The bending frequencies have been calculated repeatedly while changing the axial load level and the subsequent changes in both frequency and damping ratio, with increasing axial load level have been analysed to determine if the results are statistically significant. It has been determined that *"compression-softening"* theory is not valid for pre- or post-tensioned steel sections.

4.1. Introduction

In order to isolate this problem, a study must first be conducted into the validity of the aforementioned *"compression-softening"* effect. Subsequently,

the aim of this chapter is to report on the impact hammer testing and experimental modal analysis conducted on both externally axially loaded steel rectangular hollow sections (RHSs), and their post-tensioned counterparts. The purpose of the research is first to determine under what conditions *"compression-softening"* theory holds true. The assumption that an external axial load is dynamically equivalent to an internal post-tensioning force is investigated in this chapter. Previous results dealing with the change in fundamental frequency with increasing axial load for both externally axially loaded RHSs and post-tensioned RHSs have been presented by Noble et al. (2014b).

This chapter is organised as follows; Section 4.2 presents the details of the initial design of the dynamic experiments on the steel RHSs in the lab. Details of the sections themselves are presented, accompanied by materials testing, and design checks of the buckling and bending capacity of the steel RHS sections, along with estimations of the natural bending frequencies for each beam section. Section 4.4 describes the experimental set-up in the laboratory, for the dynamic tests conducted, while Section 4.5 describes the set-up for the static tests. Section 4.6 describes the signal processing procedure used on the obtained data, and the calculation of the fundamental bending frequencies and damping ratios for the given beam and load case combinations. Section 4.8 describes the experimental results obtained, and describes the observed changes in fundamental natural bending frequency and damping ratio with increasing axial load level. Section 4.11 outlines the main conclusions of the chapter derived from the experimental results and also outlines the results of statistical analysis on the obtained results, by regressing both fundamental natural bending frequency and damping ratio on axial load level.

4.2. Experimental Design

The following sections outline the details of the experimental set-up and some of the design calculations behind the static and dynamic tests that was performed on the steel rectangular hollow sections in the lab.

4.2.1. Sections Tested

This chapter describes the results of static and dynamic testing conducted on externally axially loaded and post-tensioned rectangular hollow steel sections. Two different sections were tested, in order to investigate the effect of slenderness ratios on the results. The individual sections tested were a RHS $50 \times 30 \times 3$ and a RHS $120 \times 60 \times 3$. These sections were chosen in order to have a slenderness ratio of approximately $\lambda \approx 60$ and $\lambda \approx 120$. In member buckling design, it is found that sections with very low slenderness ratios ($\lambda < 30$) these sections fail in axial crushing of the section. Sections with slenderness ratio greater than 120 ($\lambda > 120$) tend to fail in a manner consistent with Euler buckling theory, whereas sections with intermediate slenderness ($30 \leq \lambda \geq 120$) tends to deviate from both crushing and Euler buckling and fail in a combined manner. The purpose of the testing was to determine whether "compression-softening is valid to sections that behave in accordance with Euler buckling only. Since the member length was limited to approximately 1.5m in order to have specimens small enough to work with in the laboratory, section cross section sizes were chosen in order to have two different members with slenderness ratios ≈ 60 and ≈ 120 respectively. Hence, the sections chosen were a RHS $50 \times 30 \times 3$ and a RHS $120 \times 60 \times 3$ which had slenderness ratios of ≈ 60 and ≈ 120 respectively for a simply-supported beam span length of 1.5m. Figure 4.1 shows schematic diagrams of the cross sections of each steel specimen tested. The sections were tested in different load cases - externally axially loaded vs. post-tensioned, and further detail is given in Section 4.4. The design details of the experimental set-up is outlined further in Section 4.2.2.

4.2.2. Detailed Design of Experimental Set-up

The external axial load set-up, as shown later in Figure 4.11 required the design of a pinned connection, in order to achieve the required mode-shape of vibration and in order to compare the experimental modal frequencies obtained from each load case/test set-up condition. The pinned connection detail was fixed to the frame, and the sections were slotted into the pin-ended connections, as shown in Figure 4.11. Figure 4.2 shows detailed drawings for the male and female connection of the designed pin-ended connection in grade S235 steel. The section sizes were designed to resist the

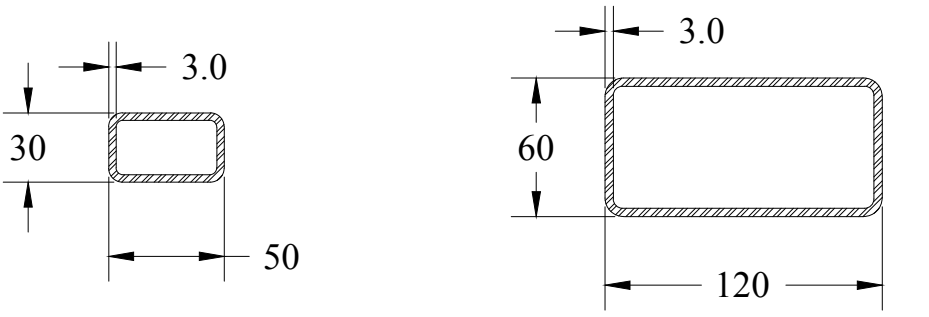

RHS 50.0x30.0x3.2mm
D = 50.0mm
B = 30.0mm
t = 3.0 mm

RHS 120.0x60.0x3.0mm
D = 120.0mm
B = 60.0mm
t = 3.0 mm

Figure 4.1.: Rectangular hollow steel sections (RHSs) tested. All dimensions are in mm.

applied design forces in dowel double shear, bearing and crushing.

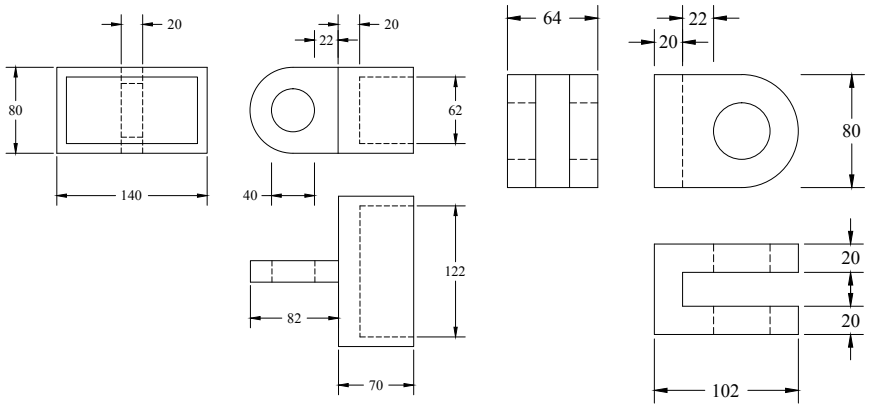

(a) (b)

Figure 4.2.: Pinned Connection Details; (a) Male connection; (b) Female Connection. All dimensions are in mm.

Figure 4.3 shows the pinned connections connected together, as designed and manufactured in the lab. Figure 4.4 shows the pinned connections as built and in-situ in the laboratory during testing. As shown in Figures 4.4c and 4.4d, the pinned connections enabled rotation to occur at the supports

and therefore the required mode-shapes of vibration could be obtained.

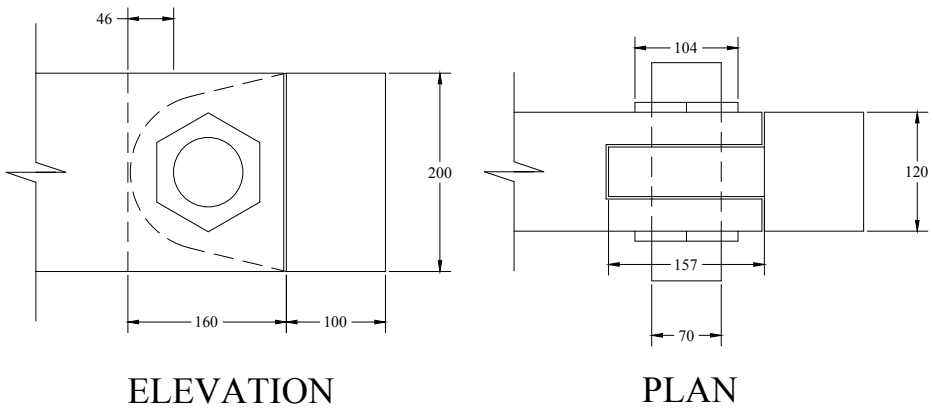

Figure 4.3.: Pinned Connection Details; connected together.

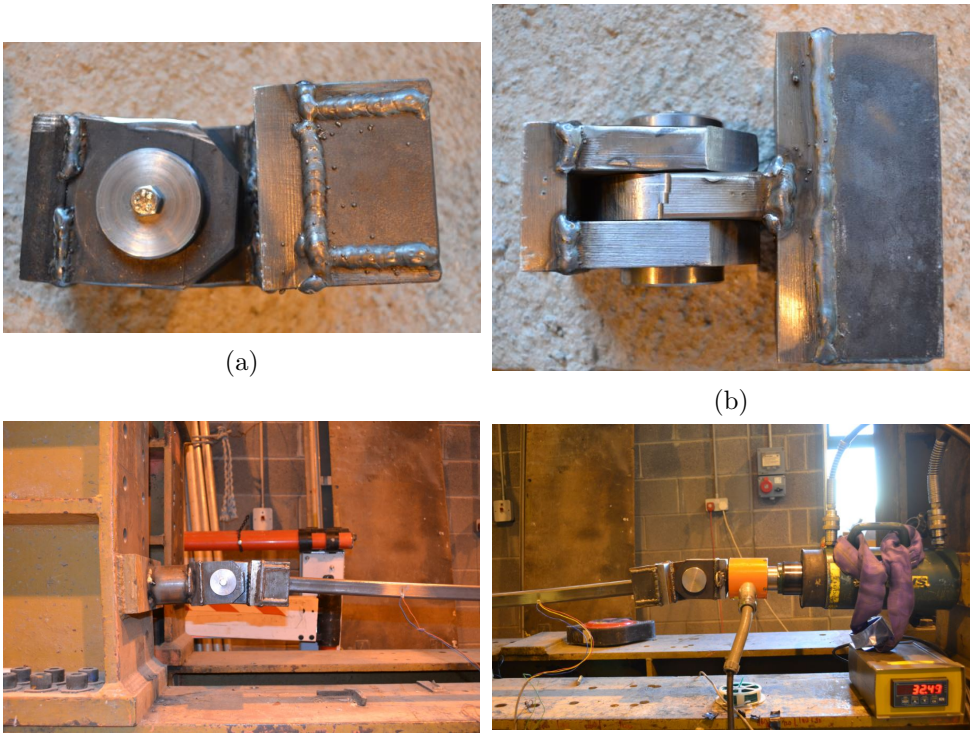

(a) (b)

(c) (d)

Figure 4.4.: Pictures of the pinned connection in the lab.

4.2.3. Coupon Testing

Young's Modulus testing was carried out on some samples taken from the steel specimens tested in the lab. The samples were prepared in accordance with the method set out in the relevant British Standard - BS EN ISO 6892-1:2009 Metallic materials Tensile testing Part 1: Method of test at ambient temperature (British Standards Institute, 2009). The steel coupons were prepared as shown in Figure 4.5.

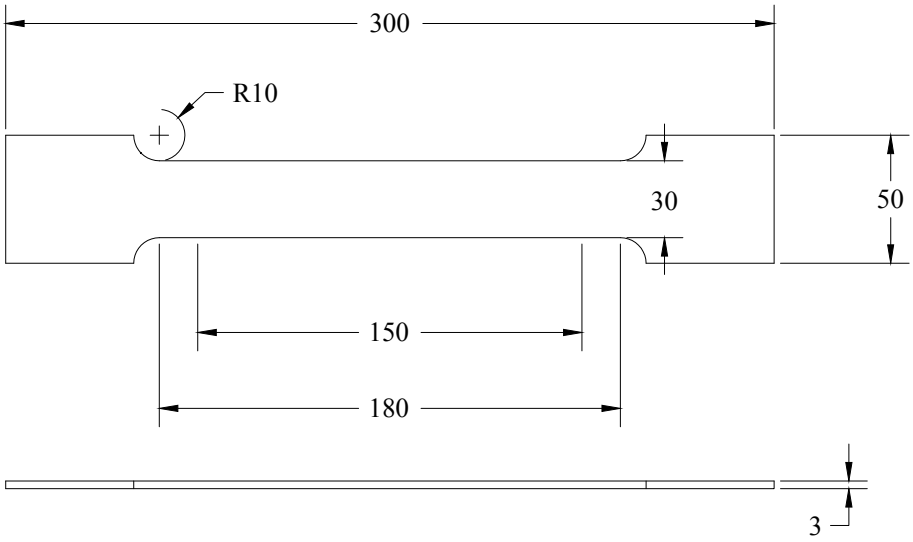

Figure 4.5.: Tensile Testing; Steel Coupons tested. All dimensions are in mm.

The specimens were tested in a Zwick/Roell materials testing machine. The specimens were clamped in place and gripped at either end in the machine. Strain gauges were affixed to the machine and strain readings were obtained. A Zwick incremental short-travel clip-on extensiometer was clipped onto the coupon. The extensiometer measured the extension of the section in mm under tensile loading. The machine was set running and it applied a tensile force to the specimens. The strain gauges were used in order to calibrate the extensiometer and for further accuracy. Figure 4.6 shows the Zwick/Roell materials testing machine used and the Zwick/Roell

short-travel clip-on extensiometer used.

(a) (b)

Figure 4.6.: Coupon test set up; (a) Zwick/Roell Materials testing machine; (b) Zwick/Roell short-travel clip-on extensiometer

5 coupons were taken from each steel specimen and were tested in the Zwick machine. The extensiometer values were converted into strain measurements and the corresponding force values were converted into stress by normalising by the cross sectional area. The corresponding stress-strain readings were graphed against one another, with stress, σ, on the y-axis and strain, ϵ, on the x-axis. The results for all 10 coupons tested are shown in Figure 4.7. Figure 4.7a shows the results of coupon testing from Beam 1, RHS $50 \times 30 \times 3$, and Figure 4.7b shows the results of coupon testing from Beam 2, RHS $120 \times 60 \times 3$. As shown in Figure 4.7, the results indicate that in fact, the specimens comprised of different grade steel. From the yield values of the coupons, Beam 1, RHS $50 \times 30 \times 3$, is grade S275 steel whereas Beam 2, RHS $120 \times 60 \times 3$, is grade S355.

Table 4.1 shows the estimation of the Young's Modulus of Elasticity for each of the beam specimens tested. The Young's Modulus has been estimated by calculating the ratio of the yield stress, σ_y, to the yield strain, ϵ_y, i.e. $E_s = \sigma_y/\epsilon_y$, for each coupon. The mean, μ, and the standard deviation, σ, of the results are also given. For Beam 1, RHS $50 \times 30 \times 3$, the average value of Young's Modulus is $212GPa$, which is consistent with the design

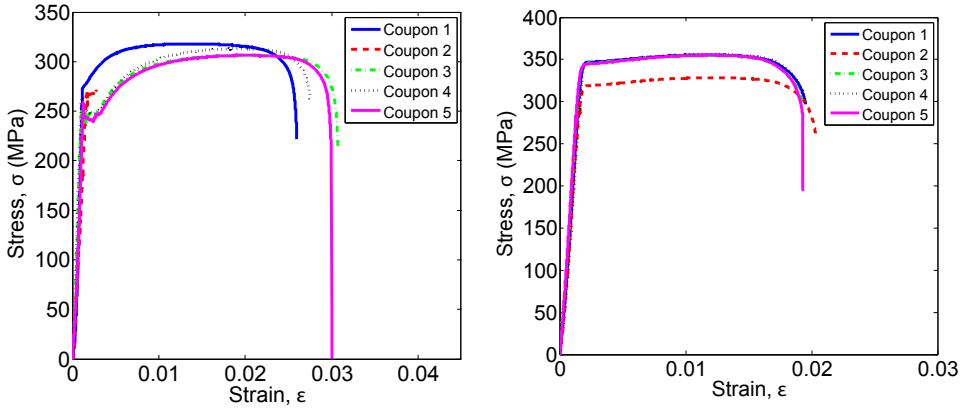

Figure 4.7.: Coupon tests - Young's Modulus (a) Beam 1 (b) Beam 2

value of $200 - 210GPa$ for steel. The results for Beam 2, RHS $120 \times 60 \times 3$ show an average value of approximately $200GPa$, which is also consistent with the expected design value.

Table 4.1.: Young's Modulus testing of Beam coupons

Coupon #	σ_y (MPa)	ϵ_y	E (GPa)
	Beam 1		
1	274.5	1.24×10^{-3}	221.4
2	272.0	1.68×10^{-3}	161.9
3	252.5	1.10×10^{-3}	229.5
4	264.2	1.08×10^{-3}	244.6
5	257.9	1.26×10^{-3}	204.7
μ_1	264.2	1.27×10^{-3}	212.4
σ_1	9.3	2.42×10^{-4}	31.7
	Beam 2		
1	300.0	1.52×10^{-3}	197.4
2	300.0	1.65×10^{-3}	181.8
3	300.0	1.43×10^{-3}	209.8
4	300.0	1.63×10^{-3}	184.1
5	300.0	1.33×10^{-3}	225.6
μ_2	300.0	1.51×10^{-3}	199.7
σ_2	0.0	1.35×10^{-5}	18.3

Figure 4.8 shows some coupons following testing. Some coupons fractured completely, while others did not, as shown. There is clear evidence of elongation and subsequent necking in both of the coupons.

Figure 4.8.: Tensile Testing; Steel Coupons tested

4.2.4. Slippage of the coupons in the tensile testing machine

Figure 4.9 shows the results of the tensile testing on a zoomed-in scale, accounting for the linear elastic portion of the constitutive model for steel. A directly proportional (linear) relationship between stress and strain is predicted by elastic theory. As shown in Figures 4.9a and 4.9b, the obtained results deviate from the perfectly linear elastic response predicted by theory. This is due to the effect of slippage of the test coupons in the tensile testing machine. Under tensile loading, the "feet" of the test coupon are susceptible to slippage from the grip of the testing machine, hence, some non-linear stress strain relationship is recorded, as indicated in both Figures 4.9a and 4.9b. The machine records a drop-off in load for a given strain when the "feet" of the coupon slip in the machine's vice.

Not only is there potential for slippage of the coupon within the vice grips of the tensile testing machine, there is also potential for slippage of the extremely sensitive extensiometer, which measures the strain of the specimen being tested. Furthermore, the alignment of the grips is also a factor that can affect experimental accuracy. If the grips are not perfectly aligned, this will induce bending stresses in the specimen being tested, and subsequently will cause lower tensile stress readings by altering the net stress

(and subsequently strain) throughout the cross-section.

These are all factors that can affect the final result for the Young's Modulus of Steel, however, as outlined in Section 4.2.3, the results obtained are consistent with the predicted design value of $E_s = 200 - 210GPa$.

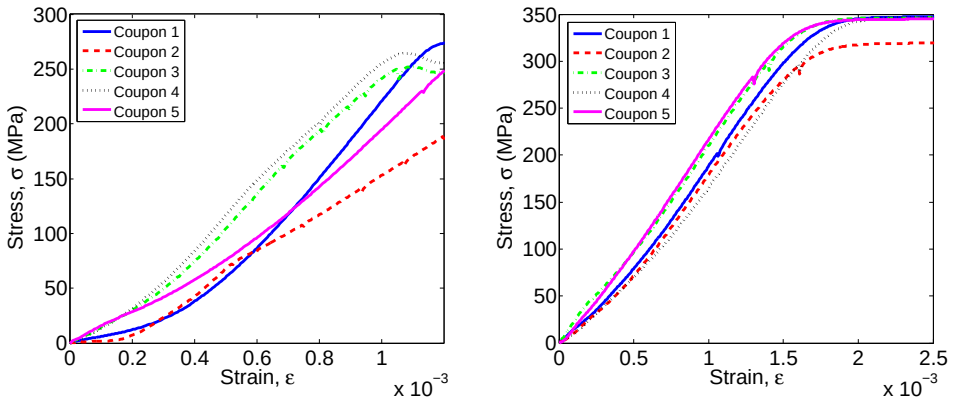

Figure 4.9.: Coupon tests (zoomed in results) - Young's Modulus (a) Beam 1 (b) Beam 2

4.2.5. Buckling Capacity of Members

The following design calculations follow the British Standards Institute (2005) method for calculating the buckling capacity of the externally axially loaded steel strut shown in Figure 4.11. The British Standards Institute (2005) method requires the classification of the cross section;

$$\begin{aligned} \epsilon &= \sqrt{235/f_y} \\ &= \sqrt{235/235} \\ &= 1.0 \end{aligned} \tag{4.1}$$

where f_y is the design yield strength of the steel in MPa. The section is classified by the ratio between the web depth, c, to web thickness, t. For sections subjected to compression only, Class 1 sections obey the following;

$c/t \leq 33\epsilon$;

$$\begin{aligned} c/t &\leq 33\epsilon \\ (50.0 - 3 \times 3.0)/3.0 &\leq 33 \\ 13.67 &< 33 \quad \checkmark\checkmark\checkmark \end{aligned} \tag{4.2}$$

This indicates that the section is Class 1. For Class 1 hot-rolled sections such as these, buckling curve (a) is used (British Standards Institute, 2005), Figure 4.10.

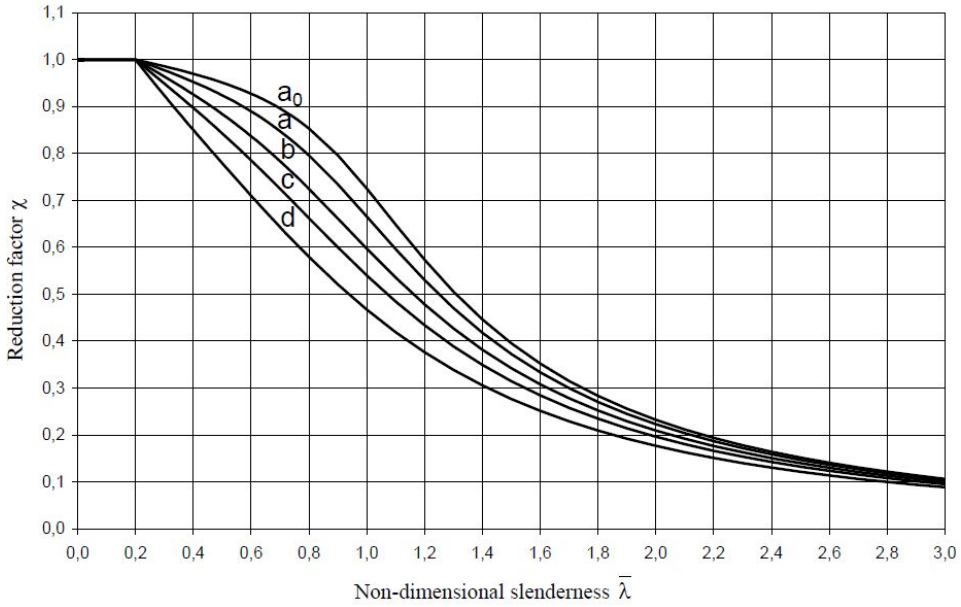

Figure 4.10.: Buckling curves pp. 59 Eurocode 3, British Standards Institute (2005)

The slenderness ratio is then calculated about both of the sections axes - the weak axis and the strong axis. The radius of gyration, i, of the cross section is calculated with respect to the relative axes, where $i = \sqrt{I/A}$, therefore; $i_{xx} = \sqrt{I_{xx}/A}$ and similarly, $i_{yy} = \sqrt{I_{yy}/A}$, where I is the second moment of area about the given cross section axis and A is the cross sectional

area.

$$\begin{aligned} \lambda_{yy} &= L_E/i_{yy} \\ &= 1624/11.6 \\ &= 140.0 \end{aligned} \tag{4.3}$$

$$\begin{aligned} \lambda_{xx} &= L_E/i_{xx} \\ &= 1624/17.5 \\ &= 92.8 \end{aligned}$$

The values for i_{xx} and i_{yy} are tabulated in the Tata Steel *'Blue Book'* (Tata Steel Europe Limited, 2013). The strut was tested in a pinned-pinned arrangement, with rotation allowed to occur at both ends of the section by means of hinge joints that were designed and fitted in the laboratory. As such, the effective length, $L_E = \ell = 1,624 \quad mm$, where ℓ is the span length. The relative slenderness is then calculated using the following;

$$\begin{aligned} \lambda_1 &= \pi\sqrt{E_s/f_y} \\ &= \pi\sqrt{210 \times 10^3/235} \\ &= 93.91 \end{aligned} \tag{4.4}$$

where E_s is the Young's Modulus of the steel and is taken to be $210GPa$, and;

$$\begin{aligned} \overline{\lambda_{yy}} &= \lambda_{yy}/\lambda_1 \\ &= 140.0/93.91 \\ &= 1.49 \end{aligned} \tag{4.5}$$

$$\begin{aligned} \overline{\lambda_{xx}} &= \lambda_{xx}/\lambda_1 \\ &= 92.8/93.91 \\ &= 0.99 \end{aligned}$$

Having obtained $\overline{\lambda_{yy}}$ and $\overline{\lambda_{xx}}$, using linear interpolation with curve (a), Fig-

ure 4.10, values for the buckling reduction factors, χ_{xx} and χ_{yy} are obtained.

$$\begin{aligned} \chi_{yy} &= 0.3724 \\ \chi_{xx} &= 0.6656 \end{aligned} \tag{4.6}$$

The buckling resistance is given in Eurocode 3 as;

$$N_{b,Rd} = \frac{\chi A f_y}{\gamma_{m1}} \tag{4.7}$$

where $N_{b,Rd}$ is the buckling resistance of a section about a given axis, A is the cross sectional area, f_y is the design yield strength of the steel, and γ_{m1} is a material factor of safety, given as; $\gamma_{m1} = 1.1$.

$$\begin{aligned} N_{b,Rd,yy} &= \frac{\chi_{yy} A f_y}{\gamma_{m1}} \\ &= \frac{(0.3724)(421)(235)}{1.1} \\ &= 33.5 \quad kN \end{aligned} \tag{4.8}$$

$$\begin{aligned} N_{b,Rd,xx} &= \frac{\chi_{xx} A f_y}{\gamma_{m1}} \\ &= \frac{(0.6656)(421)(235)}{1.1} \\ &= 59.9 \quad kN \end{aligned} \tag{4.9}$$

The crushing strength of the member is also calculated in accordance with Eurocode 3 (British Standards Institute, 2005);

$$\begin{aligned} N_{c,Rd} &= \frac{A f_y}{\gamma_{m0}} \\ &= \frac{(421)(235)}{1.05} \\ &= 94.2 \quad kN \end{aligned} \tag{4.10}$$

Finally, the Euler buckling capacity of the section about both axes are also

calculated;

$$\begin{aligned} P_{CR,yy} &= \frac{\pi^2 E I_{yy}}{L_E^2} \\ &= \frac{\pi^2 (210 \times 10^9)(5.70 \times 10^{-8})}{(1.624)^2} \\ &= 44.8 \quad kN \end{aligned} \tag{4.11}$$

$$\begin{aligned} P_{CR,xx} &= \frac{\pi^2 E I_{xx}}{L_E^2} \\ &= \frac{\pi^2 (210 \times 10^9)(12.8 \times 10^{-8})}{(1.624)^2} \\ &= 100.6 \quad kN \end{aligned}$$

The design loads for Beam 2 (RHS $120 \times 60 \times 3$) are calculated in the same manner and are outlined in Table 4.2.

Table 4.2.: Design loads of steel RHS sections tested

Property	**Beam 1** **RHS** $50 \times 30 \times 3$			**Beam 2** **RHS** $120 \times 60 \times 3$		
Steel Grade	**S235**	**S275**	**S355**	**S235**	**S275**	**S355**
$N_{b,Rd,yy}$ (kN)	33.9	34.7	35.7	185.6	209.5	251.8
$N_{b,Rd,xx}$ (kN)	59.9	64.9	71.2	207.6	240.1	305.2
$N_{c,Rd}$ (kN)	94.2	105.3	142.3	228.3	255.0	344.9
$P_{CR,yy}$ (kN)	44.8	44.8	44.8	506.1	506.1	506.1
$P_{CR,xx}$ (kN)	100.6	100.6	100.6	1,485.3	1,485.3	1,485.3

4.2.6. Bending Capacity of Members

To facilitate the 3-point bending tests conducted on the steel RHS sections, the sections were analysed in accordance with Eurocode 3 (British Standards Institute, 2005) to determine their bending capacity. The analysis is outlined in the following section. The bending capacity of a steel section is

defined by the following;

$$\begin{aligned} M_{c,Rd} &= M_{pl,Rd} \quad (Class \quad 1,2) \\ M_{c,Rd} &= M_{el,Rd} \quad (Class \quad 3) \end{aligned} \tag{4.12}$$

where;

$$\begin{aligned} M_{pl,Rd} &= \frac{W_{pl} f_y}{\gamma_{m0}} \\ M_{el,Rd} &= \frac{W_{el} f_y}{\gamma_{m0}} \end{aligned} \tag{4.13}$$

From Equations 4.1 and 4.2 in Section 4.2.5, we can deduce that the sections are Class 1 sections, therefore, the bending capacity of the sections are given by the plastic modulus, W_{pl}. The beams were tested about their weak axis (z axis). The corresponding plastic modulus is given as $W_{pl,z}$, and obtained from the Tata Steel Interactive Blue Book (Tata Steel Europe Limited, 2013). For steel grade S235, the bending capacity of the RHS $50 \times 30 \times 3$ section is given as;

$$\begin{aligned} M_{pl,Rd} &= \frac{W_{pl} f_y}{\gamma_{m0}} \\ &= \frac{(4.58 \times 10^3)(235)}{1.1} \\ &= 0.98 \quad kN - m \end{aligned} \tag{4.14}$$

Since the static testing carried out was in the form of 3-point bending for a simply supported beam, the maximum bending moment is given at mid-span as;

$$M_{max} = \frac{P\ell}{4} \tag{4.15}$$

where P is the magnitude of the point load and ℓ is the span length. The equivalent point load to cause yield was then calculated in accordance with;

$$\begin{aligned} P_{max,z} &= \frac{4M_{pl,Rd}}{\ell} \\ &= \frac{(4)(0.98)}{1.5} \\ &= 2.61 \quad kN \end{aligned} \tag{4.16}$$

which gives the maximum value of load before yield occurs in accordance with Eurocode 3. This value was divided by a factor of 1.35, giving a maximum allowable point load applied to the steel sections during the static 3-point bending tests conducted; $P_{allow,z} = 2.61/1.35 = 1.93kN$. The design bending moments and maximum allowable point loads applied to the beam sections are given in Table 4.3. The calculations have been conducted for varying steel grade (S235, S275 & S355). Later, it will be shown that for the RHS $120 \times 60 \times 3$ section, at a post-tensioning load level of 140kN, a 50% reduction in load carrying capacity was observed.

Table 4.3.: Bending capacity of beam sections in accordance with EC3 (British Standards Institute, 2005)

Property	**Beam 1** **RHS** $50 \times 30 \times 3$			**Beam 2** **RHS** $120 \times 60 \times 3$		
Steel Grade	**S235**	**S275**	**S355**	**S235**	**S275**	**S355**
$W_{pl,z} \quad (cm^3)$	4.58	4.58	4.58	21.5	21.5	21.5
$M_{pl,z} \quad (kN-m)$	0.98	1.15	1.48	4.59	5.38	6.94
$P_{max,z} \quad (kN)$	2.61	3.07	3.95	12.24	14.35	18.51
$P_{allow,z} \quad (kN)$	1.93	2.27	2.93	9.07	10.63	13.71

4.2.7. Calculation of Natural bending frequencies

The natural bending frequencies of the steel rectangular hollow sections were calculated in accordance with the formula for a simply-supported beam;

$$\omega_n = \left(\frac{n\pi}{\ell}\right)^2 \sqrt{\frac{EI}{m}} \tag{4.17}$$

where n is the mode number, ℓ is the span length, E is the Young's Modulus of Elasticity, I is the second moment of area of the cross section and m is

the mass per unit length of the beam. Taking the design Young's Modulus of Elasticity of the steel to be $E_s = 210GPa$ and the second moment of area, I, and mass per unit length of the beam, m in accordance with Table 4.4.

Table 4.4.: Properties of the beam sections

Property	**Beam 1** **RHS** $50 \times 30 \times 3$	**Beam 2** **RHS** $120 \times 60 \times 3$
$I_z \quad (cm^4)$	5.70	64.4
$m \quad (kg/m)$	3.30	8.01

The natural bending frequency for the beam sections were calculated as follows;

$$\begin{aligned} \omega_n &= \left(\frac{n\pi}{\ell}\right)^2 \sqrt{\frac{EI}{m}} \\ &= \left(\frac{(1)\pi}{(1.624)}\right)^2 \sqrt{\frac{(210 \times 10^9)(5.70 \times 10^{-8})}{3.30}} \\ &= 225.4 \quad rad/s \end{aligned} \tag{4.18}$$

In order to convert from natural circular frequency in radians per second to Hertz (Hz), or oscillations per second, the following formula; $\omega = 2\pi f$, where f is the frequency in Hz and ω is the frequency in rad/s, is used. Therefore, $f = \omega/2\pi = 225.4/2\pi = 35.9Hz$. Table 4.5 shows the prediction of the first three natural bending frequencies for each of the RHS sections tested in accordance with the properties outlined in Table 4.4 and Equation 4.17.

Table 4.5 shows the predicted natural bending frequencies, using the design Young's Modulus for steel, $E_s = 210GPa$. Table 4.6 shows the predicted natural bending frequencies, using the Young's Modulus calculated for each of the steel coupons tested and outlined in Section 4.2.3, and in Table 4.1.

For Beam 1, the design value of 210GPa is very similar to the mean of the 5 samples tested and outlined in Table 4.1, given as 212.4GPa. This has minimal effect on the prediction for the fundamental bending frequencies, as highlighted in Table 4.5 and Table 4.6. For Beam 2, from the Young's Modulus Testing conducted and discussed in Section 4.2.3, the Young's

Table 4.5.: Calculation of natural bending frequency of steel RHS sections

		Case 1	**Case 2**
	Figure #	Figure 4.11	Figure 4.12
	Span, ℓ (m)	1.624	1.500
Beam 1	$n = 1$, ω_{1_1} (Hz)	35.9	42.0
RHS	$n = 2$, ω_{2_1} (Hz)	143.5	168.2
$50 \times 30 \times 3$	$n = 3$, ω_{3_1} (Hz)	322.8	378.4
Beam 2	$n = 1$, ω_{1_2} (Hz)	77.4	90.7
RHS	$n = 2$, ω_{2_2} (Hz)	309.6	362.9
$120 \times 60 \times 3$	$n = 3$, ω_{3_2} (Hz)	696.5	816.4

Table 4.6.: Calculation of natural bending frequency of steel RHS sections with different Young's Modulus

			Case 1	**Case 2**
Beam 1		$n = 1$, ω_{1_1} (Hz)	36.1	42.3
RHS	E=212.4GPa	$n = 2$, ω_{2_1} (Hz)	144.3	169.1
$50 \times 30 \times 3$		$n = 3$, ω_{3_1} (Hz)	324.7	380.6
Beam 2		$n = 1$, ω_{1_2} (Hz)	75.4	88.3
RHS	E=199.7GPa	$n = 2$, ω_{2_2} (Hz)	301.3	353.2
$120 \times 60 \times 3$		$n = 3$, ω_{3_2} (Hz)	677.3	794.6

Modulus was found to be similar to the predicted design value. The mean of the 5 samples tested was found to be 199.7GPa.

4.3. Type of prestressing

There are two main types of prestressing;

1. **External Prestressing:** when prestressing is achieved by elements located outside the member cross section, it is called *"external prestressing"*. The tendons can lie outside the member, or inside the hollow of the section.

2. **Internal Prestressing:** when the prestressing is achieved by elements located inside the extents of the member cross section (most

commonly by embedded tendons inside the extents of the concrete cross section), it is known as *"internal prestressing"*. Most of the applications of prestressing are internal prestressing.

In the case of the post-tensioned rectangular hollow steel sections tested and described in this chapter, the post-tensioning strand is threaded through the hollow, external to the extents of the steel cross section, and as such, the post-tensioned rectangular steel hollow sections are ***externally prestressed***.

4.4. Dynamic Testing

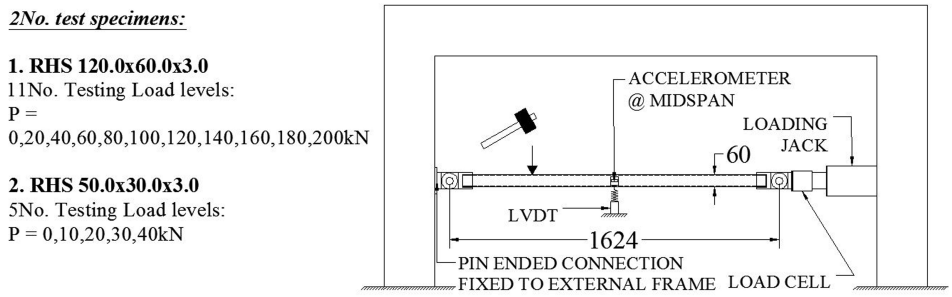

Figure 4.11.: Case 1; External axial load case.

Dynamic impact hammer testing was conducted on 4No. grade S235 steel RHSs, with a design Youngs Modulus of 210GPa. The results of coupon testing are reported in Section 4.2.3. The properties of the steel sections are outlined in Table 4.8 and Table 4.9. Figure 4.11 shows the external axial load case (case 1), where dynamic impact hammer testing was carried out on 2No. specimens, a RHS $50 \times 30 \times 3$ (Beam 1) and a RHS $120 \times 60 \times 3$ (Beam 2), respectively. Each section had a different slenderness ratio, as outlined in Table 4.9. The purpose of varying the slenderness ratio was to test the validity of Equation 2.1 for slender members, which are expected to fail, in compression, close to an Euler buckling condition, and stocky members, which show deviation from classical Euler buckling theory.

The test programme is outlined in Table 4.7. Four separate dynamic tests were carried out, as outlined in Figure 4.7. Two different beam sections were tested, namely a RHS $50 \times 30 \times 3$, and a RHS $120 \times 60 \times 3$. Each beam was tested for two differing load cases, namely, an external axial load case, and

a post-tensioning load case. Dynamic impact hammer testing was carried out on each of the beam sections to determine the fundamental bending frequency at varying values of axial load. The purpose of the testing is to determine under what conditions "compression-softening" theory holds true. It is postulated that "compression-softening" is valid only for externally axially loaded slender sections, as it is based on Euler buckling theory. Euler buckling theory is very accurate for long, slender sections, but deviates from empirical data for stocky sections, hence test have been conducted on sections with a slenderness, $\lambda \approx 60$, and on sections with a slenderness, $\lambda \approx 120$.

Table 4.7.: Test programme for steel rectangular hollow sections

#	**Description**	**Beam**	**Case**	ℓ	λ	Load Type	Figure
1	Beam 1 Case 1	1	1	1.624	139	Ext. Axial	Figure 4.11
2	Beam 1 Case 2	1	2	1.624	64	Ext. Axial	Figure 4.11
3	Beam 2 Case 1	2	1	1.500	128	Post-tension	Figure 4.12
4	Beam 2 Case 2	2	2	1.500	59	Post-tension	Figure 4.12

Table 4.8.: Properties of steel RHS sections tested

Property	**RHS** $50 \times 30 \times 3$	**RHS** $120 \times 60 \times 3$
Beam #	Beam 1	Beam 2
m (kg/m)	3.41	8.12
A (cm^2)	4.34	10.30
I_{zz} (cm^4)	5.94	65.50

Since Equation 2.1 is consistent with Euler buckling theory, it was expected that the dynamic results for the stocky section would deviate from the *compression-softening* theory. The test specimen was placed in the small test frame and inserted into two pinned connection joints. One pin was fixed directly to the frame. The other was attached to a load cell, which was in turn connected to a 300 ton loading jack. The jack was mounted on the other side of the frame, as shown in Figure 4.11. A hydraulic hand pump was connected to the loading jack to vary the external axial load. Impact

hammer testing was conducted on the 2 test specimens at different axial load levels until failure had occurred.

Table 4.9.: Properties of experimental cases

	Case 1	**Case 2**
Figure #	Figure 4.11	Figure 4.12
Span, ℓ (m)	1.624	1.500
Slenderness Beam 1, λ_{zz_1}	139	128
Slenderness Beam 2, λ_{zz_2}	64	59
Beam 1, ω_{1_1} (Hz)	35.9	42.0
Beam 2, ω_{1_2} (Hz)	77.4	90.7

Figure 4.12 shows the post-tensioned load case (case 2) where impact hammer testing was carried out on the same RHSs. The sections were post-tensioned using a 15.7mm Freysinnet 7 wire concentric strand. The strand was anchored with the appropriate collets either side of two 300 ton loading jacks. A load cell and a baseplate were positioned between the jack and the end of the steel RHS section, helping to evenly transfer the post-tensioning load into the section. Two jacks and two load cells were used in order to balance the mass under vibration. Multiple load cells ensured an even distribution of post-tensioning load throughout the length of the section. The post-tensioned section was supported on either side by knife-edge supports that were a distance of 1.500m apart. One of the jacks was connected to a hydraulic hand pump to transfer a post-tensioning load into the section.

The Multiple Input, Multiple Output (MIMO) method of dynamic impact testing was implemented, in which there were multiple dynamic excitation points and multiple instrumentation response points. Five equally spaced input locations were used as both input points and response points as shown in Figure 4.13. Strain gauges were placed at each of the response points, labelled L1-L5, and an accelerometer was mounted at mid-span on each section, at location L3. Ten strikes of the sledge hammer were applied at each input point for each load increment, for repeatability, giving a total of 50 frequency data points per axial load level.

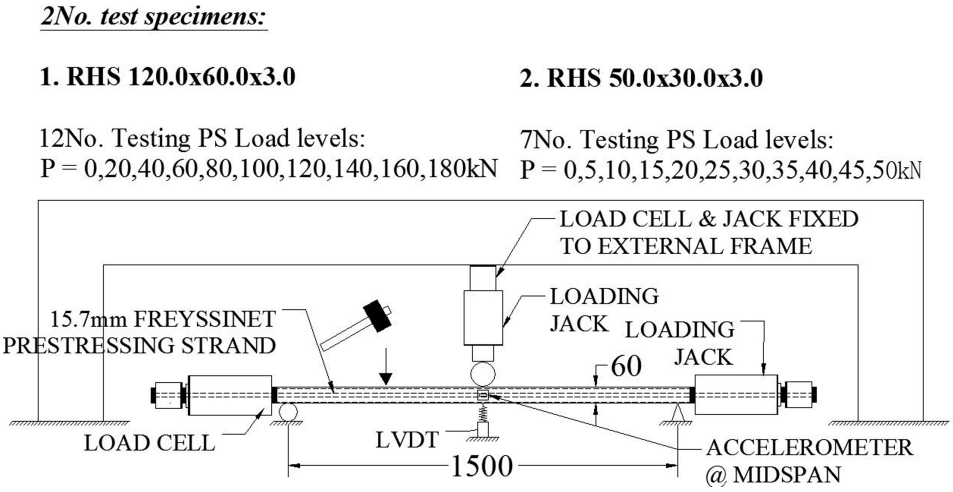

Figure 4.12.: Case 2; post-tensioned load case

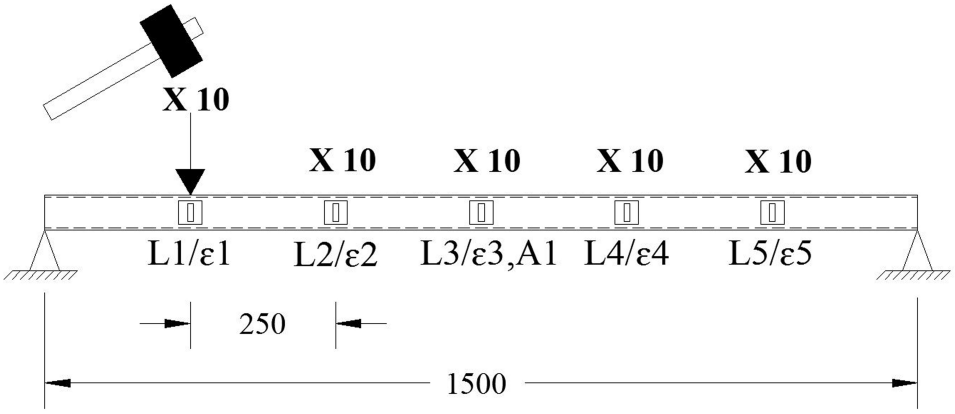

Figure 4.13.: Instrumentation of steel specimens

4.5. Static Testing

Static 3 point bending tests were conducted on both Beam 1 and Beam 2 for the post-tensioned load case (Beam 1, case 2 and Beam 2, case 2). The apparatus was set up as outlined in Figure 4.12 and Figure 4.13. The beams were supported at a span distance of 1.500m by two knife-edge supports in the form of equal angle sections. Jacks were placed on either end of the respective beams and a 15.7mm diameter Freyssinet post-tensioning strand was threaded through the hollow in the respective RHS beams. The post-

tensioning load level was increased, and at each load increment, a point load was applied at midspan by an external reaction frame (Figure 4.12). The corresponding deflection was measured using an LVDT placed at midspan. The load-deflection relationship enabled the static flexural rigidity of the beams to be calculated at each post-tension load increment using the following deflection equation for a simply supported beam, with a point load at midspan;

$$\delta = \frac{P\ell^3}{48EI} \tag{4.19}$$

where δ is the midspan deflection of the beam, P is the magnitude of the midspan point load, ℓ is the span length between supports, E is the Young's Modulus of elasticity of the material (in this case S235 steel), and I is the second moment of area of the beam about the axis of bending. Rearranging Equation 4.19 allows the effective static flexural rigidity, EI_{eff} to be calculated;

$$EI_{eff} = \frac{P\ell^3}{48\delta} \tag{4.20}$$

The corresponding static-equivalent prediction for the n^{th} natural frequency of the post-tensioned RHS section is then given as;

$$\omega_n = \left(\frac{n\pi}{\ell}\right)^2 \sqrt{\frac{EI_{eff}}{m}} \tag{4.21}$$

This has been compared to the values that were obtained dynamically and the results are given in Section 4.8.

4.6. Calculation of Fundamental Natural Frequency, ω_1

Following collection of the impact hammer data, the raw signal (acceleration-time data) was imported into MATLAB (MATLAB, 2014). The Fast Fourier Transform (FFT) was then performed on the acceleration data in the time domain in order to represent the signal in the frequency domain. A peak picking algorithm was then used to identify the peaks in the frequency domain. The peak picking method is the simplest means of determining the modal characteristics in the frequency domain, in which the natural frequen-

cies correspond to the peaks in the FFT (Ewins, 2000), however as pointed out by Foti et al. (2014) *"this method is not reliable when the different modes of vibration are not sufficiently separated from each other."*

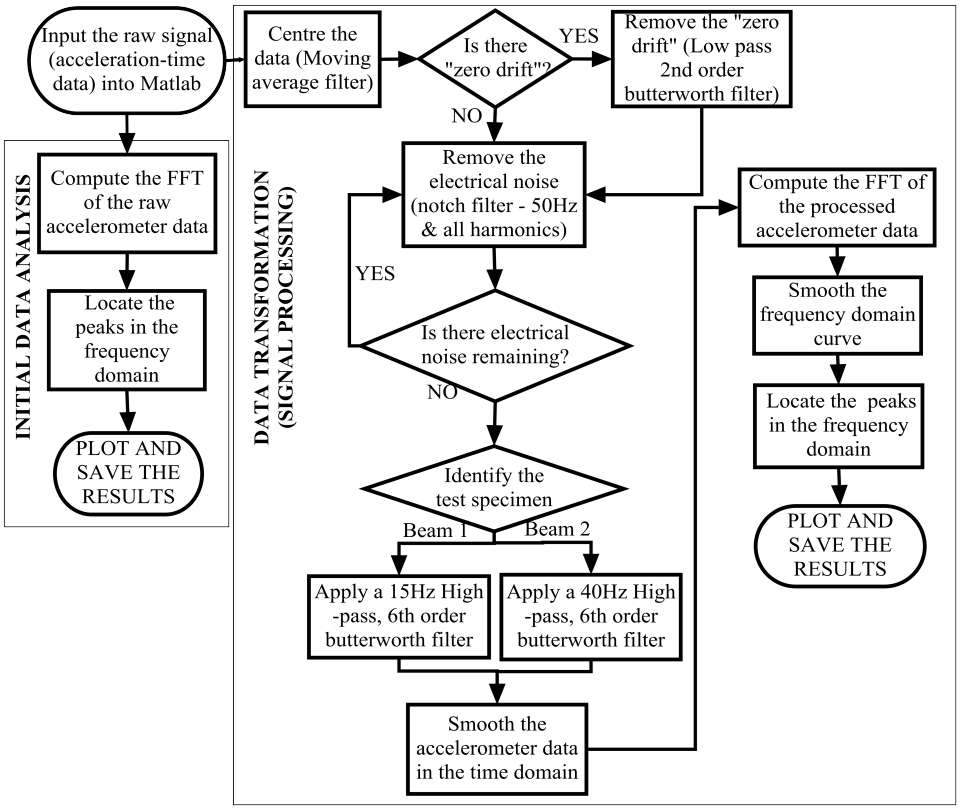

Figure 4.14.: Signal Processing Procedure

The raw signal contained significant electrical noise. In some cases, a "zero drift" in the accelerometer was observed. Subsequently, the peaks in the frequency domain were initially difficult to determine. A signal processing algorithm was developed in MATLAB (MATLAB, 2014) and is outlined in Figure 4.14. The signals were processed to eliminate noise and remove the zero drift. The processed acceleration data was then smoothed in the time domain and the FFT was recomputed. Finally, the data was smoothed in the frequency domain. Following smoothing in the frequency domain, the peak picking algorithm was reused and the peaks were again determined. The search bands for the fundamental frequency of each beam were defined as 15-45Hz for Beam 1 and 60-85Hz for Beam 2. The raw data and the processed data were compared, and following processing, the structural peaks

were much easier to identify. The peaks in the frequency domain were identified as the natural frequencies of the structural system. This algorithm is required to deal with the high levels of noise associated with impact hammer testing of these types of metallic sections.

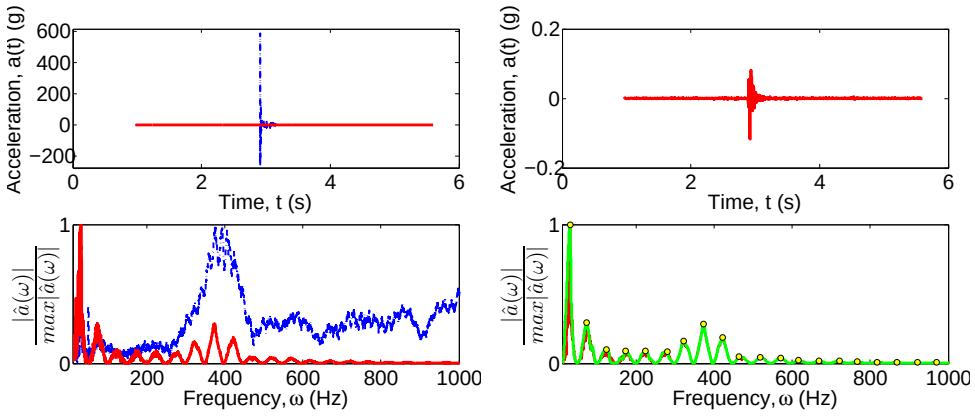

Figure 4.15.: Signal processing (a) and peak identification (b); Beam 1 Case 1

Figures 4.15-4.18 show typical accelerometer response for each beam and case combination. Figures 4.15a-4.18a show the accelerometer signals in both the time and frequency domain, before the signal was processed to eliminate noise (blue) and after signal processing (red). The natural vibration frequencies of the respective structural systems are identified as the peaks in the frequency domain. The peaks are initially difficult to determine in the unfiltered (blue) signals, however, following processing (red) the peaks become readily identifiable. The zero drift in the signal has been removed, along with the 50Hz electrical noise and all of its harmonics, using a high-order notch (bandpass) filter. Finally, a high pass filter is invoked, removing all low frequency noise, below the expected first natural frequency peak.

Figures 4.15b-4.18b show the processed signal in both the time and the frequency domain. The scale of the acceleration axis in the time domain of each signal is significantly reduced from Figures 4.15a-4.18a to Figures 4.15b-4.18b, indicating the extent of of the amplitude attributable to noise components. For the Figures shown, the reduction in amplitude is between $\times 500$, for Figure 4.17 and $\times 2250$, for Figure 4.15. The peaks are

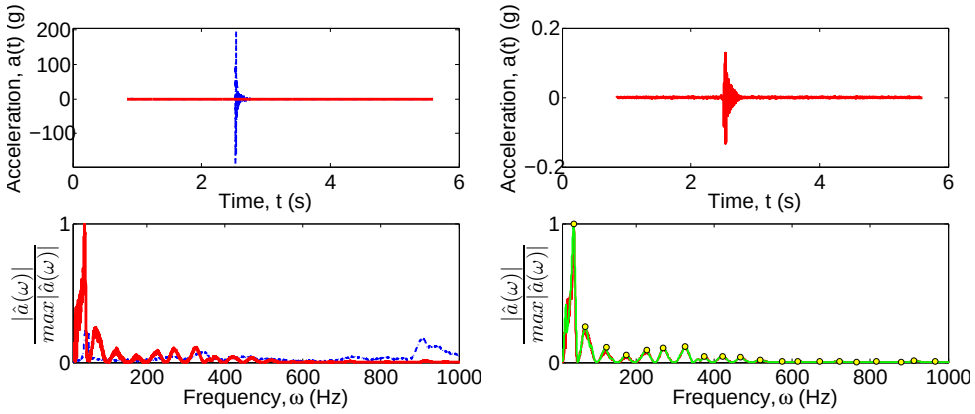

(a) (b)

Figure 4.16.: Signal processing (a) and peak identification (b); Beam 1 Case 2

identified in Figures 4.15b-4.18b as the yellow points. The first 20 peaks in the range of 0-1000Hz have been identified.

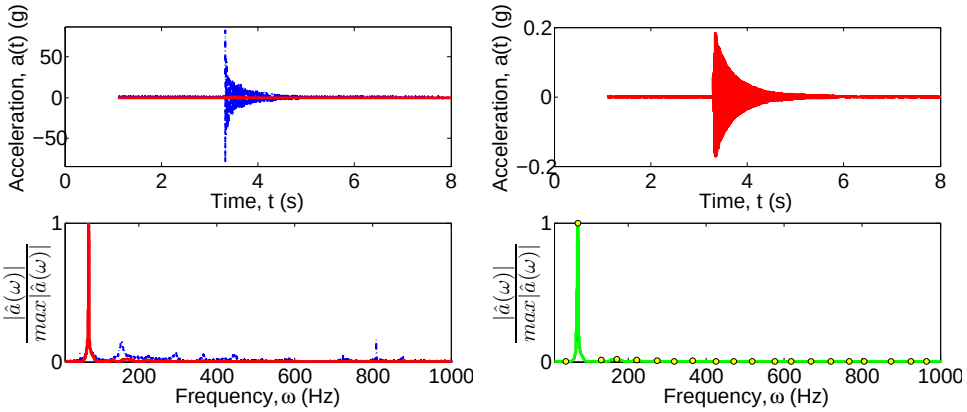

(a) (b)

Figure 4.17.: Signal processing (a) and peak identification (b); Beam 2 Case 1

4.7. Calculation of Damping Ratio, ξ

The damping ratio, ξ of the beams were calculated for each axial load level using the half-power bandwidth method, as outlined by Clough and Pen-

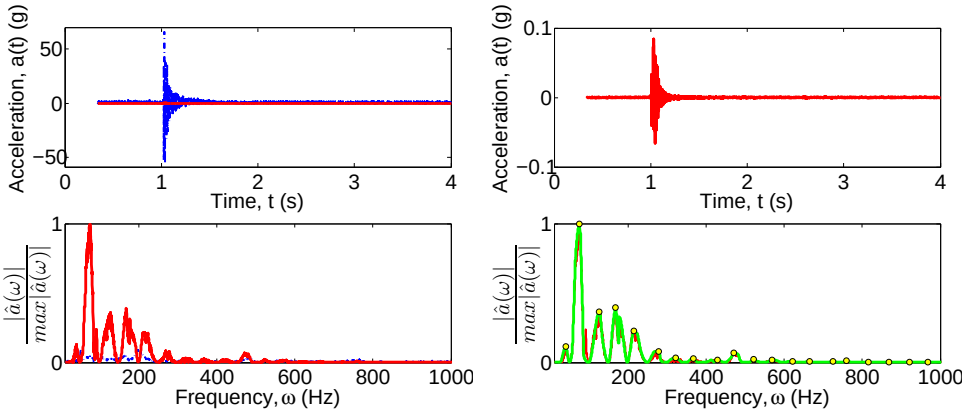

Figure 4.18.: Signal processing (a) and peak identification (b); Beam 2 Case 2

zien (1993), Chopra (2012) and Wu (2014). According to Wu (2014), the half-power bandwidth method enables evaluation of damping from forced vibration tests without knowing the applied force, and is thus used in vibration and modal testing. By assuming that the damping ratio, ξ, is small and that the frequency at maximum amplitude is approximately equal to the undamped fundamental frequency, ω_1, the classical result relating the damping ratio to the half-power bandwidth can be written as;

$$\xi = \frac{\omega_b - \omega_a}{2\omega_1} \tag{4.22}$$

where ω_a and ω_b are the half-power frequencies (i.e. the frequencies of the function at Max. Amplitude/$\sqrt{2}$). As pointed out by Wu (2014), the classical result is only valid for damping ratios less than 0.1, and is not a good prediction for $\xi > 0.1$. An example of the calculation of the damping ratio in accordance by the half-power bandwidth method is shown in Figure 4.19. Figure 4.19 shows a graph of the frequency domain representation of the impulse response signals obtained from the steel beams tested. Figure 4.19a shows the relative modal amplitude mapped against frequency for the fundamental mode, in the range of 0-100Hz. The half-power bandwidth method, as described in Equation 4.22 requires the determination of the frequencies of the function at Max. Amplitude/$\sqrt{2}$=0.7071. This is shown in Figure 4.19b. Once these values have been determined (denoted ω_a and

ω_b), and the natural frequency has been determined from peak picking, the damping ratio, ξ, may be calculated in accordance with Equation 4.22.

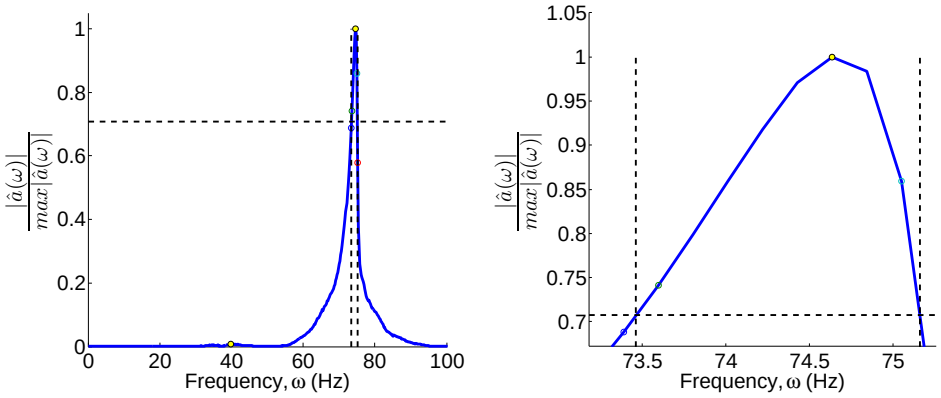

(a) (b)

Figure 4.19.: Half-power bandwidth method of calculation of damping ratio, ξ

Both the fundamental frequencies, ω_1, and the respective damping ratios, ξ, have been calculated for increasing axial load levels, and the results are presented in Figures 4.20 and 4.21, in conjunction with Table 4.10. The fundamental frequencies have been identified as the main peak in the expected range. The damping ratios have been calculated in accordance with the half-power bandwidth method.

Table 4.10 shows the calculated linear regression intercept parameter (β_0), and slope parameter (β_1) when regressing ξ_1 on N for all four permutations of beam (i) and load cases (j). The corresponding linear regression equations are obtained by substituting into the following formula;

$$\xi_1 = \beta_{0,ij} + \beta_{1,ij} N \tag{4.23}$$

4.8. Fundamental Bending Frequencies, ω_1

Figure 4.22 shows the peaks in the frequency domain for each axial load level and for each impact hammer test conducted. There are 50 iterations of the impact response signals at each axial load level. The relative modal amplitude is displayed on the vertical axis, while the horizontal plane con-

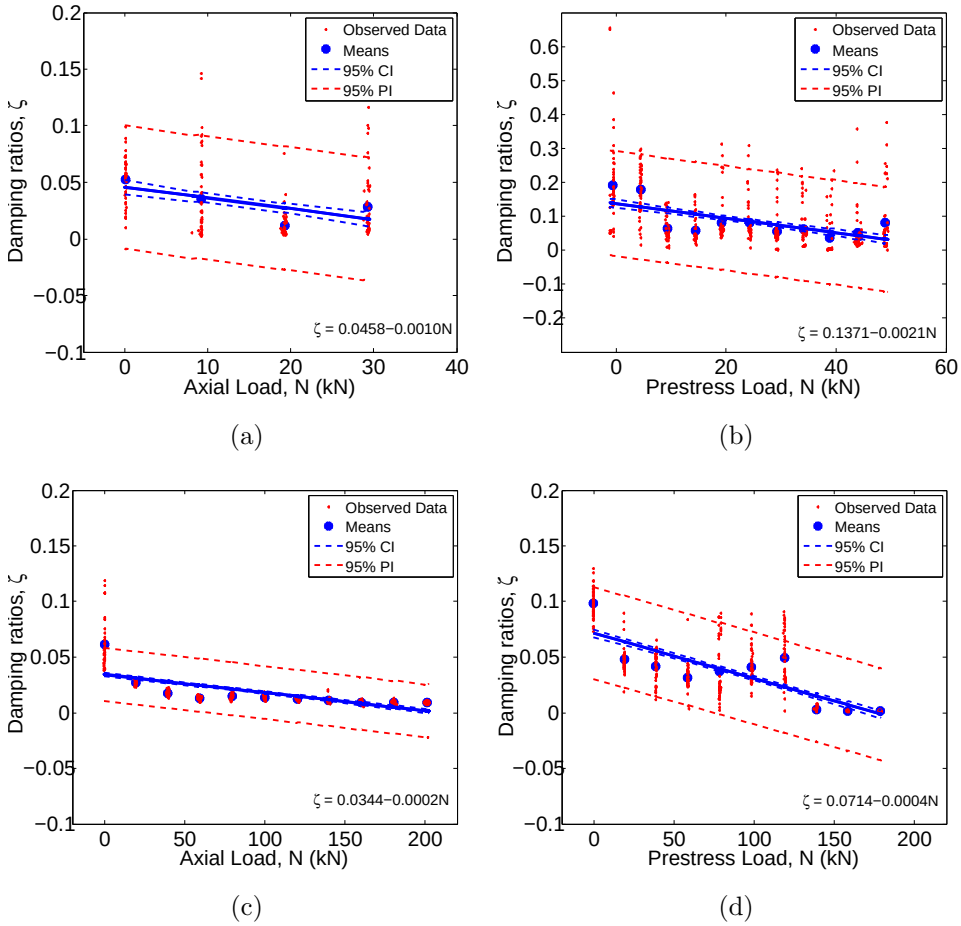

Figure 4.20.: Regression analysis; ξ vs. N for different steel beams; (a) Beam 1, Case 1; (b) Beam 1, Case 2; (c) Beam 2, Case 1; (d) Beam 2, Case 2.

sists of the frequency axis (Hz) and the axial load level (kN). The size of the data point is directly related to the relative modal amplitude. The modal amplitude has been normalised by dividing by its maximum value, expressed as $\frac{|\hat{a}(\omega)|}{max|\hat{a}(\omega)|}$. The relative participation of each mode to the overall dynamic response of the beams can be compared in these graphs. For example, for both post-tensioned beams (Beam 1, case 2, Figure 4.22b & Beam 2, case 2, Figure 4.22d) it can be seen that the overall response of the beam is quite complex and contains a significant proportion due to many modes. In comparison, for the externally axially load case (Beam 1, case 1, Figure 4.22a & Beam 2, case 1, Figure 4.22c), the dominance of the first

Table 4.10.: Statistical analysis on regression parameters for ξ_1 on N

B/C	Reg. P.	Value	SE	t-value	t-crit.	p	95% CI
B1 C1	$\beta_{0,11}$	0.0458	0.0032	14.2186	1.9720	0.0000	(0.0395,0.0522)
	$\beta_{1,11}$	-0.0010	0.0002	-5.3699	1.9720	0.0000	(-0.0013,-0.0006)
B1 C2	$\beta_{0,12}$	0.1371	0.0062	22.1801	1.9643	0.0000	(0.1249,0.1492)
	$\beta_{1,12}$	-0.0021	0.0002	-9.8760	1.9643	0.0000	(-0.0026,-0.0017)
B2 C1	$\beta_{0,21}$	0.0344	0.0010	35.8787	1.9644	0.0000	(0.0325,0.0363)
	$\beta_{1,21}$	-0.0002	0.0000	-19.4633	1.9644	0.0004	(-0.0002,-0.0001)
B2 C2	$\beta_{0,22}$	0.0714	0.0017	41.2609	1.9647	0.0000	(0.0680,0.0748)
	$\beta_{1,22}$	-0.0004	0.0000	-24.6953	1.9647	0.0000	(-0.0004,-0.0004)

mode is more readily identifiable. This is exceptionally clear for Beam 2, case 1 in Figure 4.22c, where the dominance of the first mode of vibration is evident.

Comparing Figure 4.22 to Figure 4.23, which presents the estimated fundamental frequency as a function of axial load level, leads to an interesting observation. When the total response of the structural system is complex, with components that can be attributed to many different modes, as can be seen in Figures 4.22b and 4.22d, and to a lesser extent, Figure 4.22a, the scatter in the prediction of the first natural frequency is very high, as can be seen in Figures 4.23b, 4.23d and 4.23a and indicated by the standard deviation in the data. However, in the case where the response of the structural system is significantly dominated by the fundamental frequency, as in Figure 4.22c, the standard deviation is significantly decreased and the prediction of the first natural frequency is very precise, with an extremely low standard deviation, as shown in Figure 4.23c. It should be noted that for lower values of axial load, the response is slightly more complex for Beam 2, Case 1 (Figure 4.23c), with many modes contributing to the response. Consequently, a much higher scatter in the prediction of the fundamental frequency and a smaller standard deviation, is observed.

In order to analyse the significance of the changes observed in the estimation of the natural frequency of the sections with increasing axial load, a linear regression analysis was applied to each beam and load case combination. The results are presented in Figure 4.26 in conjunction with Table 4.11. It should be pointed out to begin with that the purpose of this regression

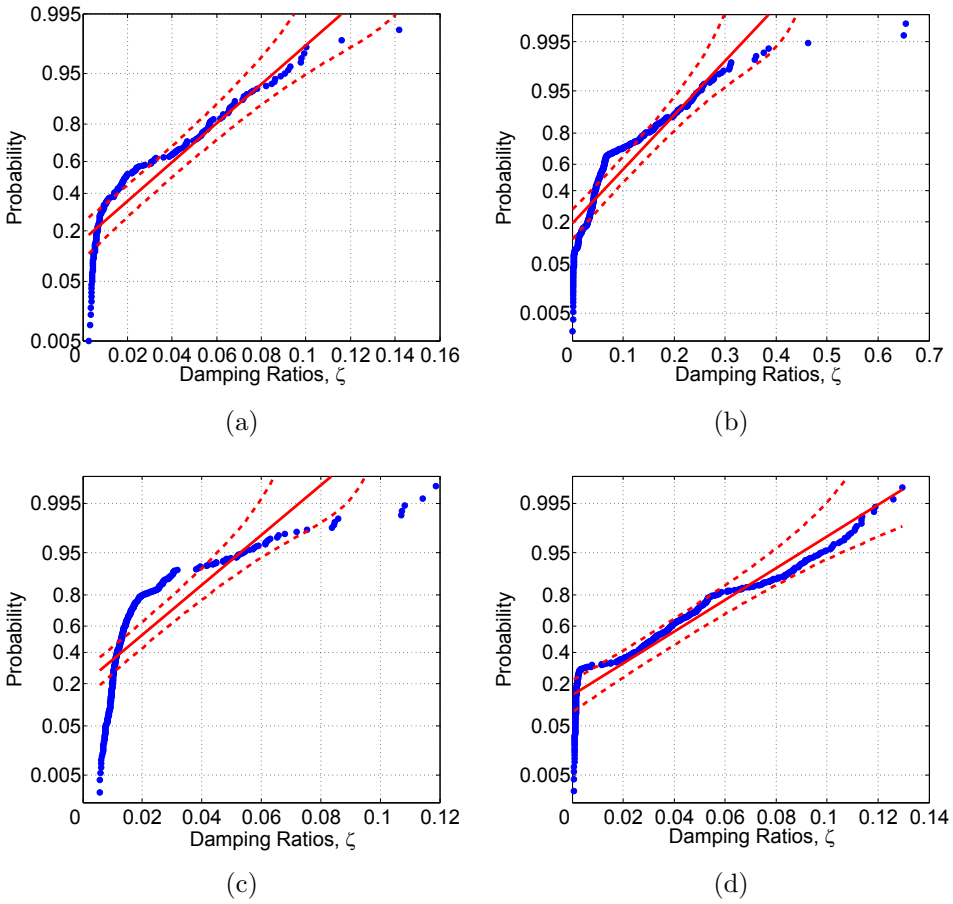

Figure 4.21.: Normal Probability Plots of Damping Ratio, ξ for each beam/load case combination; (a) Beam 1, Case 1; (b) Beam 1, Case 2; (c) Beam 2, Case 1; (d) Beam 2, Case 2.

analysis is not for interpolation, extrapolation or prediction of any values of fundamental frequency based on axial load level, but rather as a tool to analyse the statistical significance of the changes observed in the data. Table 4.11 shows the regression parameters and the results of statistical t-tests charting whether the linear regression intercept and slope parameters are statistically significantly different from zero or not for each beam and load case combination. A significance level of $\alpha = 0.05$ has been chosen for the tests. In each beam/load case combination a statistically significant change in fundamental frequency with increasing axial load level has been observed. For Beam 1, case 1, a statistically significant decreasing trend is observed,

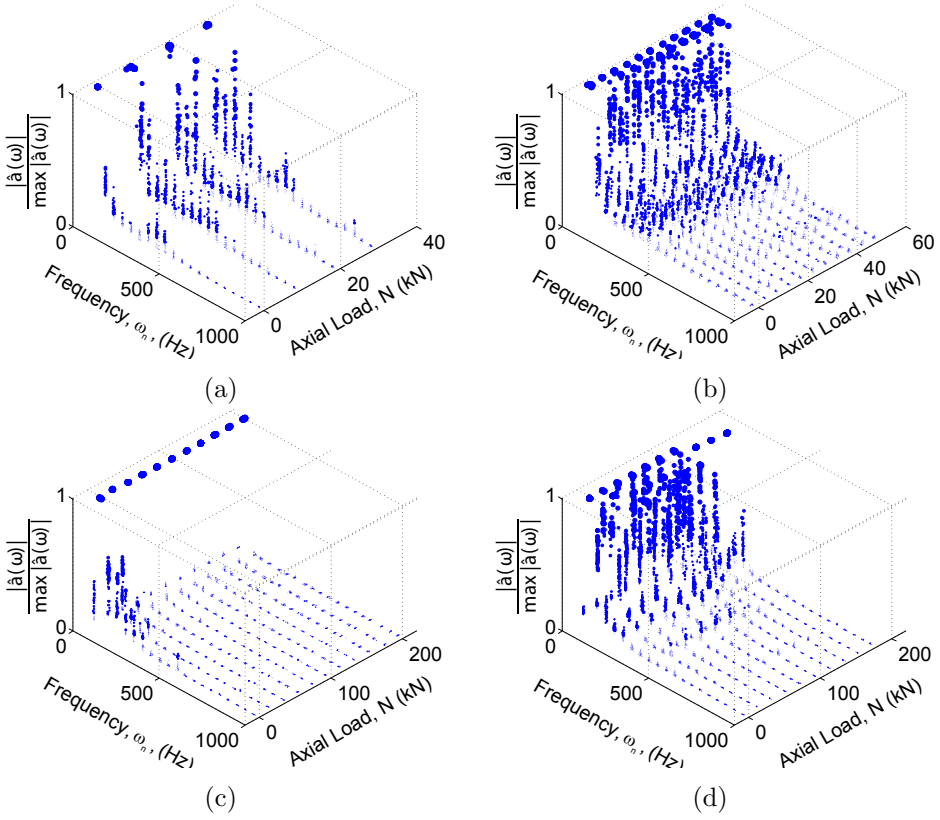

Figure 4.22.: Graph of peaks in frequency, load and relative modal amplitude, 3D-space; (a) Beam 1, Case 1; (b) Beam 1, Case 2; (c) Beam 2, Case 1; (d) Beam 2, Case 2.

indicating that the natural frequency of an externally axially loaded slender steel section will decrease with increasing external axial load. For Beam 1, case 2, a statistically significant decreasing trend is again observed, however the rate of change (magnitude of the regression slope parameter) is not as large as that for Beam 1, case 1. This indicates that the rate of change of frequency with increasing axial load level is different for an external axial load (case 1) than it is for the post-tensioned load case (case 2). This can be seen clearly in Figure 4.24. From Figure 4.24a, it is clear that the trend observed by the externally axially loaded slender section follows that predicted by *"compression-softening"*. However, evidently, the post-tensioned section that has been tested both statically and dynamically follow a different trend to that predicted by compression softening. Albeit, a statistically significant decreasing trend is observed, yet it is not of the rate exhibited

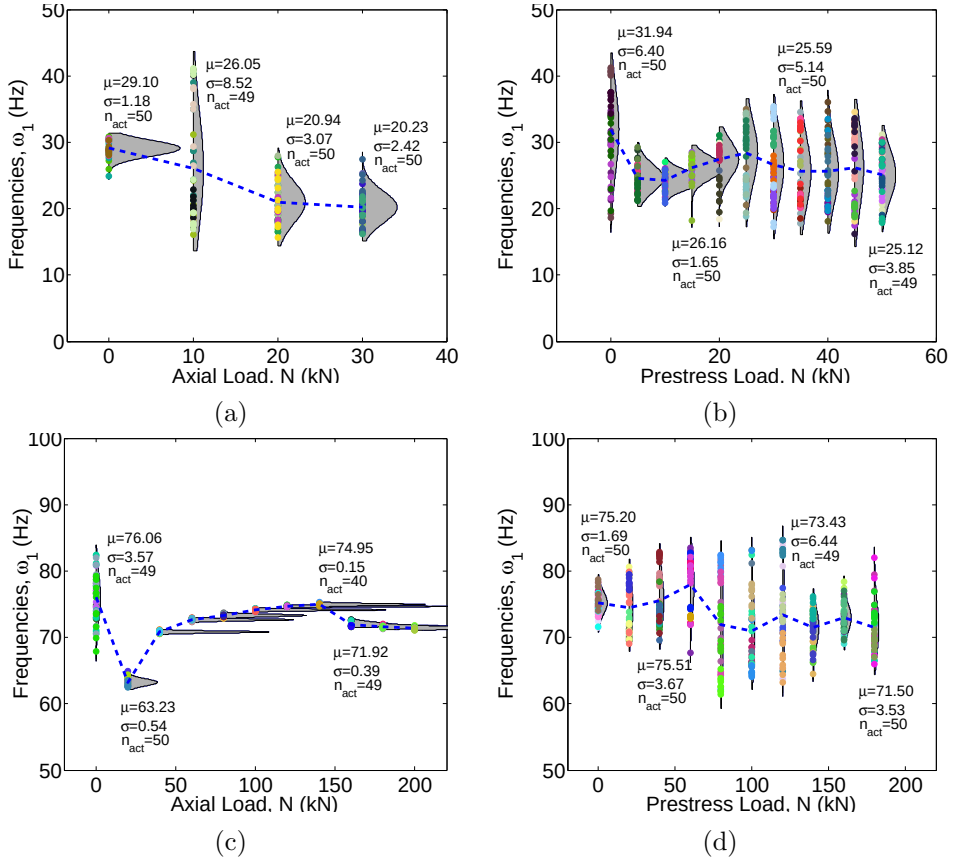

Figure 4.23.: Observed changes in ω_1 with N for different steel beams; (a) Beam 1, Case 1; (b) Beam 1, Case 2; (c) Beam 2, Case 1; (d) Beam 2, Case 2.

by the externally axially loaded section and predicted by the theory. Interestingly, Figure 4.24b indicates that in the static case, the results followed a trend similar to that predicted by compression softening. However, in both the dynamic cases, for the stocky and slender sections, the results deviated significantly with what was predicted by compression softening. The externally axially loaded section displayed a statistically significant increasing trend, whereas the post-tensioned section displayed a statistically significant decreasing trend. However, the trend did not match that predicted by compression softening. From the tests conducted and the results presented in Figure 4.24, it is concluded that *"compression-softening"* theory is valid for externally axially loaded sections only, and not for any kind of post-tensioned sections.

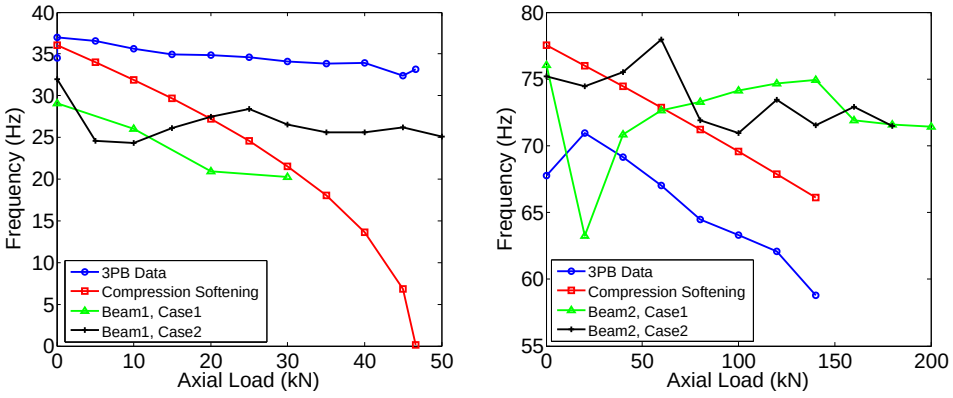

(a) (b)

Figure 4.24.: Means of dynamic test results plotted with static 3 point bending data and Equation 2.1 (a) Beam 1 (b) Beam 2.

For Beam 2, case 1 a statistically significant increasing trend is observed, indicating that for an externally axially loaded stocky section, the natural bending frequency increases with increasing external axial force. However, it is questionable whether a linear fit is correct in this case, as, from Figure 4.23c and 4.26c, a non-linear second order, or possibly an asymptotic trend is identifiable. For beam 2, case 2, again a statistically significant decreasing trend in natural bending frequency with increasing axial load level is observed, however the magnitude of the regression slope parameter is less than for both Beam 1 - load case combinations.

Figure 4.24 compares the prediction of the change in fundamental bending frequency of the beam sections according to *"compression-softening"* theory (Equation 2.1) to the means of the dynamic results for the external axial load case (load case 1), the post-tensioned load case (load case 2), and the results of the static-equivalent frequency of the post-tensioned load case (3PB Data). Figure 4.24a shows the results for Beam 1, RHS $50 \times 30 \times 3$, with a slenderness ratio of between 128 and 139, depending on the load case, as outlined in Table 4.9. It can be seen from Figure 4.24a that the external axial load case shows some good agreement in terms of the decreasing trend in fundamental bending frequency with increasing external axial load. The Beam 1 case 1 line and the *"compression-softening"* line are almost parallel. The frequency of the external axial load case has been shifted down however, and this may be attributed to lack of ideal conditions. The entire structural

system consists of a frame and loading jack, which would act as to lower the bending frequencies. Buckling was reported at an external axial load of 40kN. The predicted failure load in accordance with EC3 is 34.7kN, as outlined in Table 4.2 in Section 4.2.6. Buckling occurred when the section was loaded axially to 40kN and the beam was struck laterally with the impact hammer during dynamic testing. As a result, it was impossible to obtain an estimation of the natural frequency at this load level. However, the trend is still observable up to this point. The Beam 1 case 2 line indicates the change in the mean of the frequencies due to an increasing post-tensioning load, that is induced in the section by the way of a post-tensioning strand threaded through the beam hollow and jacking against either end of the beam to elongate the strand. It can be seen from Figure 4.24a that the post-tension load case (case 2) does not follow the same trend as either the external axial load case or that predicted by *"compression-softening"* theory (Equation 2.1). However, it does follow a very similar trend to the static prediction of the frequency due to 3-point bending tests (3PB Data), as described in Section 4.5. A downwards shift to the dynamic measurement of the fundamental frequency is again observable. It can be concluded that, for slender sections, that are expected to behave in good agreement with Euler buckling theory, that *"compression-softening"* is indeed valid for externally axially loaded members. However, Equation 2.1 is not applicable to post-tensioned structures. In this case, a slight decreasing trend in the fundamental frequency is observable, however it is not of the same rate as predicted by Equation 2.1. It can be concluded, that for slender members, a post-tensioned load is not dynamically equivalent to an external axial load. Figure 4.24b, shows the results for Beam 2, RHS $120 \times 60 \times 3$. It has a slenderness ratio of approximately 60, as outlined in Table 4.9, and, according to code-based approaches, such as Eurocode 3 (EC3) (British Standards Institute, 2005), is expected to deviate from Euler buckling theory as a result. It can be seen that both the external axial load case (Beam 2, case 1) and the post-tensioned load case (Beam 2, case 2) deviate greatly from the trend expected in accordance with Equation 2.1. The static 3-point bending prediction of the frequency (3PB Data) follows a similar decreasing trend, as predicted by Equation 2.1, however, an initial increase is observed, with seating load, as in Figure 4.24. There is also a downward shift in the 3-point bending prediction of the frequency from Equation 2.1, which again can be

attributed to the lack of ideal conditions, and the effect of the weight of the jacks on the beam response. In summary, it can be concluded that stocky sections, with low and medium slenderness ratios do not follow the trend predicted by *"compression-softening"* theory, neither for the external axial load case (load case 1) or for the post-tensioned load case (load case 2). It was found, as expected that *"compression-softening"* is only valid for externally axially loaded slender members (with a slenderness ratio greater than approximately 120) that behave in accordance with Euler buckling theory.

Figure 4.27 shows a Normal probability paper plot for the measured values of the fundamental frequencies of each of the four beam and load case combinations. Data normality is determined visually if the data follows a linear trend. The implication of data normality is that the data stems from the same normal parent distribution with one mean and standard deviation. The implication of this is that if the data stems from one normal parent distribution, the reason for any changes an simply be due to random error/variation, and not due to any sort of systematic effect. From visual inspection of the plots, it may be considered that both post-tensioned load cases (Figures 4.27b and 4.27d) are in fact visually consistent with what would be expected from data Normality, including the deviation in the tails of the plot, i.e. the extreme values. Data normality must be rejected for both external axial load cases (Figures 4.27a and 4.27c). This indicates, that for both post-tensioned steel sections that the measured natural bending frequencies come from the same normal parent distribution. As such, since the obtained results come from the same parent distribution, the deviation may be attributed to random error, and not to any systematic effect. As such, it indicates that any observed changes are due to random effects and there is no systematic relationship between post-tensioning force and fundamental bending frequency. However, for the externally axially loaded steel beams, data Normality must be rejected on the basis of visual inspection of Figures 4.27a and 4.27c. As such, this indicates that since the measured values of fundamental frequency with changing axial load level are not likely to be from the same parent distribution, we must reject the hypothesis that the effects are random, and must attribute the changes to some systematic effect. This narrative is supported when Figure 4.27 is analysed in conjunction with the corresponding Figures for each beam/case combination in Figure 4.26. Despite all four beam/load case combination

displaying statistically significant changes when subjected to a first order linear regression analysis, as outlined in Table 4.11, it can be seen from Figure 4.26 that the decreasing trend predicted by the *"compression-softening"* effect is evident for the externally axially loaded slender section. This is further enforced by the fact that data normality has been rejected on the basis of Figure 4.27a. However, for both post-tensioned cases, despite showing a statistically significant decreasing trend, the rate of decrease is not of the magnitude predicted by *"compression-softening"*, the error in the estimation of the frequency is large, and the data shows evidence of being from the one parent distribution, leading to the conclusion that the effects are random and supporting the evidence that *"compression-softening"* is only valid for externally axially loaded slender sections, and is not valid for any type of post-tensioned section. It should also be noted, that in the case of the externally axially loaded stocky beam section, there is strong evidence of a statistically significant increasing trend in fundamental frequency with increasing external axial load, and this supports the idea that *"compression-softening"* is only valid for externally axially loaded slender sections, as they are the sections that are susceptible to the Euler buckling phenomenon.

Figure 4.20 shows a linear regression analysis by regressing the measured damping ratio, ξ, on the axial load level, N. When analysed in conjunction with Table 4.10, this indicates that there is a statistically significant decreasing trend in estimation of the damping ratio with increasing axial load level. Figure 4.21 shows the Normal Probability Papers of the measured damping ratio for each of the four beam and load case combinations. Using the visual method, normality must be rejected for all four beam and load cases.

Table 4.11 shows the calculated linear regression intercept parameter (α_0), and slope parameter (α_1) when regressing ω_1 on N for all four permutations of beam (i) and load cases (j). The corresponding linear regression equations are obtained by substituting into the following formula;

$$\omega_1 = \alpha_{0,ij} + \alpha_{1,ij} N \tag{4.24}$$

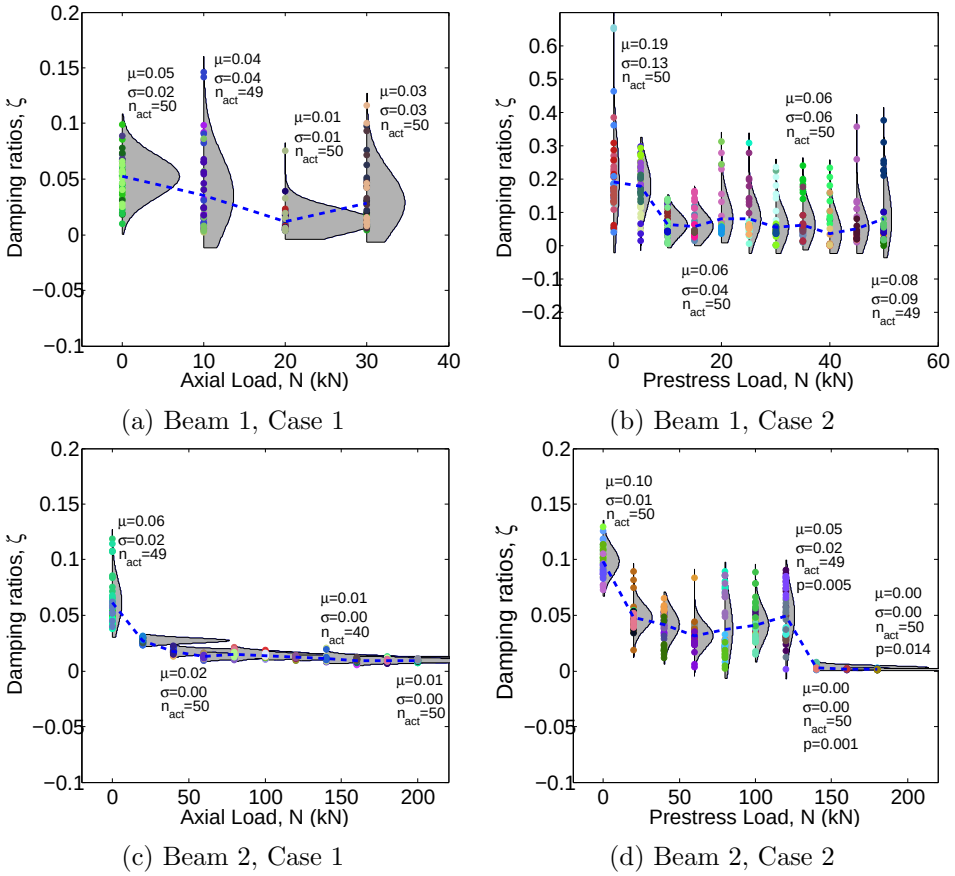

(a) Beam 1, Case 1

(b) Beam 1, Case 2

(c) Beam 2, Case 1

(d) Beam 2, Case 2

Figure 4.25.: Observed changes in ξ with N for different steel beams

4.9. Beam Failure Conditions

The failure conditions for each of the four beam and load case combinations were very different. Table 4.12 charts the failure load of the external axially loaded sections, and compares the values to what is predicted in accordance with EC3 (British Standards Institute, 2005) ($N_{b,Rd_{yy}}$), what is predicted from Euler buckling theory ($P_{CR_{yy}}$) and what is predicted from crushing of the member, in accordance with EC3 (British Standards Institute, 2005) ($N_{c,Rd}$). Figure 4.28 shows the beam failure conditions in the laboratory. The slender section, beam 1 - RHS 50 × 30 × 3, as shown in Figure 4.28a, failed in a manner consistent with what is predicted by Euler buckling theory at a load of 40 kN, which is 15.3% greater than the EC3 design load of 34.7kN, and 22.5% less than the critical load predicted by Euler buckling theory. The stocky section, Beam 2 - RHS 120 × 60 × 3, as shown in Fig-

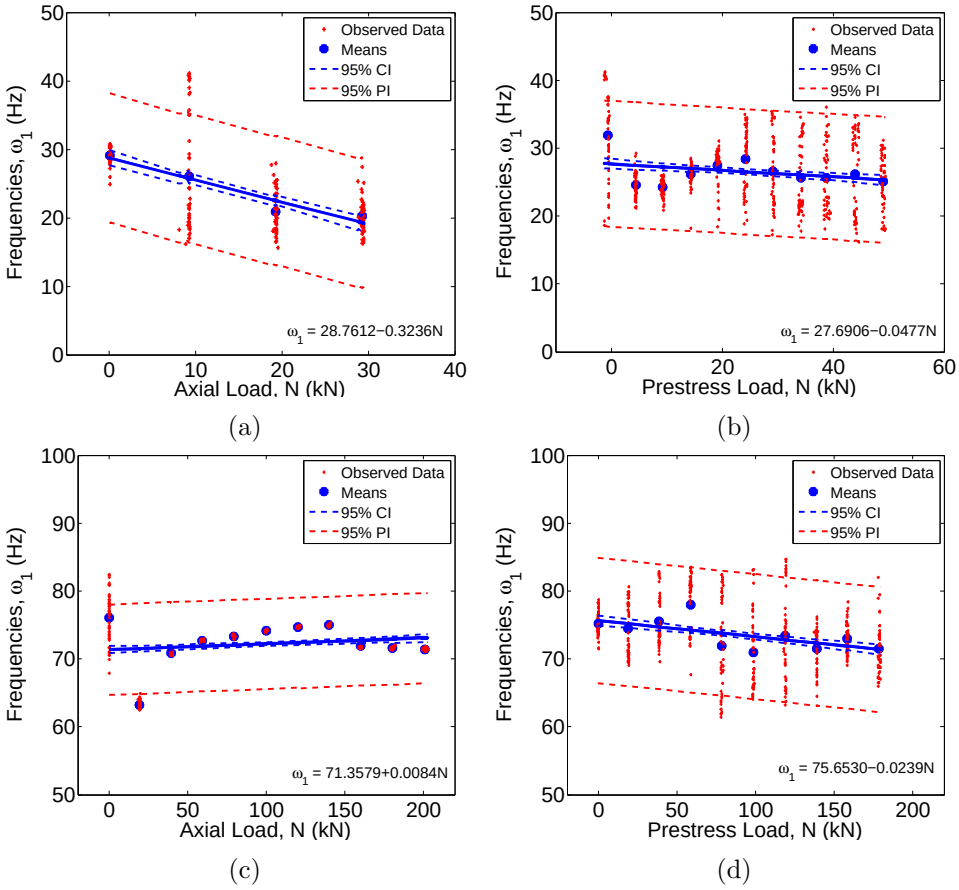

Figure 4.26.: Regression analysis; ω_1 vs. N for different steel beams; (a) Beam 1, Case 1; (b) Beam 1, Case 2; (c) Beam 2, Case 1; (d) Beam 2, Case 2.

ure 4.28b, failed in a local manner, close to the support at a value of 260kN. Interestingly, this value is similar to the design buckling load in accordance with EC3 (British Standards Institute, 2005). However, as expected, for a stocky section, it is well below the predicted Euler buckling critical load of 506.1kN.

No failure condition was reached for the slender post-tensioned section (i.e. Beam 1, case 2). In the case of the post-tensioned stocky section, a plastic hinge formed at midspan at an axial load of 140kN, combined with a midspan point load of 6kN. This can be seen in Figure 4.28c. The section, in accordance with EC3 British Standards Institute (2005), is designed to resist a midspan point load of 12.24kN, therefore, at a post-tension load of 140kN, a 50% reduction in load carrying capacity was observed.

Table 4.11.: Statistical analysis on regression parameters for ω_1 on N

B/C	Reg. P.	Value	SE	t-value	t-crit.	p	95% CI
B1 C1	$\alpha_{0,11}$	28.7612	0.5574	51.5969	1.9720	0.0000	(27.6620,29.8605)
	$\alpha_{1,11}$	-0.3236	0.0308	-10.5204	1.9720	0.0000	(-0.3842,-0.2629)
B1 C2	$\alpha_{0,12}$	27.6906	0.3709	74.6608	1.9643	0.0000	(26.9621,28.4192)
	$\alpha_{1,12}$	-0.0477	0.0130	-3.6845	1.9643	0.0003	(-0.0732,-0.0223)
B2 C1	$\alpha_{0,21}$	71.3579	0.2682	266.0298	1.9644	0.0000	(70.8310,71.8848)
	$\alpha_{1,21}$	0.0084	0.0023	3.5894	1.9644	0.0004	(0.0038,0.0130)
B2 C2	$\alpha_{0,22}$	75.6530	0.3855	196.2659	1.9647	0.0000	(74.8956,76.4103)
	$\alpha_{1,22}$	-0.0239	0.0037	-6.5195	1.9647	0.0000	(-0.0311,-0.0167)

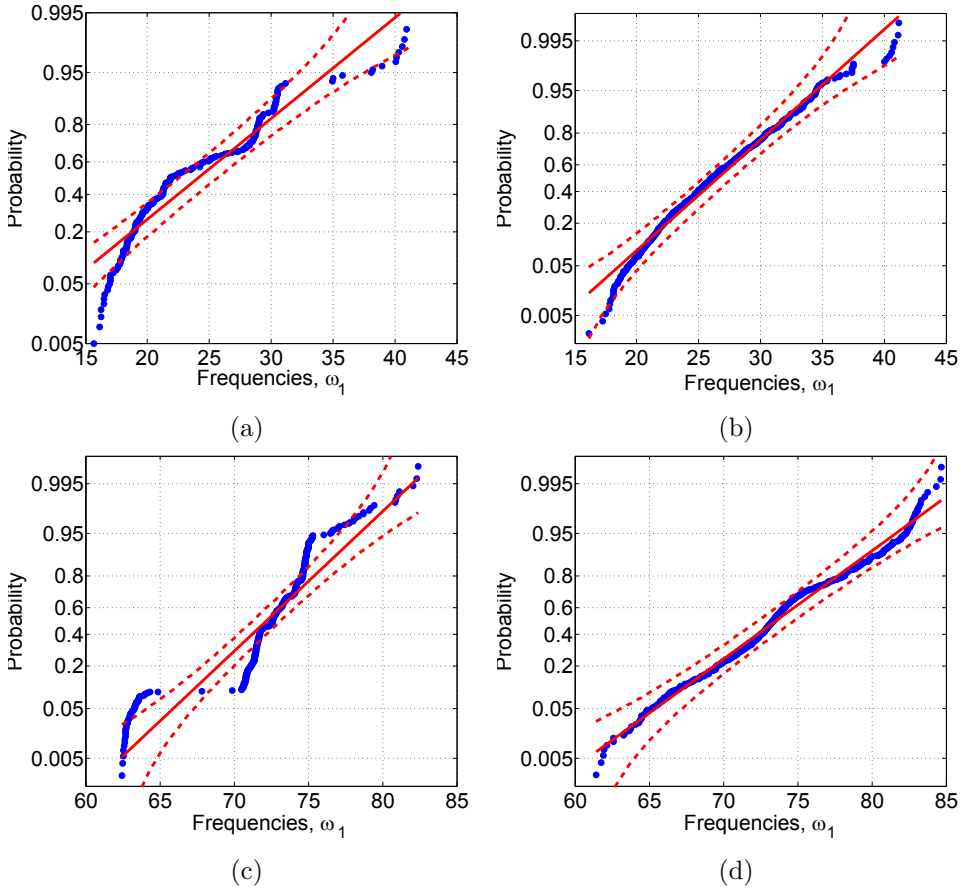

Figure 4.27.: Normal Probability Plots of Fundamental Bending Frequency, ω_1 for each beam/load case combination; (a) Beam 1, Case 1; (b) Beam 1, Case 2; (c) Beam 2, Case 1; (d) Beam 2, Case 2.

Table 4.12.: Failure conditions of RHS sections, Case 1

Property	**RHS** $50 \times 30 \times 3$	**RHS** $120 \times 60 \times 3$
Beam #	Beam 1	Beam 2
$N_{b,Rd_{yy}}$ (kN)	34.7	251.8
$P_{CR_{yy}}$ (kN)	44.8	506.1
$N_{c,Rd}$ (kN)	105.3	344.9
Failure Reported (kN)	40	260

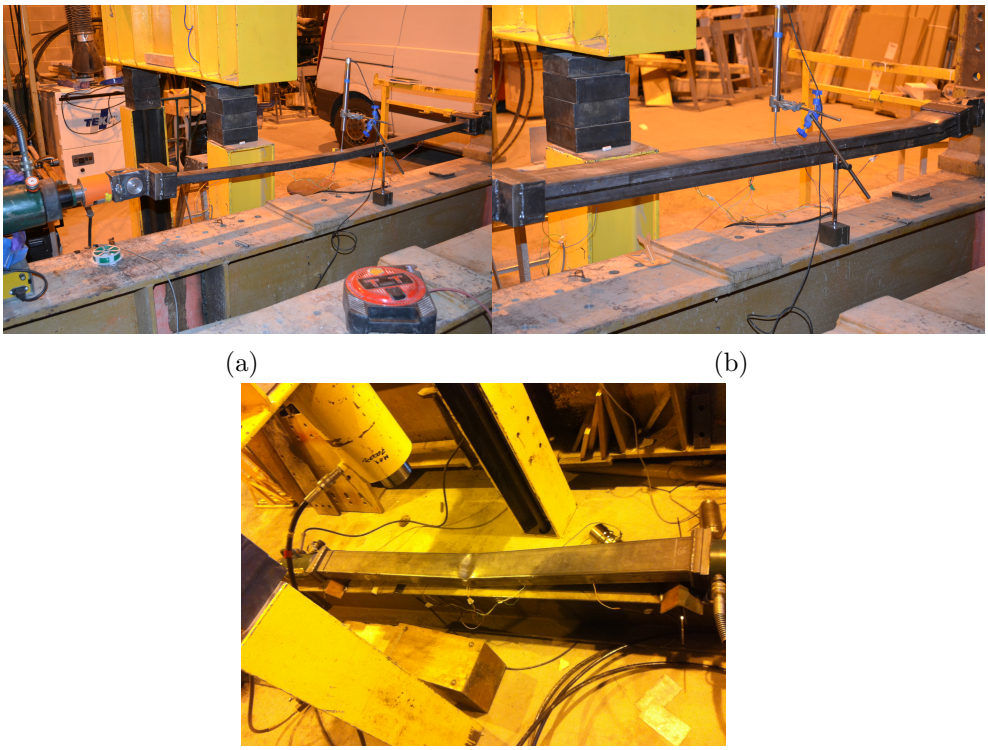

(a) (b)

(c)

Figure 4.28.: Failure conditions of RHS sections; (a) Beam 1, Case 1; (b) Beam 2, Case 1; (c) Beam 2 Case 2.

4.10. Discussion of Accuracy of Experimental Results

This chapter presents the results of both static and dynamic testing on steel rectangular sections. In all cases, the fundamental frequency and the damping ratio were determined through analysis of impact response signals

from each of the beam sections at different axial load levels. In some cases, the accuracy of the estimation of the natural frequency, and subsequently the damping ratio is poor, with a relatively large standard deviation. For instance, this can be observed in Figure 4.23. The standard deviation in the estimation of the fundamental frequency in case of the steel beams, is as large as 8.5Hz in some cases. In these cases there is a complex contribution of all modes to the overall structural dynamic response of the vibrating beam, and the fundamental vibration mode does not dominate as expected. During testing of the steel specimens, significant "rattle" was noticed as a result of construction tolerance in the pin-ended joint connections, and in some cases due to "jumping" of the beam specimens off the knife edge supports following dynamic excitation with a hammer. Rattle and jumping cause a non-linear dynamic response, in which the boundary conditions of the structure are constantly changing throughout the vibration, and this can cause the aforementioned complex dynamic response and significant contribution of the higher modes. As such, this inaccuracy in the estimation of the modal parameters is attributed to this rattle/jumping and subsequent non-linear dynamic response and contribution of the higher modes to the overall structural vibration.

The results for the externally axially loaded stocky steel section (Beam 2, Case 1), as shown in Figure 4.23c, at a certain seating load, the accuracy of the estimation of the natural frequency is greatly improved due to the removal of the rattle. In this case, the beam section fitted tightly into the pinned support fixture, and no rattle was reported. Once the seating load was reached and the rattle was removed, the fundamental mode of vibration dominated the response of the beam section, and the standard deviation of the estimation of the natural frequency drops significantly from approximately 3.57Hz down to 0.15Hz for 50 data points. In such a case, the estimation of the fundamental frequency is extremely accurate, and highlights the inaccuracies in the other results.

In all cases, the error in the estimation of the bending frequency may have been minimised by measuring the dynamic input force, increasing the number of excitation points, and increasing the number of response points. In the case of the steel sections, the non-linear effects of rattle should be minimised to obtain precise estimations of the fundamental bending frequency.

4.11. Conclusions

The above results have been obtained after gathering and analysing 1750 different dynamic response measurements, including the cases of slender and stocky sections that have been both post-tensioned and externally axially loaded. The volume of data collected enabled a statistical analysis of the results for a combination of beam and load cases to be conducted. The main conclusions derived from this broad study are as follows;

1. An externally axially loaded slender section displays good agreement with the *"compression-softening"* effect, as the obtained results have shown. A post-tensioned slender section deviates from what is expected from *"compression-softening"* theory, however, does display a decreasing trend in fundamental bending frequency, ω_1, with increasing post-tensioning load.

2. An externally axially loaded stocky section does not follow the trend predicted by *"compression softening"* theory. A statistically significant increasing trend in ω_1 is observed with increasing axial load level. A post-tensioned stocky section also deviates from *"compression-softening"* theory, however a statistically significant decreasing trend was observed.

3. Post-tension load is phenomenologically different to an external axial load and is not equivalent to an external axial load.

4. A post-tensioning load does not cause Euler buckling to occur.

5. *"Compression-softening"* is not valid for pre- or post-tensioned structures, therefore the use of Equation 2.1 is erroneous for all types of post-tensioned structures.

6. In all cases, a decrease in damping ratio, ξ, is observed with increasing axial load level.

7. The precision of prediction of the fundamental frequency is related to the complexity of dynamic response of the signal, and the proportion of dynamic response attributed to the fundamental mode.

The main implications of the results are that the *"compression-softening"* equation must be eliminated from discussion of all forms of post-tensioned structures, as the effect of an external axial load and a post-tensioning load on the dynamics of post-tensioned structures are different on a phenomenological level.

Further research is required to determine exactly how the fundamental frequency of pre- and post-tensioned concrete structures changes with increasing post-tensioning force, however, based on the above results, the fundamental frequency of pre- and post-tensioned concrete structures are not predicted to behave in accordance with *"compression-softening"* theory.

The statistical significance of the regression slope and intercept parameters for regressing both fundamental bending frequencies, ω_1, and Damping Ratios, ξ, on applied axial load, N, for all beam and load case combinations are given in Table 4.11 and Table 4.10. Statistical t-tests have been carried out to determine if the regression slope and intercept parameters are statistically significantly different from zero, or not.

Linear regression lines have been fitted to the data and the results are observed in Figures 4.26 and 4.20. The Normality of both the fundamental bending frequency and the damping ratios have been tested by plotting the results on a Normal Probability Paper, and the results are displayed in Figures 4.27 and 4.21. As outlined previously, since data Normality is to be rejected for both external axial load cases, the observed changes in fundamental bending frequency may be attributed to systematic effects due to the magnitude of the external axial load. However, in the case of the post-tensioned load case, since data Normality cannot be rejected for the entire data set, the observed changes are likely to be due to random effects and should not be attributed to any sort of systematic effect, lending support to the theory that the "compression-softening" effect is valid for externally axially loaded slender sections only, and is not applicable to any type of post-tensioned structures.

5. Modelling effect of prestress force on natural bending frequency

This chapter presents a linear mathematical model predicting changes in fundamental bending frequency with increasing post-tensioning force magnitude. Changes in Young's Modulus, axial length, second moment of area and mass per unit length with increasing post-tensioning force magnitude are calculated, and subsequently, the changes in fundamental bending frequency are determined.

The chapter outlines the development of a theoretical prediction model and applies the results to a series of 9 different straight-profiled post-tensioned concrete beams that were subsequently tested in the laboratory, and outlined in Chapters 6 and 7. The properties of the beam sections modelled (Beams 1-9) are outlined fully in Chapter 6, and reference should be made to Section 6.6.1 and Figures 6.14, 6.17 and 6.19 specifically for full details of the modelled beams.

5.1. Introduction

This chapter outlines the results of mathematical modelling in MATLAB (MATLAB, 2014) in order to predict the effect of prestress force magnitude, N, and eccentricity, e, on the natural frequencies of prestressed concrete structures, ω_n. A simple linear mathematical model is proposed by predicting changes in each of the parameters outlined in Equation 5.1 with increasing post-tensioning force magnitude. Changes in span length of the post-tensioned concrete sections were modelled in accordance with axial shortening, $\ell(N)$, as outlined in Section 5.2. Changes in Young's Modulus of the concrete with increasing post-tensioning force magnitude, $E(N)$,

were modelled in accordance with a model presented by Attard and Setunge (1996), as outlined in Section 5.3. Changes in second moment of area of the cross section with increasing post-tensioning load, $I(N)$, were modelled in accordance with a binary model outlined in Section 5.4. Finally, changes in the mass per unit length of the cross section due to axial shortening, $m(N)$, were modelled and outlined in Section 5.5. These changes in the parameters are then combined as outlined in Equation 5.1, providing a prediction for the change in natural bending frequency with increasing post-tensioning force magnitude;

$$\omega_n(N) = \left(\frac{n\pi}{\ell(N)}\right)^2 \sqrt{\frac{E(N)I(N)}{m(N)}} \tag{5.1}$$

A sensitivity analysis on the effect that changing each parameter has on the changes in fundamental bending frequency, highlighting the relative importance of the changes in each individual parameter, is outlined in Section 5.6. Section 5.7 outlines the predicted changes in fundamental frequency, ω_1, with increasing post-tensioning load magnitude, N, for the 9 uncracked post-tensioned concrete beams that tested in the lab, as described in detail in Chapter 6. Section 5.8 compares the changes predicted by the new model proposed in this chapter with the models previously proposed by Saiidi et al. (1994), Zhang et al. (2012), Dall'Asta and Dezi (1996), Miyamoto et al. (2000) and Kim et al. (2004). Section 5.9 outlines the results of some Finite Element Modelling conducted in Autodesk Robot Structural Analysis (Autodesk ROBOT Structural Analysis Professional 2012 - Student Evaluation Version, 2012) to predict the *'virgin'* fundamental bending frequency (i.e. the fundamental frequency for zero post-tensioning load) of the beams tested. Finally, the conclusions drawn from the modelling conducted and described throughout this chapter are outlined in Section 5.10.

5.2. Axial shortening, $\ell(N)$

The effect of the post-tensioning force, N, on the span length, ℓ, of the concrete beams has been modelled in accordance with axial shortening. The

normal stress, σ_n, due to a compressive axial force is given by;

$$\sigma_n = \frac{N}{A_c} \tag{5.2}$$

where N is the post-tensioning load magnitude and A_c is the gross area of the concrete cross section. The axial strain due to the applied stress is given as;

$$\epsilon_n = \frac{\delta\ell}{\ell} \tag{5.3}$$

where $\delta\ell$ is the change in span length due to axial shortening and ℓ is the original span length. In accordance with Hooke's Law, which states that, for materials in the linear elastic range, the stress, σ, is directly proportional to the strain, ϵ, and the constant of proportionality is known as the Young's Modulus of Elasticity, E_c, and is a measure of the relative stiffness of a material, such that;

$$E_c = \frac{\sigma_n}{\epsilon_n} \tag{5.4}$$

Substituting Equations 5.2 and 5.3 into Equation 5.4, the following is obtained;

$$\delta\ell = \frac{N\ell}{A_c E_c} \tag{5.5}$$

The span length is then modified as a function of the post-tensioning load level, N, such that $\ell(N)$ is given by;

$$\begin{aligned} \ell(N) &= \ell - \delta\ell \\ &= \ell - \frac{N\ell}{A_c E_c} \\ &= \ell\left(1 - \frac{N}{A_c E_c}\right) \end{aligned} \tag{5.6}$$

Figure 5.1 shows the change in length of the modelled post-tensioned concrete beam with increasing post-tensioning force magnitude due to the effect of axial shortening. As shown in Figure 5.1, the effect of axial shortening is very very slight. The modelled beam decreases in length by 0.02% over the practical ranges of post-tensioning load shown.

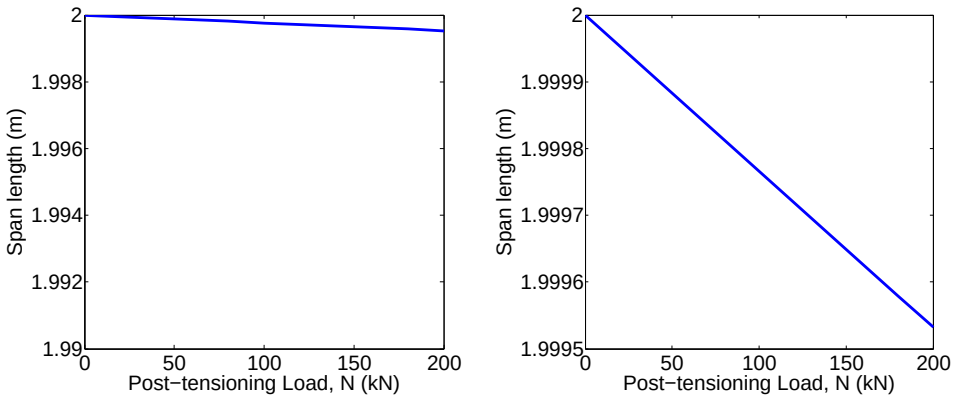

(a) (b)

Figure 5.1.: Change in axial length of post-tensioned concrete beam with increasing post-tensioning load magnitude on different scales; (a) and (b)

Figure 5.2 shows the change in predicted fundamental bending frequency from axial shortening. By keeping all of the other variables constant, and just changing the length of the post-tensioned concrete beam;

$$\omega_n(N) = \left(\frac{n\pi}{\ell(N)}\right)^2 \sqrt{\frac{EI}{m}} \tag{5.7}$$

where $\ell(N)$ is given by Equation 5.6 such that;

$$\omega_n(N) = \left(\frac{n\pi}{\ell\left(1 - \frac{N}{A_c E_c}\right)}\right)^2 \sqrt{\frac{E_c I}{m}} \tag{5.8}$$

and E_c, I and m are kept constant. The change in predicted natural frequency, over the modelled, practical range of post-tensioning force magnitude, is of the order of $+0.04\%$ as shown in Figure 5.3. This is a very small change in predicted natural frequency due to the effect of axial shortening on the span length of the post-tensioned concrete beam, and may be considered to be negligible.

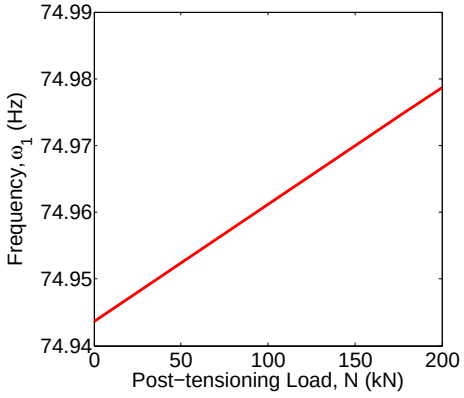

Figure 5.2.: Subsequent change in ω_1, by changing $\ell(N)$ while keeping the other parameters constant

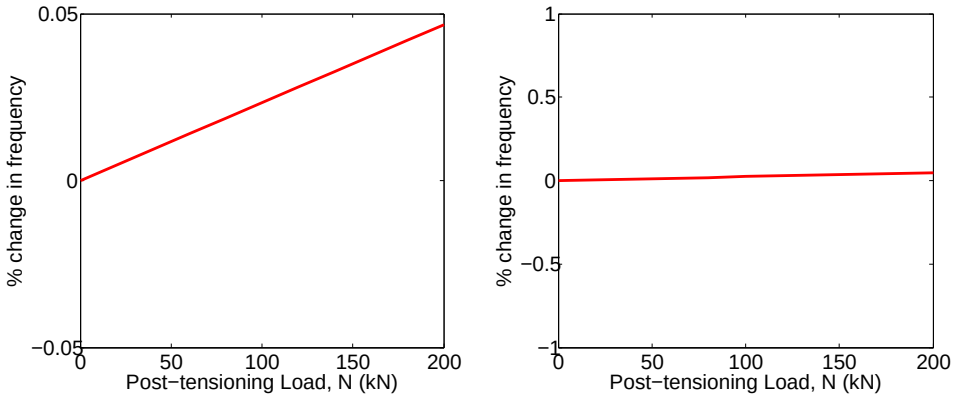

(a) (b)

Figure 5.3.: Percentage change in ω_1 by changing $\ell(N)$ while keeping the other parameters constant, on different scales (a) and (b)

5.3. Change in Young's Modulus with post-tensioning force, $E(N)$, (Attard and Setunge, 1996)

This section outlines the predicted changes in the Young's Modulus of Elasticity of the post-tensioned concrete sections with increasing post-tensioning load magnitude in accordance with the stress-strain model for concrete proposed by Attard and Setunge (1996). The model is split into two distinct models - specifically, one for unconfined concrete, and the other for con-

fined concrete. An analysis of the predicted changes in natural bending frequencies has been conducted in both cases, as outlined in Sections 5.3.1 and 5.3.2.

5.3.1. Unconfined Stress-Strain Model

The change in the Young's Modulus of Elasticity of the post-tensioned concrete section with increasing post-tensioning force has also been modelled. This change has been modelled in accordance with a paper written by Attard and Setunge (1996), entitled *"Stress-Strain Relationship of Confined and Unconfined Concrete"*. First, an empirical formula is used to calculate the static elastic modulus of concrete, E_c, based on the work of Pauw (1960) and subsequently adopted into code (ACI Committee 318, 2008; American Concrete Institute, 1989) and outlined by Attard and Setunge (1996);

$$E_c = 0.043\rho^{1.5}\sqrt{f'_c} \quad MPa \tag{5.9}$$

where ρ is the surface dry unit weight in kg/m^3 and f'_c is the concrete cube strength in MPa, and taken to be $f'_c = 33MPa$ for the purposes of this modelling. This value has been deduced as the characteristic concrete strength based upon materials testing conducted on the concrete in the laboratory. The characteristic cube strength is defined as the strength below which 5% of all samples fall. The results of the material testing are outlined further in Chapter 6, Section 6.3.2. The density of concrete was taken to be; $\omega_c = 24kN/m^3$ and was converted to ρ in kg/m^3 by the following; $\rho = 1000\omega_c/g$, where $g = 9.81m/s^2$, the acceleration due to gravity, therefore;

$$\begin{aligned} E_c &= 0.043\rho^{1.5}\sqrt{f'_c} \\ &= 0.043\left(\frac{(1000)(24)}{9.81}\right)^{1.5}\sqrt{33} \qquad (5.10) \\ &= 29.9 \quad GPa \qquad (5.11) \end{aligned}$$

Attard and Setunge (1996) suggest the following equations for the strain at peak uniaxial compression, depending on the aggregate type used in the

concrete;

$$\epsilon_c = \frac{f'_c}{E_c}\frac{4.26}{\sqrt[4]{f'_c}} \quad MPa \quad (Crushed \quad aggregates) \tag{5.12}$$

$$\epsilon_c = \frac{f'_c}{E_c}\frac{3.78}{\sqrt[4]{f'_c}} \quad MPa \quad (Gravel \quad aggregates) \tag{5.13}$$

For the purposes of the modelling conducted, crushed aggregates were used in the concrete mix and therefore the strain at peak uniaxial compression, ϵ_c is given as;

$$\begin{aligned} \epsilon_c &= \frac{f'_c}{E_c}\frac{4.26}{\sqrt[4]{f'_c}} \\ &= \frac{33}{29.9 \times 10^3}\frac{4.26}{\sqrt[4]{33}} \\ &= 0.002 \end{aligned} \tag{5.14}$$

The stress, f_{ic}, and strain, ϵ_{ic}, at the inflexion point on the graph is given as;

$$\epsilon_{ic} = \epsilon_c \left(2.5 - 0.3ln\left(f'_c\right)\right) \tag{5.15}$$

$$f_{ic} = f'_c \left(1.41 - 0.17ln\left(f'_c\right)\right) \quad MPa \tag{5.16}$$

therefore;

$$\begin{aligned} \epsilon_{ic} &= (\epsilon_c)\left(2.5 - 0.3ln\left(f'_c\right)\right) \\ &= (0.002)\left(2.5 - 0.3ln\left(33\right)\right) \\ &= 0.0028 \end{aligned} \tag{5.17}$$

$$\begin{aligned} f_{ic} &= f'_c \left(1.41 - 0.17ln\left(f'_c\right)\right) \\ &= (33)\left(1.41 - 0.17ln\left(33\right)\right) \\ &= 26.91 \quad MPa \end{aligned} \tag{5.18}$$

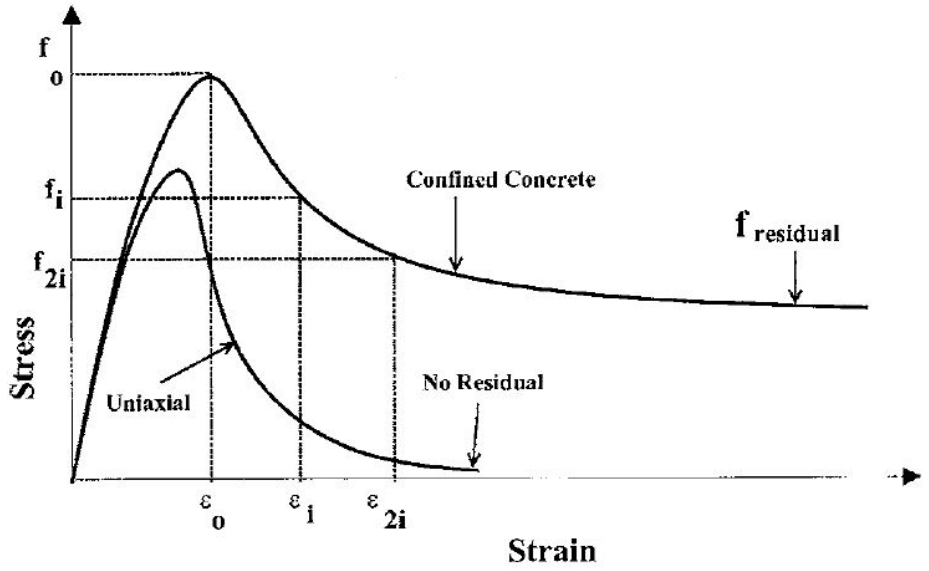

Figure 5.4.: Stress - strain model for confined and unconfined concrete as presented by Attard and Setunge (1996)

For the uniaxial case, $f_0 = f_c$ and $\epsilon_0 = \epsilon_c$, the ascending curve boundary conditions, as shown in Figure 5.4, are given by;

(a) at $f = 0$, $df/d\epsilon = E_{ti}$

(b) at $f = f_0$, $df/d\epsilon = 0$

(c) at $f = f_0$, $\epsilon = \epsilon_0$

(d) at $f = f_{pl}$, $\epsilon = f/E_c$

E_{ti} is the initial tangent modulus at zero stress, and E_c is the secant modulus, measured at a stress of f_{pl}, which is usually given as $0.45f'_c$ (Attard and Setunge, 1996). The equation for the stress-strain relationship is given as;

$$Y = \frac{AX + BX^2}{1 + CX + DX^2} \tag{5.19}$$

where $Y = f/f_0$ and $X = \epsilon/\epsilon_0$, and the coefficients, A, B, C and D are given, for $\epsilon \leq \epsilon_c$ as;

$$
\begin{aligned}
A\left(\epsilon \leq \epsilon_c\right) &= \frac{E_{ti}\epsilon_0}{f_0} \\
B\left(\epsilon \leq \epsilon_c\right) &= \frac{\left(A-1\right)^2}{\alpha\left(1-\frac{f_{pl}}{f_0}\right)} + \frac{A^2\left(1-\alpha\right)}{\alpha^2\frac{f_{pl}}{f_0}\left(1-\frac{f_{pl}}{f_0}\right)} - 1 \\
C\left(\epsilon \leq \epsilon_c\right) &= \left(A-2\right) \\
D\left(\epsilon \leq \epsilon_c\right) &= \left(B+1\right)
\end{aligned} \tag{5.20}
$$

and coefficients A, B, C and D are given, for $\epsilon > \epsilon_c$, as;

$$
\begin{aligned}
A\left(\epsilon > \epsilon_c\right) &= \frac{f_{ic}}{\epsilon_c\epsilon_{ic}}\frac{\left(\epsilon_{ic}-\epsilon_c\right)^2}{f'_c - f_{ic}} \\
B\left(\epsilon > \epsilon_c\right) &= 0 \\
C\left(\epsilon > \epsilon_c\right) &= \left(A-2\right) \\
D\left(\epsilon > \epsilon_c\right) &= 1
\end{aligned} \tag{5.21}
$$

5.3.2. Confined Stress-Strain Model

For the case of a confined stress-strain model, it requires the definition of a second point on the descending curve, ϵ_{2i}. First, the split cylinder strength of the concrete must be determined from;

$$
f_{sp} = 0.32\left(f'_c\right)^{0.67} \quad MPa \quad (No \quad silica \quad fume) \tag{5.22}
$$

$$
f_{sp} = 0.62\sqrt{f'_c} \quad MPa \quad (Silica \quad fume) \tag{5.23}
$$

For the purposes of the modelling, no silica fume was used in the production of the concrete, therefore;

$$
\begin{aligned}
f_{sp} &= 0.32\left(f'_c\right)^{0.67} \\
&= 0.32\left(33\right)^{0.67} \\
&= 3.33 \quad MPa
\end{aligned} \tag{5.24}
$$

The tensile strength of the concrete is therefore given as (Attard and

Setunge, 1996);

$$\begin{aligned} f_t &= 0.9 f_{sp} \\ &= (0.9)(3.33) \\ &= 3.00 \quad MPa \end{aligned} \tag{5.25}$$

The confining pressure in the concrete is then calculated. This is a passive confining pressure and indicates, according to Mander et al. (1988) and Attard and Setunge (1996), that confined concrete is an anisotropic material as it has different confining pressures in different directions for assymetric cross sections, resulting in different values of Young's Modulus. In this case, the minimum value of confining pressure was chosen. First the area of confining steel in each direction must be calculated in accordance with (Mander et al., 1988);

$$\begin{aligned} A_{sx} &= 2 \times \frac{\pi \phi_s^2}{4} \\ A_{sy} &= 2 \times \frac{\pi \phi_s^2}{4} \end{aligned} \tag{5.26}$$

where A_{sx} and A_{sy} are the areas of confining steel in the x and y direction of the cross section respectively, and ϕ_s is the diameter of the shear link. The area of the confined concrete is calculated by first calculating the length of the individual sides;

$$\begin{aligned} b_c &= b - 2 \times (cover + \phi_s/2) \\ d_c &= h - 2 \times (cover + \phi_s/2) \end{aligned} \tag{5.27}$$

where h is the total height of the cross section, b is the total breadth of the cross section (Mander et al., 1988). The lateral confining pressure in the x and y direction is then calculated. This is a passive pressure and is defined according to the confining steel design stress and confining steel cross sectional area;

$$\begin{aligned} f_{lx} &= f_{yh}\frac{A_{sx}}{sd_c} \\ f_{ly} &= f_{yh}\frac{A_{sy}}{sb_c} \end{aligned} \tag{5.28}$$

where s is the design spacing between the shear links, and f_{yh} is the factored design yield stress of the shear (confining) reinforcement, $f_{yh} = f_{yh}/\gamma_{m1} = 500/1.05 = 476.2MPa$. The confining pressure, f_r is given by;

$$f_r = min\left(f_{lx}, f_{ly}\right) \tag{5.29}$$

A factor representing the effectiveness of the confinement, k, is calculated (Attard and Setunge, 1996);

$$k = 1.25\left[1 + 0.062\frac{f_r}{f_c'}\right]\left(f_c'\right)^{-0.21} \quad MPa \tag{5.30}$$

The ultimate strength of the confined concrete is then calculated (Attard and Setunge, 1996);

$$f_0 = f_c'\left(\frac{f_r}{f_t} + 1\right)^k \quad MPa \tag{5.31}$$

where f_t is the tensile strength of the concrete, given by Equation 5.25. The strain at confined peak stress was then calculated using Equation 5.32;

$$\epsilon_0 = \epsilon_c\left[1 + \left(17 - 0.06f_c'\right)\left(\frac{f_r}{f_c'}\right)\right] \quad MPa \tag{5.32}$$

however, it must be pointed out that Equation 5.32 is not dimensionally consistent and is a result of regression modelling (Attard and Setunge, 1996). The ascending curve is as per the unconfined stress-strain model in Section 5.3.1, Equation 5.20. The descending curve boundary conditions, as shown in Figure 5.4, are given by (Attard and Setunge, 1996);

(a) at $f = f_0$, $df/d\epsilon = 0$

(b) at $f = f_0$, $\epsilon = \epsilon_0$

(c) at $f = f_i$, $\epsilon = \epsilon_i$

(d) at $f = f_{2i}$, $\epsilon = \epsilon_{2i} = 2\epsilon_i - \epsilon_0$

$$
\begin{aligned}
A\left(\epsilon > \epsilon_c\right) &= \left[\frac{\epsilon_{2i} - \epsilon_i}{\epsilon_0}\right]\left[\frac{\epsilon_{2i} E_i}{(f_0 - f_i)} - \frac{4\epsilon_i E_{2i}}{(f_0 - f_{2i})}\right] \\
B\left(\epsilon > \epsilon_c\right) &= (\epsilon_i - \epsilon_{2i})\left[\frac{E_i}{(f_0 - f_i)} - \frac{4E_{2i}}{(f_0 - f_{2i})}\right] \\
C\left(\epsilon > \epsilon_c\right) &= (A - 2) \\
D\left(\epsilon > s\epsilon_c\right) &= (B + 1)
\end{aligned} \tag{5.33}
$$

where $E_i = f_i/\epsilon_i$ and $E_{2i} = f_{2i}/\epsilon_{2i}$. In order to establish the full stress-strain relationship for confined concrete, the parameters required are the confined peak stress, strain at peak stress, elastic modulus, stress and strain at inflection point, and the stress and strain at a second point, defined by f_{2i},ϵ_{2i} (Attard and Setunge, 1996). The stress and strain at the point of inflection was calculated using an empirically based regression equation (Attard and Setunge, 1996);

$$
f_i = f_0\left(\frac{\frac{f_{ic}}{f'_c} - 1}{5.06\left(\frac{f_r}{f'_c}\right)^{0.57} + 1} + 1\right) \quad MPa \tag{5.34}
$$

The strain at the inflection point is calculated using a similar analysis (Attard and Setunge, 1996);

$$
\epsilon_i = \epsilon_0\left(\frac{\frac{\epsilon_{ic}}{\epsilon_c} - 2}{1.12\left(\frac{f_r}{f'_c}\right)^{0.26} + 1} + 2\right) \tag{5.35}
$$

Attard and Setunge (1996) report that the same trends are observed for the stress corresponding to a strain of $2\epsilon_i - \epsilon_0$;

$$
f_{2i} = f_0\left(\frac{\frac{f_{2ic}}{f'_c} - 1}{6.35\left(\frac{f_r}{f'_c}\right)^{0.62} + 1} + 1\right) \tag{5.36}
$$

where the universal values can be calculated from;

$$
f_{2ic} = f'_c\left(1.45 - 0.25ln\left(f'_c\right)\right) \quad MPa \tag{5.37}
$$

5.3.3. Modelling changes in frequency due to changes in Young's Modulus

Sections 5.3.1 and 5.3.2 describe the unconfined and confined stress-strain model for concrete as proposed by Attard and Setunge (1996). This model was subsequently applied to the concrete tested in the lab. The tangent modulus was taken to be $E_{ti} = 26.8GPa$, as measured through Young's modulus testing (cylinder testing) in the lab. The details and results of the testing conducted are outlined further in Chapter 6, Section 6.3.3. The results of the unconfined and confined stress-strain model for the given concrete is shown in Figure 5.5a. The peak strength for the unconfined case is defined by the characteristic cube strength, $f'_c = 33MPa$, and the strain at peak stress was calculated to be $\epsilon_c = 0.002$;

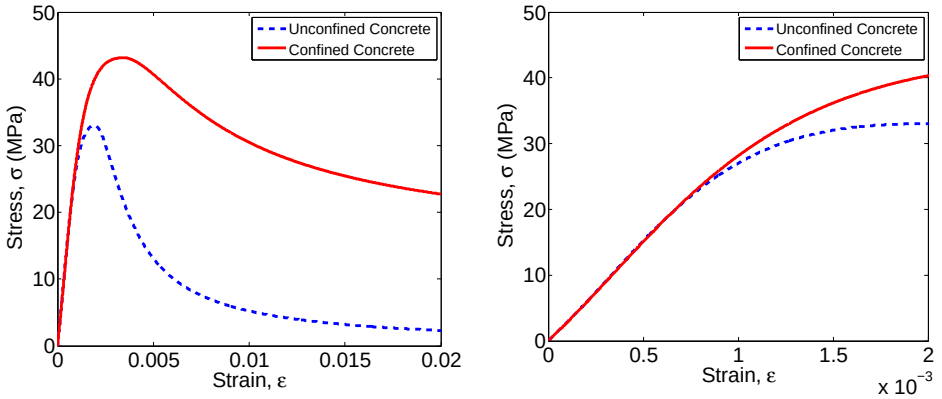

(a) (b)

Figure 5.5.: The stress-strain model for confined and unconfined concrete (Attard and Setunge, 1996), on different scales (a) and (b)

Figure 5.5 is in line with what was expected from Figure 5.4. It shows the axial stress as a function of strain, i.e. $\sigma(\epsilon)$. In accordance with Hooke's law, by computing the differential, the Young's Modulus of Elasticity, E is obtained, such that; $E = \frac{d\sigma}{d\epsilon}$. This enables the Young's Modulus of Elasticity to be expressed as both a function of stress and of strain, such that; $E(\sigma)$ and $E(\epsilon)$. Figure 5.7 shows the Young's Modulus as a function of stress, and indicates that for small initial increments in stress, the Young's Modulus of Elasticity increases up to a threshold value. This is intuitive, as the compression of the concrete matrix increases it's stiffness initially. Once

the concrete matrix had been fully compressed, no additional stiffness is to be gained, and a drop off in stiffness is subsequently observed. Figure 5.6 shows the Young's Modulus of the given concrete as a function of the axial strain in the concrete, $E(\epsilon)$ and Figure 5.7a shows the Young's Modulus as a function of the axial stress, $E(\sigma)$;

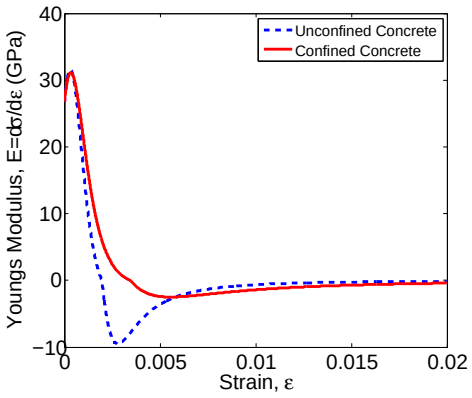

Figure 5.6.: Young's Modulus of Elasticity, E as a function of strain, ϵ, i.e. $E(\epsilon)$

There are two values of Young's Modulus defined at any given stress level, however, there is a unique value of Young's Modulus for a given strain. In the case of the testing conducted in the lab, the axial stress levels were very low and calculated based on the axial stress due to the applied post-tensioning load, i.e. $\sigma_n = N/A_u$ where N is the post-tensioning load level, i.e. $N = \{0, 20, 40, 60, 80, 100, 120, 140, 160, 180, 200\}kN$ and A_u is the equivalent cross sectional area of the concrete cross section, accounting for the presence of reinforcing steel, and making allowances for the cross sectional area lost due to the presence of the post-tensioning strand, internal to the cross section, such that $A_u = 31,918mm^2$. Consequently, the axial stress, $\sigma_n = \{0, 0.63, 1.25, 1.88, 2.51, 3.13, 3.76, 4.39, 5.01, 5.64, 6.27\}MPa$. It should be noted from Figures 5.6 and 5.7a that negative values for Young's Modulus are predicted at stresses and strains exceeding the ultimate strength/strain of the material. The concrete is deemed to have crushed at the ultimate strength and subsequently has no meaningful stiffness/load bearing capacity. The concept of negative stiffness is not accurate and is merely a symptom of the definition of Young's Modulus (i.e. the first derivative of stress as a function of strain). Since the stress-strain graph

displays negative slope for stress and strain greater than ultimate values, the theoretical value of Young's Modulus is negative. This is not deemed to be of any physical significance. The corresponding values of Young's Modulus for both the unconfined and confined cases are then interpolated from the Figure 5.7b, as shown.

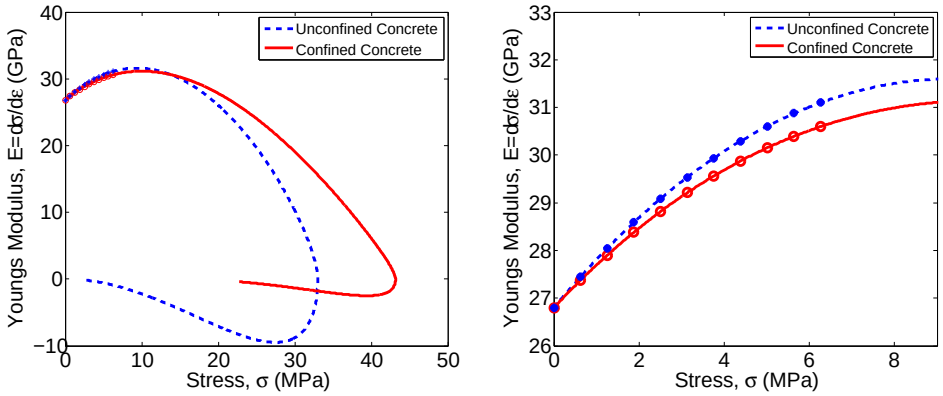

(a) (b)

Figure 5.7.: Young's Modulus of Elasticity, E as a function of stress, σ, on different scales (a) and (b) i.e. $E(\sigma)$

Table 5.1 shows the interpolated values of Young's Modulus based on the values of axial load, and subsequent axial normal stress, for both the confined and unconfined case, coupled with the predicted corresponding fundamental bending frequencies. These frequencies have been calculated by assuming all parameters remain constant, but varying the Young's Modulus with increasing post-tensioning load magnitude, as outlined in Equation 5.38;

$$\omega_n(N) = \left(\frac{n\pi}{\ell}\right)^2 \sqrt{\frac{E_c(N)I}{m}} \tag{5.38}$$

Whereas the predicted change in axial length of the beam sections (axial shortening) due to increasing post-tensioning load led to a minor change in fundamental bending frequency, in the range of +0.05% over the given range of post-tensioning force, the subsequent changes in fundamental bending frequency due to increasing Young's Modulus with increasing post-tensioning load magnitude are relatively much larger, predicted to be roughly +6/8% over the practical ranges of post-tensioning force tested, depending on whether

Table 5.1.: Interpolation of Young's Modulus from corresponding axial stress

N (kN)	σ_n (MPa)	E_{uc} (GPa)	E_c (GPa)	ω_{uc} (Hz)	ω_c (Hz)
0	0	26.8000	26.8000	74.9437	74.9437
20	0.6266	27.3747	27.4476	75.7429	75.8437
40	1.2532	27.9009	28.0434	76.4674	76.6624
60	1.8798	28.3810	28.5889	77.1225	77.4045
80	2.5064	28.8169	29.0856	77.7125	78.0740
100	3.1330	29.2107	29.5346	78.2417	78.6743
120	3.7596	29.2638	29.9372	78.7132	79.2086
140	4.3862	29.8780	30.2942	79.1303	79.6795
160	5.0128	30.1545	30.6066	79.4956	80.0893
180	5.6394	30.3946	30.8751	79.8115	80.4399
200	6.2661	30.5994	31.1006	80.0800	80.7331

the confined or unconfined case is taken into account, as shown in Figure 5.8.

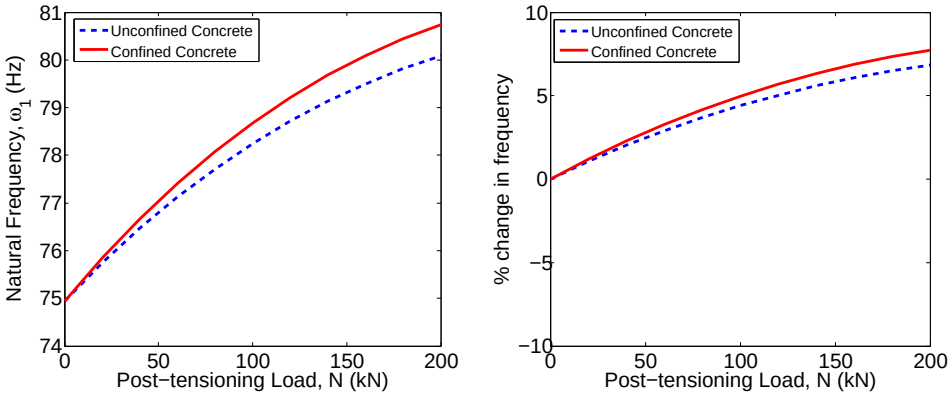

(a) (b)

Figure 5.8.: Change in ω_1 with N due to changes in E

5.4. Change in Second Moment of area with post-tensioning force, $I(N)$

The change in second moment of area of the cross section is modelled using two different models in this section. Firstly, the Binary Model is outlined

in Section 5.4.1, in which the second moment of area is taken as either the uncracked second moment of area, I_u, if the tensile stress in the bottom fibre of the beam is less than the cracking strength of the concrete, f_t, or the cracked second moment of area, if the tensile stress in the bottom fibre of the beam exceeds f_t. Secondly, the Williams and Falati (1999) (American Concrete Institute, 1989) model is used to model the changes in the second moment of area, as outlined previously in Section 2.5.3, and further in Section 5.4.3.

5.4.1. Binary Model

The change in second moment of area, I, with increasing post-tensioning force magnitude, N, has also been modelled, i.e. $I(N)$. The model is a binary type model. In this model, the stress level in the bottom fibre of the cross section is calculated. If the stress in the bottom fibre is greater than the tensile strength of the concrete, it is concluded that cracking must occur in the bottom fibre. If cracking occurs, the cracked second moment of area of the concrete cross section, I_c, should be used. If however, the stress in the bottom fibre of the cross section is less than the tensile strength of the concrete, the concrete cross section will remain uncracked and the uncracked second moment of area, I_u, is used. This is outlined in full in Equation 5.39;

$$I(N) = \begin{cases} I_u, & \sigma_b(N) \leq f_t \\ I_c, & \sigma_b(N) > f_t \end{cases} \tag{5.39}$$

where the stress level in the bottom fibre, σ_b, is a function of the post-tensioning load level, N, i.e. $\sigma_b(N)$, and f_t is the tensile strength of the concrete. The tensile strength, f_t, is calculated from the ACI method (ACI Committee 318, 2008; American Concrete Institute, 1989) outlined in Equation 5.25. Conservatively, a comparison is made with a concrete with a tensile strength of $0MPa$. Firstly, the maximum bending moment, at mid-span due to self weight of the simply-supported concrete specimens tested was calculated using Equation 5.40;

$$M_{x=\ell/2} = \frac{\omega_c \ell^2}{8} \tag{5.40}$$

where $M_{x=\ell/2}$ is the bending moment at mid-span due to the beam self-

weight, ω_c is the applied force per unit length due to the self weight of the post-tensioned concrete beams tested, and ℓ is the span length of the beam, i.e. the distance between the continuous supports. The bending stress at midspan due to the applied moment due to self-weight was then calculated using;

$$\sigma_{b,SW} = -\frac{M_{x=\ell/2} y_{max}}{I_u} \tag{5.41}$$

where $\sigma_{b,SW}$ is the bottom fibre stress due to beam self-weight, $y_{max} = h - x_u$, where $h = 200mm$ is the overall depth of the cross section and x_u is the uncracked neutral axis depth.

The moment due to the applied post-tensioning force was then calculated by multiplying the applied post-tensioning force, N, by the eccentricity, e, i.e. the moment due to post-tensioning force, $M_{PS} = N.e$. The eccentricity (i.e. the distance from the uncracked neutral axis to the centroid of the post-tensioning strand) that promoted cracking in the bottom fibre was defined to be negative, whereas the eccentricity that promoted an upward pre-camber of the beam was deemed to be positive. Hence, the moment due to the self-weight of the beam, by this sign convention, is deemed negative, as per Equation 5.41.

$$\sigma_{b,PS} = \pm\frac{M_{PS} y_{max}}{I_u} \tag{5.42}$$

The normal axial stress due to the applied post-tensioning force creates a compressive stress (positive) throughout the entire cross section and is given as;

$$\sigma_{b,n} = +\frac{N}{A_u} \tag{5.43}$$

The net stress on the bottom fibre is then calculated using Equation 5.44;

$$\sigma_b = \sigma_{b,n} + \sigma_{b,SW} + \sigma_{b,PS} \tag{5.44}$$

substituting Equations 5.41, 5.42, and 5.43 into Equation 5.44 gives the bottom fibre stress as a function of the post-tensioning load magnitude, N;

$$\begin{aligned}\sigma_b(N) &= \frac{N}{A_u} - \frac{M_{x=\ell/2} y_{max}}{I_u} \pm \frac{N e y_{max}}{I_u} \\ &= \frac{N}{A_u} - \frac{y_{max}}{I_u}\left(M_{x=\ell/2} \pm Ne\right) \\ &= \frac{N}{A_u} - \frac{1}{z_b}\left(M_{x=\ell/2} \pm Ne\right)\end{aligned} \tag{5.45}$$

where $z_b = I_u/y_{max}$ is the section modulus about the bottom fibre.

5.4.2. Effect of Binary Model on different beam sections

The binary relationship as outlined in Equation 5.39 is applied to all 9 post-tensioned concrete beams tested, obtaining predictions for the changes in second moment of area, I, with increasing post-tensioning force magnitude. All beams have a different post-tensioning strand eccentricity, e. Beam 1 has a post-tensioning strand eccentricity (e=0mm), Beams 2-5 have post-tensioning strand eccentricity that promote an upward pre-camber of the section and act as to introduce a net compressive stress in the bottom fibre. Beams 6-9 have the opposite effect. Their eccentricity is such that tensile stress and cracking is promoted in the bottom fibre of the section. Figure 5.9 shows the predicted changes in effective second moment of area, I_e, for Beam 1 (e=0mm) with increasing post-tensioning force magnitude, N, as per the conditions outlined in Equation 5.39 and Equation 5.45. The graph shows the effect with concrete of two different tensile strengths. The green dashed line shows the effect of concrete with a tensile strength of $f_t = -3.00MPa$, as given in Equation 5.25 in accordance with ACI code-based approaches (ACI Committee 318, 2008; American Concrete Institute, 1989), whereas the red solid line shows the effect of concrete with a tensile strength of $f_t = 0MPa$. In the case of the concrete with zero tensile strength, the effective second moment of area of the cross section jumps from the cracked value at zero post-tensioning force, $I_e = I_c$ at $N = 0$, to the uncracked value at a post-tensioning force of 20kN, $I_e = I_u$ at $N = 20kN$.

Figure 5.10 shows the predicted relationship between post-tensioning load magnitude, N, and effective second moment of area, I_e, for Beams 2-5, which have straight-profiled post-tensioning strand eccentricities of e=+13mm, +26mm, +39mm and +52mm respectively. The effect of the post-tensioning

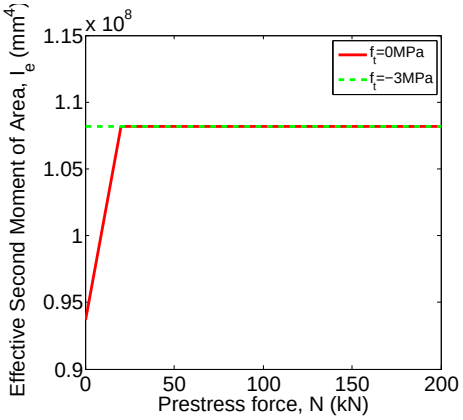

Figure 5.9.: Change in I with N for Beam 1 (e=0mm)

force is to promote compression in the bottom fibre, closing cracks and subsequently increasing the second moment of area from the cracked value, I_c, to the uncracked value, I_u.

Figure 5.11 shows the predicted relationship between post-tensioning load magnitude, N, and effective second moment of area, I_e for Beams 6-9, which have straight-profiled post-tensioning strand eccentricities of e=-13mm, -26mm, -39mm and -52mm respectively. The effect of the post-tensioning force is to promote cracking in the bottom fibre. As the post-tensioning force increases, the cracks on the bottom fibre open up, and as such, at high values of post-tensioning force and high values of negative post-tensioning strand eccentricity, the effective second moment of area is predicted to transition from the uncracked value ot the cracked value, as shown in Figure 5.11d.

Figures 5.12-5.14d show the effect of changing the effective second moment of area, I_e, with increasing post-tensioning force magnitude, N, i.e. $I(N)$, on the fundamental bending frequencies, ω_1, of the 9 post-tensioned concrete beams tested in the lab, while keeping all other variables constant, as per Equation 5.46;

$$\omega_n(N) = \left(\frac{n\pi}{\ell}\right)^2 \sqrt{\frac{EI(N)}{m}} \tag{5.46}$$

Figures 5.15-5.17d show the predicted percentage change in fundamental bending frequency, ω_1, with increasing post-tensioning force magnitude, N. The predicted percentage change is between -12% and +10% for Beam 6 (e=-13mm) and Beam 9 (e=-52mm) respectively. This is on par with the predicted percentage change due to changes in Young's Modulus with in-

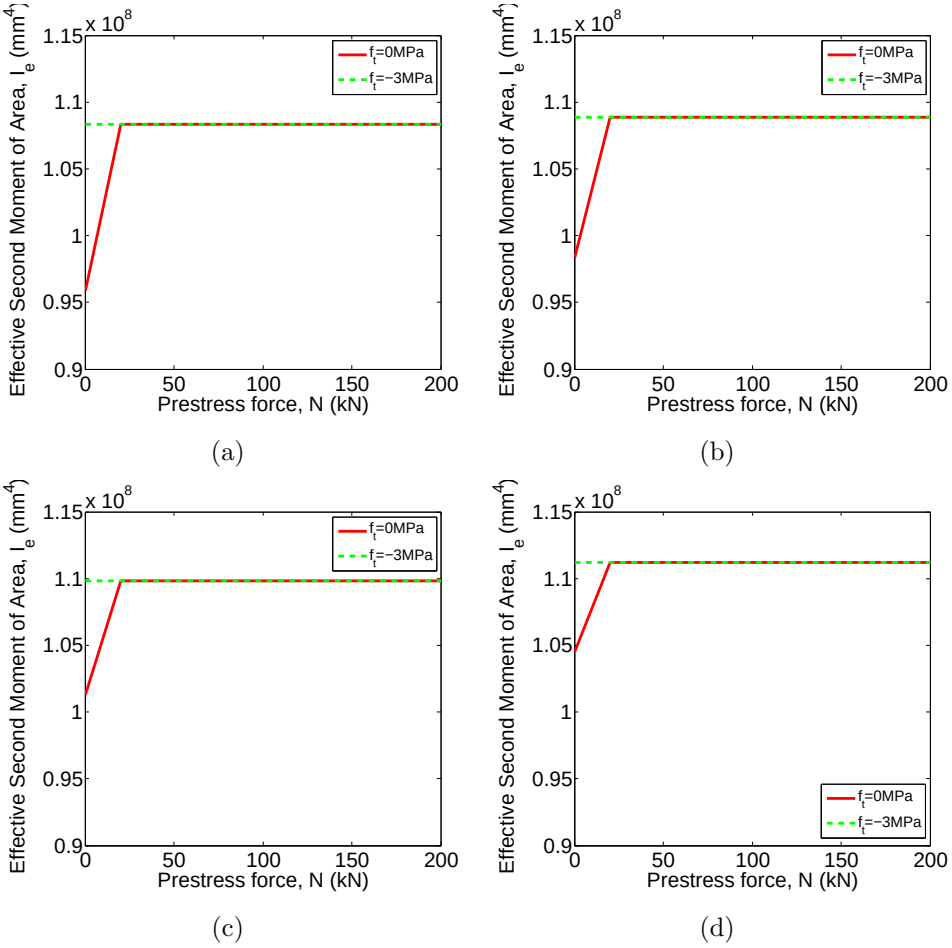

Figure 5.10.: Change in I with N for (a) Beam 2 (e=+13mm); (b) Beam 3 (e=+26mm); (c) Beam 4 (e=+39mm); (d) Beam 4 (e=+52mm)

creasing post-tensioning load magnitude, N, i.e. $E(N)$. This indicates that the effect of modelling changes in Young's Modulus, $E(N)$, is as important as modelling changes in second moment of area, $I(N)$, and that the changes in span length due to axial shortening, $\ell(N)$ are negligible in comparison.

5.4.3. Williams and Falati (1999) Model

Williams and Falati (1999) proposed a model for the variation in second moment of area of a specimen with differing applied moment. This is based on an ACI code based approach (American Concrete Institute, 1989), wherein

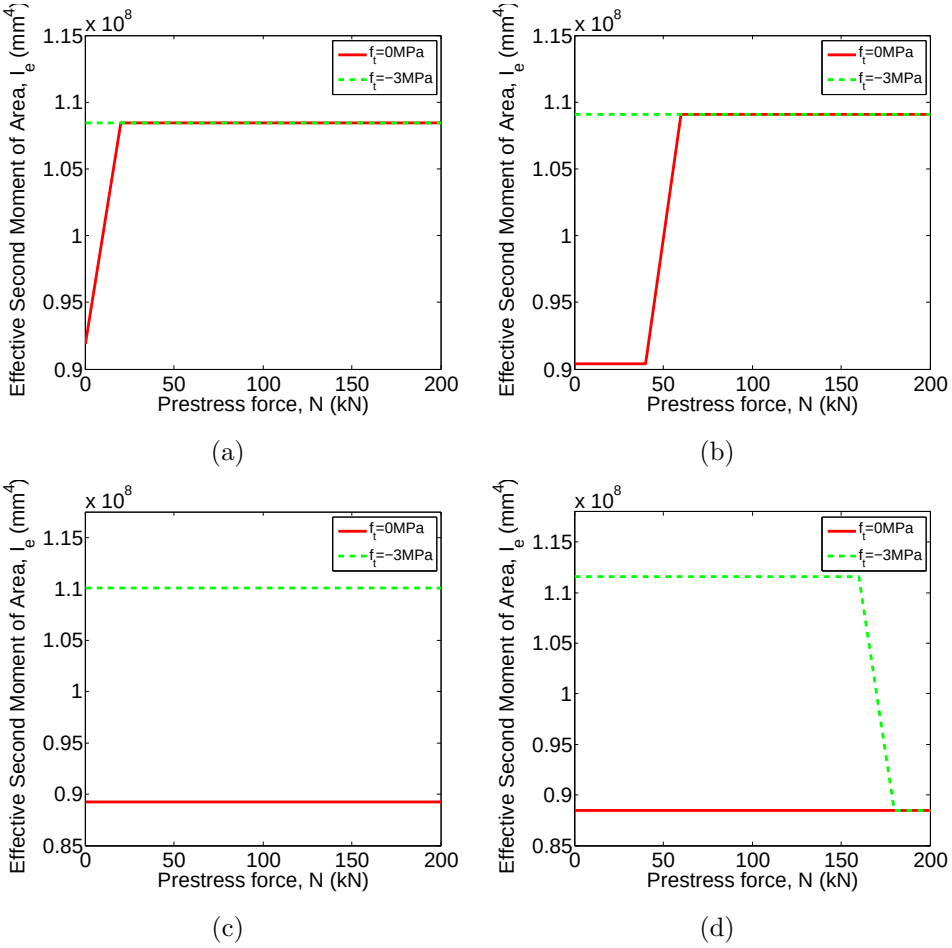

Figure 5.11.: Change in I with N for (a) Beam 6 (e=-13mm); (b) Beam 7 (e=-26mm); (c) Beam 8 (e=-39mm); (d) Beam 9 (e=-52mm)

the second moment of area is expressed as a function of the applied moment, M_a. This is compared to the cracking moment for the section, M_{cr}, and the second moment of area for the section is expressed as a weighted linear combination of the value of the uncracked second moment of area of the section, I_u, and the uncracked second moment of area of the section, I_c.

The model proposed by Williams and Falati (1999) (American Concrete Institute, 1989) is outlined in Section 2.5.3. Equation 5.47 outlines the calculation of the second moment of area as a function of the applied moment to the section in accordance with Williams and Falati (1999) and American

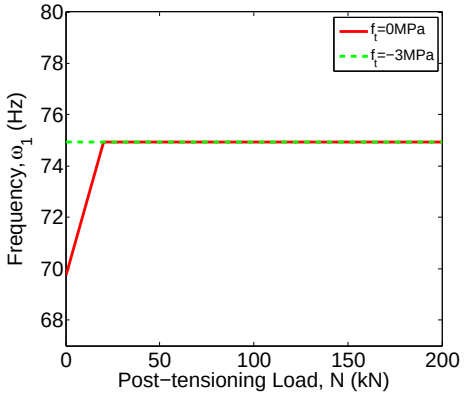

Figure 5.12.: Change in ω_1 with varying $I(N)$ for Beam 1 (e=0mm), while keeping all other parameters constant

Concrete Institute (1989).

$$I_e = \left(\frac{M_{cr}}{M_a}\right)^3 I_u + \left[1 - \left(\frac{M_{cr}}{M_a}\right)^3\right] I_{cr} \tag{5.47}$$

where M_a is the maximum gross moment and M_{cr} and the cracking moment. The level of cracking in the slab depends on the design tensile stress, f_t, where for a reinforced beam;

$$f_t = \frac{M_{cr} y_t}{I} \tag{5.48}$$

However, when prestressing is present, the stress is reduced to;

$$f_t = \frac{M_{cr} y_t}{I} - \frac{P}{A} - \frac{P e y_t}{y} \tag{5.49}$$

This indicates that increasing the prestressing force increases the magnitude of the cracking moment, or if the section is already cracked, has the effect of reducing the level of cracking. This leads to overall stiffening of the system and subsequent increase in the natural frequency. Including the self weight of the section, the applied moment for the uncracked beam sections at midspan is given as $M_a = \omega_{sw}\ell^2/8 - N.e$, where ω_{sw} is the applied uniformly disdributed load due to the beam self-weight, N is the applied prestress force, and e is the eccentricity of the post-tensioning strand from the neutral axis. This is outlined fully in Section 2.5.3, and is the basis of the calculation of the natural frequency as a function of the second moment

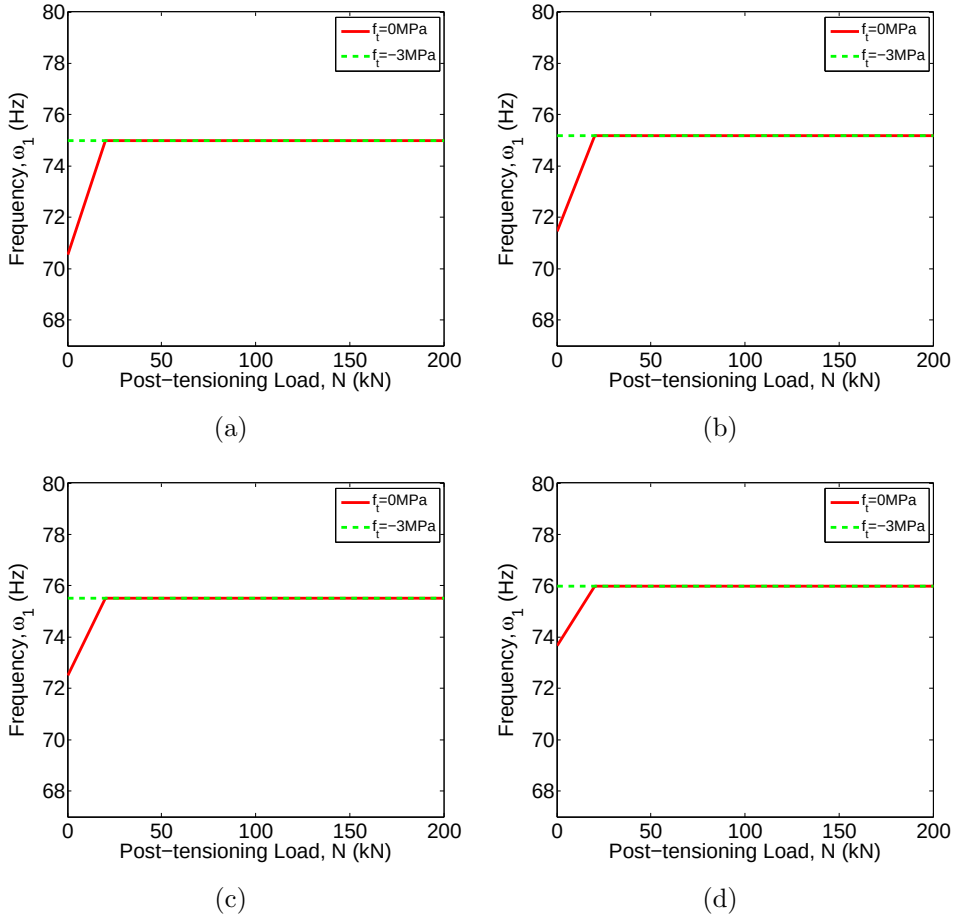

Figure 5.13.: Change in ω_1 with varying $I(N)$ for (a) Beam 2 (e=+13mm); (b) Beam 3 (e=+26mm); (c) Beam 3 (e=+39mm); (d) Beam 4 (e=+52mm), while keeping all other parameters constant

of area;

$$\omega_n(N) = \left(\frac{n\pi}{\ell(N)}\right)\sqrt{\frac{E(N)\,I_e(N)}{m(N)}} \tag{5.50}$$

where;

$$I_e(N) = \left(\frac{M_{cr}}{\omega_{sw}\ell^2/8 - N.e}\right)^3 I_u + \left[1 - \left(\frac{M_{cr}}{\omega_{sw}\ell^2/8 - N.e}\right)^3\right] I_{cr} \tag{5.51}$$

Figure 5.18 shows both the predicted variation of the second moment of

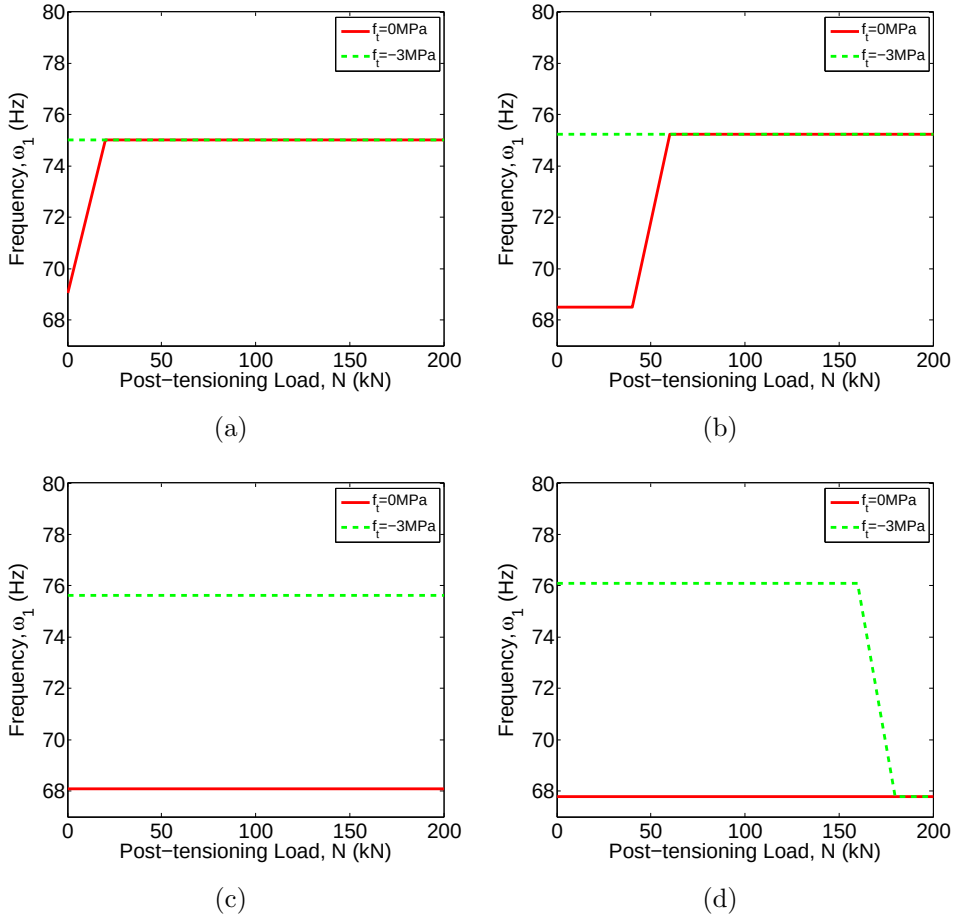

Figure 5.14.: Change in ω_1 with varying $I(N)$ for (a) Beam 6 (e=-13mm); (b) Beam 7 (e=-26mm); (c) Beam 8 (e=-39mm); (d) Beam 9 (e=-52mm), while keeping all other parameters constant

area, I with increasing post-tensioning force magnitude, N, in accordance with the Williams and Falati (1999) model (American Concrete Institute, 1989) (Figure 5.18a), and the subsequent predicted variation in the fundamental frequency, ω_1 (Hz), with increasing post-tensioning force magnitude, N (Figure 5.18b) for both confined and unconfined concrete case, in accordance with Section 5.3, for Beam 1 ($e = 0mm$). For Beam 1, the magnitude of the applied moment, M_a is small relative to the cracking moment, M_{cr}, for all values of post-tensioning force, as it is due to the self-weight of the beam only, since $e = 0$ and therefore $M_a = \omega_{sw}\ell^2/8 \forall N$. Consequently, the second moment of area remains as the uncracked value, I_u for all values

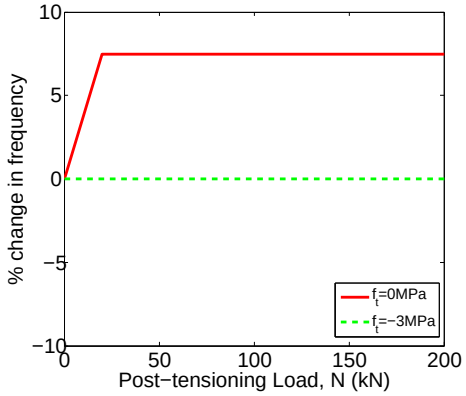

Figure 5.15.: Percentage change in ω_1 with varying $I(N)$ for Beam 1 (e=0mm), while keeping all other parameters constant

of post-tensioning force magnitude, and predicted changes in the natural frequency are due to predicted changes in the Young's Modulus $E(N)$, the mass per unit length $m(N)$, and the span length of the beam $\ell(N)$, as outlined in Sections 5.3, 5.5 and 5.2 respectively, such that;

$$\omega_n(N) = \left(\frac{n\pi}{\ell(N)}\right)\sqrt{\frac{E(N)\,I_u}{m(N)}} \tag{5.52}$$

Beams 2,3,6 and 7 follow the same pattern as Beam 1, in which the combination of post-tension force magnitude and eccentricity is not significant enough to make a substantial difference to the predicted second moment of area of the section, and the second moment of area remains unchanged as it's uncracked value, I_u, as with Beam 1, outlined above. Subsequently, the predicted changes in frequency are due to variation in Young's Modulus, mass per unit length, and span length of the beam only for Beams 1,2,3,6&7.

Figure 5.19 shows the variation in the predicted variation of the second moment of area, I with increasing post-tensioning force magnitude, N, in accordance with the Williams and Falati (1999) model (American Concrete Institute, 1989) (Figure 5.19a), and the subsequent predicted variation in the fundamental frequency, ω_1 (Hz), with increasing post-tensioning force magnitude, N (Figure 5.19b) for both confined and unconfined concrete case, in accordance with Section 5.3, for Beam 4 ($e = +39mm$). In this case, there is a predicted drop-off in the second moment of area for post-

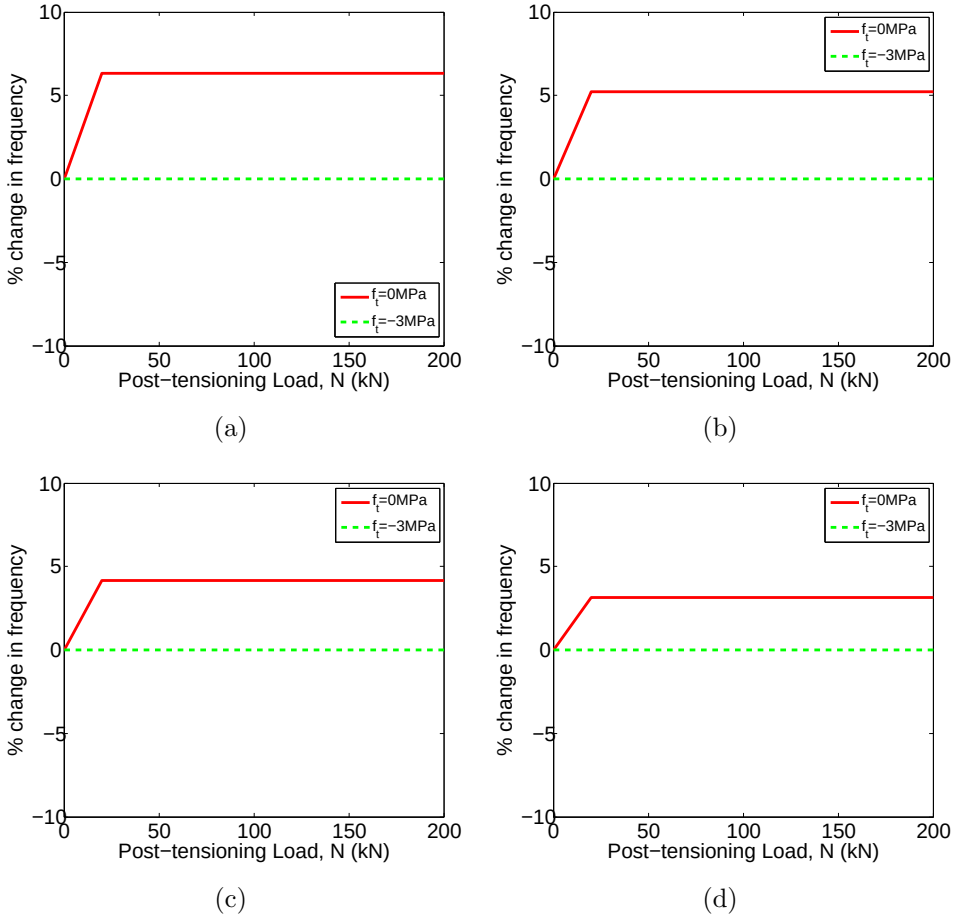

Figure 5.16.: Percentage change in ω_1 with varying $I(N)$ for (a) Beam 2 (e=+13mm); (b) Beam 3 (e=+26mm); (c) Beam 3 (e=+39mm); (d) Beam 4 (e=+52mm), while keeping all other parameters constant

tensioning force values greater than and equal to 800kN approximately. It should be noted that this value of post-tensioning load was not possible to obtain during testing with one 15.7mm diameter post-tensioning strand only as the strand is rated to a value of 280kN maximum. As a result, these values are practically unattainable. Furthermore, for the sections modelled and tested, the crushing strength of the concrete beam section is estimated to be 900kN. The second moment of area rapidly drops off from it's uncracked value, I_u, to it's cracked value, I_c, and causes the natural frequency to drop off further as a result.

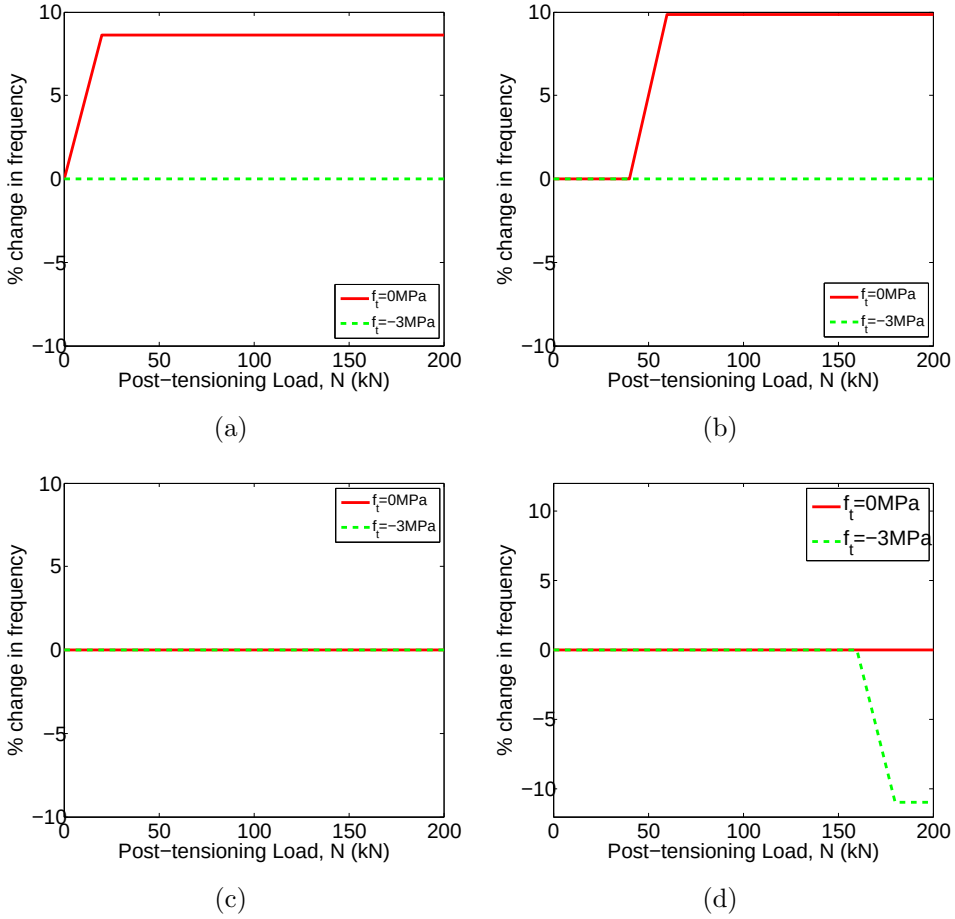

Figure 5.17.: Percentage change in ω_1 with varying $I(N)$ for (a) Beam 6 (e=-13mm); (b) Beam 7 (e=-26mm); (c) Beam 8 (e=-39mm); (d) Beam 9 (e=-52mm), while keeping all other parameters constant

Figure 5.20 shows the variation in the predicted variation of the second moment of area, I with increasing post-tensioning force magnitude, N, in accordance with the Williams and Falati (1999) model (American Concrete Institute, 1989) (Figure 5.20a), and the subsequent predicted variation in the fundamental frequency, ω_1 (Hz), with increasing post-tensioning force magnitude, N (Figure 5.20b) for both confined and unconfined concrete case, in accordance with Section 5.3, for Beam 5 ($e = +52mm$). In this instance, the drop off in second moment of area is predicted to occur at a much lower value of approximately 200kN, due to the combination of

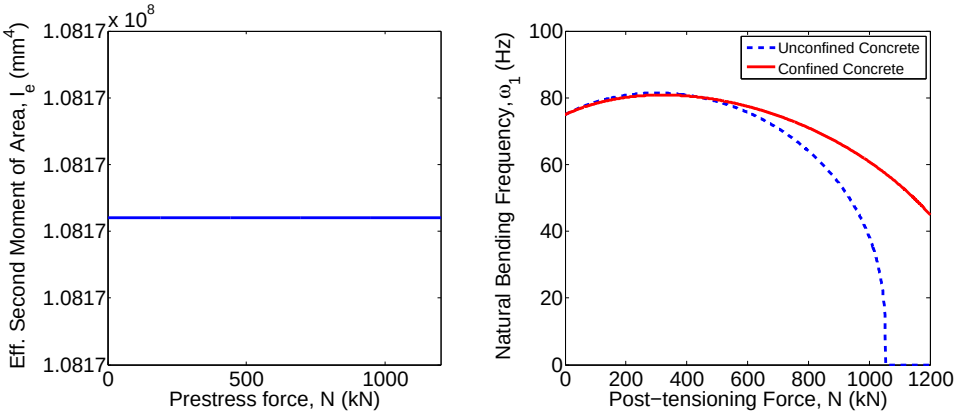

(a) (b)

Figure 5.18.: (a) Variation in I with N, for Beam 1, according to Williams and Falati (1999); (b) Subsequent variation in ω with N, for Beam 1, according to Williams and Falati (1999).

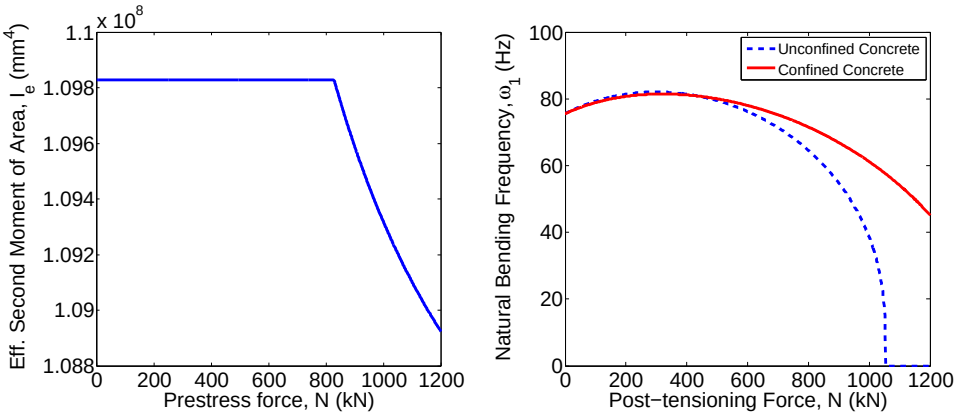

(a) (b)

Figure 5.19.: (a) Variation in I with N, for Beam 4, according to Williams and Falati (1999); (b) Subsequent variation in ω with N, for Beam 4, according to Williams and Falati (1999).

post-tensioning load magnitude and post-tensioning strand eccentricity.

Figure 5.21 shows the variation in the predicted variation of the second moment of area, I with increasing post-tensioning force magnitude, N, in accordance with the Williams and Falati (1999) model (American Concrete Institute, 1989) (Figure 5.21a), and the subsequent predicted variation in the fundamental frequency, ω_1 (Hz), with increasing post-tensioning force

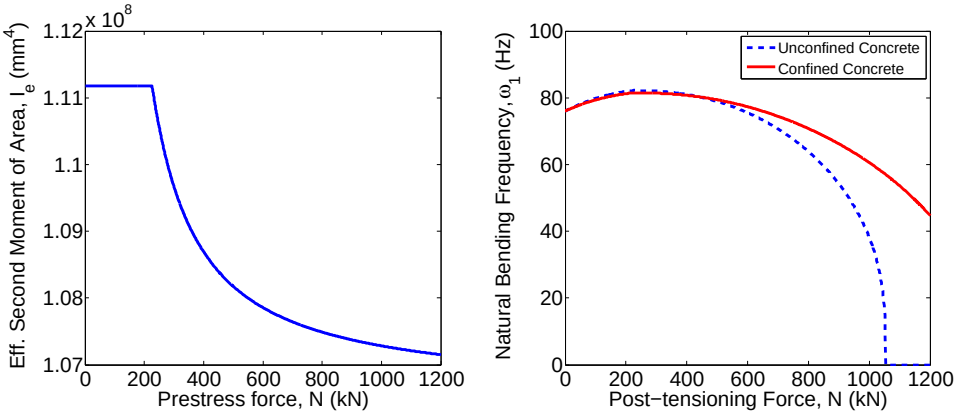

(a) (b)

Figure 5.20.: (a) Variation in I with N, for Beam 5, according to Williams and Falati (1999); (b) Subsequent variation in ω with N, for Beam 5, according to Williams and Falati (1999).

magnitude, N (Figure 5.21b) for both confined and unconfined concrete case, in accordance with Section 5.3, for Beam 8 ($e = -39mm$). For Beam 8, the eccentricity of the post-tensioning strand is such that it promotes cracking in the bottom fibre, and, as a result, there is a value of post-tensioning force at which the section cracks, and there is a corresponding immediate drop in the predicted second moment of area of the cross section. From this point onwards, the additional axial load helps to close cracks and move the second moment of area from I_c back towards I_u. This has similar implications for the bending frequency, where a clear sudden drop in bending frequency is predicted, at this can be seen in Figure 5.21b.

Figure 5.22 shows the variation in the predicted variation of the second moment of area, I with increasing post-tensioning force magnitude, N, in accordance with the Williams and Falati (1999) model (American Concrete Institute, 1989) (Figure 5.22a), and the subsequent predicted variation in the fundamental frequency, ω_1 (Hz), with increasing post-tensioning force magnitude, N (Figure 5.22b) for both confined and unconfined concrete case, in accordance with Section 5.3, for Beam 9 ($e = -52mm$). Similarly to Beam 8, the eccentricity of the post-tensioning strand is such that it promotes cracking in the bottom fibre, and, as a result, there is a value of post-tensioning force at which the section cracks, and there is a corresponding immediate drop in the predicted second moment of area of the cross

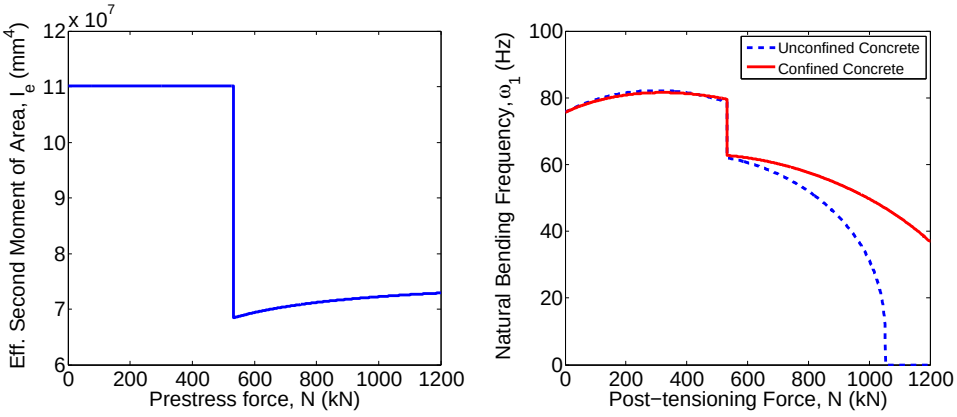

(a) (b)

Figure 5.21.: (a) Variation in I with N, for Beam 8, according to Williams and Falati (1999); (b) Subsequent variation in ω with N, for Beam 8, according to Williams and Falati (1999).

section. Since the eccentricity is greater in this case for Beam 9 than it is for Beam 8, the value of pos-tensioning force magnitude at which the sudden drop is predicted to be at approximately 180kN, as opposed to 550kN for Beam 8. interestingly, this is within the 0-200kN range tested on the concrete beams that is described in depth in Chapter 6.

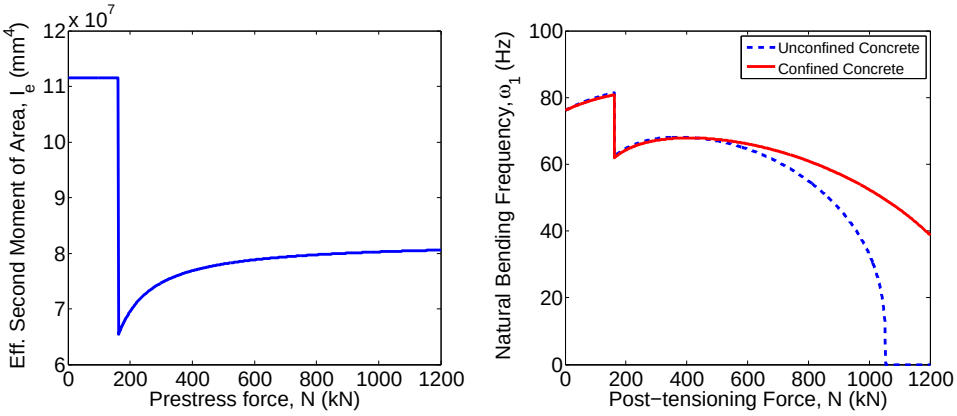

(a) (b)

Figure 5.22.: (a) Variation in I with N, for Beam 9, according to Williams and Falati (1999); (b) Subsequent variation in ω with N, for Beam 9, according to Williams and Falati (1999).

Section 5.4.4 compares the Binary Model described and outlined in Sec-

tion 5.4.1 to the Williams and Falati (1999) Model (American Concrete Institute, 1989), and the implications it has for the prediction of the fundamental frequency of the post-tensioned concrete beam sections.

5.4.4. Comparison of Binary Model with Williams and Falati (1999) Model

This section sets out to compare the Binary Model described and outlined in Section 5.4.1 to the Williams and Falati (1999) Model (American Concrete Institute, 1989) described in Section 5.4.3, and the implications each model has on the fundamental bending frequency of 9 different post-tensioned concrete beams, with differing post-tensioning strand eccentricities that are subsequently tested and described in full in Chapter 6.

No comparison can be drawn from comparing the models for Beams 1,2,3,6 or 7 as the post-tensioning strand eccentricity in each of these beams is not great enough to induce a moment great enough to cause the beam to crack, and therefore, no reduction in second moment of area is predicted for Beams 1,2,3,6 or 7. However, as outlined in Section 5.4.3, specifically in Figures 5.19, 5.20, 5.21 and 5.22, the post-tensioning strand eccentricity was great enough to induce a cracking moment in the section, and hence to predict a drop off in the second moment of area, from its uncracked value, I_u, towards its cracked value, I_c. These results are compared to the results obtained for the Binary Model outlined in Section 5.4.1 in Figures 5.23, 5.24, 5.25 and 5.26.

Figure 5.23a compares the variation in second moment of area, I, with varying post-tensioning force magnitude, N, for Beam 4 (e=+39mm) for both the binary model and the Williams and Falati (1999) model (American Concrete Institute, 1989). The Williams and Falati (1999) model predicts a slight drop off in I at post-tensioning load magnitudes of approximately 900kN, however, the binary model predicts that $I = I_u \forall N$. Figure 5.23b shows the subsequent predicted changes in fundamental frequency when either model is considered. It is clear from Figure 5.23b that the small differences in modelling I make little difference to the prediction of the fundamental frequency of the beam sections, albeit, the Williams and Falati (1999) model slightly under predicts the frequency relative to the Binary model in this case, for Beam 4.

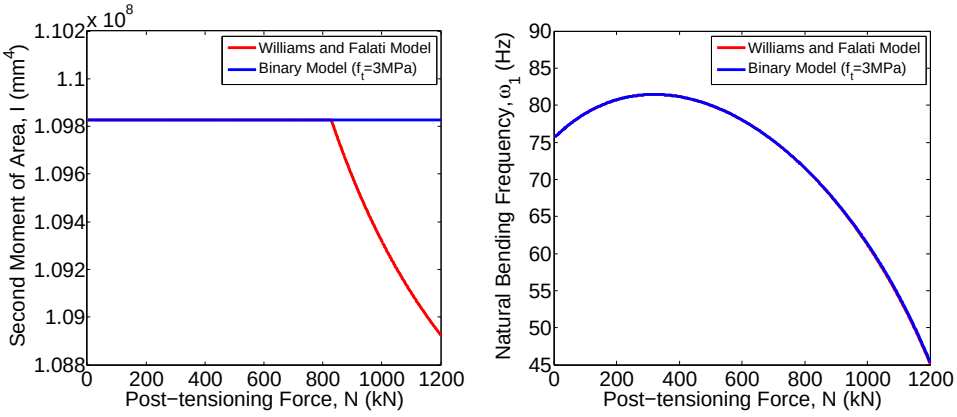

(a) (b)

Figure 5.23.: (a) Variation in I with N, for Beam 4, comparison of Binary Model to Williams and Falati (1999) Model; (b) Subsequent variation in ω with N, for Beam 4, comparison of Binary Model to Williams and Falati (1999).

Figure 5.24a compares the variation in second moment of area, I, with varying post-tensioning force magnitude, N, for Beam 5 (e=+52mm) for both the binary model and the Williams and Falati (1999) model (American Concrete Institute, 1989). In this case, for Beam 5, with a greater post-tensioning strand eccentricity, the Williams and Falati (1999) model predicts a drop off in I at a value of approximately 200kN, since the moment induced in the section is greater than the cracking moment of the section at values of post-tensioning force greater than 200kN. However, the binary model, as before indicates that $I = I_u \forall N$, since the net stress in the bottom fibre is compressive. In this case, there is a clear difference that each model has for the prediction of the fundamental frequency. It can be seen in Figure 5.24b that the Williams and Falati (1999) model again under predicts the frequency relative to the binary model, as was the case with Beam 4 previously. However, in this case, the discrepancy is much more obvious as the value of I is predicted to decrease by a much greater amount than with Beam 4.

Beam 4 and 5 have post-tensioning strand eccentricities that promote compression in the bottom fibre, and tension in the top fibre, however, Beams 8 and 9 have post-tensioning strand eccentricities that promote tension in the bottom fibre and compression in the top fibre. Since the binary

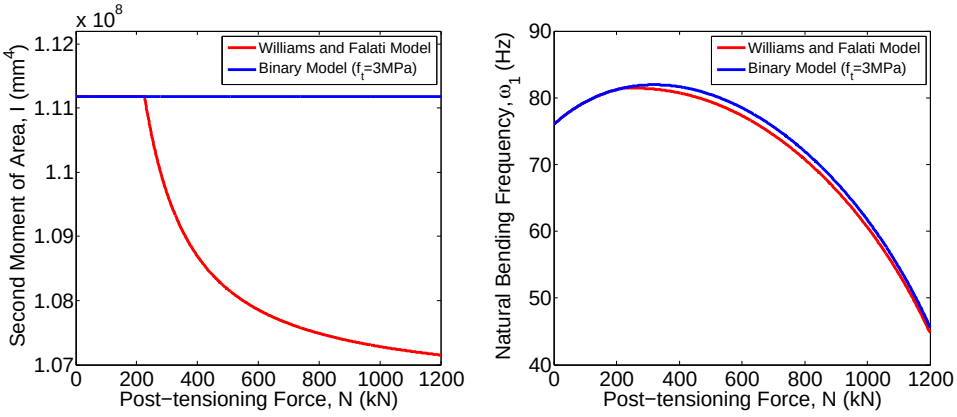

(a) (b)

Figure 5.24.: (a) Variation in I with N, for Beam 5, comparison of Binary Model to Williams and Falati (1999) Model; (b) Subsequent variation in ω with N, for Beam 5, comparison of Binary Model to Williams and Falati (1999).

model states that $I = I_u$ when σ_b (the stress in the bottom fibre) is greater than $-f_t$ (the tensile strength of the concrete), and $I = I_c$ when σ_b is less than $-f_t$, it indicates that a drop off in I is expected for large combinations of N and e (post-tensioning force magnitude and eccentricity). Figure 5.25 compares the variation in second moment of area, I, with varying post-tensioning force magnitude, N, for Beam 8 (e=-39mm) for both the binary model and the Williams and Falati (1999) model (American Concrete Institute, 1989). Figure 5.25 shows that for sections that promote tension in the bottom fibre, the Williams and Falati (1999) model grossly under predicts the value of I to be much less than the cracked second moment of area I_c. There is a sudden drop-off from the uncracked value, I_u, in the case of the binary model, to the cracked value, I_c, and in the case of the Williams and Falati (1999) model, a value much less than I_c. Subsequent post-tensioning load application acts as to close cracks and stiffen the structure, pushing the value of I back upwards towards the cracked design value of I_c. This has obvious implications for the prediction of the fundamental frequency, and indicates that, for Beam 8, the initial drop-off in frequency occurs at a lower value of post-tensioning force (approximately 500kN as opposed to 650kN in this case) and that again, also, the Williams and Falati (1999) model under predicts the frequency of the beam relative to the binary model, as

is the case with the previous beams that were studied.

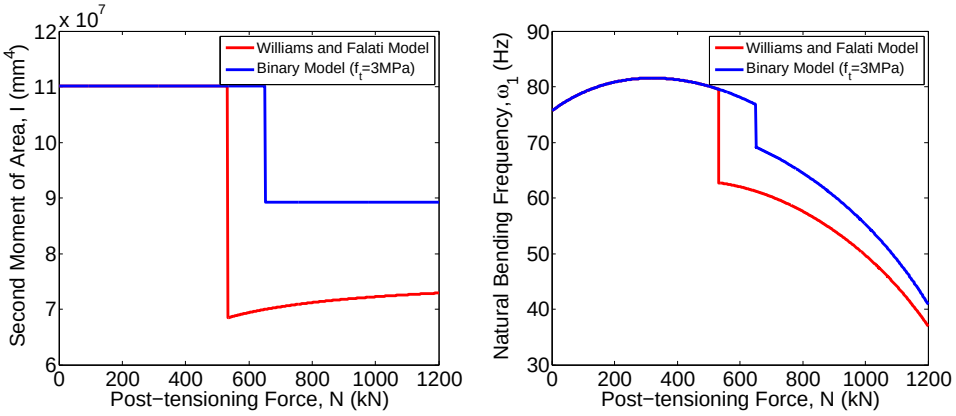

(a) (b)

Figure 5.25.: (a) Variation in I with N, for Beam 8, comparison of Binary Model to Williams and Falati (1999) Model; (b) Subsequent variation in ω with N, for Beam 8, comparison of Binary Model to Williams and Falati (1999).

Figure 5.26 compares the variation in second moment of area, I, with varying post-tensioning force magnitude, N, for Beam 9 (e=-52mm) for both the binary model and the Williams and Falati (1999) model (American Concrete Institute, 1989). As with Beam 8 (Figure 5.25), a sudden drop-off in I is predicted. In the case of Beam 9, this drop-off is predicted to occur at a similar post-tensioning load magnitude (approximately 180kN) in the case of the Williams and Falati (1999) model and the binary model. However, as observed with Beams 4,5 and 8 previously (Figures 5.23, 5.24, and 5.25), the Williams and Falati (1999) model under predicts the value of the second moment of area, I, relative to the binary model. As a result, the Williams and Falati (1999) model also under predicts the frequency of the beam section in comparison to the binary model. As with Beam 8, the value of I is theoretically predicted to fall below its carcked design value of I_c, and any further post-tensioning force added to the system from then on is predicted to close cracks and stiffen the beam (i.e. the post-tensioning force is predicted to initially soften the beam and any subsequent addition of post-tensioning load added after a threshold value is predicted to stiffen the beam), that is to say that the post-tensioning load is predicted to have the dual effect of both softening and subsequently stiffening the beam.

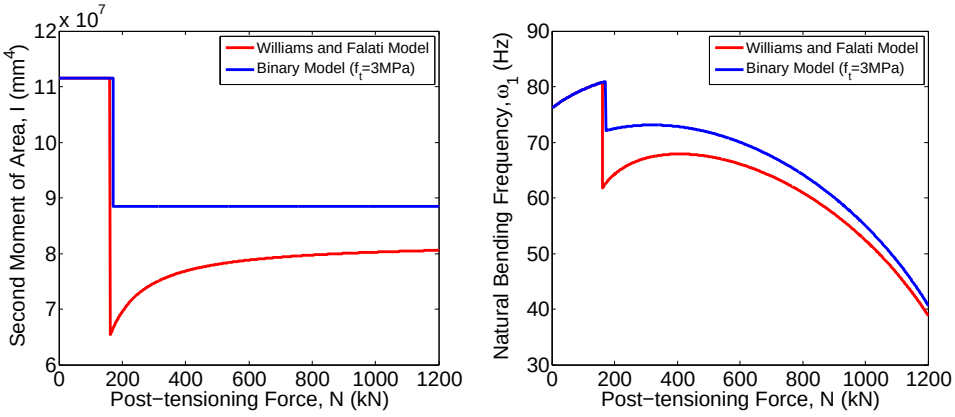

(a) (b)

Figure 5.26.: (a) Variation in I with N, for Beam 9, comparison of Binary Model to Williams and Falati (1999) Model; (b) Subsequent variation in ω with N, for Beam 9, comparison of Binary Model to Williams and Falati (1999).

In summary, the Williams and Falati (1999) model (American Concrete Institute, 1989) under predicts both the second moment of area, and as a result, the fundamental frequency of the beam sections when compared to the binary model, as outlined when comparing Beams 4,5,8&9 in Figures 5.23, 5.24, 5.25, and 5.26. The Williams and Falati (1999) model theoretically allows values of I that are less than I_c to be predicted, as outlined in Figures 5.25, and 5.26, which may be a downside of the model.

5.5. Change in mass per unit length with post-tensioning force, $m(N)$

The change in mass per unit length, m, with increasing post-tensioning force magnitude, N, of the post-tensioned concrete beam sections has also been modelled, i.e. $m(N)$, and the subsequent changes in natural bending frequency, ω_n have also been calculated, as per Equation 5.53;

$$\omega_n(N) = \left(\frac{n\pi}{\ell}\right)^2 \sqrt{\frac{EI}{m(N)}} \tag{5.53}$$

Firstly, the total mass of the post-tensioned concrete sections was calculated, by first calculating the mass of both the reinforced concrete and the post-tensioning steel as per Equation 5.54 and 5.55;

$$m_c = \frac{1000\rho_c\,(A_u)\,(1\times10^{-6})}{g} \tag{5.54}$$

$$m_{ps} = \rho_{ps}\,(A_{ps})\,(1\times10^{-6}) \tag{5.55}$$

where $\rho_c = 24kN/m^3$ is the weight density of concrete, A_u is the adjusted area of the reinforced concrete section, accounting for the presence of reinforcing steel. $\rho_{ps} = 7,810kg/m^3$ is the mass density of the prestressing steel used in the experimentation, and A_{ps} is the cross sectional area of the prestressing steel strand. The total mass of the steel and the concrete is then calculated as per Equation 5.56 and 5.57;

$$M_c = m_c\ell \tag{5.56}$$

$$M_{ps} = m_{ps}\ell \tag{5.57}$$

where $\ell = 2.0m$ is the original span length of the post-tensioned concrete section. The total mass of the post-tensioned concrete section was then calculated;

$$M_{tot} = M_c + M_{ps} \tag{5.58}$$

The mass per unit length of the section was calculated in accordance with the axial shortening model outlined in Equation 5.6, Section 5.2;

$$\begin{aligned} m(N) &= \frac{M_{tot}}{\ell(N)} \\ &= \frac{M_{tot}}{\ell\left(1-\frac{N}{A_cE_c}\right)} \end{aligned} \tag{5.59}$$

Figure 5.27 shows the effect of post-tensioning force magnitude on the mass per unit length of the section due to axial shortening effects. Since axial shortening causes the span length to decrease ever so slightly over the tested range, it follows that the mass per unit length of the cross section should increase, ever so slightly, as the mass of the section remains constant, but the denominator, the span length, $\ell(N)$, decreases as the post-tensioning force magnitude, N, increases.

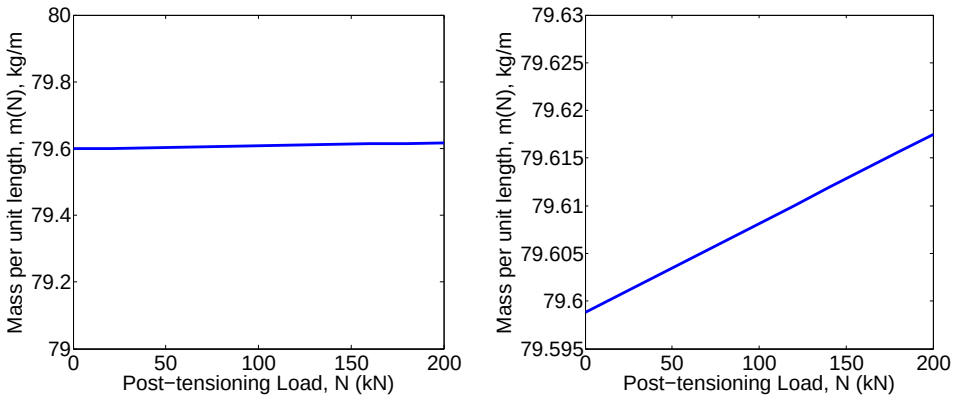

(a) (b)

Figure 5.27.: Change in m, with N due to axial shortening effects

Figure 5.28 shows the effect of the small changes in mass per unit length due to axial shortening effects, $m(N)$, on the fundamental bending frequency, ω_1, of the post-tensioned concrete beams tested in the lab. The mass per unit length of the sections increases with increasing post-tensioning force magnitude, due to axial shortening of the member. Since the mass per unit length, $m(N)$, is the denominator in Equation 5.53, this means that the natural bending frequency decreases with increasing post-tensioning force magnitude due to the subsequent change in mass per unit length.

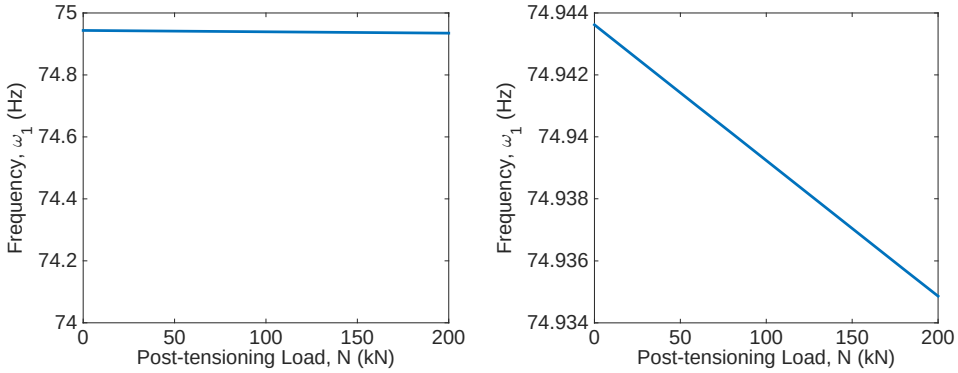

(a) (b)

Figure 5.28.: Change in ω_1 due to changes in $m(N)$ only

Figure 5.29 shows the percentage change in natural frequency due to the corresponding changes in mass per unit length with increasing post-

tensioning force magnitude. The changes are negligible over the practical ranges of post-tensioning force modelled, in the range of -0.0125%, as shown in Figure 5.29. These changes are negligible in comparison to the changes induced by altering the second moment of area of the cross section, $I(N)$, and the Young's Modulus, $E(N)$.

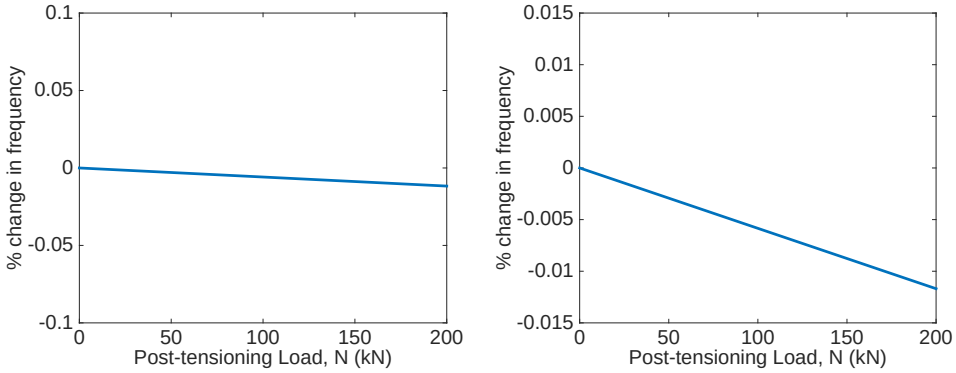

(a) (b)

Figure 5.29.: Percentage change in ω_1 due to changes in $m(N)$ only

5.6. Sensitivity analysis on the parameters

The following section reports on the results of a sensitivity analysis on the modelled parameters, $E(N)$, $I(N)$, $\ell(N)$, and $m(N)$, comparing the effect of changes in each of the parameters modelled on the fundamental bending frequencies, ω_1, of the post-tensioned concrete beams. Figure 5.30 shows the predicted percentage change in natural bending frequencies with increasing post-tensioning force magnitude, due to changes in the individual parameters, $I(N)$, $E(N)$, $\ell(N)$, and $m(N)$, for the 9 different post-tensioned concrete beams modelled and tested in the lab. What is clear from the graphs, is that the effect of changes in frequency due to axial shortening, $\ell(N)$, and due to changes in mass per unit length, $m(N)$, are negligible compared to the changes in second moment of area, $I(N)$, and changes in Young's Modulus, $E(N)$. In the extreme examples, changes due to second moment of area, $I(N)$, account for changes in fundamental frequency between -12% and +10%, and the changes in Young's Modulus, $E(N)$, account for changes of up to +8% in fundamental bending frequency. The changes in frequency due to axial shortening and change in mass per unit length are negligible

in comparison. Changes in Young's Modulus and second moment of area with increasing post-tensioning force magnitude dominate the subsequent changes in fundamental bending frequency.

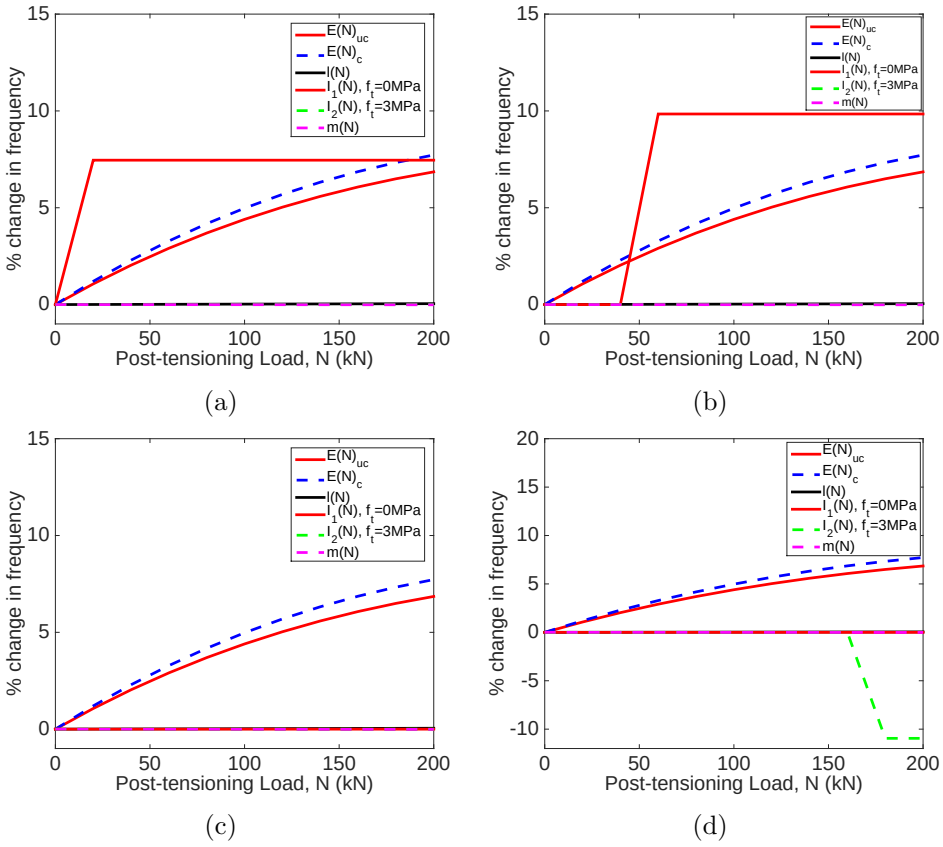

Figure 5.30.: Sensitivity study; % change in ω_1 due to changes in individual parameters $I(N)$, $E(N)$, $\ell(N)$, and $m(N)$ for (a) Beam 1; (b) Beam 7; (c) Beam 8; (d) Beam 9

5.7. Prediction of changes in fundamental frequency with increasing post-tensioning force, $\omega_1(N)$

Figure 5.31 shows the prediction of the change in natural bending frequency for Beam 1 (e=0mm) and Beam 9 (e=-52mm) based on the proposed model outlined in Sections 5.1 to 5.6. The model predicts changes in the range of +8% to -5% as shown in Figure 5.33. The model is based on modelling linear

changes in the parameters outlined in Sections 5.2 to 5.5, in accordance with Equation 5.1. Figures 5.31a and 5.31b show the predicted model for concrete with different assumed tensile strengths. The concrete with a tensile strength, $f_t = 0MPa$ is represented by the solid red line, whereas the concrete with a tensile strength of $f_t = 3.00MPa$ is represented by the dashed green line. For Beam 1 (e=0mm), an overall increasing trend in fundamental bending frequency with increasing post-tensioning load magnitude is predicted. For the case of the concrete with a tensile strength of $f_t = 0MPa$, there is a jump in the predicted frequencies at a post-tensioning load value of 20kN as the concrete is deemed to have moved from a cracked to an uncracked condition, therefore the second moment of area moves from the cracked to the uncracked value, i.e. I_c to I_u. Conversely, in the case of the concrete with a tensile strength of $f_t = 3.00MPa$, no such jump is predicted as the second moment of area is deemed constant at the uncracked value, I_u, for all values of post-tensioning load, N. For Beam 9 (e=-52mm), the eccentricity of the post-tensioning strand is such that it promotes cracking in the bottom fibre. Consequently, for the case of concrete with a tensile strength of $f_t = 3.00MPa$, at high values of post-tensioning load magnitude, N, a sudden decrease in second moment of area is predicted as it jumps from the uncracked value, I_u down to the cracked value, I_c due to the tensile stress in the bottom fibre exceeding f_t. Despite an initial predicted increase in fundamental frequency, ω_1, with increasing post-tensioning force, N, there is an overall decreasing trend in the prediction over the modelled range of post-tensioning force, due to this decrease in I.

It should also be pointed out, that for greater values of post-tensioning force, the Young's Modulus is predicted to decrease significantly with increasing axial normal stress, after reaching a maximum value, therefore, as crushing of the concrete occurs, the stiffness is predicted to decrease significantly, and the natural frequency is also predicted to decrease as a result, over a greater range of post-tensioning force than tested and originally modelled. This is illustrated in Figure 5.32. Figure 5.32a shows the predicted fundamental frequency, ω_1, with increasing post-tensioning load magnitude, N, for both the confined and unconfined concrete case. As shown, the predicted frequency drops to zero for the unconfined concrete at a post-tensioning load value of approximately 1100kN. This is due to the predicted decrease in Young's Modulus for high values of axial stress, as

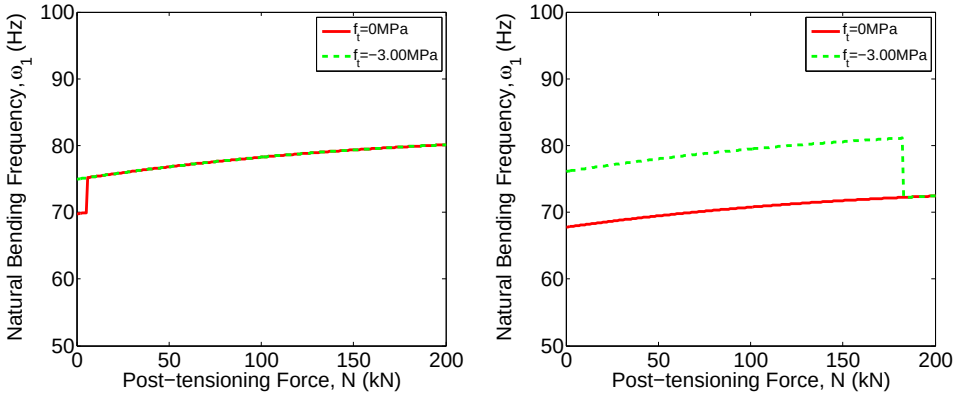

(a) (b)

Figure 5.31.: Prediction of the change in ω_1 with increasing N for the proposed model, for (a) Beam 1 (e=0mm); (b) Beam 2 (e=-52mm)

outlined in Figure 5.7a. Figure 5.32b shows the predicted change in frequency for the case of unconfined concrete, with different concrete tensile strengths, as outlined previously.

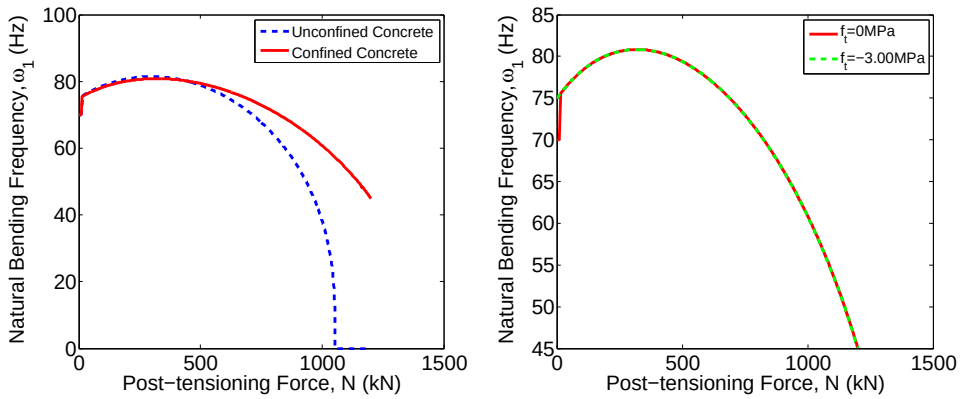

(a) (b)

Figure 5.32.: Predicted variation in ω_1 with increasing N over greater post-tensioning force range for (a) unconfined vs. confined concrete; (b) confined concrete with different tensile strength, $f_t = 0MPa$, $f_t = 3.00MPa$

This model will be compared to obtained results for the beams tested, and outlined further in Chapter 6, Section 6.8.6.

5.8. Comparison of proposed model with existing models

The proposed model is compared with the predicted changes from the models proposed by Saiidi et al. (1994), Zhang et al. (2012), Dall'Asta and Dezi (1996), Miyamoto et al. (2000) and Kim et al. (2004). The proposed model, by changing each of the parameters, $E(N)$, $I(N)$, $\ell(N)$ and $m(N)$, predicts a percentage change in the region of +8% for the modelled range of post-tensioning force (0-200kN). This predicted change is greater than predicted by the models suggested by other authors (Saiidi et al., 1994; Zhang et al., 2012; Dall'Asta and Dezi, 1996; Miyamoto et al., 2000; Kim et al., 2004). The model will be compared to obtained results for the beams tested, and outlined in Chapter 6, Section 6.8.6. It will be shown that there is good agreement between the proposed model and the obtained results, however, due to the absence of a statistical significant relationship between post-tensioning force magnitude and fundamental bending frequency, the paper written by Hamed and Frostig (2006) suggesting, due to second order non-linear effects that there is no relationship between post-tensioning force magnitude and fundamental frequency is deemed to be the most accurate. Furthermore, Peeters and De Roeck (2001) point out that frequency differences in the range of 14-18% are reported due to normal environmental changes such as temperature changes, lack of ideal support conditions, material variability etc. The changes in fundamental frequency predicted by the cited models is therefore considered negligible in relation to these large environmental effects.

To recap from Chapter 2, in order to facilitate a comparison of the above models, Saiidi et al. (1994) present an empirical model predicting changes in fundamental frequency with increasing post-tensioning force magnitude. The effective flexural rigidity of the tested specimens was back-calculated from the results of impact hammer testing on post-tensioned concrete beam sections (Equation 2.68). Subsequently, a first order regression prediction model was fitted to the obtained data, resulting in a dimensionally inconsistent prediction of the flexural rigidity of each specimen and varying values of post-tensioning force (Equation 2.69). The corresponding natural frequencies are subsequently calculated from the effective flexural rigidity. Note that the beam specimen this model was based on was reported by

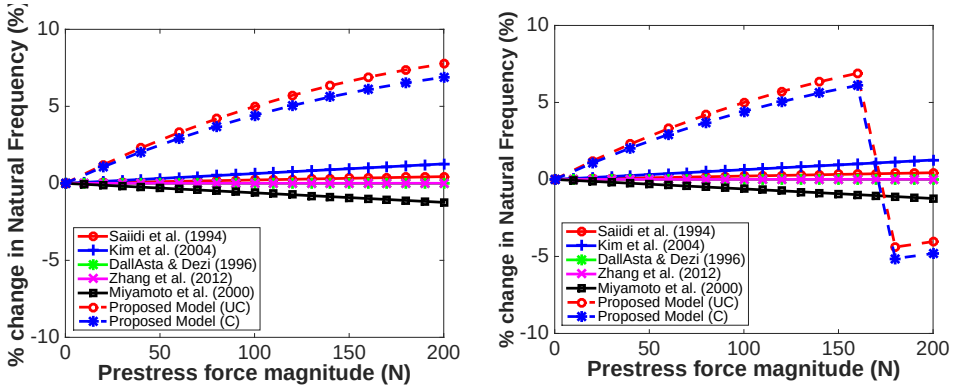

Figure 5.33.: Proposed model vs. existing models (Saiidi et al., 1994; Kim et al., 2004; Miyamoto et al., 2000; Zhang et al., 2012; Dall'Asta and Dezi, 1996), for (a) Beam 1 (e=0mm); (b) Beam 2 (e=-52mm)

the authors to have a crack at midspan. The authors attributed all observed changes in frequency to the closure of micro-cracks present in the concrete, and not to the crack that formed under self weight while lifting the specimens.

Miyamoto et al. (2000) present a model based upon *"compression softening"* theory, in which provisions are included in the model for the geometric effects of the eccentricity of the post-tensioning tendon. This model is based on the assumption that an external axial load is equivalent to a post-tensioning load. The final equation of motion is derived from first principles based on Kirchoff's linear kinematic relations, and is valid only for small displacements. As outlined in Chapter 4, a post-tensioning force should not be treated as equivalent to an external axial load (Noble et al., 2015a). As a result, this model is not considered to be suitably applicable to post-tensioned concrete sections.

Zhang et al. (2012) suggest another empirically based model exploring changes in Young's Modulus as a function of changes in post-tensioning force magnitude. However, the changes in Young's Modulus were again determined from back calculating in a similar manner to Saiidi et al. (1994), however, the authors state that since the specimens remained uncracked throughout the course of testing, the observed increases in frequency were due to changes in Young's Modulus only. The regression model derived from

the testing conducted is also dimensionally inconsistent (Equation 2.71) and therefore the model is deemed unsuitable for use.

Kim et al. (2004) produce a "tension-strength" model in which the flexural vibration frequency of a cable under tension is considered to be equal to the vibration frequency of a beam with the same cross sectional properties as the cable. Equating, this leads to the expression of the flexural rigidity of the steel prestressing cable as a function of the post-tensioning force, in direct contrast with *"compression-softening"* theory, the force is now considered as an equal, but opposite stiffening effect. This stiffening effect is added to the flexural rigidity of the concrete beam specimen and an increase in natural frequency with increasing prestressing force is subsequently predicted. The model produced by Kim et al. (2004) is the opposite to the compression softening model and the interaction of the stiffening effect with a softening effect on the beam section (as conducted by Dall'Asta and Dezi (1996)) is ignored.

Dall'Asta and Dezi (1996) derive the final equation of motion from first principles using Kirchoff's linear kinematic relations. The effect of the prestressing according to the authors acts as a combination of softening of the beam section under compressive load and stiffening of the post-tensioning strand due to tensile load. The authors however consider the second moment of area of the cable to be negligible in all practical cases, and also consider the N/A_b term to be negligible also, and subsequently consider that the post-tensioning force has little or no effect on natural frequency (Equations 2.76, 2.77).

Hamed and Frostig (2006) present a non-linear kinematic model. The final equation of motion of the vibrating pre- and post-tensioned concrete beams are found to be independent of pre- and post-tensioning force magnitude. The non-linear mathematical model allows for large displacements and moderate rotations as opposed to the small displacements of Kirchoff's linear kinematic relations (Sections 2.10).

The model proposed in this Chapter does not return to the theoretical derivation of the final equations of motion as these have been covered ad nauseum by previous authors (Tse et al., 1978; Miyamoto et al., 2000; Dall'Asta and Dezi, 1996; Hamed and Frostig, 2006). The proposed model instead considers the derivation of the natural frequency of a simply supported Euler-Bernoulli beam and predicts the changes in each of the pa-

rameters affecting natural frequency, as a function of post-tensioning force (Equation 5.1). The eccentricity of the post-tensioning force is accounted for in the calculation of the transformed second moment of area of the cross section as a function of post-tensioning force (Section 5.4). The jump from cracked value of second moment of area (I_c) to the uncracked value of second moment of area (I_u) is also accounted for and these are two big strengths of the proposed model. Another important strength of the proposed model is that it accounts for changes in Young's Modulus as a function of post-tensioning force in accordance with the empirical model derived by Attard and Setunge (1996). One of the most encouraging properties of this model is that it allows for the predicted drop-off in frequencies after the crushing strength of the concrete has been reached, as per Figure 5.32. Another strength of the model includes the provision of the reduction in the prediction of frequency with post-tensioning force if the strand profile and post-tensioning force magnitude is such that it causes flexural cracking to occur in the cross-section, as evident in Figure 5.33b. The final main strength of the model is that it is a simple mathematical model that can be easily implemented for more complex, real world post-tensioned structural systems, and is not restricted to simply-supported post-tensioned concrete beams, as some of the other derived mathematical models are. The main weakness of the proposed model is the suitability of the empirically based Attard and Setunge (1996) model is yet to be determined for an application such as post-tensioning. Furthermore, the Attard and Setunge (1996) does make use of regression prediction modelling in some areas, as outlined in Section 5.3, and in some cases the models are also not dimensionally consistent, as with some of the other models presented. The proposed model also predicts changes in frequency that are much larger than the changes predicted by existing models.

Ultimately, the model presented and suggested by Hamed and Frostig (2006) seems to be the most appropriate for use in the case of the uncracked concrete beam sections, especially when comparison is made with the results of testing conducted in Chapter 6. This model is the most mathematically robust and accounts for the inclusion of large displacements and moderate rotations.

5.9. Finite Element Modelling

Finite Element Modelling was conducted in Autodesk ROBOT Structural Analysis Professional 2012 - Student Evaluation Version (2012) to predict the natural bending frequencies of the post-tensioned concrete beams tested. There is no provision for modelling post-tensioning accurately in the software, and subsequently it was used to predict the *'virgin'* fundamental bending frequency (i.e. the fundamental frequency for zero post-tensioning load). The effect of the strand on the beam cross section was neglected. FE software such as Autodesk ROBOT Structural Analysis Professional 2012 - Student Evaluation Version (2012) treats a post-tensioning load as equivalent to an external axial load and therefore uses *"compression-softening"* theory as the basis for the FE Modelling. Since this is deemed inappropriate and erroneous for post-tensioned structures (Noble et al., 2015a), this highlights the unsuitability of many commercial software packages to tackle such a problem, and highlights the need for a viable mathematical model that can accurately predict changes in fundamental frequency with changing post-tensioning force. As such, the purpose of this FE modelling was to check the closed form solution against the FE Model prediction for increasing degree of freedom (DOF) simply supported concrete beam systems.

Table 5.2 shows the results of FE modelling on the modal analysis of a reinforced concrete beam with similar properties to the post-tensioned concrete beams tested in the lab. The depth, $d = 200mm$, the breadth, $b = 150mm$, and the Young's Modulus, $E_c = 28.6GPa$. Figure 5.34 shows the lumped mass FE model applied to the reinforced concrete beam section. Figure 5.34a shows the geometric properties of the beam modelled, Figure 5.34b shows a representation of the first bending 3 mode shapes of vibration, Figure 5.34c shows the lumped mass model for representing the beam as a single degree of freedom (SDOF) system, Figure 5.34d shows the lumped mass model for the 10 degree of freedom representation of the beam system. Figure 5.35 shows the results of the FE modelling and modal analysis for both the SDOF system and the 10 DOF system.

Table 5.2 compares the results of the FE estimation of the fundamental bending frequency for the reinforced concrete beam sections to the closed form solution. There is good agreement between the FE modelling conducted and the closed form solution, with the percentage difference varying

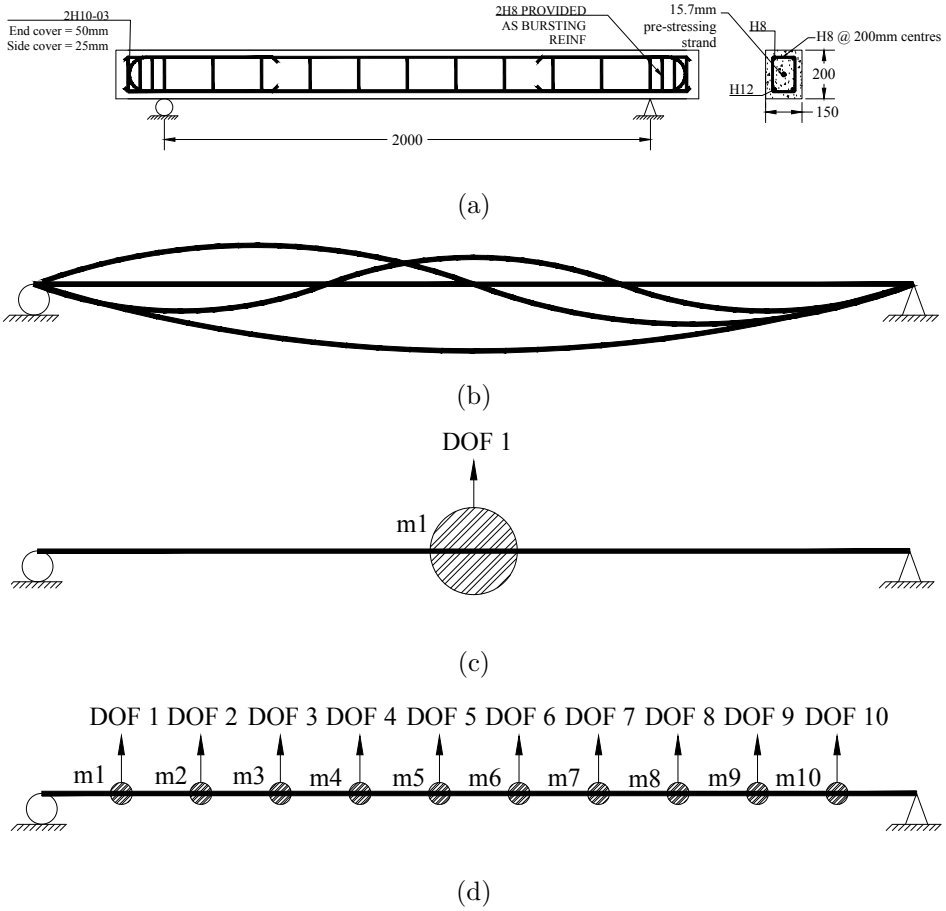

Figure 5.34.: (a) Geometric properties of the reinforced concrete beams tested; (b) Representation of the first 3 bending mode shapes of vibration; (c) Single degree of freedom (SDOF) representation of beam system; (d) 10 DOF representation of beam system

between -0.68% and +0.04% from the closed form solution. Figure 5.36 illustrates the convergence of the FE solution as the number of degrees of freedom is increased.

5.10. Conclusions

In this chapter the results of mathematical modelling in MATLAB to model the effect of prestress force, N, on the natural frequencies of prestressed concrete structures, ω_n was outlined. A linear model was presented by tracking

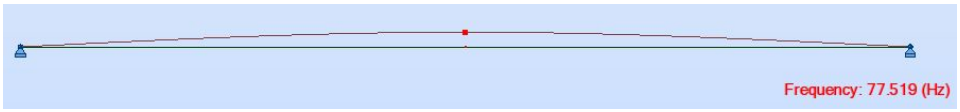

(a)

(b)

Figure 5.35.: Results of the FE modelling - estimation of the fundamental bending frequency for (a) 1 dof (b) 10 dof

Table 5.2.: Predictions of fundamental frequencies for RC Beam - FE Model

Type	$\omega_{1,c}(Hz)$	% Diff.
Closed Form Solution	78.05	0
FE Model (1 DOF)	77.519	-0.68
FE Model (2 DOF)	78.002	-0.06
FE Model (3 DOF)	78.062	+0.02
FE Model (4 DOF)	78.076	+0.03
FE Model (5 DOF)	78.081	+0.04
FE Model (6 DOF)	78.083	+0.04
FE Model (7 DOF)	78.084	+0.04
FE Model (8 DOF)	78.085	+0.04
FE Model (9 DOF)	78.085	+0.04
FE Model (10 DOF)	78.085	+0.04

changes in each of the parameters outlined in Equation 5.1 with increasing post-tensioning force magnitude. Changes in span length, $\ell(N)$, Young's Modulus, $E(N)$, second moment of area, $I(N)$, and mass per unit length, $m(N)$, was modelled. A sensitivity analysis on the effect of changing the above parameters, highlighting the relative importance of the changes in each individual parameter was outlined. The predicted changes in fundamental frequency with increasing post-tensioning load magnitude for the 9 Beams tested was detailed. The changes predicted by the new proposed model was compared with the models previously proposed by Saiidi et al. (1994), Zhang et al. (2012), Dall'Asta and Dezi (1996), Miyamoto et al. (2000) and Kim et al. (2004). Finite Element Modelling was conducted to predict the *'virgin'* fundamental bending frequency of the beams tested.

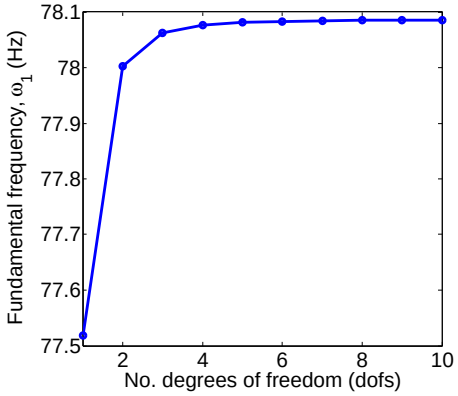

Figure 5.36.: Convergence of the estimation of fundamental bending frequency through FE modelling by increasing no. dofs

It was found that;

1. The proposed model presented in this chapter predicts an initial increase in natural bending frequencies, ω_n, of the modelled post-tensioned concrete beams with increasing post-tensioning load magnitude, N, over the range of post-tensioning force tested in the lab (0-200kN), as shown in Figure 5.31. However, when modelled over a greater range of post-tensioning force, the frequency is initially predicted to increase, and then drop off as the concrete begins to crush under post-tensioning force magnitude (Figure 5.32).

2. The proposed model predicts a greater initial increase in fundamental bending frequency than any of the existing models proposed by other authors (Saiidi et al., 1994; Kim et al., 2004; Miyamoto et al., 2000; Dall'Asta and Dezi, 1996; Zhang et al., 2012), as shown in Figure 5.33. As outlined in Section 5.8, modelling the changes in the parameters affecting natural frequency with varying post-tensioning force magnitude is a novel approach, and has not been conducted to date.

3. The proposed model is a linear kinematic model that accounts for small deflections only (i.e. Kirchoff's kinematic model) and models changes in Young's Modulus, second moment of area, span length, and mass per unit length with increasing post-tensioning force magnitude,

i.e. $E(N)$, $I(N)$, $\ell(N)$, $m(N)$, as per Equation 5.1.

4. The effect of changing the Young's Modulus, $E(N)$, and second moment of area, $I(N)$, with increasing post-tensioning force magnitude are of similar importance with regard to the subsequent changes in bending frequency, and is much greater than the effect of changing span length, $\ell(N)$, and mass per unit length, $m(N)$,, which can be considered negligible in comparison.

5. By taking non-linear kinematic effects into account, and allowing for large displacements and moderate rotations, Hamed and Frostig (2006) have proved that the final equation of motion for a post-tensioned concrete beam is independent of post-tensioning force magnitude, therefore there is no relationship between natural frequency and post-tensioning force magnitude. This is to be evaluated through experimentation in Chapter 6, and is found to be the most suitable model for uncracked post-tensioned concrete specimens.

6. Dynamic impact testing of uncracked post-tensioned concrete beams

This chapter describes the outcome of static 3-point bending testing and output only experimental modal analysis on 9 uncracked post-tensioned concrete beams. Static 3-point bending testing and dynamic impact testing were conducted on each of the 9 beams at different levels of post-tensioning force. The Fast Fourier Transform (FFT) was implemented on the dynamic accelerometer impact response data, and the fundamental frequencies of the simply supported post-tensioned concrete beams were determined by a peak-picking algorithm at each post-tensioning load level. The tests were repeated 10 times at each impact location to ensure repeatability of the experiment. There were 3 impact locations per post-tensioning load level, and there were 11 post-tensioning load levels at which the beams were tested. A first-order linear regression model was then applied to the measured fundamental bending frequencies with increasing post-tensioning load. Statistical significance tests were then conducted on the recorded data to determine if any statistically significant changes in fundamental bending frequency with increasing post-tensioning load was observed, for both static and dynamic results. The results obtained for the static 3-point bending tests were then compared and contrasted with the results obtained from dynamic testing.

6.1. Introduction

The prediction of the change in natural vibration frequencies with varying prestress force magnitude for prestressed concrete (PSC) structures is a particularly important problem. It has implications in the field of PSC bridge girders and for post-tensioned concrete wind turbine towers, both

of which are structures that are susceptible to extreme dynamic excitation. The effect of applied prestressing force on the dynamic behaviour of pre- and post- tensioned structures is a widely debated topic (Quilligan et al., 2012). Some authors argue that the natural vibration frequencies of PSC structures tend to decrease as the magnitude of the pre-stressing force is increased. This is known as the *"compression-softening"* effect and is based on classical Euler-Bernoulli beam theory of an externally axially loaded homogeneous beam (Tse et al., 1978; Raju and Rao, 1986; Dall'Asta and Leoni, 1999; Miyamoto et al., 2000; Chan and Yung, 2000; Law and Lu, 2005; Dai and Chen, 2007). Others (Dall'Asta and Dezi, 1996; Kerr, 1976; Dai and Chen, 2007) suggest that the NFs of PSC structures are unaffected by pre-stress force magnitude. This argument has been taken to the fore by Hamed and Frostig (2006), who present a non-linear kinematic model and conclude that the final equation of motion for the vibrating beam system is independent of the prestress force magnitude. Finally, there is also the argument that the NFs of PSC structures tend to increase as the magnitude of the pre-stressing force is increased. This has found to be the case in numerous empirical studies, conducted (Saiidi et al., 1994; Hop, 1991; Zhang and Li, 2007) however, a satisfactory mathematical model predicting the increase in NFs with increasing pre-stressing force has yet to be formulated, despite some attempts (Zhang and Li, 2007; Kim et al., 2004). A comprehensive review of these models and studies has been outlined in Chapter 2. Prestress force decreases over time due to concrete creep, steel relaxation, anchorage pull in and other factors. Structural engineers should thus be able to monitor or estimate changes in the natural bending frequency of PSC structures over the course of their design life to ensure their safety and serviceability. As a result, prediction of change in natural frequency of PSC structures over time is of great importance.

The aim of this chapter is to report on results of both static and dynamic testing on uncracked post-tensioned concrete beams in the laboratory. The purpose of the research is to determine the relationship between post-tensioning force magnitude and fundamental bending frequency for uncracked post-tensioned concrete beams. This chapter is organised as follows; Section 6.3 describes the initial design of the concrete beam specimens, including the mix design of the concrete, material testing, erection of formwork and casting, an analysis on the bending capacity of the sections, the determi-

nation of the rating of the prestressing strand used, and finally a prediction of the natural bending frequencies of the sections. Section 6.5 describes the set-up of two experiments in the laboratory. The first experiment is a static 3-point bending tests conducted on 9 post-tensioned concrete beams at different levels of post-tensioning force magnitude. The second experiment is a dynamic impact test, conducted on the same 9 beams, at the same post-tensioning load levels. Section 6.7 outlines the analysis of the results from both static and dynamic test regimes. It also describes the extensive signal-processing regime that was designed and implemented for the dynamic signals obtained. Section 6.8 describes the results of the static and dynamic experiments conducted, and compares the outcomes of both sets of experiments. The change in both natural frequency and damping ratio with increasing post-tensioning load magnitude for the uncracked concrete sections tested, are outlined as are the detailed statistical parameters determining the statistical significance of the data collected and presented. Section 6.10 summarises the chapter, drawing some significant conclusions.

6.2. Experimental Design

Table 6.1 outlines the different post-tensioned concrete beam specimens dynamically tested in the laboratory, in order to determine their fundamental bending frequency with differing post-tensioning load magnitude. The concrete used in each beam specimen was C30/37, as specified in Section 6.3.1. The beam sections were 200mm deep and 150mm wide, and spanned 2m onto simple supports. The span to depth ratio for each beam section was 10:1. Each beam section was reinforced with 2 H8 hanger bars as top reinforcement, and 2 H12 bottom tensile reinforcement. H8 shear links were provided at 200mm centres, and H10 U-bars were provided for continuity and anchorage. The span of 2m was chosen in order to keep the test specimens small enough to transport and lift around the laboratory easily. The cross-sectional properties (breadth and depth) were chosen such that minimum shear and bending reinforcement could be provided in accordance with Eurocode 2 to mitigate cracking. The variable in the 9 test specimens was the post-tensioning strand eccentricity. The greater the eccentricity, the greater the predicted virgin fundamental bending frequency, due to the increase in second moment of area attributed to the parallel axis theorem.

The effect of post-tensioning force magnitude and eccentricity was intended to be tested, and the effect of positive and negative eccentricity on the bending frequency, coupled with the interaction effects of both post-tensioning force and strand eccentricity on the fundamental bending frequency was also intended to be investigated. Testing the 9 beams with varying post-tensioning strand eccentricities, as outlined in Table 6.1 enabled these tests and subsequent comparison of the results to be conducted.

Table 6.1.: Experimental design - concrete test specimens

Beam	**e (mm)**	**Predicted Freq (Hz)**
1	0	78.05
2	+13	78.10
3	+26	78.30
4	+39	78.64
5	+52	79.12
6	-13	78.14
7	-26	78.37
8	-39	78.74
9	-52	79.26

6.3. Details of test set-up

The purpose of this section is to outline the detailed design and set-up of the concrete specimens cast in the laboratory for the purpose of the static and dynamic experimental tests conducted and described in this chapter and in Chapter 7 following.

6.3.1. Concrete Mix Design

The concrete mix specified for the project was as follows, in accordance with BS EN 1992-1-1:2004 (British Standards Institute, 2004);

1. **Classification**
   - Exposure class XC1.
   - Concrete inside building with low air humidity.
2. **Consistence Class**

- Consistence Class S3.
- Slump 100-150mm.
- Slump test conducted on concrete upon delivery, in accordance with BS EN 12350-2:2000 (British Standards Institute, 2000) from the truck to determine whether or not it is to be accepted.
- A slump of 140mm was obtained upon completion of the standardised slump test.

3. **Maximum aggregate size**

   - Max. aggregate size, $D_{max} = 20mm$.
   - $10mm$ aggregate was included to ensure good grading.

4. **Compressive Strength**

   - Concrete class C30/37 was specified.
   - $f_{ck,cyl} = 30MPa$, $f_{ck,cube} = 37MPa$.
   - f_{ck} is defined as the characteristic strength of the concrete, defined by the significance level of 5%, i.e. the concrete strength below which 5% of all samples will fail.
   - The target mean strength, $TMS = f_{ck}+1.64\sigma$, where σ is defined as the population standard deviation.

5. **Additions**

   - No additions were added to the mix.

6. **Admixtures**

   - No additional admixtures were added to the mix.
   - A plasticiser was added as standard.

The concrete mix specifications are summarised and outlined in Table 6.2. The concrete itself was cast for use in a laboratory environment so it's durability class was not of great concern. Due to the tight, confined spaces of the formwork, the consistency was important so as to ensure the concrete flowed freely and developed sufficient bond with the reinforcement, however, it was ensured that the mix was not too diluted so that a good homogeneous mix was ensured and segregation was avoided.

During pouring of the post-tensioned concrete beam sections in the laboratory, 10 concrete cylinders were cast and 12 concrete cubes were cast

Table 6.2.: Summary of concrete specifications

Exposure class	XC1	
Consistence class	S3	
Slump class	100-150	mm
Slump	140	mm
Max. agg. size	20	mm
Incl. good grading	10	mm
Comp. Strength	C30/37	
$f_{ck,cyl}$	30	MPa
$f_{ck,cube}$	37	MPa
Additions	NONE	
Admixtures	Plasticiser as standard	

for Young's Modulus and strength testing following curing of the concrete. The strength testing procedure and results are presented in Section 6.3.2, in accordance with the standard BS EN 12390-3:2001 (British Standards Institute, 2001), and the Young's Modulus testing procedure and results are presented in Section 6.3.3, in accordance with the standard BS EN 12390-13:2013 (British Standards Institute, 2013).

6.3.2. Strength Testing

Strength testing was carried out on concrete cube and cylinders cast from the concrete batch used to cast the 9 post-tensioned concrete beams tested throughout the course of the PhD project described in this thesis. Figure 6.1 shows the crushing of a cube in a compression testing machine in conformance with EN 12390-4 (British Standards Institute, 2001). This testing was carried out as a means of quality testing the concrete batch received from the supplier, ensuring it reached the requested strength.

Four $100 \times 100 \times 100$ mm concrete cubes were tested to failure in a compression testing machine, conforming to EN 12390-4. The cubes were cast in moulds using C30/37 designated concrete, with 100-150mm slump (i.e. consistence class S3) which was used to pour 9 post-tensioned concrete beams. The beams were cast for the purpose of impact hammer and modal testing at varying post-tensioning force levels and for different post-tensioning strand eccentricities. The date of the concrete pour was Thursday 27^{th} February 2014 (27/02/2014).

Figure 6.1.: Compression testing of concrete cube specimens

Twelve 100 × 100 × 100 mm concrete cubes were cast, each specimen labelled DN1-DN12. Ten 150mm diameter × 300mm high concrete cylinders were cast for the purpose of Young's Modulus testing, and labelled DN1-DN10. An accurate prediction of the Young's Modulus of the concrete is more important than strength in dynamic prediction modelling. The Young's Modulus testing is carried out on such cylinders, in accordance with BS EN ISO 12390-3:2001 (British Standards Institute, 2001).

(a) (b)

Figure 6.2.: (a) 10 concrete cylinders cast for Young's Modulus testing; (b) 12 concrete cube specimens cast for strength testing.

The concrete cubes were poured (trowelled) in 2 layers, with each layer

being vibrated for 5 seconds on the shake table to ensure full compaction. It was ensured by inspection that the duration of excitation was sufficient enough to achieve full compaction but not overly excessive to induce bleeding and segregation. The top surface was then floated off using a trowel.

The concrete cylinders were poured (trowelled) in 3 layers, with each layer being vibrated for 5 seconds on the shake table to ensure full compaction. It was ensured by inspection that the duration of excitation was sufficient enough to achieve full compaction but not overly excessive to induce bleeding and segregation. The top surface was then floated off using a trowel.

The cubes and cylinders were covered with damp hessian and sheet plastic for the first 5 days while they were allowed to set and develop strength in the moulds. The hessian was wetted every day with water. After 5 days, the cubes and cylinders were removed from the moulds using the pressure pump. The samples were then weighed and placed in a curing tank at 20^oC for a further 23 days, as shown in Figure 6.3.

(a) (b)

Figure 6.3.: (a) Concrete specimens stored in curing tank at 20^oC for a further 23 days; (b) Cubes and cylinders stored in the curing tank

Four cubes were removed from the curing tank on Thursday 27th March 2014 (27/03/2014) after 28 days curing, and tested to failure in a compression testing machine, conforming to EN 12390-4.

5 of the 6 surfaces of the cube were completely smooth and the final surface was floated. It was ensured during testing that the cubes were loaded into the compression testing machine with loading applied to two surfaces. This was to ensure an even distribution of load throughout the

specimens, which is required for satisfactory failure conditions to hold.

The loading rate in the compression testing machine was set at 0.4MPa/s and the concrete cubes were tested until failure, which was defined as yielding, i.e. a significant increase in deformation for little or no additional load, or until the specimen could not withstand any further applied load. The failure load of the specimens are outlined in Table 6.3, alongside the mass and standard deviation of the strengths for the tested cube specimens.

Table 6.3.: Failure loads of tested concrete specimens

Specimen	**Mass (g)**	**Failure Load (kN)**	**Failure (MPa)**	**Failure (nearest 0.5MPa)**	**% diff from ave.**
DN1	2416.5	415	41.5	41.5	-0.84%
DN2	2413.0	427	42.7	42.5	+1.55%
DN3	2411.7	429	42.9	43.0	+2.75%
DN4	2390.7	403	40.3	40.5	-3.23%
Average, μ	(MPa)		41.85	41.88	
Std. D., σ	(MPa)		1.20	1.11	

The concrete specified for use in the beam specimens was C30/37, which indicates a characteristic cube strength of $f_{ck} = 37.0MPa$, below which not more than 5% of all specimens should fall (at a one-sided significance level of 0.10). Since the sample size is small (n=4), this means that the number of degrees of freedom is defined by $\nu = n - 1 = 3$. From the studentised t-distribution with $\nu = 3$ and a significance level of $\alpha = 0.05$, this means that the characteristic cube strength is defined by $f_{ck} = \mu - 2.35\sigma = 41.88 - 2.35 \times 1.11 = 39.3MPa$. This value of $39.3 > 37MPa$, which was the specified value, indicating that the actual concrete strength is at least 37MPa, and in fact, the actual significance level is less than 0.05. This indicates that the concrete was up to the requested standard.

Another important consideration during strength testing of concrete cube specimens is to ensure that the specimens fail in a satisfactory manner, ensuring homogeneity of the test specimen, and an even loading distribution. All specimens failed in a manner consistent with the satisfactory requirements, set out in BS EN ISO 12390-3:2001 (British Standards Institute, 2001), as shown in Figure 6.4.

The uniformity of the concrete cube specimen failure conditions is high-

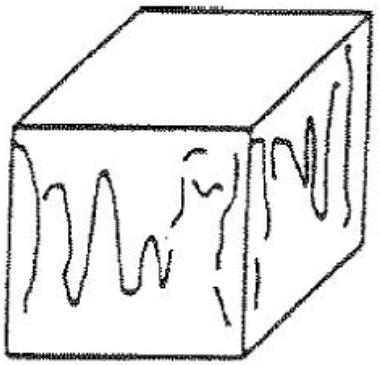

Figure 6.4.: Satisfactory cube failure in accordance with IS EN 12390-3:2001 (British Standards Institute, 2001).

lighted in Figure 6.5, where Figure 6.5a and 6.5b show the failure conditions for specimen DN1, and Figure 6.5c and 6.5d show the failure conditions for specimen DN2.

Table 6.4 indicates the calculated mass density of the cube specimens tested. The cubes and cylinders were covered with damp hession and sheet plastic from when they were cast for 5 days. The hession was wetted each day to ensure a sufficient moisture regime. After 5 days the specimens were demoulded and placed in a curing tank for a further 23 days at 20 degrees Celsius.

Table 6.4.: Apparent density of tested concrete specimens

Specimen	**Mass (kg)**	**Density** (kg/m^3)	**Density (nearest** $10kg/m^3$**)**
DN1	2.4165	2416.5	2420
DN2	2.4130	2413.0	2410
DN3	2.4117	2411.7	2410
DN4	2.3907	2390.7	2390

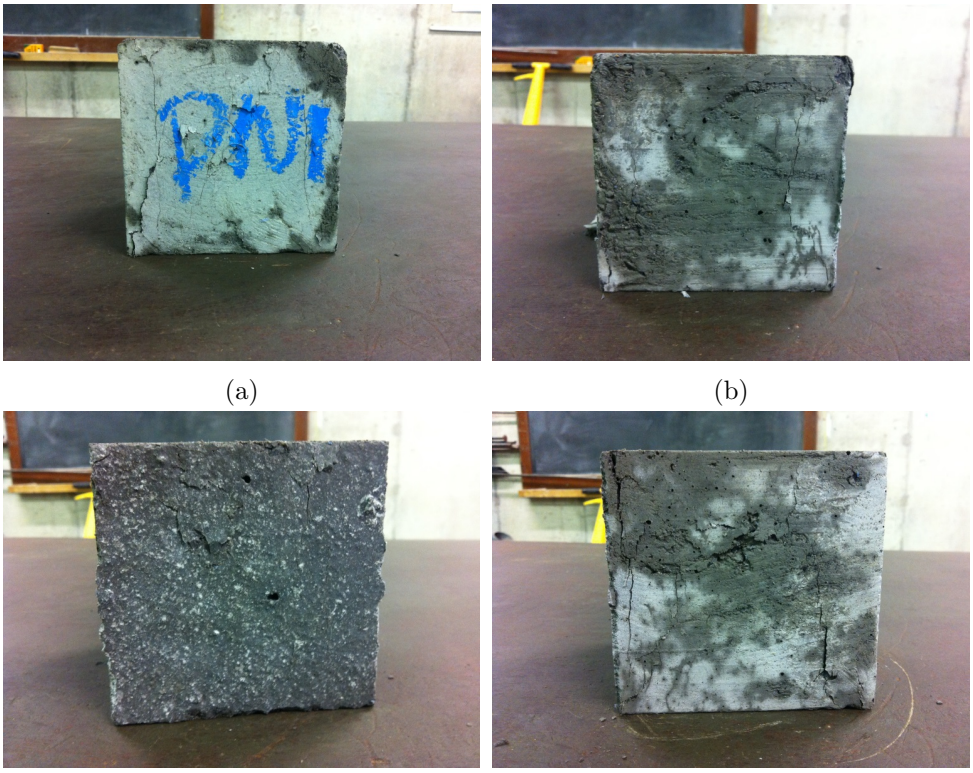

(a) (b)

(c) (d)

Figure 6.5.: Examples of satisfactory failure of concrete cube specimens; (a) & (b) specimen DN1; (c) & (d) specimen DN2.

6.3.3. Young's Modulus Testing

Young's Modulus testing was carried out on concrete cylinder specimens (300 mm in length, 150 mm in diameter), in accordance with BS EN 12390-13:2013 (British Standards Institute, 2013). A concrete cylinder test specimen was loaded under axial compression in a standardised compression testing machine. The stresses and strains are recorded, and the slope of the secant to the stress-strain curve was determined after three loading cycles. The initial secant modulus of elasticity, $E_{C,0}$, is defined as the secant slope of the stress-strain curve at first loading. The stabilised secant modulus of elasticity, $E_{C,S}$, is the secant slope of the stress-strain curve after three loading cycles.

Instrumentation was affixed to the sides of the cylinder test-specimens during loading, in the form of extensiometers. The extensiometers either measure strain directly or measure the change in length from which the

strain can be calculated directly. The base or gauge length is defined as the length of specimen used as the reference base for the strain measurement. The base or gauge length was ensured to be between two-thirds of the specimen diameter, and one-half of the specimen length.

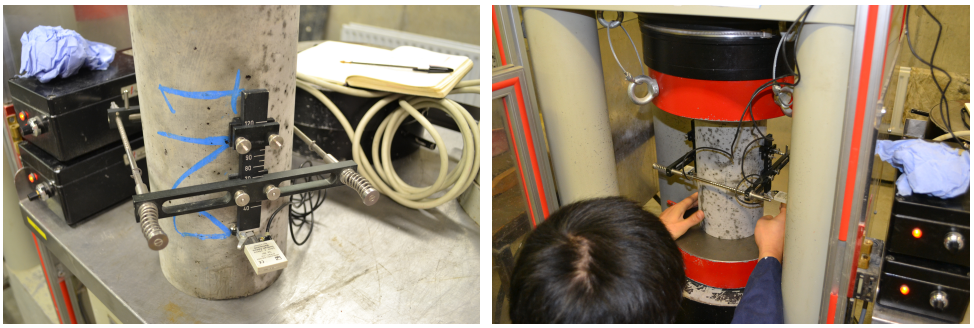

(a) (b)

Figure 6.6.: Young's Modulus test set-up; (a) Extensiometer placed on cylinder specimen (b) Cylinder loaded into compression testing machine

The specimens were cured and stored in accordance with EN 12390-2, and stored in a curing tank at a steady temperature of 20^oC from the time of sufficient strength development (5 days) until 28 days, at which time the specimens were tested.

The cylinder specimens were placed in the centre of the lower platen of the standardised compressive testing machine. This ensures that the load is applied evenly to both extensiometers. The compressive strength of the cylinder specimens were first determined in accordance with EN 12390-3, as this determines the maximum testing stress for the Young's Modulus. This is defined as $f_{cm}/3$, where f_{cm} is the characteristic cylinder strength of the tested specimens, as shown in Figure 6.7.

The locking clamps of the extensiometer were released and using the potentiometer knobs were adjusted on the amplifier until the % difference between the two extensiometer readings was zeroed. The test was then begun by starting the compression testing machine. The platen moved up and the cycle of load application began for 3 load cycles. If the difference between the two extensiometers exceeded 15% the test was stopped and the extensiometers were rebalanced appropriately. The loading rate of the compression testing machine was set at 0.6MPa/s as per EN 12390-3 (British

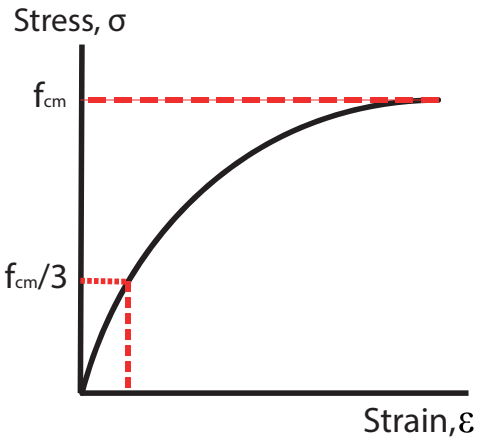

Figure 6.7.: Loading cycles of Young's Modulus testing

Standards Institute, 2013). The stress was increased from the preload stress, σ_p to the upper stress, $\sigma_a = f_{cm}/3$ and held for no longer than 20s. The corresponding strain is recorded for each stress value, and this cycle of loading/unloading is repeated 3 times.

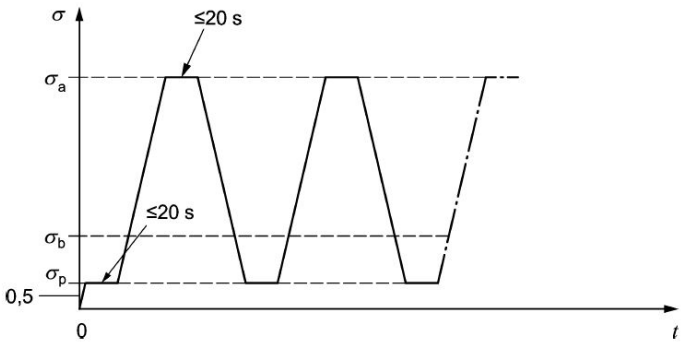

Key

———	loading cycle
—·—	loading cycle for the determination of stabilized secant modulus of elasticity – Method B
σ	applied stress in MPa
σ_a	upper stress – f_c / 3
σ_b	lower stress – 0,10 × f_c ≤ σ_b ≤ 0,15 × f_c
σ_p	preload stress – 0,5 MPa ≤ σ_p ≤ σ_b
t	time in s

Figure 6.8.: Cycle for determination of stabilised secant modulus of elasticity (British Standards Institute, 2013)

The stabilised secant modulus of elasticity, $E_{C,S}$ is defined as;

$$E_{C,S} = \frac{\Delta\sigma}{\Delta\epsilon_s} = \frac{\sigma_a^m - \sigma_p^m}{\epsilon_{a,3} - \epsilon_{p,2}} \tag{6.1}$$

where σ_a is the nominal upper stress, σ_p is the nominal preload stress, which is an arbitrary value between 0.5MPa and σ_b. σ_b is the nominal lower stress, which is an arbitrary value between 10% and 15% of f_{cm}. $\epsilon_{a,n}$ is the average strain at upper stress on loading cycle n, while $\epsilon_{p,n}$ is the average strain at preload stress on loading cycle n. σ_a^m is the measured stress corresponding to the nominal upper stress, σ_a and σ_p^m is the measured stress corresponding to the nominal preload stress, σ_p.

The results of the Young's Modulus testing on the tested concrete specimens labelled DN1 and DN2 are outlined in Table 6.5. The cylinder compressive strengths of the specimens tested are outlined in Table 6.6. The mean of the measured Young's Modulus is calculated to be $26.88GPa$.

Table 6.5.: Young's Modulus test results for cylinder specimens DN1 and DN2

Specimen	DN1			DN2			
	Cycle 1	Cycle 2	Cycle 3	Cycle 1	Cycle 2	Cycle 3	
σ_a	11.02	11.02	11.02	11.01	11.01	11.01	MPa
ϵ_a	-0.420	-0.418	-0.419	-0.409	-0.409	-0.410	
σ_p	0.86	0.86	0.85	0.86	0.87	0.86	MPa
ϵ_p	-0.038	-0.040	-0.040	-0.031	-0.035	-0.034	
$E_{C,S}$	26.59	26.88	26.83	26.85	27.11	26.99	GPa

6.3.4. Casting of beam specimens

9 post-tensioned concrete beams were cast with different straight profiled post-tensioning duct eccentricities. The beams were cast in wooden formwork assembled in the laboratory, as shown in Figure 6.9. The reinforcement cages were assembled in the laboratory by hand and welded together. The cages consisted of 2 H12 diameter reinforcement bars as bottom reinforcement, and 2 H8 *"hanger"* bars as top reinforcement. Four H10 U-bars were

Table 6.6.: Concrete cylinder compression strength of 5 different specimens tested

Specimen	**Mass (kg)**	**Failure (MPa)**	**Failure (nearest 0.5MPa)**
DN3	12.7517	31.2	31.0
DN4	12.6768	32.5	32.5
DN5	12.7331	35.7	35.5
DN1	12.6980	35.1	35.0
DN2	12.7779	34.6	34.5
μ	12.7275	33.8	33.7
σ	0.0406	1.90	1.89

affixed to the beam ends as continuation reinforcement, and as anchorage. H8 shear links are placed at 200mm spacings as shear reinforcement, and an additional 2 shear links are provided in the anchorage zone as *"bursting"* reinforcement to resist the high bursting forces that the post-tensioning can induce.

(a) (b)

Figure 6.9.: Concrete beam casting; (a) formwork; (b) concrete poured into mould

The concrete was vibrated using a poker vibrator to ensure full compaction. This is important for strength and durability of the finished concrete specimen. The concrete was then floated off and covered in wet hessian and further covered with polyurethane sheeting. The concrete was inspected daily and was continually wetted to ensure the continuation of the hydration

reaction and the development of the required strength.

The concrete beam specimens cast are outlined in detail in Figure 6.10. The associated bar-bending schedules for the beams are also given in Table 6.7.

Table 6.7.: Bar bending schedule for concrete specimens cast

Bar Mark	Type	No. each	Total No.	Length (mm)	kg/m	Tot. Wt. (kg)	Shape code	A (mm)	B (mm)
01	H12	2	18	2200	0.888	35.2	01	2200	
02	H8	2	18	2200	0.395	15.6	01	2200	
03	H10	4	36	1390	0.617	30.8	13	520	110
04	H8	17	153	600	0.395	36.3	51	100	150

6.3.5. Bending Capacity of Members

The ultimate moment capacity, M_{ult}, of the concrete sections was calculated, given the areas of reinforcement; $A_{s,bot} = 226.19mm^2$, $A_{s,top} = 100.53mm^2$, and the material properties; $f_{ck} = 30MPa$, $f_y = 500MPa$, $\epsilon_{ult} = 0.0035$, $E_s = 205GPa$. Firstly, expressions for the compressive (C) and tensile (T) forces, due to bending, in the concrete beam cross section are generated as functions of the neutral axis depth, x;

$$\begin{aligned} C &= b(0.8x)f_{ck} \\ &= 150(0.8x)(30) \\ &= 3600x \end{aligned} \tag{6.2}$$

The tensile force is calculated assuming that the steel has reached its design yield value;

$$\begin{aligned} T &= \frac{A_{s,bot}f_y}{\gamma_{m1}} \\ &= \frac{(226.19)(500)}{1.15} \\ &= 98.343 \quad kN \end{aligned} \tag{6.3}$$

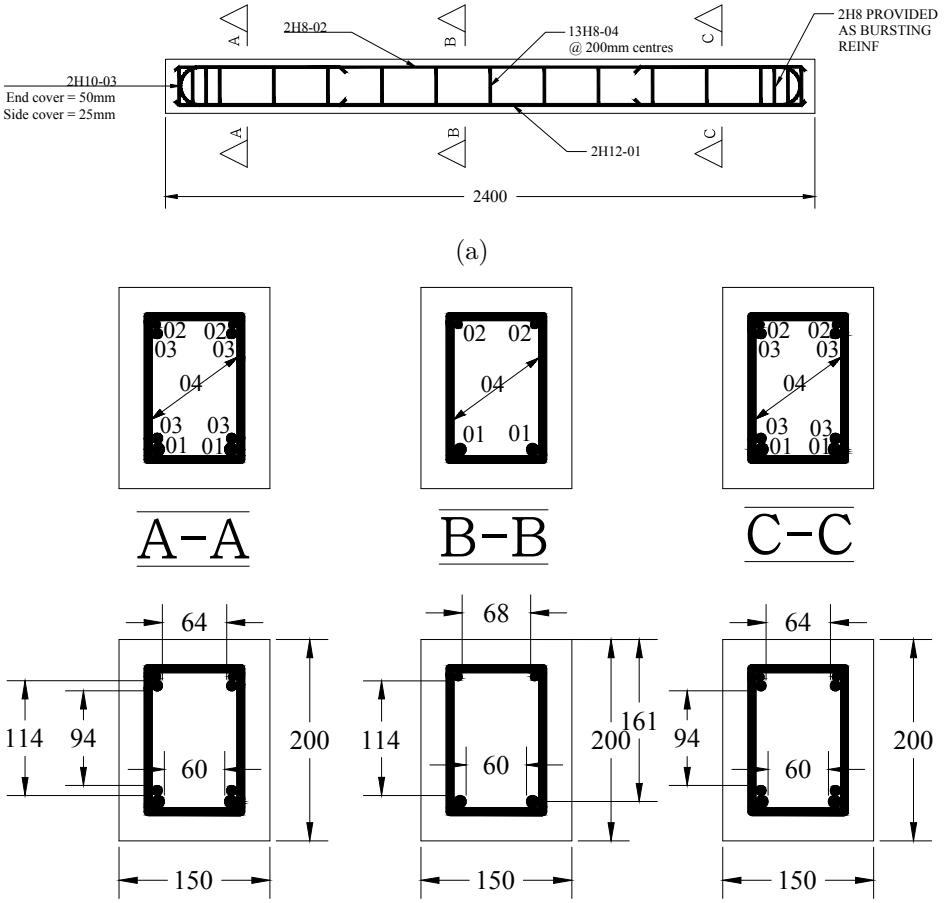

Figure 6.10.: Concrete beam design; (a) along span; (b) cross section

The compressive force, C, and the tensile force, T, are equated in order to calculate the neutral axis depth, x;

$$\begin{aligned} 3600x &= 98,343 \\ x &= 27.32mm \end{aligned} \tag{6.4}$$

Having calculated the neutral axis depth, the assumption that the steel has yielded should be verified;

$$\begin{aligned} \epsilon_s &= 0.0035\left(\frac{161-27.32}{37.32}\right) \\ &= 0.01712 \quad > \quad 0.002 \quad \checkmark\checkmark\checkmark \end{aligned} \tag{6.5}$$

The bending moment capacity, M_{ult}, can then be calculated;

$$\begin{aligned} M_{ult} &= T(d-0.04x) \\ &= (98,343)[161-0.4(27.32)] \\ &= 14.76kN-m \end{aligned} \tag{6.6}$$

This calculation can be repeated, allowing for the minimal effect of the compression reinforcement;

$$\begin{aligned} C &= [b(0.8x)+A_{s,top}(m-1)]f_{ck} \\ &= [150(0.8x)+100.53(6.65)](30) \\ &= 3600x+20,055.7 \end{aligned} \tag{6.7}$$

Replacing Equation 6.2 with Equation 6.7, a neutral axis depth of $x = 21.75mm$ is calculated. The ultimate moment capacity is increased slightly to $M_{ULT} = 14.99kN-m$, which corresponds to a 1.6% increase in ultimate state moment capacity.

6.3.6. Strand rating

The strand used during post-tensioning was a Freyssinet 15.7mm diameter 7-wire concentric strand with a yield strength, $f_{y,ps} = 1860MPa$. The tabulated cross sectional area of the strand is given as $150mm^2$, in accordance with PR EN 10138-3:2006 (British Standards Institute, 2006). The tensile capacity of the strand is therefore given as $F_{pk} = 279kN$. Code values specify that in prestressing design, the maximum allowable tensile force in the strand should be limited to $0.7F_{pk} = 195kN$. The post-tensioned concrete beams were stressed no higher than 200kN in any case throughout laboratory testing.

Figure 6.11 shows the 15.7mm 7-wire concentric Freyssinet prestressing strand and post-tensioning collet, as used in the post-tensioning of the 9 post-tensioned concrete beams tested in the laboratory.

(a)

(b)

Figure 6.11.: Freyssinet 7-wire 15.7mm concentric strand and pre-stressing collet for anchorage

6.3.7. Prediction of Natural bending frequencies

The prediction of the natural frequency of the post-tensioned concrete beams is outlined. An uncracked analysis and cracked analysis of the post-tensioned concrete beams has been compared for zero post-tensioning force. The effect of the post-tensioning force itself should act as to increase the neutral axis depth and subsequently increase the frequency of vibration, where cracking has occurred.

Uncracked Analysis

Taking moments about the top fibre to calculate the uncracked neutral axis depth, $\bar{x_u}$, the following is obtained;

$$\bar{x_u} = \frac{\frac{bh^2}{2} + \pi\left(m{r_i}^2 - {r_o}^2\right)\left(\frac{h}{2} + e\right) + (m-1)\left[A_{s_t}\left(c + \frac{\phi_t}{2}\right) + A_{s_b}\left(h - c - \frac{\phi_b}{2}\right)\right]}{bh + \pi\left(m{r_i}^2 - {r_o}^2\right) + (m-1)\left(A_{s_t} + A_{s_b}\right)} \tag{6.8}$$

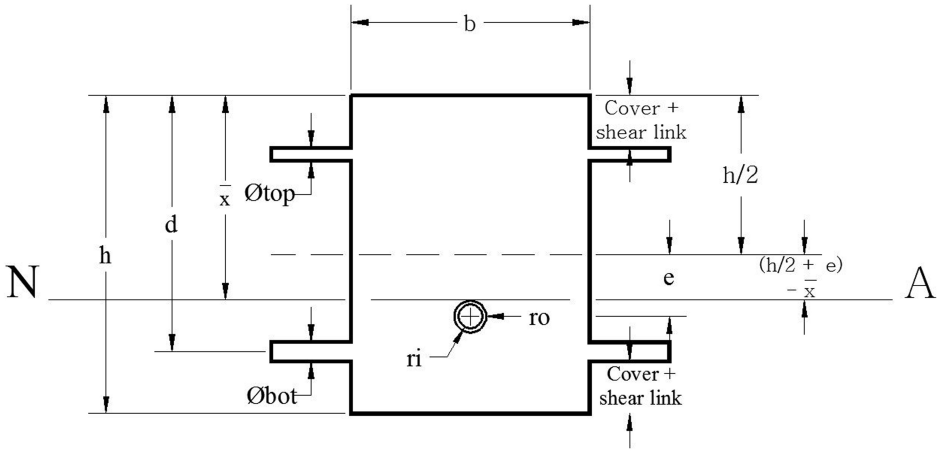

Figure 6.12.: Uncracked modelling

To calculate the uncracked second moment of area, I_u, of the section, the parallel axis theorem is applied about the neutral axis;

$$I_u = \frac{bh^3}{12} + bh\left(\bar{x_u} - \frac{h}{2}\right)^2 - \left[\frac{\pi}{4}{r_o}^4 + \pi{r_o}^2\left(\frac{h}{2} + e - \bar{x_u}\right)^2\right] + \left[\frac{\pi}{4}{r_i}^4 + m\pi{r_i}^2\left(\frac{h}{2} + e - \bar{x_u}\right)^2\right] + (m-1)\,A_{s_t}\left(\bar{x_u} - c - \frac{\phi_t}{2}\right)^2 + (m-1)\,A_{s_b}\left(h - \bar{x_u} - c - \frac{\phi_b}{2}\right)^2 \tag{6.9}$$

Cracked Analysis

Taking moments about the top fibre to calculate the cracked neutral axis depth, $\bar{x_c}$ the following is obtained;

$$\frac{b\bar{x_c}^2}{2} + \left[(m-1)\,A_{s_t}\left(c + \frac{\phi_t}{2}\right) + m\pi{r_i}^2\left(\frac{d}{2} + e\right) + mA_{s_b}\left(h - c - \frac{\phi_b}{2}\right)\right] = \left[b\bar{x_c} + (m-1)\,A_{s_t} + m\pi{r_i}^2 + mA_{s_b}\right]\bar{x_c} \tag{6.10}$$

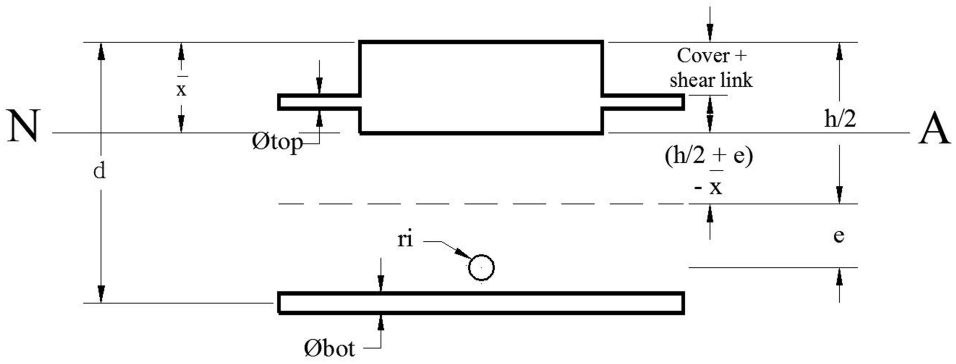

Figure 6.13.: Cracked modelling

rearranging, the following quadratic equation is obtained;

$$b\bar{x_c}^2 + 2\left[(m-1)\,A_{s_t} + m\pi {r_i}^2 + mA_{s_b}\right]\bar{x_c} - 2\left[(m-1)\,A_{s_t}\left(c + \frac{\phi_t}{2}\right) + m\pi {r_i}^2\left(\frac{d}{2} + e\right) + mA_{s_b}\left(h - c - \frac{\phi_b}{2}\right)\right] = 0 \tag{6.11}$$

making the following substitutions;

$$A = b \tag{6.12}$$

$$B = 2\left[(m-1)\,A_{s_t} + m\pi {r_i}^2 + mA_{s_b}\right] \tag{6.13}$$

$$C = -2\left[(m-1)\,A_{s_t}\left(c + \frac{\phi_t}{2}\right) + m\pi {r_i}^2\left(\frac{d}{2} + e\right) + mA_{s_b}\left(h - c - \frac{\phi_b}{2}\right)\right] \tag{6.14}$$

and solving the quadratic equation gives values for the cracked neutral axis depth, $\bar{x_c}$;

$$\bar{x_c} = \frac{-B \pm \sqrt{B^2 - 4AC}}{2A} \tag{6.15}$$

The cracked second moment of area, I_c, of the section is subsequently calculated;

$$I_c = \frac{bx_c^3}{12} + bx_c\left(\frac{h}{2} - \frac{x_c}{2}\right)^2 + (m-1)\,A_{s_t}\left(x_c - c - \frac{\phi_t}{2}\right)^2 + m\pi {r_i}^2\left(\frac{h}{2} + e - x_c\right)^2 + mA_{s_b}\left(h - x_c - c - \frac{\phi_b}{2}\right)^2 \tag{6.16}$$

The prediction of the fundamental bending frequencies of each of the 9 uncracked and cracked post-tensioned concrete beams for zero post-tensioning force magnitude are outlined in Table 6.8. The frequencies have been predicted based on the dynamic formula for a simply supported beam as outlined in Equation 6.20;

Table 6.8.: Predictions of cracked and uncracked fundamental frequencies for PSC Beams

e (mm)	x_u (mm)	x_c (mm)	I_u (mm^4)	I_c (mm^4)	$\omega_{1,u}$ (Hz)	$\omega_{1,c}$ (Hz)	I_c/I_u
-52	99.58	49.37	1.12×10^8	6.56×10^7	79.26	60.78	0.59
-39	100.05	51.06	1.10×10^8	6.64×10^7	78.74	61.15	0.60
-26	100.53	52.71	1.09×10^8	6.75×10^7	78.37	61.66	0.62
-13	101.01	54.33	1.08×10^8	6.90×10^7	78.14	62.33	0.63
0	101.49	55.91	1.08×10^8	7.08×10^7	78.05	63.15	0.65
+13	101.96	57.47	1.08×10^8	7.30×10^7	78.10	64.12	0.67
+26	102.44	58.99	1.09×10^8	7.56×10^7	78.30	65.23	0.69
+39	102.92	60.49	1.10×10^8	7.85×10^8	78.64	66.48	0.71
+52	103.40	61.97	1.11×10^8	8.18×10^8	79.12	67.87	0.73

6.4. Type of prestressing

There are many types of prestressed concrete elements, many different techniques for prestressing concrete, and varying degrees of prestressing. They are summarised in the following sections.

6.4.1. External vs. Internal prestressing

1. **External Prestressing:** when prestressing is achieved by elements located outside the member cross section, it is called *"external prestressing"*. The tendons can lie outside the member, or inside the hollow of the section.

2. **Internal Prestressing:** when the prestressing is achieved by elements located inside the extents of the member cross section (most commonly by embedded tendons inside the extents of the concrete cross section), it is known as *"internal prestressing"*. Most of the applications of prestressing are internal prestressing.

6.4.2. Pre-tensioning/Prestressing vs. Post-tensioning

Whereas the overarching term for pre-application of an axial stress throughout a cross section is "prestressing", there is a distinction to be made between pre-tensioning or pre-stressing and post-tensioning.

1. **Pre-tensioning/Prestressing:** the tensile load is applied to the tendons before the concrete is cast, and the concrete is then cast around the tendons. The concrete bonds to the prestressing steel, and once it has cured and set, the strands are released. This tensile force is released, transmitting a compressive force into the concrete.

2. **Post-tensioning:** the tendons are placed in a duct and the concrete is cast around it. The concrete hardens and the tensile load is applied to the tendons, after hardening of the concrete. The pre-compression is transferred from the steel to the concrete by means of an anchoring device at the ends of the post-tensioned element.

6.4.3. Linear vs. Circular prestressing

Prestressing can be categorised by the type of profile that the tendons follow and the direction of the prestressing force throughout the element, as outlined below;

1. **Linear prestressing:** when the prestressed members are straight or flat, in the direction of prestressing, the prestressing is known as *"linear prestressing"*, however, the profile of the tendon may be curved,

which is common to resist bending moments that arise in different locations along the span of multi-span beams, for example. Beams and slabs are subjected to linear prestressing.

2. **Circular prestressing:** When the prestressed members are curved, in the direction of prestressing, the prestressing is known as *"circular prestressing"*. Tanks, silos, wind turbine foundations, and especially nuclear reactors tend to make use of circular prestressing.

6.4.4. Full vs. Partial prestressing

The level of prestressing is also a means to distinguish;

1. **Full prestressing:** when the level of prestressing is such that no tensile stress is allowed in the concrete under service load.

2. **Limited prestressing:** when the level of prestressing is such that the tensile stress under service load is within the cracking stress of the concrete.

3. **Partial prestressing:** when the level of prestressing is such that under tensile stresses due to service load, the crack width is within an allowable limit.

In the case of the pre-stressed beams tested and described throughout the course of this chapter, the tendons have a linear profile, are embedded in the extents of the concrete cross section, within a post-tensioning duct, and, as such, the beams are internally linearly post-tensioned concrete beams. Depending on the level of varying post-tensioning load, the beams are either fully or partially prestressed.

6.5. Experimental Set-up

Section 6.3 outlined the design and subsequent materials testing of the concrete specimens to be tested in the static and dynamic experiments described in detail in this section. This section describes the experimental set-up of both static three point bending tests and dynamic impact testing conducted on the 9 uncracked post-tensioned concrete beams at different

post-tensioning load levels. Section 6.6 describes the concrete test specimens tested in the laboratory. Section 6.6.1 outlines the set-up of the static three point bending tests, while Section 6.6.2 outlines the set-up of the dynamic impact testing conducted. The analysis of the results obtained is outlined in Section 6.7.

6.6. Concrete Test Specimens

The concrete beam test specimens tested in the laboratory were 2.3m long post-tensioned concrete beams with minimum reinforcement provided, in accordance with Eurocode 2 (British Standards Institute, 2004). The span length between the simple supports was 2m. The beams were 200mm deep and 150mm wide in cross-section. The concrete had a characteristic cube strength, $f_{ck} = 37MPa$, as outlined in Section 6.3.2. The Young's Modulus of the concrete was determined experimentally to be $E_c = 26.88GPa$, as outlined in Section 6.3.3. The beams were lightly reinforced with 2 H12 as bottom reinforcement and 2 H8 as hanger bars (top reinforcement). H8 shear links were provided at 200mm centres and an additional 2 H8 shear links were provided in the anchorage zone as bursting reinforcement, in accordance with the CIRIA method, and as shown in Figure 6.14, and as outlined in Section 6.3.4. Cover to all reinforcement was specified to be a minimum of 25mm (Noble et al., 2014a, 2015c).

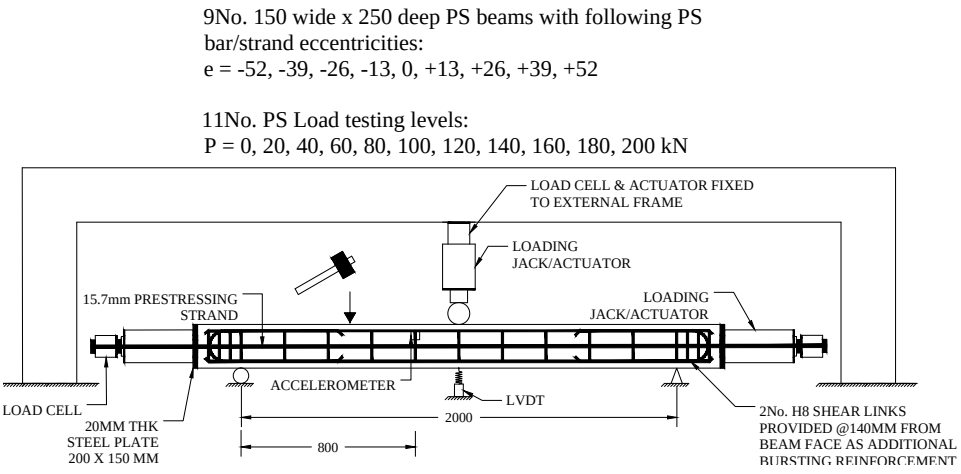

Figure 6.14.: Experimental set-up.

Figure 6.16 shows the set-up in the lab. Figure 6.16b shows the set-

up of the jacks on either end of the beam. A 15.7mm diameter 7-wire concentric Freyssinet pre-stressing strand, with a yield strength, $f_{y,ps} = 1860MPa$ was threaded through a 20mm diameter post-tensioning duct, cast into the concrete beam. 20mm thick steel plates were placed on either end of the beam. A 300 ton loading jack was placed on end against the steel plate. A TML KCM-300kNA *'through-hole compression'* load cell, rated to 300kN, was placed between the loading jack and the prestressing collet. This arrangement was identical on each end of the beam, which helped to balance the mass on either end of the beam. A prestressing collet was fixed on the prestressing strand, such that when the jacks were elongated, they jacked against the prestressing collet, gripping the strand and hence, post-tensioning the concrete beam. The jack was controlled by means of a hydraulic hand pump, as shown in Figure 6.16b (Noble et al., 2014a, 2015c).

6.6.1. Static 3-point bending tests

Three point static bending tests were conducted on post-tensioned concrete beams in the laboratory, as shown in the schematic in Figure 6.14, and later in Figure 6.16. 9 post-tensioned concrete beams were tested statically through three point bending. The 9 beams each had a different straight-profiled post-tensioning strand eccentricity, as outlined later in Figure 6.19. The beams were placed underneath a small loading frame, which is rated to 180 tons, in the laboratory, which in turn, is anchored onto a metre deep reinforced concrete strong-floor. The loading ram was placed at midspan of the beam as shown in Figure 6.14 and Figure 6.16. The loading ram was attached to a hydraulic jack, which was controlled via hand pump.

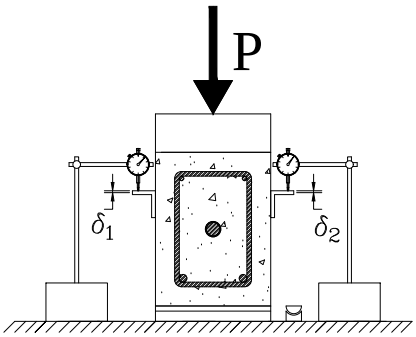

Figure 6.15.: Measuring static deflection.

Each of the 9 uncracked post-tensioned concrete beams were tested statically at different values of post-tensioning load. The post-tensioning load levels were incremented in 20kN increments from 0-200kN. The lateral load was applied to the beams in such a way that the deflection reading from the dial gauges was never greater than 1mm, giving a minimum span/deflection ratio of 2000, much greater than the code specified value of 250. In this way, the test was deflection controlled. Furthermore, at such small values of midspan deflection, flexural cracking was not induced in any of the sections. Deflection was measured by means of two right-angled steel plates that were affixed to the beam section at mid-span as shown in Figure 6.15. A measurement was taken at each beam face to account for possible torsion of the beam section due to an asymmetrically applied load. Two deflection and transverse load readings were taken at each beam face, at each post-tensioning load level. This iteration was repeated once in order to minimize error in the experiment.

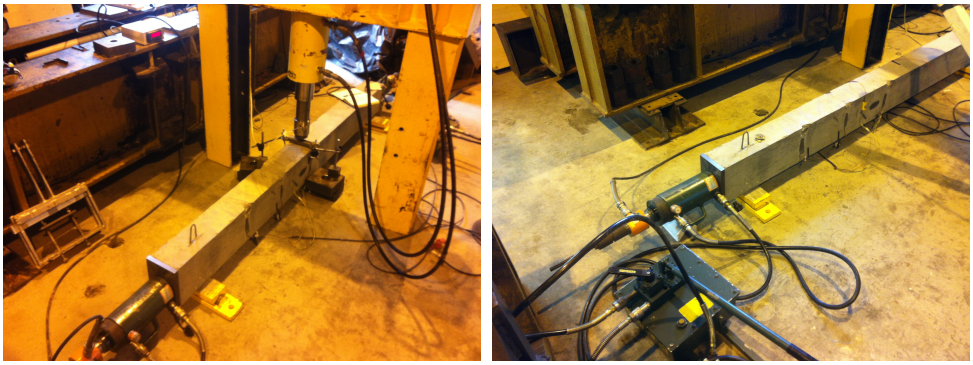

(a) (b)

Figure 6.16.: Three-point static bending test set-up in laboratory.

The results of the static testing are presented and discussed in Section 6.8.1, and the results presented in Table 6.9, and Figures 6.24 to 6.33.

6.6.2. Dynamic impact tests

Dynamic impact testing has been conducted on 9 post-tensioned concrete beams. Figure 6.14 in conjunction with Figure 6.17 shows the experimental set-up. Dynamic impact testing was conducted at three locations along the length of the beam span, as outlined in Figure 6.17, labelled L1-L3. The beam was struck 10 times at each location using an impact rig assembled

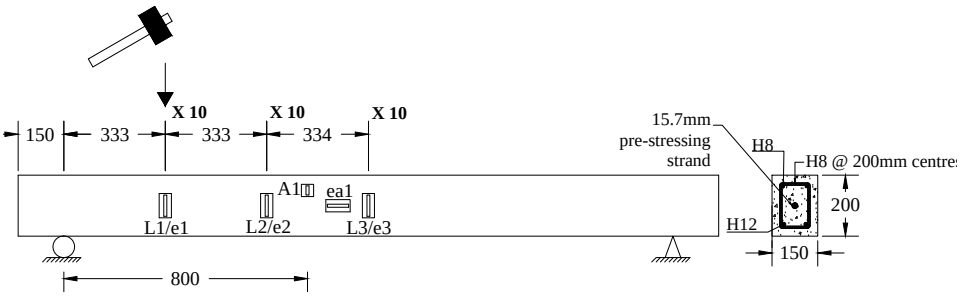

Figure 6.17.: Instrumentation and set-up of dynamic test in laboratory

in the lab with a rope and pulley system. The impact rig in question can be seen in the foreground of Figure 6.18a. Figure 6.18a shows the set-up of the experiment as it was in the laboratory. The beam being tested can be seen on the left hand side of the picture. Affixed to the beam was a Dytran model 3200b4 10,000g range accelerometer. The accelerometer, 2 load cells and 4 strain gauges were connected to a System 6000 data logging system. The data was sampled at a rate of 10,000Hz, ensuring a Nyquist frequency of 5,000Hz. Since the fundamental bending frequency was expected to be approximately 78Hz, this sampling rate theoretically enabled the first 8 bending modes of vibration to be detected by the instrumentation (i.e. $78 \times 8^2 = 4,992$ Hz). The experiment was repeated at different post-tensioning load levels, as outlined in Figure 6.14. The post-tensioning load was increased in intervals of 20kN from 0-200kN. This helped ensure repeatability of the experiment. Strain gauges were fixed at the three impact locations (e1- e3) in order to obtain the mode shapes of vibration. The accelerometer (A1) was strategically placed at a distance of 800mm from the support, in order to identify all of the first three modes of vibration. Placement at midspan would eliminate the opportunity to obtain the second mode of vibration as it is a nodal point for the second mode. A fourth strain gauge (ea1) was placed in the axial direction, close to midspan, in order to compare the axial strain data with the pre-stress load data obtained from the load cells (Noble et al., 2014a, 2015c, 2016). Figure 6.18 shows a picture of the instrumentation as affixed to a beam in the laboratory. The 3 strain gauges can be seen affixed parallel to the direction of vibration at the 3 impact locations. In Figure 6.18b, some light, superficial damage to the concrete cover can be seen in the locations where the impact rig struck

the beam.

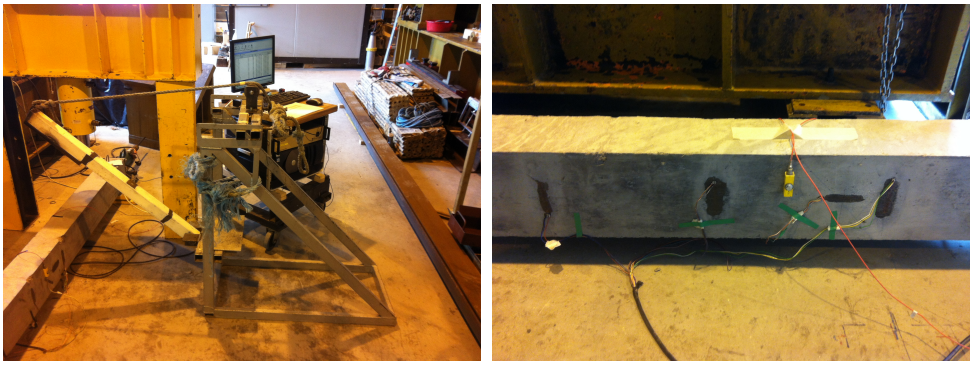

(a) (b)

Figure 6.18.: (a) Experimental set-up in laboratory; (b) Instrumentation of the beam sections.

Figure 6.19 shows the cross-sections of each of the 9 post-tensioned concrete beams tested. Each beam has a different post-tensioning strand eccentricity, as shown.

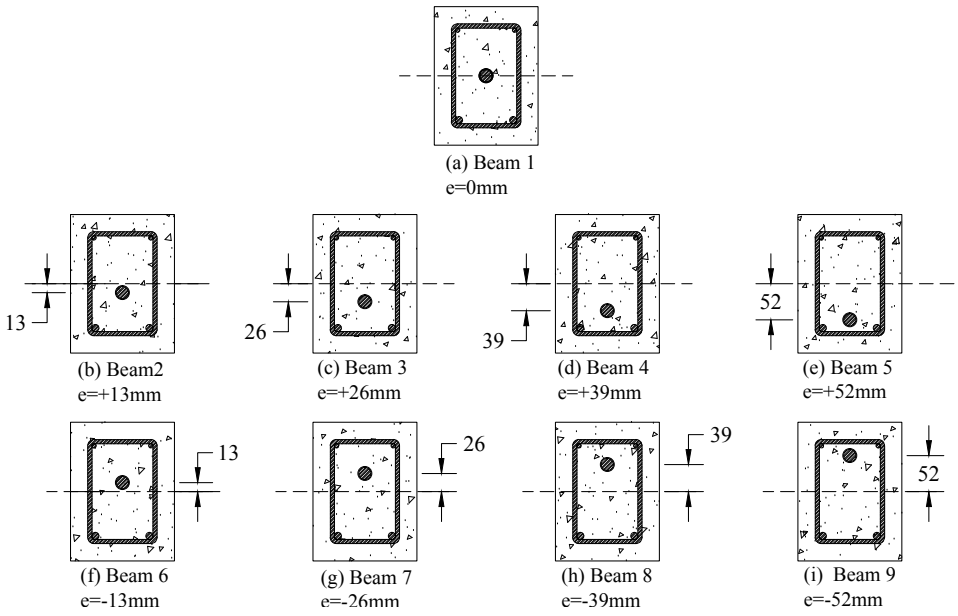

Figure 6.19.: Cross sections of 9 beams tested.

6.7. Experimental Analysis

Section 6.5 described the set-up of the static and dynamic testing on the 9 uncracked post-tensioned concrete beams in the laboratory, including details of the instrumentation used to monitor the beams during testing. This section describes the analysis of the dynamic results obtained, including the signal processing and peak picking regime invoked to extract the natural frequencies of the post-tensioned concrete beams, in Section 6.7.1. Section 6.7.2 outlines the calculation of the damping ratios of the post-tensioned concrete beams via the half-power bandwidth method.

6.7.1. Analysis of Dynamic data

The signal processing regime outlined had been reported previously (Noble et al., 2015c, 2016). Following collection of the impact hammer data in the System 6000, the raw acceleration-time signals were imported into MATLAB (MATLAB, 2014). The Fast Fourier Transform (FFT) was then performed on the acceleration data in the time domain, representing the signal in the frequency domain. A peak picking algorithm was used to identify the peaks in the frequency domain. Sample results can be seen in Figure 6.20, which shows the unprocessed noisy data in both the time and the frequency domain. As shown, the fundamental bending frequency can be identified from peak picking. The peak picking method is the simplest means of determining the modal characteristics in the frequency domain, in which the natural frequencies correspond to the peaks in the FFT, however as pointed out by Foti et al. (2014) *"this method is not reliable when the different modes of vibration are not sufficiently separated from each other."*

The raw signal contained significant electrical noise. Subsequently, the peaks in the frequency domain were initially difficult to determine. This is outlined in Figure 6.20. The fundamental peak is readily identifiable at a value of approximately 71.8Hz, as shown in Figure 6.20a and Figure 6.20b, however all subsequent peaks are distorted due to high frequency noise components in the signal. A signal processing algorithm was developed in MATLAB (MATLAB, 2014) and is outlined in Figure 6.21. Following smoothing in the frequency domain, the peak picking algorithm was reapplied and the peaks were again determined. The search bands for the fundamental frequency of each beam were defined as 55-85Hz (Noble et al., 2015c, 2016).

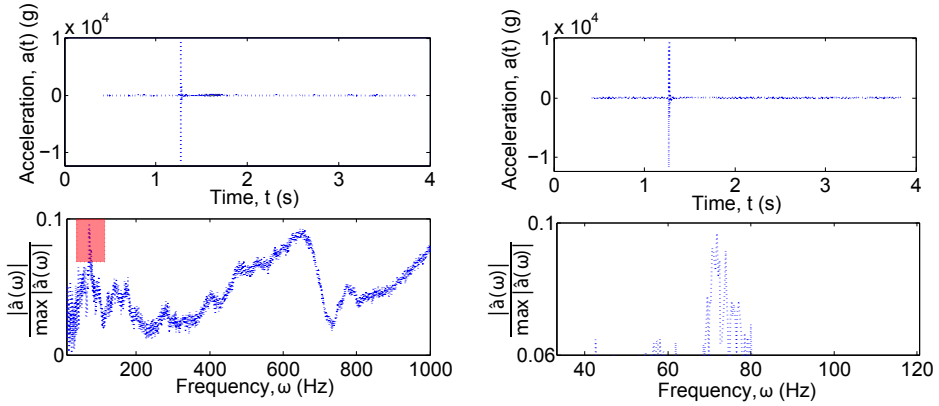

Figure 6.20.: Unprocessed, noisy signal at different scales (a) and (b). Identification of fundamental bending frequency possible. Higher modes unintelligible.

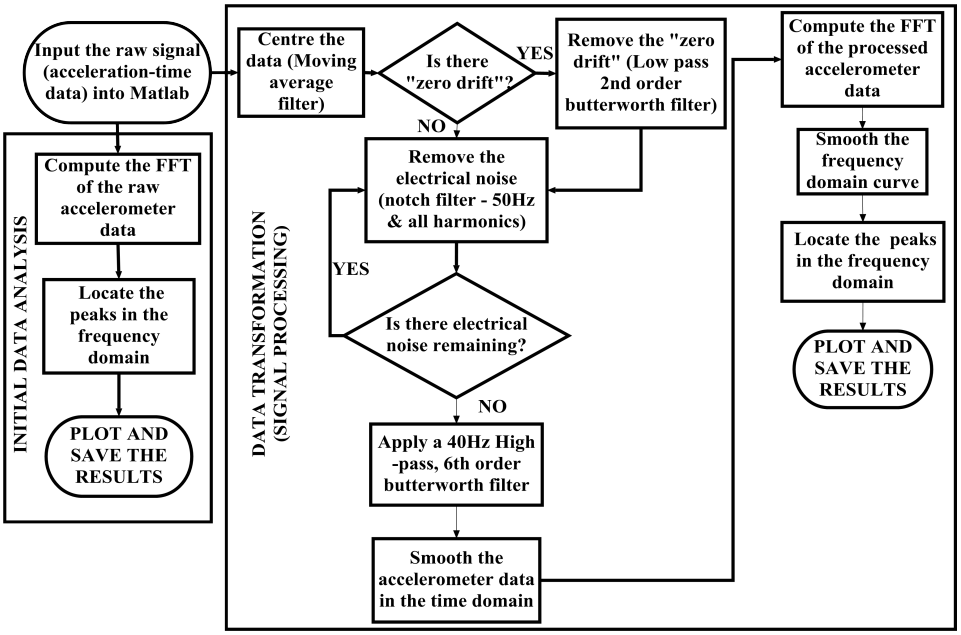

Figure 6.21.: Signal processing algorithm flow chart.

Following signal processing, the structural peaks were much easier to identify as outlined in Figure 6.22a. The peaks in the frequency domain were identified as the natural frequencies of the structural system, as shown in Figure 6.22b. This algorithm is required to deal with the high levels of noise associated with impact testing of concrete beams with a relatively

high fundamental bending frequency, which is expected to be in the region of 78Hz (Noble et al., 2015c, 2016).

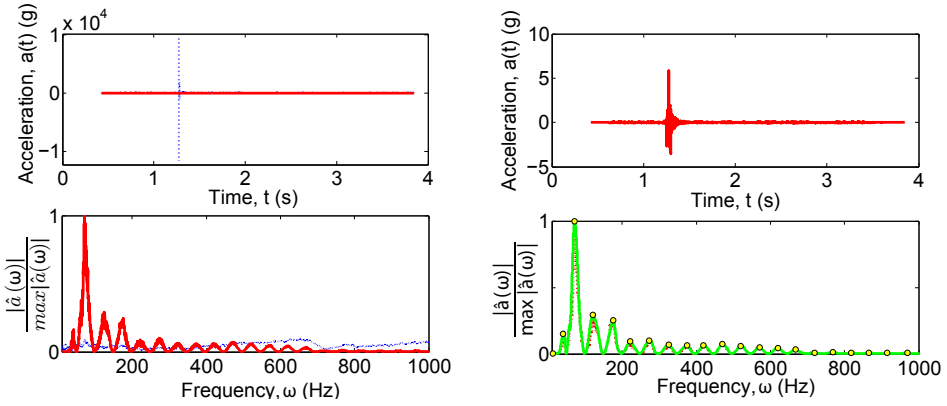

(a) (b)

Figure 6.22.: (a) Signal Processing and (b) Peak Picking to identify correct fundamental bending frequencies.

Figure 6.22 shows a typical accelerometer response of a post-tensioned concrete beam. Figure 6.22a and 6.22b show the accelerometer signals in both the time and frequency domain, before the signal was processed to eliminate noise and after signal processing. The scale of the acceleration axis in the time domain of each signal is significantly reduced following signal processing, indicating the extent of the amplitude attributable to noise components (Noble et al., 2015c, 2016).

6.7.2. Calculation of Damping Ratios, ξ

The damping ratio, ξ of the 9 uncracked post-tensioned concrete beams were calculated for each axial load level using the half-power bandwidth method, as described by Noble et al. (2015a). The half-power bandwidth method enables evaluation of damping from forced vibration tests without knowing the applied force, and is thus used in vibration and modal testing. By assuming that the damping ratio, ξ, is small and that the frequency at maximum amplitude is approximately equal to the undamped fundamental frequency, ω_1, the classical result relating the damping ratio to the half-power bandwidth can be written as (Wu, 2014);

$$\xi = \frac{\omega_b - \omega_a}{2\omega_1} \tag{6.17}$$

ω_a and ω_b are the half-power frequencies (i.e. the frequencies of the function at Max. Amplitude/$\sqrt{2}$). According to Wu (2014), the classical result is only valid for damping ratio less than 0.1, and is not a good prediction for $\xi > 0.1$. An example of the calculation of the damping ratio in accordance by the half-power bandwidth method is shown in Figure 6.23, and using the formula presented in Equation 6.17.

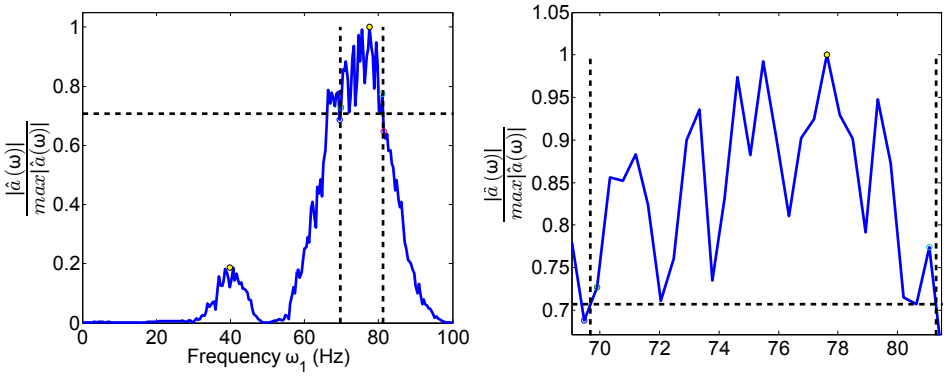

(a) (b)

Figure 6.23.: Half-power bandwidth method of calculation of damping ratio, ξ, on different scales on x and y axis; (a) and (b)

6.8. Experimental Results

Section 6.7 outlined the analysis of the dynamic results obtained from the dynamic impact testing of the 9 uncracked post-tensioned concrete beams tested, including the signal processing regime and peak picking algorithm used to identify the natural frequencies of the system. Furthermore, the estimation of the damping ratios, via the half-power bandwidth method is also presented.

In this section, the results of the static and dynamic testing will be described and analysed. Section 6.8.1 presents the results and statistical significance of the three point static bending tests conducted. Section 6.8.2 outlines the results and statistical significance of the dynamic impact testing, which include the three dimensional graphs of relative modal amplitude vs. frequency and post-tensioning load level, and the regression analysis of the fundamental frequency on post-tensioning load. Section 6.8.3 presents the

comparison of the static and dynamic regression models. Section 6.8.4 describes the relationship between the damping ratios and the post-tensioning force magnitude, including a regression analysis of damping ratios on post-tensioning force magnitude. Finally, Section 6.8.6 compares the obtained results to the mathematical prediction model outlined in Chapter 5.

6.8.1. Static Results

Static three-point bending tests were conducted on all 9 uncracked post-tensioned concrete beams. The post-tensioning force magnitude was varied and a point load was applied at midspan to the simply-supported post-tensioned concrete beam. The deflection corresponding to each transverse point load was measured, as described in Section 6.6.1 previously. This was repeated twice for each beam tested to help reduce experimental error. Both iterations were recorded and the results are displayed in Figures 6.25-6.33, labelled as *'Iteration 1'* and *'Iteration 2'*. A sample set of results are displayed in Table 6.9. From the collected load-deflection data, the equivalent static flexural rigidity, EI was estimated using the following equation for deflection at midspan of a simply-supported beam due to a point-load applied at mid-span;

$$\delta = \frac{P\ell^3}{48EI} \tag{6.18}$$

Rearranging, the equivalent static flexural rigidity is given as;

$$EI = \frac{P\ell^3}{48\delta} \tag{6.19}$$

The equation for the n^{th} natural bending frequency of a simply-supported beam is given as;

$$\omega_n = \left(\frac{n\pi}{\ell}\right)^2 \sqrt{\frac{EI}{m}} \tag{6.20}$$

Where n is the mode number, ℓ is the span length, E is the Young's Modulus of Elasticity and I is the second moment of area of the cross section. In order to obtain a predicted static-equivalent bending frequency, $\omega_{n,S}$ the

following substitution is made;

$$\omega_{n,S} = \left(\frac{n\pi}{\ell}\right)^2 \sqrt{\frac{P\ell^3}{48\delta m}} \tag{6.21}$$

This transformation from equivalent static flexural rigidity to fundamental natural bending frequency (i.e. $n = 1$) is given for Beam 1 (e=0mm) in Figure 6.24. Sample data for Beam 3 (e=+26mm) is given below in Table 6.9. The difference between the deflection data on either beam face is significant in this instance, highlighting the extent of the error in the experiment, and the possibility of torsion in the concrete beam section.

Table 6.9.: Sample static data for Beam 3 (e=+26mm)

N (kN)	P (kN)	δ_1 (mm)	δ_2 (mm)	EI_1 $(kNmm^2)$	EI_2 $(kNmm^2)$	EI_{ave} $(kNmm^2)$	$\omega_{1,S_{ave}}$ Hz
0.15	10.1	0.80	1.00	2.10E+09	1.68E+09	1.89E+09	63.08
0.16	10.5	0.79	1.00	2.22E+09	1.75E+09	1.98E+09	64.54
23.06	10.6	0.64	1.00	2.76E+09	1.77E+09	2.26E+09	68.96
23.00	10.7	0.63	1.00	2.83E+09	1.78E+09	2.31E+09	69.62
44.53	11.3	0.53	1.00	3.55E+09	1.88E+09	2.72E+09	75.58
44.39	11.5	0.55	1.00	3.48E+09	1.92E+09	2.70E+09	75.33
63.07	12.5	0.47	1.00	4.43E+09	2.08E+09	3.26E+09	82.74
62.95	12.5	0.48	1.01	4.34E+09	2.06E+09	3.20E+09	82.02
82.34	13.7	0.44	1.01	5.19E+09	2.26E+09	3.73E+09	88.47
82.26	13.4	0.44	1.00	5.08E+09	2.23E+09	3.65E+09	87.63
100.69	14.1	0.40	1.00	5.88E+09	2.35E+09	4.11E+09	92.96
100.72	14.5	0.43	1.01	5.62E+09	2.39E+09	4.01E+09	91.75
121.04	15.2	0.41	1.00	6.18E+09	2.53E+09	4.36E+09	95.67
120.77	15.3	0.40	1.00	6.38E+09	2.55E+09	4.46E+09	96.83
141.48	15.8	0.34	1.00	7.75E+09	2.63E+09	5.19E+09	104.42
141.31	15.7	0.40	1.00	6.54E+09	2.62E+09	4.58E+09	98.09
161.64	16.0	0.39	1.00	6.84E+09	2.67E+09	4.75E+09	99.92
161.20	16.4	0.40	1.00	6.83E+09	2.73E+09	4.78E+09	100.25
179.96	16.8	0.38	1.02	7.37E+09	2.75E+09	5.06E+09	103.08
179.49	16.5	0.36	1.00	7.64E+09	2.75E+09	5.19E+09	104.47
202.42	16.9	0.38	1.02	7.41E+09	2.76E+09	5.09E+09	103.38
201.54	16.7	0.37	1.00	7.52E+09	2.78E+09	5.15E+09	104.05

Figure 6.24a shows the measured change in static flexural rigidity, EI, with increasing post-tensioning force magnitude for Beam 1 (e=0mm), and Figure 6.24b shows the equivalent static prediction of the fundamental bending frequency using Equation 6.21. Figures 6.25-6.33 show the static prediction of natural bending frequency based on the measured 3-point bending

data for all 9 uncracked post-tensioned concrete beams for varying post-tensioning force magnitude. In the case of Beams 1-6, a statistically significant increasing trend is observed in predicted static-equivalent fundamental bending frequencies with increasing post-tensioning force. In the case of Beams 2-5, the effect of the post-tensioning strand eccentricity is to cause the beams to camber upwards and the downward deflection to be reduced. In the case of Beams 6-9, the effect of the post-tensioning strand eccentricity is such as to induce further cracking in the bottom fibre and cause further sagging in the simply supported beam, therefore a lesser magnitude of midspan point load would be required to induce the 1mm deflection, and therefore, the static flexural rigidity, and hence the natural bending frequency is predicted to decrease. Beam 1 (e=0mm) has zero eccentricity, and therefore no moment due to prestressing force. In this case, the axial normal stress acts so as to ensure the entire section acts in pure compression, significantly increasing its capacity to resist transverse load before cracking occurs in the bottom fibre of the section.

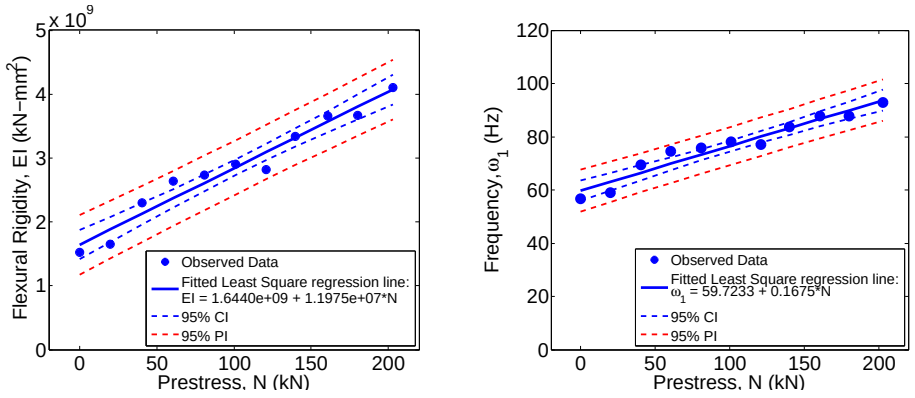

(a) (b)

Figure 6.24.: (a) Beam 1 (e=0mm); Static, EI (b) Beam 1 (e=0mm); Dyn. equiv. ω_1

For Figures 6.25 to 6.30, it is determined that for Beam 1-6, a statistically significant increase in static-equivalent natural bending frequency with increasing post-tensioning load magnitude is apparent. However, for Beam 7-9, no statistically significant trend can be identified in the data. This is concurrent with what was predicted due to the different stress distributions in the given sections. Beam 7-9 have eccentricities that promote further

bending and cracking in the bottom fibre, and hence increasing the post-tensioning load acts as to open cracks and theoretically decrease the bending frequency. This has not been found experimentally. At best, from this data, a non-significant statistical trend is all that can be observed.

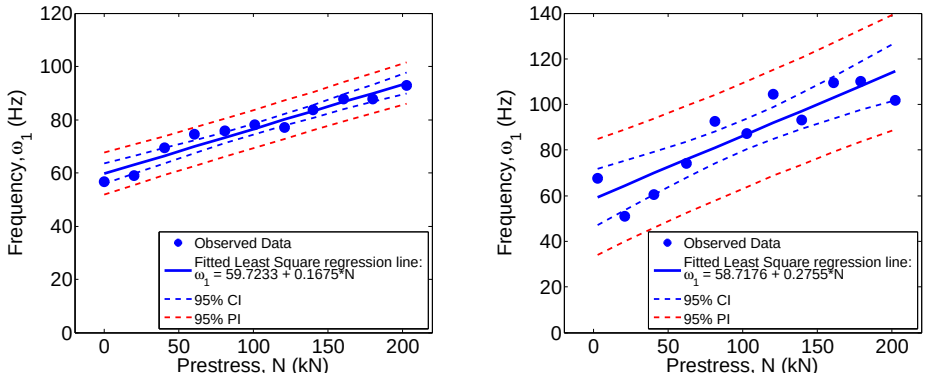

(a) (b)

Figure 6.25.: Equivalent static frequency as a function of post-tensioning load; (a) Beam 1 (e=0mm); Iteration 1 (b) Beam 1 (e=0mm); Iteration 2

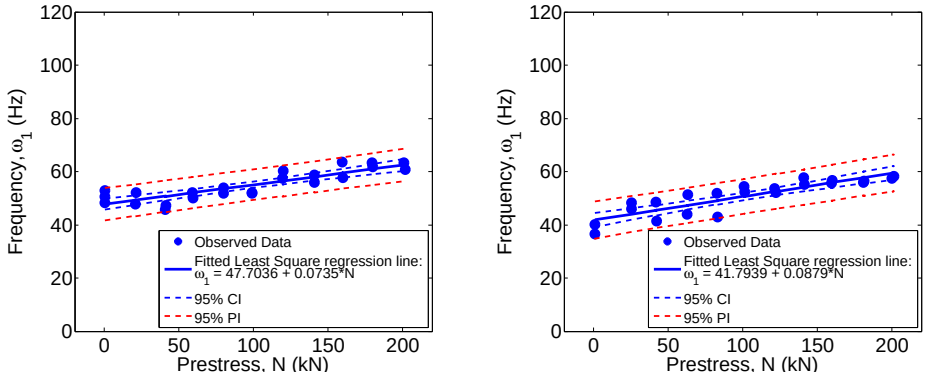

(a) (b)

Figure 6.26.: Equivalent static frequency as a function of post-tensioning load; (a) Beam 2 (e=+13mm); Iteration 1 (b) Beam 2 (e=+13mm); Iteration 2

These static-equivalent bending frequencies shall be compared against the measured natural bending frequencies obtained from dynamic impact testing on the same post-tensioned concrete sections in Section 6.8.3.

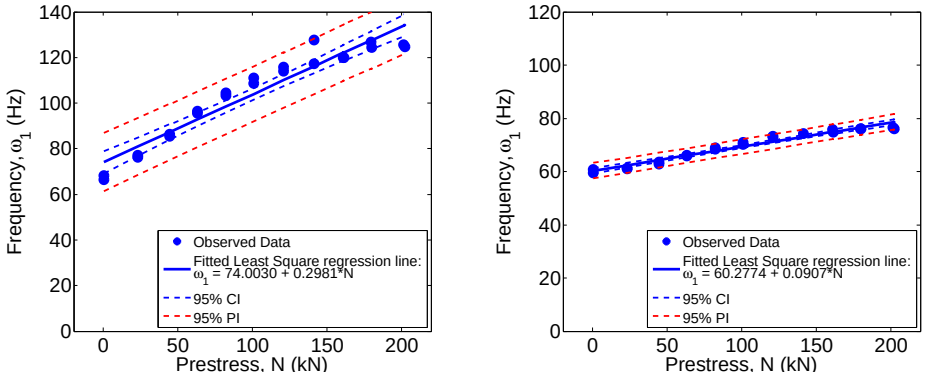

(a) (b)

Figure 6.27.: Equivalent static frequency as a function of post-tensioning load; (a) Beam 3 (e=+26mm); Iteration 1 (b) Beam 3 (e=+26mm); Iteration 2

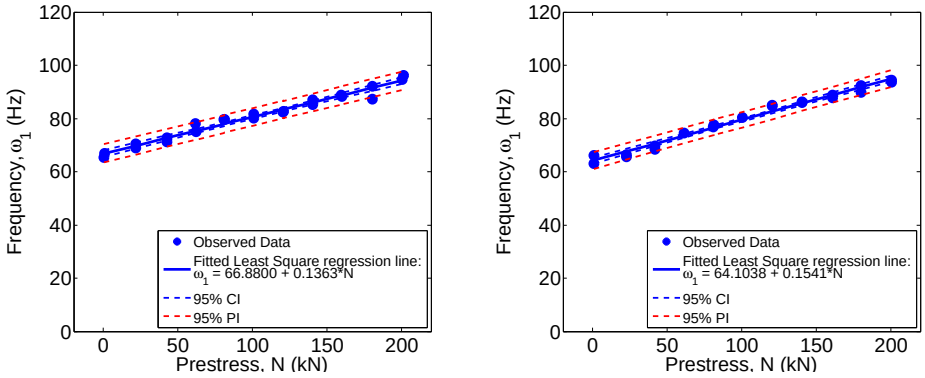

(a) (b)

Figure 6.28.: Equivalent static frequency as a function of post-tensioning load; (a) Beam 4 (e=+39mm); Iteration 1 (b) Beam 4 (e=+39mm); Iteration 2

6.8.2. Dynamic Results

Figure 6.34 shows sample results for Beam 2 (e=+13mm). Figure 6.34a shows the peaks of the frequency domain representation of all 30 signals superimposed on each other for each post-tensioning load level. In total, there are 330 signals superimposed in the graph. The dominance of the fundamental bending mode of vibration is evident from this figure, due to the relative contribution of this mode to the overall structural dynamic response of the

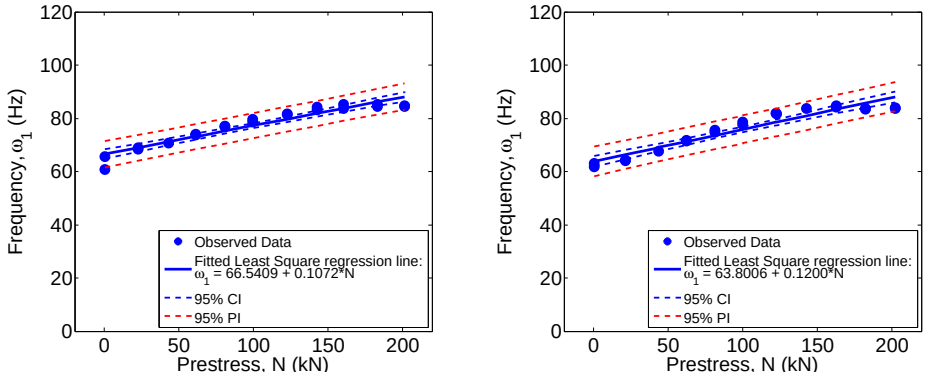

(a) (b)

Figure 6.29.: Equivalent static frequency as a function of post-tensioning load; (a) Beam 5 (e=+52mm); Iteration 1 (b) Beam 5 (e=+52mm); Iteration 2

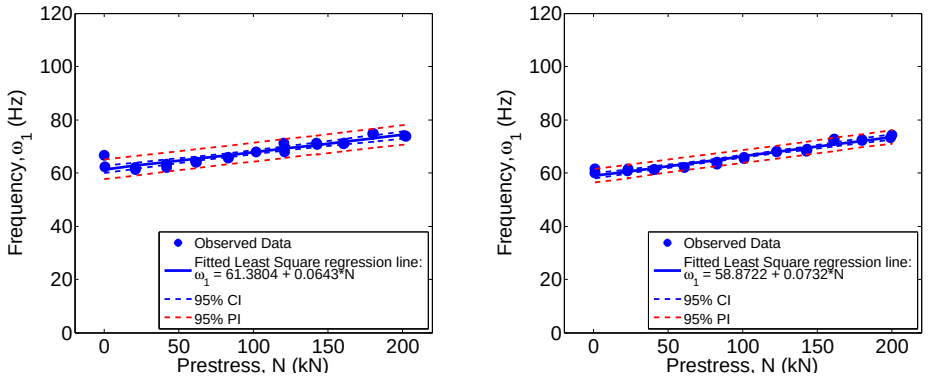

(a) (b)

Figure 6.30.: Equivalent static frequency as a function of post-tensioning load; (a) Beam 6 (e=-13mm); Iteration 1 (b) Beam 6 (e=-13mm); Iteration 2

system. This dominance of the first bending mode was observed for all 9 beams tested. The vertical axis shows the normalised relative modal amplitude of the response of the system. Figure 6.34b represents Figure 6.34a in two dimensions. The diameter of the data points is directly proportional to the relative modal amplitude. All peaks in the frequency domain in the range of 0-1000Hz are plotted against the post-tensioning load level of the tested specimen. The fundamental bending frequency has been identified to lie within the search bands of 55 to 85Hz. Figure 6.34c zooms in on

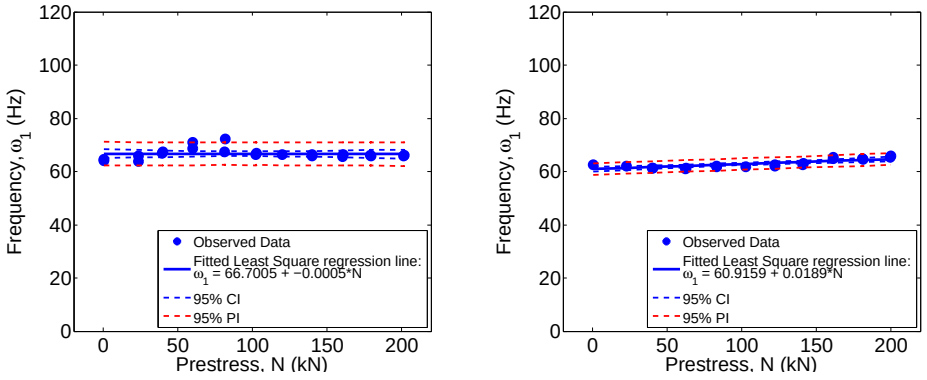

(a) (b)

Figure 6.31.: Equivalent static frequency as a function of post-tensioning load; (a) Beam 7 (e=-26mm); Iteration 1 (b) Beam 7 (e=-26mm); Iteration 2

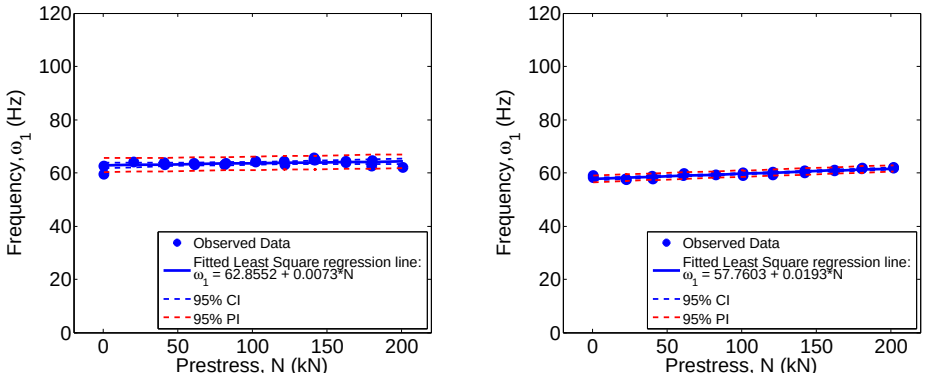

(a) (b)

Figure 6.32.: Equivalent static frequency as a function of post-tensioning load; (a) Beam 8 (e=-39mm); Iteration 1 (b) Beam 8 (e=-39mm); Iteration 2

Figure 6.34b and shows the estimation of the first modal frequency from peak picking of each of the 330 dynamic signals obtained, at different post-tensioning load levels. The scatter in the estimation of the fundamental frequency is noted to be large. Figure 6.34d shows some simple data analytics. The standard deviation, σ of the data ranges between 2 and 4Hz, which is between 3 and 5% of the mean, μ of each data set (Noble et al., 2015c).

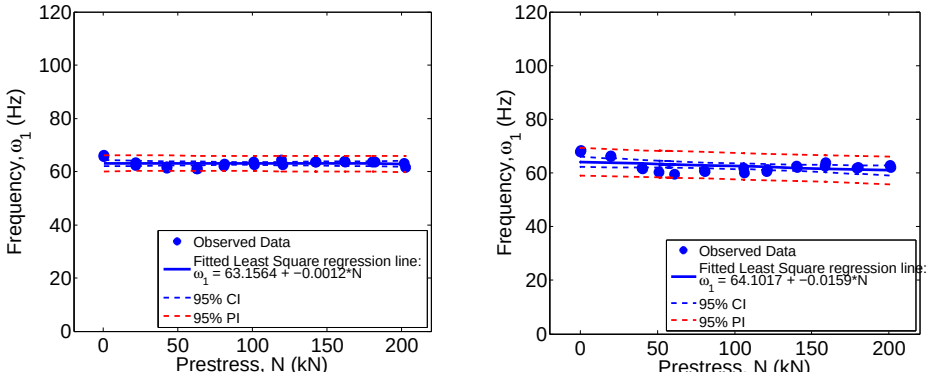

(a) (b)

Figure 6.33.: Equivalent static frequency as a function of post-tensioning load; (a) Beam 9 (e=-52mm); Iteration 1 (b) Beam 9 (e=-52mm); Iteration 2

3D Graphs

Figures 6.35 to 6.37d show 3D graphs of normalised relative modal amplitude of the response of the system versus frequency and post-tensioning load level. As can be seen in each of the graphs, the dominance of the first bending mode of vibration in the overall structural dynamic response of the system is evident. Figure 6.35 shows the frequency response of Beam 1 (e=0mm) for each axial load level. Figure 6.36 shows the frequency response of Beams 2, 3, 4 and 5, who have post-tensioning strand eccentricities that promote upward camber and compression in the bottom fibre of the section. Figure 6.37 shows the frequency response of Beams 6, 7, 8 and 9 who have post-tensioning strand eccentricities that conversely, promote tension in the bottom fibre. The importance of these graphs is that they highlight the dominance of the first bending mode of vibration in the overall structural dynamic response of all 9 post-tensioned concrete beams tested in the laboratory.

Regression Analysis

Figures 6.40 to 6.42 show the results of a linear regression analysis that has been applied to the relationship between the fundamental bending mode of vibration and the post-tensioning load level. The results for Beam No.2 have been published previously (Noble et al., 2015c), but this chapter expands on

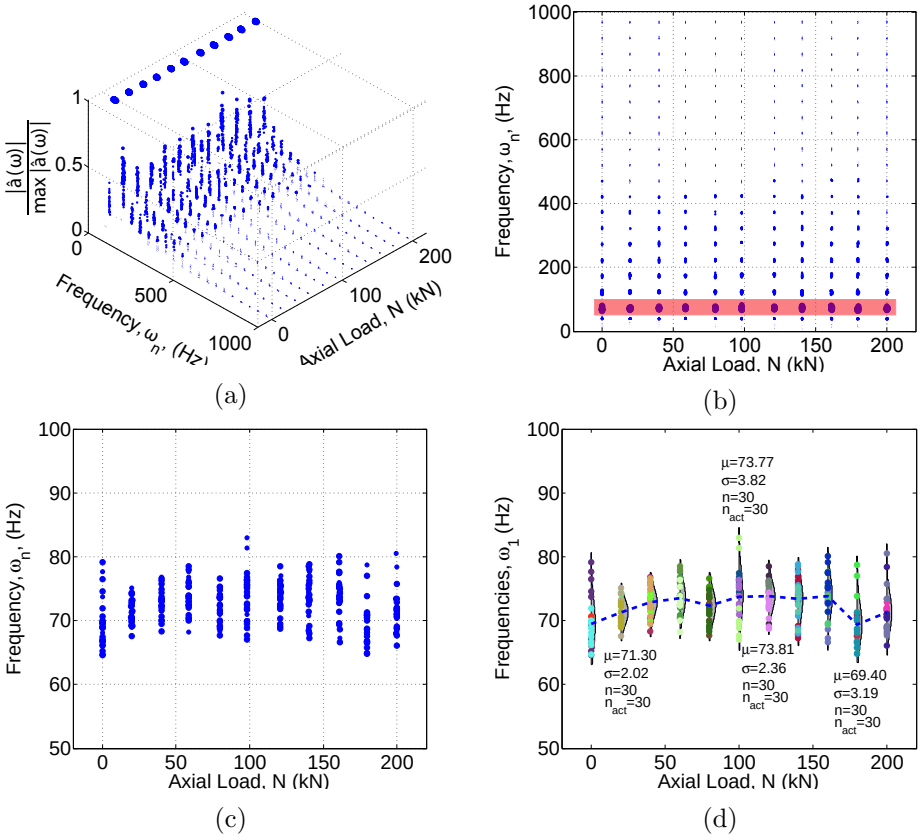

Figure 6.34.: (a) Processed signals in frequency domain as a function of axial load (3D); (b) All modes plotted against axial load (2D); (c) Zooming in on the fundamental bending frequency; (d) Simple data analytics on the measured frequencies as a function of axial force (Beam 2).

previous studies and reports on results for a whole suite of 9 post-tensioned concrete beams. The smaller data points represent each individual estimation of the fundamental frequency, while the larger data points represent the mean of each data set. The inner dashed lines represents the 95% confidence interval for the regression line, while the outer dashed lines are the 95% prediction interval for an individual estimation. The results of statistical t-test on the regression slope parameter, for each of the 9 beams tested, are displayed in Table A.4 in Appendix A.3 on page 337. It was found, for 6 of the 9 uncracked post-tensioned concrete beams (namely, Beams 1,2,3,4,6,9) that there is no statistically significant change in fundamental bending frequency with prestress force magnitude. Three beams showed a statistically

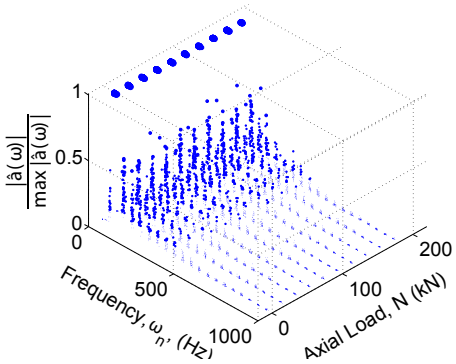

Figure 6.35.: Rel. Modal Amplitude vs. frequency and post-tensioning load; Beam 1 (e=0mm)

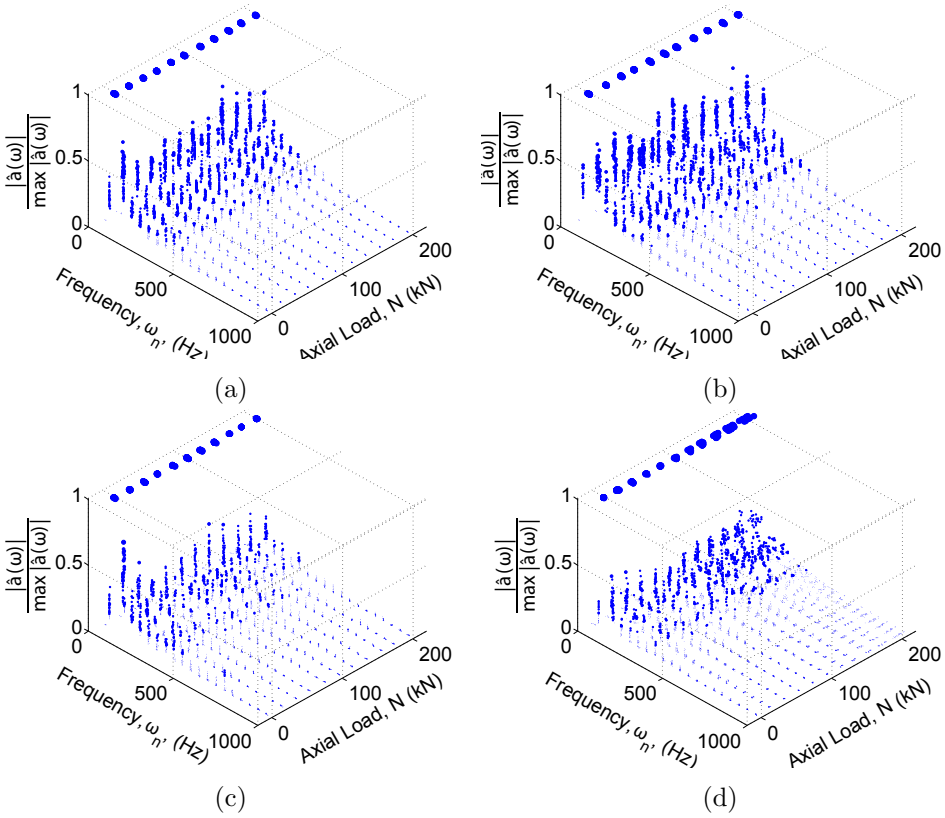

Figure 6.36.: Rel. Modal Amplitude vs. frequency and post-tensioning load; (a) Beam 2 (e=+13mm); (b) Beam 3 (e=+26mm); (c) Beam 4 (e=+39mm); (d) Beam 5 (e=+52mm)

significant increase in fundamental bending frequency with increasing post-tensioning force magnitude (namely Beams 5,7,8). Furthermore, Figure 6.38

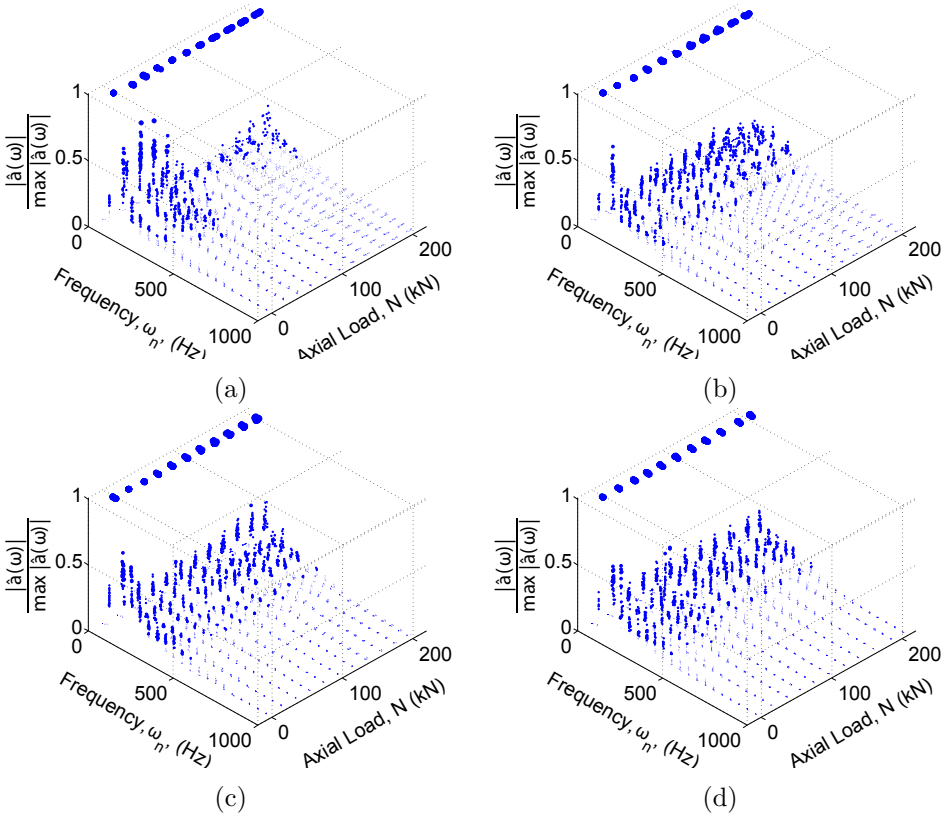

Figure 6.37.: Rel. Modal Amplitude vs. frequency and post-tensioning load; (a) Beam 6 (e=-13mm); (b) Beam 7 (e=-26mm); (c) Beam 8 (e=-39mm); (d) Beam 9 (e=-52mm)

shows all data for Beam No.2 plotted on a normal probability paper plot. All data points lie within the boundaries that would be expected if it were from the same, Normal parent distribution. This further indicates that any observed changes in natural frequency with post-tensioning load magnitude is likely due to chance rather than any systematic effect. Similar results have been observed for 6 of the 9 beams tested.

As outlined by Noble et al. (2015c), Figure 6.39 shows a comparison of the different regression lines for each of the 9 beams plotted against one another. Figure 6.39a shows the results for Beams 1-5 while Figure 6.39b shows the results for Beam 1 and Beams 6-9. Theory would suggest that as the eccentricity increases, the intercept values of the regression lines should also increase, as there is increased second moment of area due to the parallel axis theorem, and a subsequent expected increase in 'virgin' natural bending

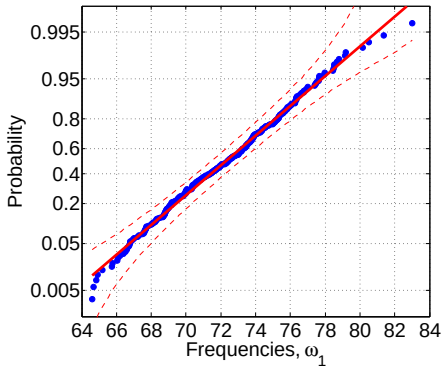

Figure 6.38.: All data for Beam 2 (e=+13mm) plotted on a normal probability paper, indicating data normality.

frequencies for the simply supported post-tensioned beams. However, as shown in Figure 6.39, this is not the case. Statistically significant increases in natural frequency with increasing post-tensioning load were observed for Beam Nos. 5,7 & 8. All other beams displayed no statistically significant changes in natural frequency. This is outlined further in Table 4.11. From Figure 6.39 there is some evidence to suggest that the variation in the fundamental frequency with increasing post-tensioning load magnitude is greater for the largest values of eccentricity, e, as the trend for Beam 5 (e=+52mm) shows a much larger increase in frequency over the tested range than for the other beams.

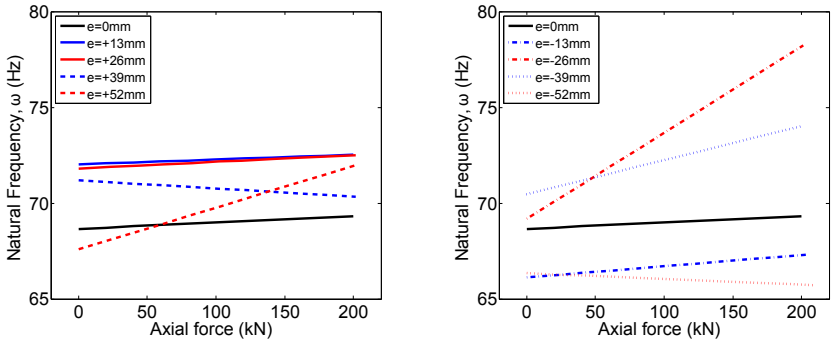

Figure 6.39.: Collated data of linear regression of fundamental bending frequency as a function of post-tensioning load for (a) Beams 1-5 and (b) Beams 1, 6-9.

Table 4.11 shows the calculated linear regression intercept parameter

$(\alpha_{0,i})$, and slope parameter $(\alpha_{1,i})$ when regressing ω_1 on N for all 9 beams (i). The corresponding linear regression equations are obtained by substituting into the following formula;

$$\omega_1 = \alpha_{0,i} + \alpha_{1,i}N \tag{6.22}$$

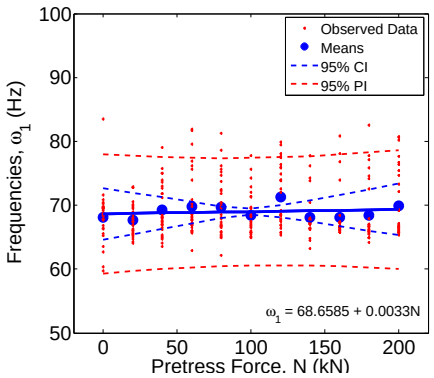

Figure 6.40.: Regression of ω_1 on N; Beam 1 (e=0mm)

6.8.3. Static vs. Dynamic results

Figure 6.43 to 6.45 shows the comparison between the static-equivalent prediction of fundamental bending frequency to the measured frequencies from the dynamic data. The linear regression lines for both the static-equivalent predictions and the dynamic data are plotted against one another for each of the 9 beams tested. For Beams 1,2,3,4,5,6 the static-equivalent prediction of fundamental bending frequency shows a statistically significant increase in the bending frequency with increasing post-tensioning force magnitude. However, in comparison, the results from the dynamic testing show no statistically significant trend in the data. For Beams 7,8 & 9, the static-equivalent data shows no statistically significant trend with increasing post-tensioning force magnitude.

6.8.4. Damping ratios

Figures 6.46 to 6.48 shows the results of a statistical regression analysis of calculated critical damping ratios versus post-tensioning force magnitude. Figures 6.46- 6.48d should be analysed in conjunction with Table A.6, which

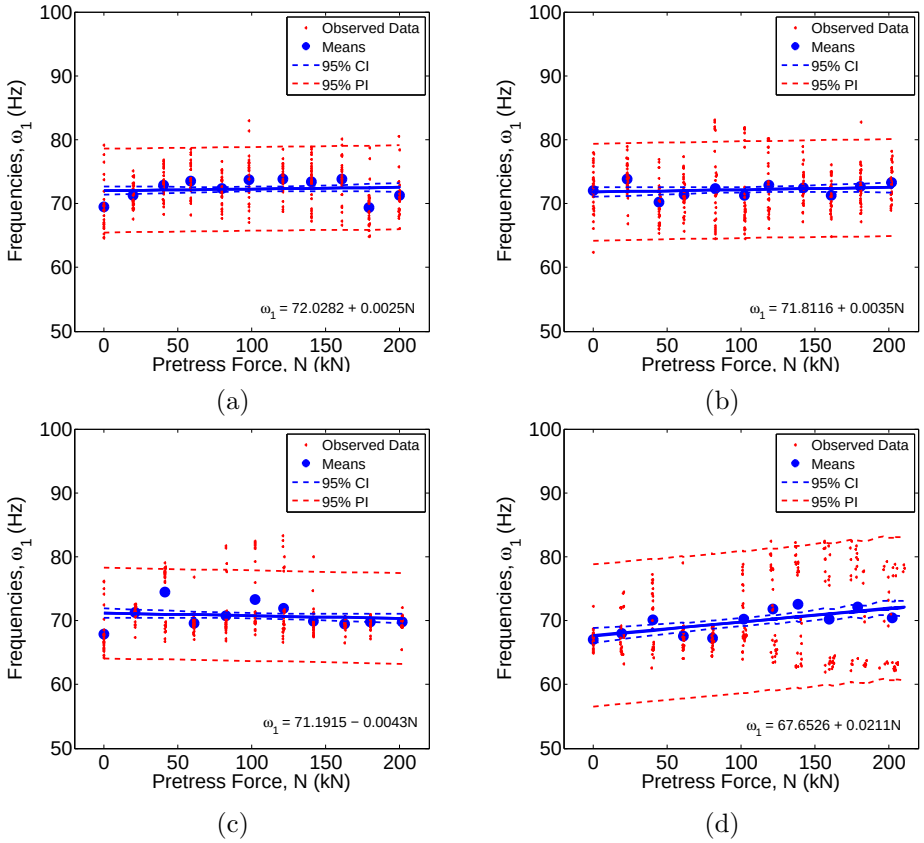

Figure 6.41.: Regression of ω_1 on N; (a) Beam 2 (e=+13mm); (b) Beam 3 (e=+26mm); (c) Beam 4 (e=+39mm); (d) Beam 5 (e=+52mm)

outlines the statistical linear regression parameters, indicating the statistical significance of the changes observed in Figures 6.46- 6.48d. Beams 1,4 & 6 show no statistically significant relationship between damping ratio and post-tensioning load level. Beams 2,8 & 9 show a statistically significant decreasing trend in damping ratio with increasing post-tensioning load level, while Beams 3,5 & 7 show a statistically significant increasing trend in damping ratio with increasing post-tensioning load level. As such, the testing results are inconclusive. No definitive statement on the relationship between damping ratio and post-tensioning force magnitude can be made, based on the obtained results, as depending on the beam tested, different statistical significance conclusions have been observed. The value of the critical damping ratio measured ranges between 0.23-5.01%, which is in the range predicted for concrete structures.

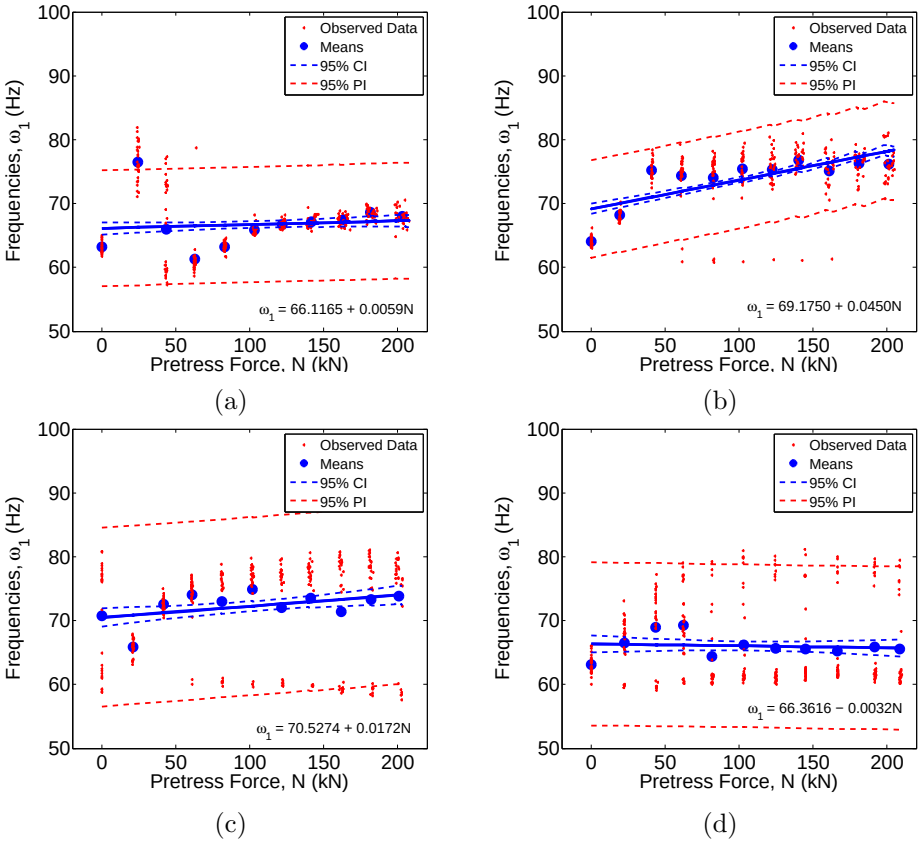

Figure 6.42.: Regression of ω_1 on N; (a) Beam 6 (e=-13mm); (b) Beam 7 (e=-26mm); (c) Beam 8 (e=-39mm); (d) Beam 9 (e=-52mm)

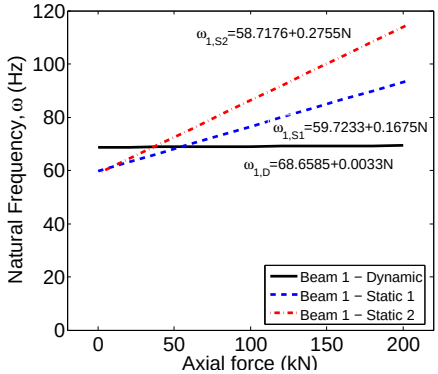

Figure 6.43.: Comparing regression lines - static vs. dynamic results; Beam 1 (e=0mm)

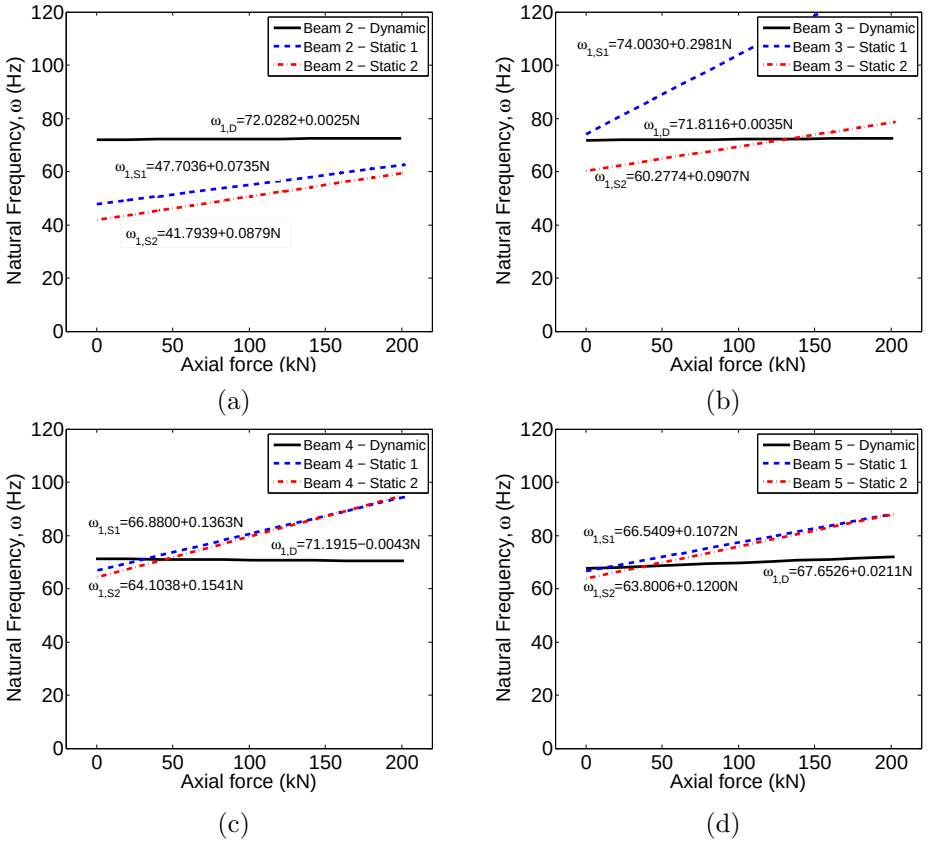

Figure 6.44.: Comparing regression lines - static vs. dynamic results; (a) Beam 2 (e=+13mm); (b) Beam 3 (e=+26mm); (c) Beam 4 (e=+39mm); (d) Beam 5 (e=+52mm)

6.8.5. Comparison of results with existing models

Chapter 2 outlines a series of models predicting changes in natural frequency with increasing post-tensioning force magnitude, compares and contrasts the models, while offering critique on the validity and accuracy of each of the models. Figures 6.49, 6.50 and 6.51 show the results obtained from the dynamic impact hammer testing and subsequent frequency analysis on the nine different uncracked post-tensioned concrete beams tested in the laboratory, compared to the predicted changes in fundamental bending frequencies according to the models proposed by Saiidi et al. (1994), Miyamoto et al. (2000), Kim et al. (2004), Zhang et al. (2012) and Dall'Asta and Dezi (1996).

Figure 6.49 shows good agreement between obtained results and the pre-

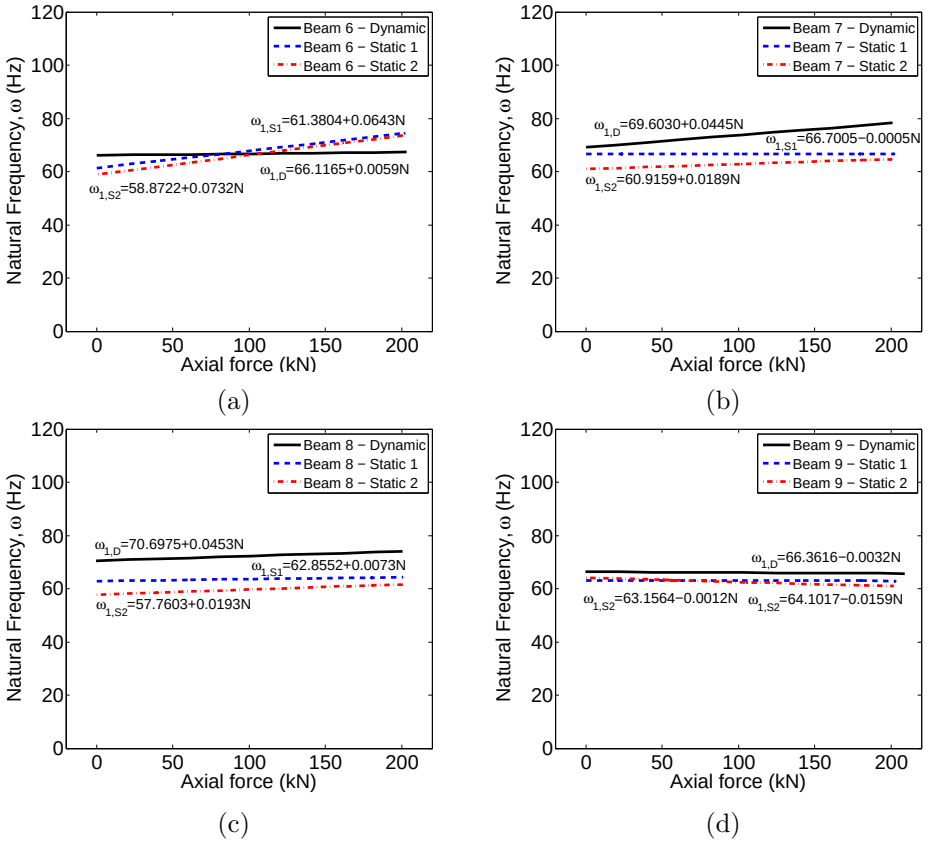

Figure 6.45.: Comparing regression lines - static vs. dynamic results; (a) Beam 6 (e=-13mm); (b) Beam 7 (e=-26mm); (c) Beam 8 (e=-39mm); (d) Beam 9 (e=-52mm)

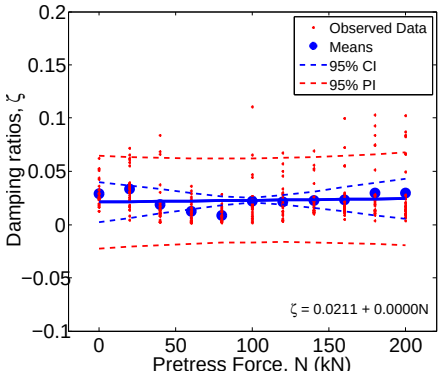

Figure 6.46.: Regression of ξ on N; Beam 1 (e=0mm)

diction models outlined by Saiidi et al. (1994), Miyamoto et al. (2000), Kim et al. (2004), Zhang et al. (2012) and Dall'Asta and Dezi (1996). The re-

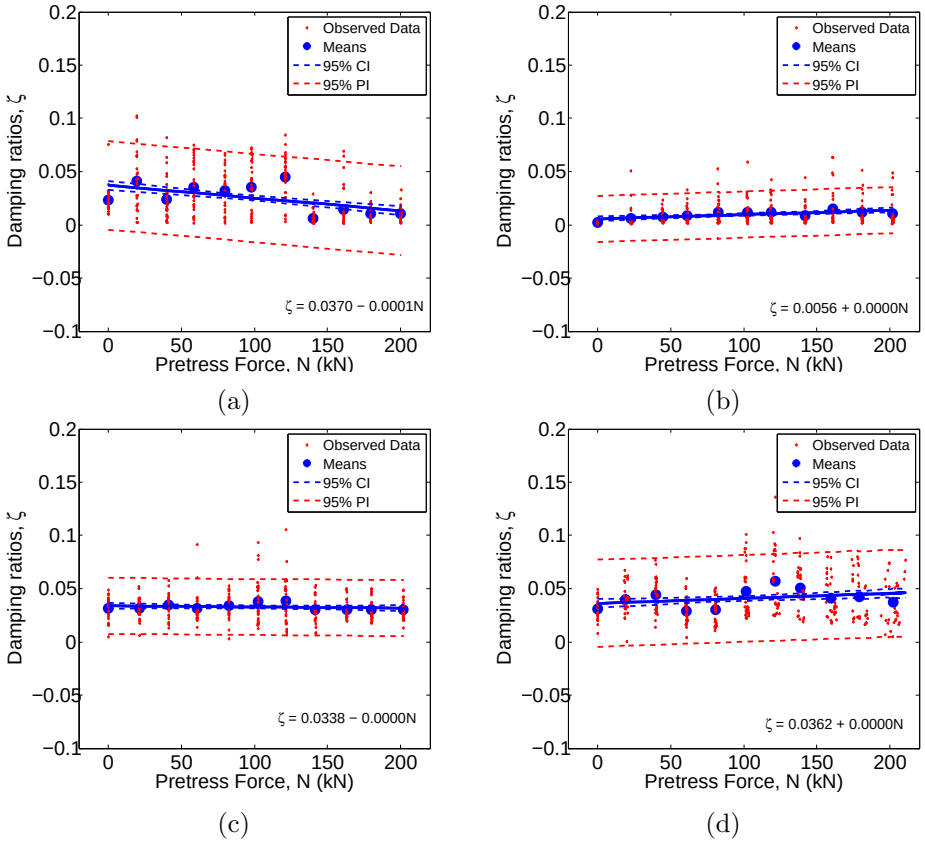

Figure 6.47.: Regression of ξ on N; (a) Beam 2 (e=+13mm); (b) Beam 3 (e=+26mm); (c) Beam 4 (e=+39mm); (d) Beam 5 (e=+52mm)

sults indicate that there is no statistically significant relationship between post-tensioning force magnitude and fundamental bending frequency for the beam with zero eccentricity, and as such, follows that predicted by Hamed and Frostig (2006). However, the calculated linear regression line in this instance, indicates a slightly increasing trend in fundamental frequency with increasing post-tensioning force magnitude, and is bounded by the prediction models outlined by Saiidi et al. (1994) and Kim et al. (2004).

Figures 6.50a-6.50d show the results for the beams labelled 2-5, with positive post-tensioning strand eccentricities, promoting tension in the top fibre of the beam. Beams 2 & 3 (Figures 6.50a & 6.50b) indicate no statistically significant increasing or decreasing trend in fundamental frequency with increasing post-tensioning force magnitude, however, like Beam 1 previously,

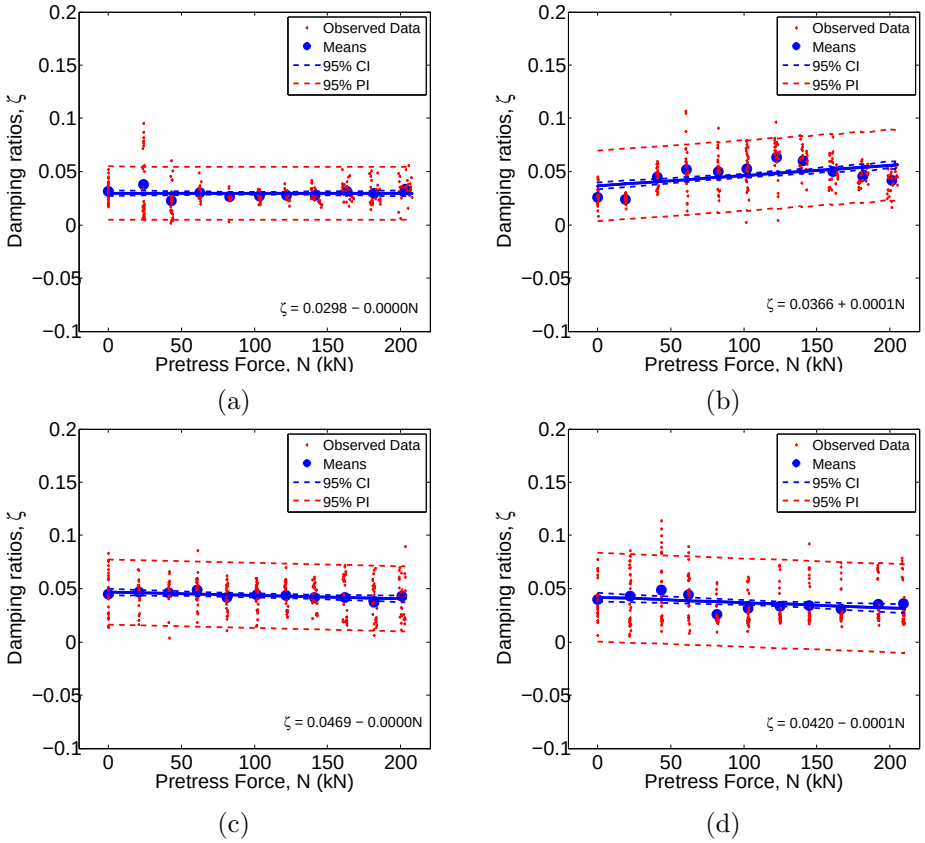

Figure 6.48.: Regression of ξ on N; (a) Beam 6 (e=-13mm); (b) Beam 7 (e=-26mm); (c) Beam 8 (e=-39mm); (d) Beam 9 (e=-52mm)

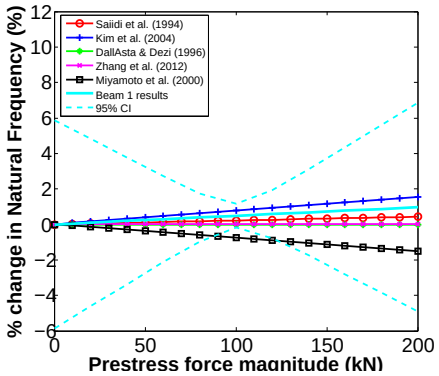

Figure 6.49.: Comparison of obtained results to existing models; Beam 1 (e=0mm)

the plotted linear regression lines in this instance show an increasing trend in fundamental frequency with increasing post-tensioning force magnitude,

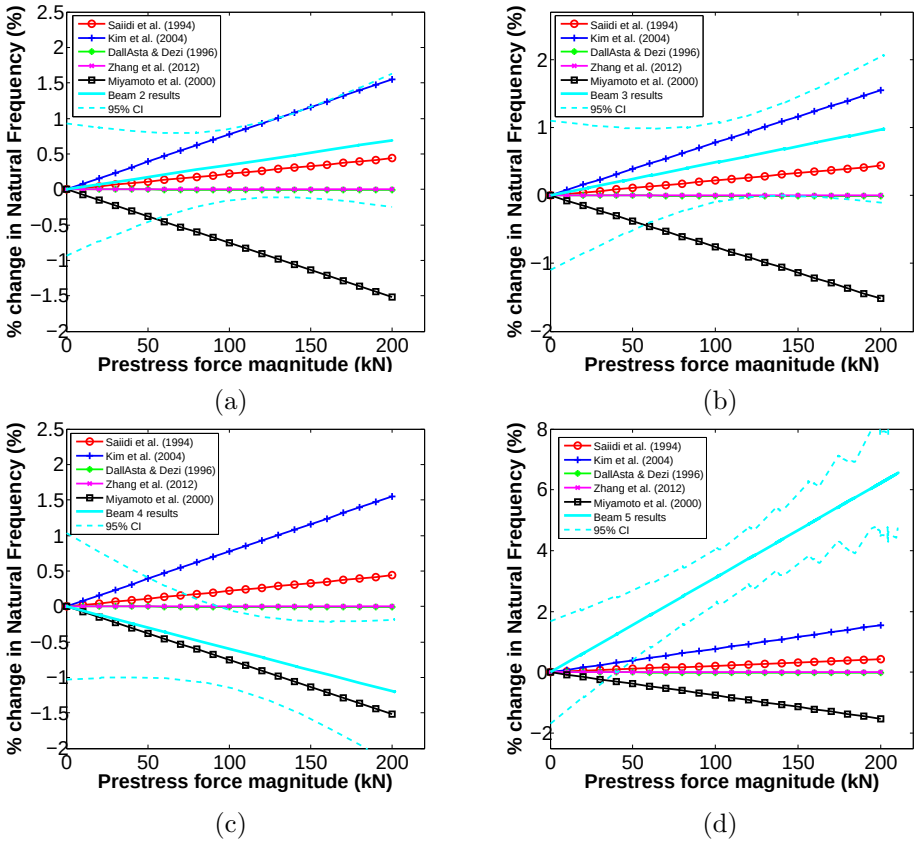

Figure 6.50.: Comparison of obtained results to existing models; (a) Beam 2 (e=+13mm); (b) Beam 3 (e=+26mm); (c) Beam 4 (e=+39mm); (d) Beam 5 (e=+52mm)

and as before, the results are bounded by the prediction models proposed by Saiidi et al. (1994) and Kim et al. (2004). Figure 6.50c shows a statistically significant decreasing trend in the fundamental bending frequency with increasing post-tensioning force magnitude, and follows the *"compression-softening"* model, as outlined by Miyamoto et al. (2000). Figure 6.50d shows a statistically significant increasing trend in fundamental bending frequency with increasing post-tensioning force magnitude, and the best fit linear regression line plotted to the obtained data indicates an increase much greater than any of the prediction models outlined previously (Saiidi et al., 1994; Miyamoto et al., 2000; Kim et al., 2004; Zhang et al., 2012; Dall'Asta and Dezi, 1996).

Figures 6.51a-6.51d show the results for the beams labelled 6-9, with neg-

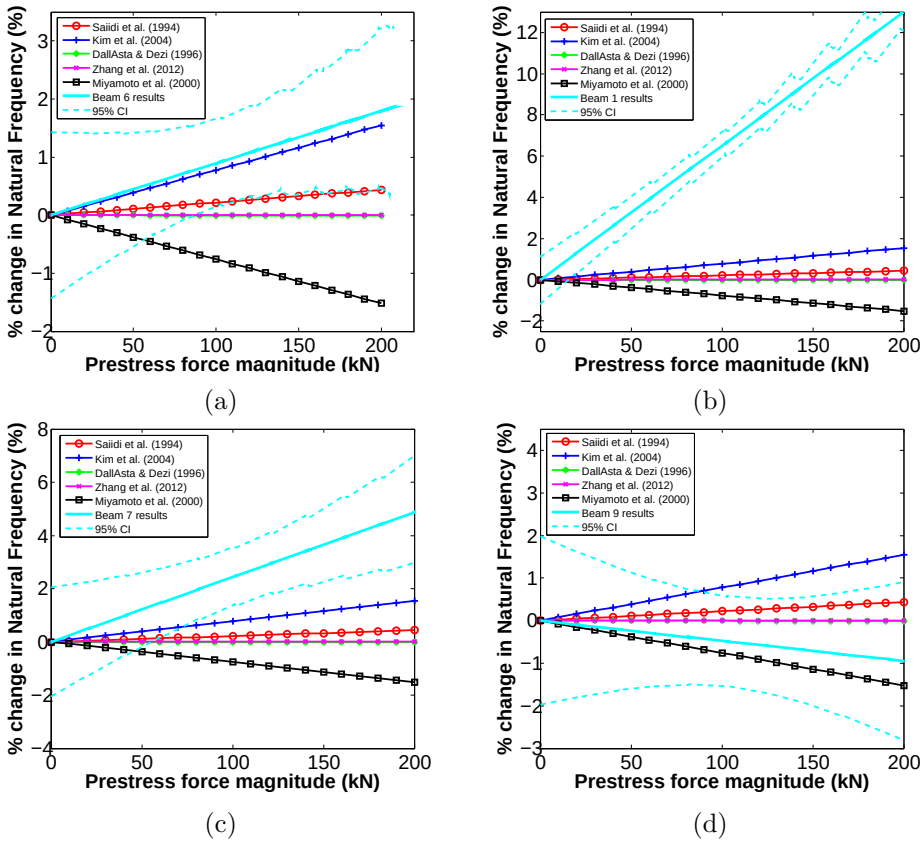

Figure 6.51.: Comparison of obtained results to existing models; (a) Beam 6 (e=-13mm); (b) Beam 7 (e=-26mm); (c) Beam 8 (e=-39mm); (d) Beam 9 (e=-52mm)

ative post-tensioning strand eccentricities, promoting tension in the bottom fibre of the beam. Figures 6.51a and 6.51d indicate good agreement with the previous prediction models. Beam 6 (Figure 6.51a) indicates results in close agreement with the prediction model proposed by Kim et al. (2004), while Beam 9 (Figure 6.51d) indicates results in close agreement with the "compression-softening" model outlined by Miyamoto et al. (2000). Figures 6.51b & 6.51c show statistically significant increasing trends in fundamental frequency with increasing post-tensioning force that is far greater than predicted by the previous prediction models.

In summary, the majority of results obtained indicate good agreement with the prediction models outlined in the literature, however, for some beams, i.e. Figures 6.50d, 6.51b & 6.51c, the results indicated a much

greater increase in fundamental bending frequency with increasing post-tensioning force than predicted by the existing prediction models (Saiidi et al., 1994; Miyamoto et al., 2000; Kim et al., 2004; Zhang et al., 2012; Dall'Asta and Dezi, 1996).

6.8.6. Comparison of results with proposed model

In Chapter 5, a mathematical model was proposed, predicting the changes in natural bending frequencies, ω_n, of post-tensioned concrete structures by increasing the post-tensioning force magnitude, N, i.e. $\omega_n(N)$. The proposed model is a linear kinematic model allowing for small deflections only, in accordance with Kirchoff's kinematic model. The second moment of area of the cross section, the Young's Modulus, the span length and the mass per unit length of the beam section are all modelled as functions of the post-tensioning force magnitude, i.e. $I(N)$, $E(N)$, $\ell(N)$ and $m(N)$, and have a subsequent effect on the natural bending frequencies of the beams, in accordance with Equation 5.1, Chapter 5.

Figures 6.52-6.54d show the comparison of the prediction model to the observed results for the uncracked concrete beam sections. In some cases, there is an acceptable level of agreement between the experimental results and the experimental observations such as for Beams 2,3,7,8 in Figures 6.53a, 6.53b, 6.54b and 6.54c, however, in others, there is poor agreement between the prediction model and the observed results, such as for Beams 4,6,9 in Figures 6.53c, 6.54a and 6.54d respectively. As outlined in Chapter 5, Section 5.8, the models proposed by Dall'Asta and Dezi (1996) and especially Hamed and Frostig (2006) fit best to the observed data. For 6 of the 9 uncracked beams tested, no statistically significant relationship between post-tensioning force and fundamental frequency was observable. The other 3 beams displayed a slight statistically significant increasing trend. The proposed model suggests increases greater than that observed in all cases, and the most suitable models to fit to this data are the ones suggested by Dall'Asta and Dezi (1996) and Hamed and Frostig (2006). There is no indication of a decreasing trend in natural frequency with increasing post-tensioning force magnitude, again highlighting the unsuitability of applying the *"compression softening"* model to post-tensioned concrete structures.

There are many reasons for the deviation of the model from the experimental results. For instance, the beams were modelled as idealised simply supported beams on knife-edge supports. In reality, a pad footing was used that allowed rotation to occur, therefore, lack of idealised support conditions in the lab can cause deviation from the predicted results. Concrete is a notoriously variable material, and variability in the material characteristics, such as the Young's Modulus, may also cause deviation of the model from the experimental results. Temperature effects are said to induce changes in natural frequency of between 6-18% (De Roeck, 2003), and error due to changes in temperature may also be attributed to the deviation in the prediction to the observed results. Furthermore, due to high signal-to-noise ratio in the obtained results, the estimation of the correct natural frequency experimentally is difficult due to some uncertainty in the location of the peak in the frequency domain due to noise components in the signal. Furthermore, non-linearities in the structural dynamic response of the concrete beam sections may also be attributable for the difference between the observations and the prediction, as the beams may "jump" off their supports, which in turn, changes the boundary conditions of the ordinary differential equation, causing a non-linear response of the structure. Also, in the prediction model, the mass of the jacks on either end of the beam sections have not been taken into account in the prediction model, and as such, if the mass were taken into account, it would serve as to lower the prediction of the natural frequency, bringing the prediction model closer to the observed results.

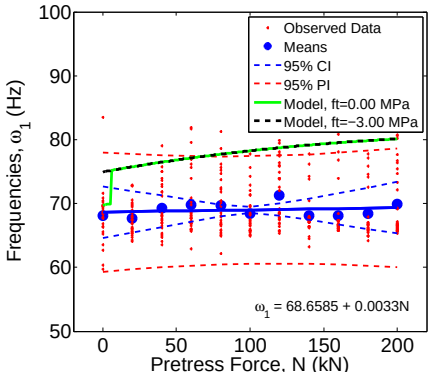

Figure 6.52.: Comparison of experimental results to the proposed model; Beam 1 (e=0mm)

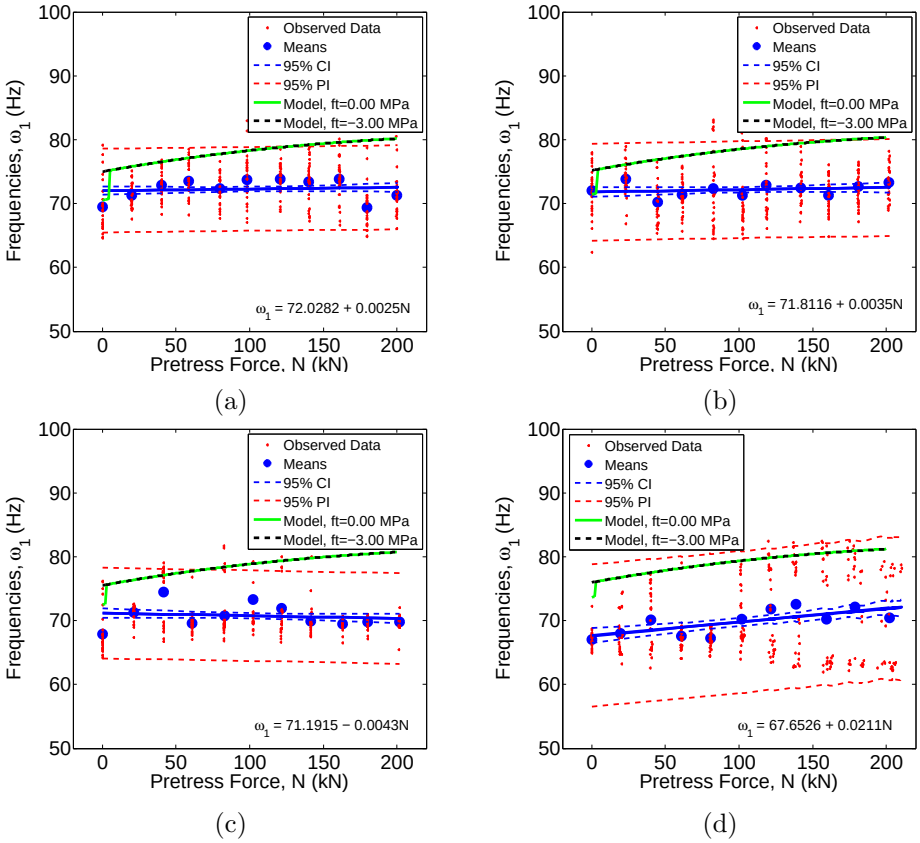

Figure 6.53.: Comparison of of experimental results to the proposed model; (a) Beam 2 (e=+13mm); (b) Beam 3 (e=+26mm); (c) Beam 4 (e=+39mm); (d) Beam 5 (e=+52mm)

6.9. Discussion of Accuracy of Experimental Results

The concrete data displays similar inaccuracies in the estimation of the natural frequency that were outlined previously in Chapter 4, Section 4.10, as shown in Figures 6.40-6.42d, with standard deviation of the estimation of the fundamental frequency ranging between 0.72Hz and 9.47Hz. In some cases, with large standard deviation, the accuracy of the estimation of natural frequency is poor. This may be attributed to a low signal-to-noise ratio of the response signals obtained, in which the structural signal is corrupted by noise components, despite the signal processing algorithm used to remove the majority of the noise corrupting the signal, uncertainty remains

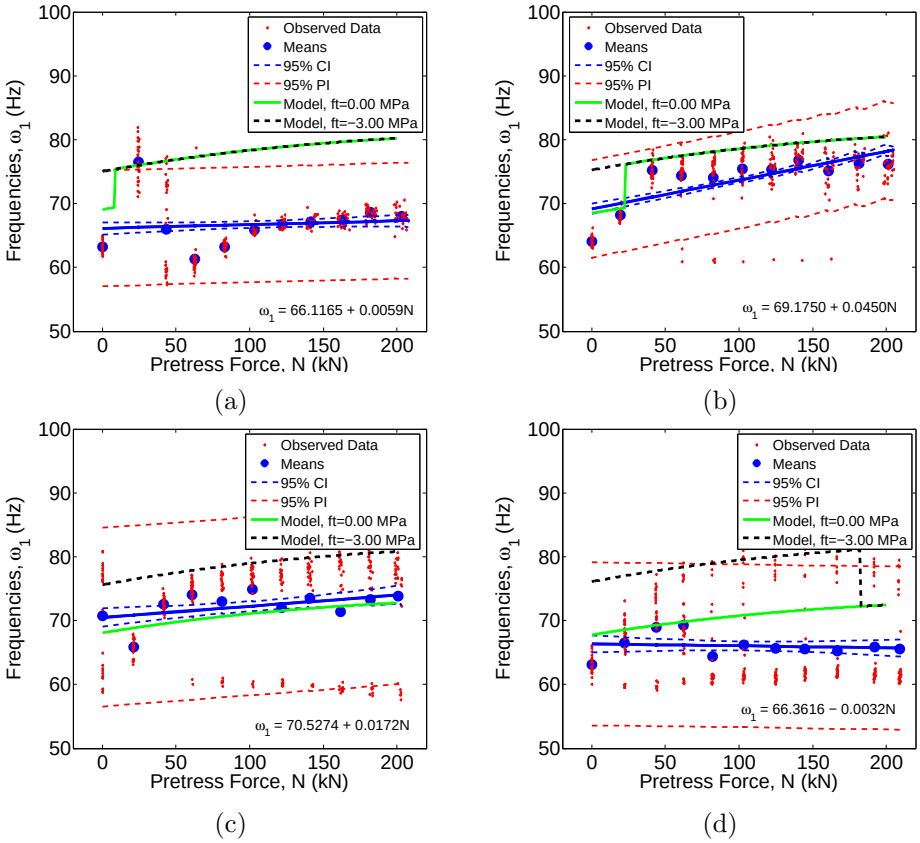

Figure 6.54.: Comparison of of experimental results to the proposed model; (a) Beam 6 (e=-13mm); (b) Beam 7 (e=-26mm); (c) Beam 8 (e=-39mm); (d) Beam 9 (e=-52mm)

regarding the location of the peak for the natural bending frequency, due to a low signal to noise ratio within the given frequency search band. The issue of low signal-to-noise ratio could have been avoided if a measurement of the dynamic impact force was collected, as a measure of the quality of the data can be obtained vis the coherence function, which measures the causality of the output signal, i.e. the correlation of the input signal to the output signal. As outlined in Chapter 3, the coherence function enables the quality of the data obtained to be monitored, and as such, Experimental Modal Analysis (EMA) would be preferable over Operational Modal Analysis (OMA), where practical. Furthermore, in some cases, the energy of the impact excitation may not have been sufficient to excite the structure sufficiently to have a sufficiently high signal-to-noise ratio to identify the

structural vibration of the system. As shown, the dominance of first vibration mode is directly linked to the accuracy of estimation of first vibration frequency. In all cases, the error in the estimation of the bending frequency may have been minimised by measuring the dynamic input force, increasing the number of excitation points, and increasing the number of response points.

6.9.1. Effect of span-to-depth ratio

The span-to-depth ratio of the concrete beam sections were relatively small in comparison to post-tensioned structures in practice. Post-tensioning allows engineers to span greater distances for a given depth by minimising the tensile stress throughout the section and minimising deflection under loading. This allows the span-to-depth ratio to be increased, minimising the amount of concrete required, and the self-weight of the structures. The span-to-depth ratio of the post-tensioned concrete beams tested was relatively small. The span length of the beams tested was set to be 2m, and the depth of the section was 200mm, giving a span-to-depth ratio of 10:1. This implies that the bending stiffness of the beam specimens is quite high, resulting in a very high first natural bending frequency, estimated to be in the region of 78Hz, as outlined previously in Chapter 6.

Such stiff structures are not anticipated to be susceptible to dynamic vibration serviceability issues, in the same way that slender post-tensioned floor slabs may be. Due to the high stiffness of the beams tested, the signal-to-noise ratio during dynamic excitation was very low. This leads to difficulties in accurately estimating the fundamental bending frequency, as outlined in Section 6.9. The modal parameters were more difficult to extract than they would have been for a very slender, wobbly, structure with a low fundamental bending frequency. The beams were specified to be such short spans in order to allow ease of casting and movement around the laboratory. The cross-sectional depth was minimised, but needed to be sufficiently large to allow for the inclusion of minimum reinforcement in accordance with Eurocode 2 (British Standards Institute, 2004). As a result, the span-to-depth ratio was small in relation to the ratios for post-tensioned structures in practice, and resulted in very stiff test-specimens, which contributed to the inaccuracy in the estimation of the fundamental

bending frequency.

6.10. Conclusions

The prediction of the change in natural bending frequencies with varying prestress force magnitude for PSC structures is an important problem, particularly in the field of PSC bridge girders and more recently for pre-cast, post-tensioned concrete wind turbine towers, both of which are structures that are susceptible to extreme dynamic excitation. Following this output-only modal analysis study, it was concluded that no statistically significant relationship was found between post-tension force magnitude and fundamental bending frequency for 6 of 9 simply supported post-tensioned concrete beams tested in the laboratory. The other 3 beams displayed a statistically significant increase in fundamental bending frequency with increasing post-tensioning load.

The full conclusions of the study are outlined as follows;

1. The "compression-softening" effect is not valid for post-tensioned concrete structures. From the static and dynamic tests conducted, no evidence of a decreasing trend in fundamental bending frequency with increasing post-tensioning force magnitude has been found.

2. From the obtained static data, the static-equivalent prediction of the fundamental bending frequency suggests that there is an increasing trend in fundamental bending frequency with increasing post-tensioning load magnitude.

3. However, from the obtained dynamic data, 6 of the 9 post-tensioned concrete beams tested displayed no indication of any relationship between post-tensioning load magnitude and fundamental bending frequency.

4. The dominance of the fundamental bending mode in the overall structural dynamic response of each of the 9 post-tensioned concrete beams is evident from the 3D graphs produced.

5. The results are inconclusive regarding the relationship between the change in critical damping ratio, ξ and the post-tensioning force magnitude, N.

6. Despite some theory predicting that there should be a direct relationship between post-tensioning strand eccentricity and fundamental bending frequency, no such non-random systematic change could be identified from the analysis of the obtained data.

Recently the interest on variability of dynamic properties of bridges (i.e. natural frequency, mode shape, damping ratio) caused by environmental effects such as temperature, humidity, wind and other factors is increasing (Ho et al., 2012). Studies conducted (Peeters and De Roeck, 2001; Cornwell et al., 1999) report frequency differences in the ranges of 6% and 14-18% respectively due to normal environmental changes (e.g. temperature effects, lack of ideal support conditions, material variability etc...). The change in natural frequency due to prestress loss may therefore be considered as negligible in relation to such large environmental effects.

7. Dynamic impact testing of cracked post-tensioned concrete beams

Chapter 6 outlined the results of static and dynamic testing on 9 uncracked post-tensioned concrete beams, and thoroughly described the experimental set-ups in the laboratory. The fundamental bending frequencies and the damping ratios have been calculated from obtained dynamic impact response data, as a function of increasing post-tensioning force magnitude. It was found that there was no statistically significant relationship between the post-tensioning force magnitude and the fundamental bending frequency for the uncracked concrete sections. As a result, it was concluded that the magnitude of the post-tensioning force does not affect the fundamental bending frequency for uncracked concrete sections. It was found that there was a statistically significant decrease in damping ratio with increasing post-tensioning load magnitude.

This chapter describes how four-point bending tests were subsequently performed on the 9 post-tensioned concrete beams previously described in Chapter 6 in order to induce a damaged (cracked) state. The impact testing, as previously described in Chapter 6 was repeated on the 9 cracked post-tensioned concrete beam specimens and the changes in fundamental frequency and damping ratio with increasing post-tensioning force magnitude were recorded. The purpose of this testing was to examine the effect that crack closure has on the modal properties of cracked post-tensioned concrete structures. It was found that for cracked post-tensioned concrete beams, there was a statistically significant relationship between post-tensioning force magnitude and fundamental bending frequency. It will be shown throughout the course of this chapter that the effect of the post-tensioning force is to close the cracks and increase the natural bending

frequency with increasing post-tensioning force magnitude. It will also be shown that there is a threshold value of post-tensioning force at which the beams begin to vibrate monolithically again, at which point, the increase in fundamental frequency with increasing post-tensioning force becomes evident.

Section 7.1 briefly describes how the majority of researchers in this field agree that the post-tensioning force closes cracks, therefore increasing the bending frequency. Section 7.2 describes the experimental set-up of the four point bending tests and subsequent repeat of the dynamic impact testing on the cracked concrete specimens. Section 7.3 describes the experimental analysis conducted on the cracked concrete results. Section 7.4 describes the experimental results of the dynamic impact testing conducted on the cracked post-tensioned concrete sections, including the change in fundamental bending frequency and changes in damping ratio with increasing post-tensioning load magnitude, and compares the results obtained from the cracked concrete beams to the uncracked beams. Section 7.6 outlines the conclusions from the testing of the 9 cracked post-tensioned concrete beams, highlighting that a relationship exists between natural frequncy and post-tensioning force for cracked post-tensioned sections only, as opposed to the uncracked sections outlined in Chapter 6.

7.1. Introduction

The effect of prestress force magnitude on the modal properties (frequency, damping and mode-shape) of uncracked prestressed concrete structures is something that has been widely debated among researchers to date (Quilligan et al., 2012), as outlined fully in Chapter 2. The effect of pre- and post-tensioning force magnitude on the natural bending frequencies of cracked prestressed concrete structures is something that is more established, and widely agreed upon. Saiidi et al. (1994) report an increase in natural frequency with increasing post-tensioning force. As pointed out by Bruggi et al. (2008) the tests carried out by Saiidi et al. (1994) were conducted on cracked beam sections only. Uncracked sections were not tested. Williams and Falati (1999) present a formula to calculate the average effective second moment of area of a cracked concrete cross section. The effect of crack closure in accordance with this method is that it increases the effective

second moment of area of the cross section, and subsequently the natural bending frequencies. Hop (1991) agrees, reporting a decrease in natural bending frequencies with increased cracking, and states that increasing the prestressing force acts as to close the cracks, stiffen the section and increase the natural bending frequencies of the beam sections. Grace and Ross (1996) also report a decrease in girder stiffness leading to a decrease in natural frequency also attributing it to cracking in the cross section. Unger et al. (2006) state that a loss in post-tensioning increases the appearance of cracks which reduces the bending stiffness and subsequent natural frequencies of the system. De Roeck (2003) concurs that prestress loss results only in measurable changes in frequency if accompanied by originating cracks. Hamed and Frostig (2004) also report that large cracking damage yields drastic reduction in the natural frequencies of cracked prestressed concrete beams.

Pavic et al. (2001) agree that prestressing is used to overcome excessive cracking and static deflection but argue that prestressing does not significantly improve dynamic behaviour, as that is governed by stiffness, mass and damping, on which prestress force has little influence. Dall'Asta and Dezi (1996) consider it is possible to determine the prestressing force by measuring the natural frequency of a PSC structure in its cracked state only. Rodríguez et al. (2010) acknowledges this fact in relation to post-tensioned concrete wind turbine towers, stating that uncracked towers maintain their original stiffness and frequency, but once the towers are cracked and the cracks have been decompressed, any vibrations in the tower will mobilise smaller stiffness, which will be shown by the vibration frequencies.

This chapter will describe the outcome of dynamic impact testing conducted on nine cracked post-tensioned concrete beam sections in the laboratory. The results for one beam will be discussed in detail. The relationship between the natural bending frequency and the post-tensioning force for cracked concrete sections will be determined through dynamic impact testing of the cracked beams. Comparisons will be made between the behaviour of the uncracked beams and the cracked beams. The conclusions have profound implications in the fields of system identification, damage detection and structural health monitoring.

7.2. Experimental Set-up

The following section outlines the set-up of the dynamic impact tests conducted on the 9 cracked post-tensioned concrete beams. The testing conducted was identical to the testing described at length in Section 6.5 in Chapter 6. The tests were repeated on the same 9 post-tensioned concrete beams, after the sections had been cracked by applying a four-point bending load. The cracking of the sections is described in Section 7.2.1 and summarised by Figure 7.1 and Table 7.2.

Table 7.1 outlines the 9 different cracked concrete beams tested dynamically to determine their fundamental bending frequency with varying post-tensioning load magnitude. The concrete used in each beam specimen was C30/37, as specified in Section 6.3.1, and outlined in Section 6.2. Like with the uncracked sections, the variable in the 9 test specimens was the post-tensioning strand eccentricity, however, in this case, a second variable was introduced, namely the applied moment due to cracking. The effect of post-tensioning force magnitude and eccentricity was intended to be tested, and the effect of positive and negative eccentricity on the bending frequency, coupled with the interaction effects of both post-tensioning force and strand eccentricity on the fundamental bending frequency was also intended to be investigated, as before. However, the effect of the level of cracking on the fundamental bending frequencies was also intended to be tested. Testing the 9 beams with varying post-tensioning strand eccentricities and varying applied cracking moments, as outlined in Table 7.1 enabled these tests and subsequent comparison of the results to be conducted.

7.2.1. Dynamic impact testing of cracked beams

Following dynamic impact tests in the lab on 9 uncracked post-tensioned concrete beam sections, which have been described previously in Chapter 6 and in Noble et al. (2014a), 4-point bending was applied to each beam as outlined in Figure 7.1, and Figure 7.2. A hydraulic loading ram was bolted onto an external loading frame, which in turn was bolted onto a meter deep strong floor in the laboratory, as shown in the schematic in Figure 7.1, and in Figure 7.2. The loading ram was operated via a hydraulic hand pump, and transferred a four-point bending load into the post-tensioned concrete beam by means of a spreader beam, as shown in Figure 7.1, and in Fig-

Table 7.1.: Experimental design - cracked concrete test specimens

Beam	**e (mm)**	M_a (kNm)	**Predicted Freq (Hz)**
1	0	21.12	63.15
2	+13	20.70	64.12
3	+26	21.39	65.32
4	+39	23.25	66.48
5	+52	21.00	67.87
6	-13	18.90	62.33
7	-26	20.40	61.66
8	-39	20.40	61.15
9	-52	21.60	60.78

ure 7.2. A load cell was affixed to the loading ram in order to determine the load applied to the spreader beam. It was ensured that the load was applied at mid-span of the spreader beam to ensure an even distribution of the four point loading onto the post-tensioned concrete beam, ensuring symmetrical support reactions and a symmetrical shear and bending distribution throughout the beam span length. Figure 7.2b shows a typical crack pattern in a damaged (yielded) post-tensioned concrete beam. The flexure cracks occurred between the supports of the spreader beam, in the area of maximum bending moment, as expected, while the diagonal shear cracks formed in the areas between the beam supports and the points of the spreader beam, in the areas of high shear, as expected, and as shown in Figure 7.2b. The individual beams differed in that they had different straight profiled post-tensioning strand eccentricities. The transverse load was applied incrementally and the crack patterns were observed at different values of load application. The loading increments and yield moment for all 9 beams are outlined in Table 7.2. First, second and third cracks were identified by visual inspection only, and were not determined scientifically (Noble et al., 2015b).

The bending capacity of the post-tensioned concrete beams was determined to be approximately $15kN - m$ in Section 6.3.5 in Chapter 6. Table 7.2 outlines the actual yield values and the real factor of safety, i.e. the ratio between the measured beam bending capacity and the design beam bending capacity outlined in Section 6.3.5. The average observed factor of safety in Table 7.2 was 1.40.

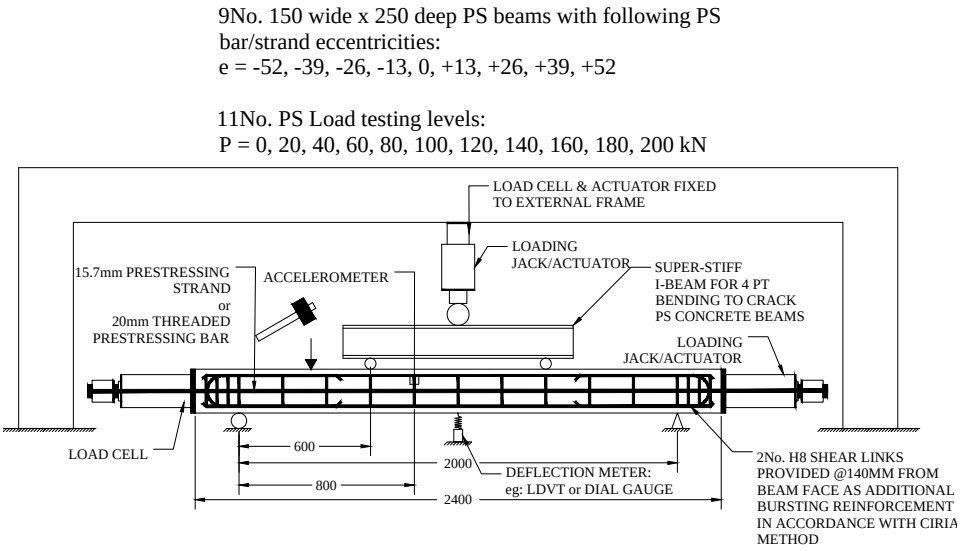

Figure 7.1.: Experimental set-up for cracked beam specimens

Table 7.2.: The incremental damage states of all 9 Beams until yielding

B#	1^{st} **crack (kN)**	2^{nd} **crack (kN)**	3^{rd} **crack (kN)**	**Yield (kN)**	M_{yield} **(kN-m)**	FOS
B1	24.6	41.3	49.8	70.4	21.12	1.41
B2	19.4	38.6	48.7	69.0	20.70	1.38
B3	19.3	39.7	50.2	71.3	21.39	1.43
B4	20.0	39.7	50.6	77.5	23.25	1.55
B5	20.0	40.0	52.8	70.0	21.00	1.40
B6	20.0	38.8	48.4	63.0	18.90	1.26
B7	20.0	38.9	50.0	68.0	20.40	1.36
B8	-	33.0	50.0	68.0	20.40	1.36
B9	-	30.1	49.0	72.0	21.60	1.44

Yielding was identified as the point where the beams could no longer hold any additional load and deflections increased significantly. Visible structural cracks formed in the section, as shown in Figure 7.2b. Vertical flexural cracks formed in the area of high moment, between the span of the spreader beam, whereas diagonal shear cracks formed in the areas between the end of the spreader beam and the supports. This can also be seen in Figure 7.2b.

Following cracking, dynamic impact testing was conducted on the beams. The set-up of the dynamic impact testing was identical to the set-up de-

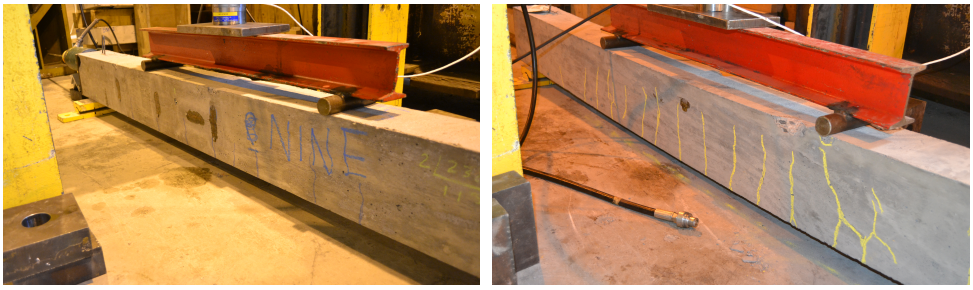

(a) (b)

Figure 7.2.: Four Point Bending test; (a) Set-up in lab; (b) Cracked concrete beam

scribed in Chapter 6 previously. Figure 7.1 shows the experimental set-up. An accelerometer was placed 800mm from one of the supports as shown, enabling the first three modes of vibration to be captured. Three strain gauges were placed equidistant between the support and mid-span, in order to capture the mode shapes of vibration. The beam was struck ten times at each strain gauge location using an impact rig assembled in the laboratory. This ensured repeatability of the experiment and enabled the error in the estimation of the frequencies to be calculated. This experimental procedure was then repeated at incremental values of post-tensioning load, as outlined in Figure 7.1. The post-tensioning load was applied using a 15.7mm Freyssinet post-tensioning strand, secured either side of the 300 ton loading jacks as shown. The different straight profiled strand eccentricities are also outlined in Chapter 6.

7.3. Experimental Analysis

Each beam was struck ten times at 3 different impact locations, for 11 different post-tensioning load levels. The response was measured by one accelerometer and three strain gauges. As such, this method of dynamic testing is known as the multiple input, multiple output (MIMO) method. The Fast Fourier Transform (FFT) was then applied to the response signals to convert into the frequency domain. No data was collected on the impact signal, and as such, the frequency response functions (FRFs) of the beams could not be determined. The FRFs are defined as the transfer function, or the ratio between the input and output signals in the frequency domain.

The study falls under the remit of Operational Modal Analysis (OMA) as opposed to Experimental Modal Analysis (EMA). However, the FFTs of the output signal were sufficient to determine the natural vibration frequencies of the structural system, via a peak-picking method.

As outlined in Chapter 6, having calculated the FFTs of the signals, the fundamental vibration mode was intelligible, however, due to the presence of significant noise in the data, higher modes were not. In order to eliminate this noise and identify higher modes, a signal processing technique was established by the authors and applied to the raw data. Figure 7.3a and Figure 7.3b show the results of two processed signals. The higher modes are now intelligible. A peak picking algorithm is invoked to determine the natural frequencies of the system. Figure 7.3a shows an accelerometer response signal of a cracked beam for zero post-tensioning load, indicating a structural dynamic response of the cracked beam for a non-fully prestressed condition, in which the cracks are open. It is evident that the structural response of the non-fully prestressed condition is complex. The fundamental mode, in this case contributes most to the response, but its contribution is not dominant. The contribution of the other modes is relatively similar.

Figure 7.3b shows an accelerometer response signal of the same cracked beam for a post-tensioning load level of 180kN, indicating a structural dynamic response of the cracked beam for a fully prestressed condition. Here, the dominance of the first mode of vibration is evident. The beam, when fully prestressed, behaves monolithically and vibrates as one entity rather than a series of individual cracked entities, and hence the dominance of the first vibration mode returns. This response is in line with the response of the uncracked *'virgin'* beams. That is to say, that there seems to be a threshold value of post-tensioning force at which the structural dynamic response of the cracked concrete beams approaches the same response as was evident for the uncracked beam sections, in which the fundamental mode of vibration dominates the response (Noble et al., 2015b).

7.4. Experimental Results

The following section presents the results of the dynamic impact testing on the 9 cracked post-tensioned concrete beams tested in the laboratory. Section 7.4.1 presents 3D graphs of relative modal amplitude versus frequency

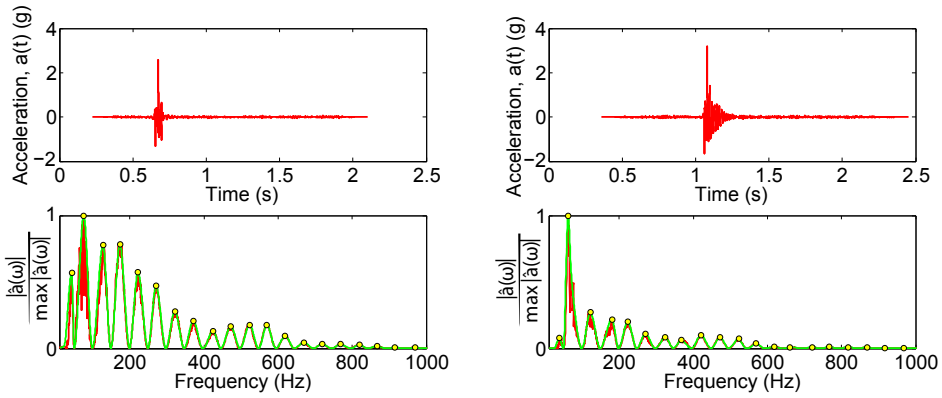

(a) (b)

Figure 7.3.: Structural dynamic response of cracked beam, Beam 1, e=0mm; (a) for non-fully prestressed case; (b) for fully prestressed case

and axial load for all 9 cracked beams. The graphs indicate the relative contribution of each mode to the overall structural dynamic response of the beams. Section 7.4.2 presents the results of a first order linear regression analysis of fundamental bending frequency versus post-tensioning load magnitude for all 9 cracked beams. An analysis of the statistical significance of the regression parameters is conducted to determine whether or not changes in frequency with increasing post-tensioning load magnitude are significant or not. Section 7.4.3 compares the first order linear regression models for the uncracked and cracked beam sections, and Section 7.4.4 presents the results of a first order linear regression analysis of damping ratio versus post-tensioning force magnitude for all 9 cracked beams. An analysis of the statistical significance of the regression parameters for the damping ratios was also conducted.

7.4.1. 3D Graphs

Figures 7.4-7.6 show graphs of relative modal amplitude versus frequency and post-tensioning load for all 9 cracked post-tensioned concrete beams tested. Figure 7.4 shows the response for Beam 1, where the eccentricity of the post-tensioning strand, $e = 0$. Figures 7.5a-7.5d shows the response for Beams 2-5, in which the post-tensioning strand eccentricity is such that it creates compression in the bottom fibre, inducing crack closure. Figures 7.6a-7.6d shows the response for Beams 6-9, in which the

post-tensioning strand eccentricity is such that it creates tension in the bottom fibre, causing the cracks to open further. As shown in all figures, the structural dynamic response is different to that of the uncracked beams, in which the fundamental frequency dominated the response, as shown in Figures 6.35-6.37d in Chapter 6. The structural dynamic response, as shown in Figures 7.4-7.6d is complex in comparison, and the fundamental bending vibration mode does not dominate, and the contribution of higher modes is much more significant (Noble et al., 2015b).

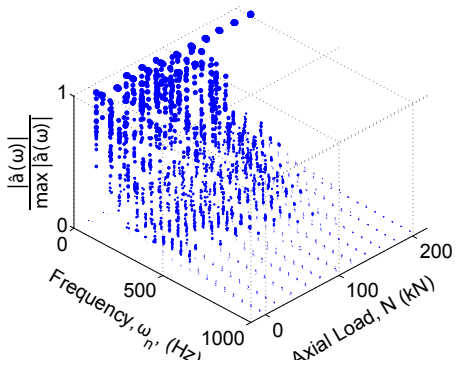

Figure 7.4.: Rel. Modal Amplitude vs. frequency and post-tensioning load; Cracked Beam 1 (e=0mm)

There is evidence however to suggest that the dominance of the fundamental bending mode returns at threshold values of post-tensioning load for the cracked beam specimens. As can be seen from Figures 7.4,7.5b and 7.5d. At threshold values of post-tensioning load, for Beams 1,3, and 5, the dominance of the fundamental vibration frequency returns. Interestingly, the return of the dominance of the first vibration mode in the case of Beams 1,3 and 5 corresponds to a statistically significant increase in the bending frequency with increasing post-tensioning load magnitude. This is illustrated further in Figure 7.8. No such trend is evident for the other beams, in which the dominance of the fundamental vibration mode does not return. This trend is only evident in the beam sections which promote compression in the bottom fibre, thereby closing cracks, and increasing the bending stiffness. This trend is not evident in any of the beam configurations that promote cracking in the bottom fibre.

Figures 7.6a-7.6d show the typical response for the cracked post-tensioned beams whose post-tensioning strand eccentricity causes the cracks to open in

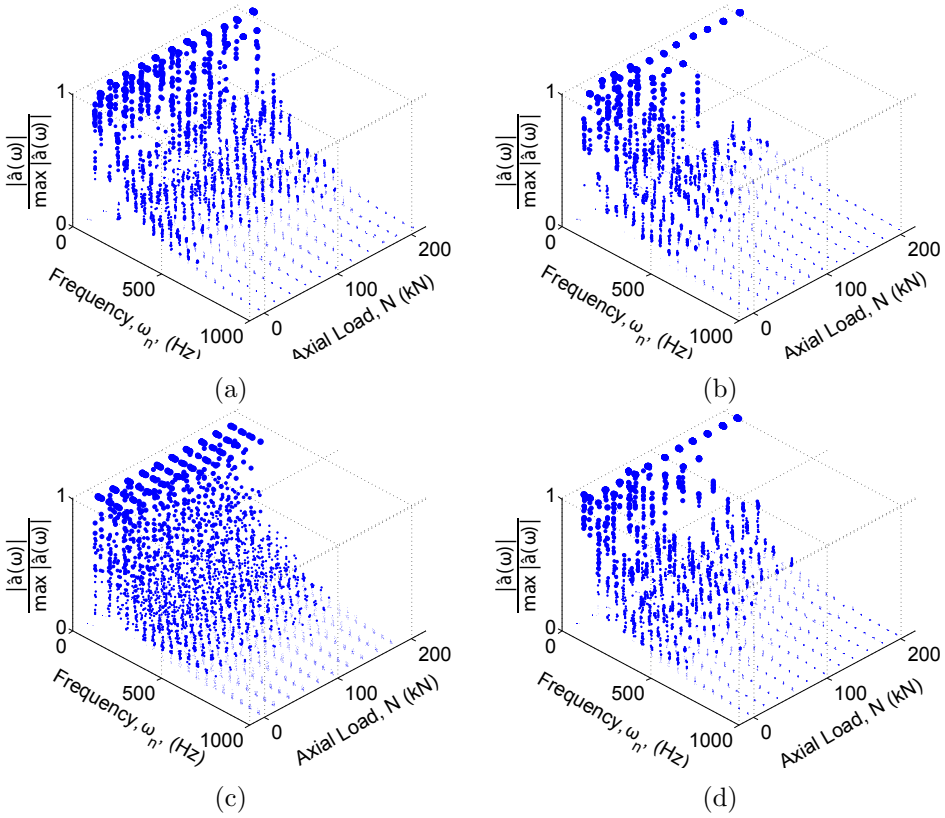

Figure 7.5.: Rel. Modal Amplitude vs. frequency and post-tensioning load for cracked beams; (a) Beam 2 (e=+13mm); (b) Beam 3 (e=+26mm); (c) Beam 4 (e=+39mm); (d) Beam 5 (e=+52mm)

the bottom fibre. As such, the effect of post-tensioning does nothing to cause the dominance of the fundamental bending vibration mode to return, as with the beams whose eccentricity promotes crack closure in the bottom fibre, as outlined in Figures 7.5a-7.5d. The structural dynamic response for these beams remains complex, with significant contributions of the higher modes of vibration to the overall structural dynamic response. This is attributed to the presence of cracking.

Figure 7.7a shows the structural dynamic response of Beam 1 (e=0) in its uncracked condition. The dominance of the first mode of vibration is evident in this case, since the relative modal amplitude of the fundamental bending mode accounts for a large proportion of the modal mass of the structure. Figure 7.7b shows the structural dynamic response of Beam 1 in its cracked condition. In this case, the dominance of the first mode

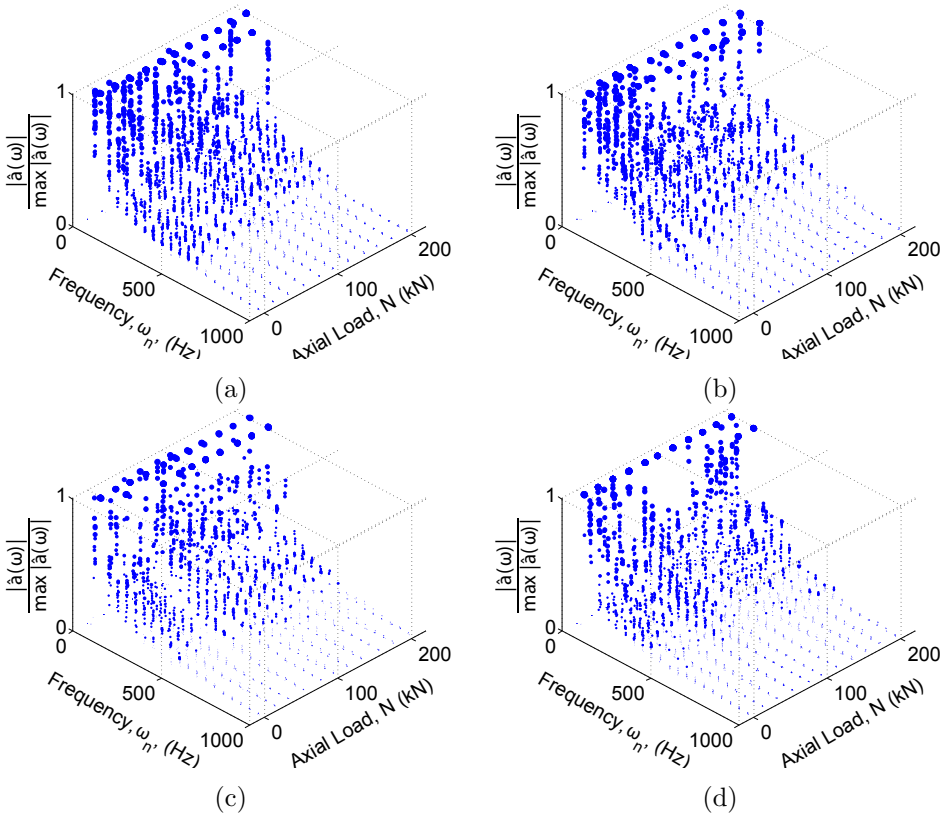

Figure 7.6.: Rel. Modal Amplitude vs. frequency and post-tensioning load for cracked beams; (a) Beam 6 (e=-13mm); (b) Beam 7 (e=-26mm); (c) Beam 8 (e=-39mm); (d) Beam 9 (e=-52mm)

of vibration is not clear. The structural dynamic response is much more complex and the contribution of the higher modes of vibration are clearly far more significant in the cracked case. This is evident up to a certain threshold value of post-tensioning force. The dominance of the first vibration mode again becomes apparent in the cracked case when the post-tensioning force causes the structure to behave as one monolithic structure rather than a series of cracked entities. This is the fully prestressed condition. In this case, for Beam 1, e=0mm, it was identified to be at a value of 160kN. This threshold value differs slightly for the other beams (Beam 3, Beam 5), but the principle remains the same.

Figure 7.8 shows the relationship between the dominance of the fundamental bending mode and a statistically significant increasing trend in natural frequency with increasing post-tensioning load for the beams whose

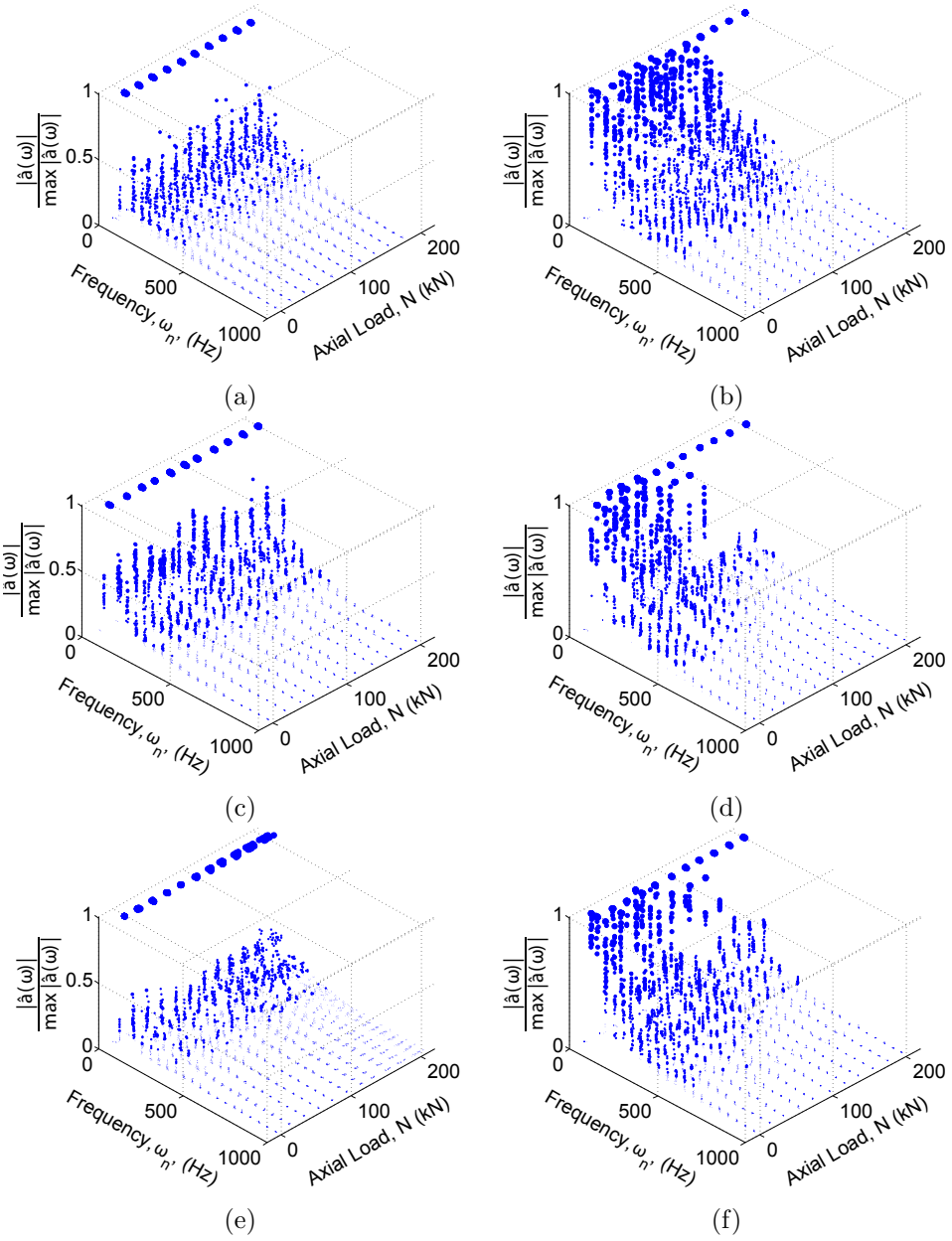

Figure 7.7.: Relative Modal Amplitude of cracked and uncracked beams - a comparison (a) Beam 1, e=0mm, Uncracked; (b) Beam 1, e=0mm, Cracked; (c) Beam 3, e=+26mm, Uncracked; (d) Beam 3, e=+26mm, Cracked; (e) Beam 5, e=+52mm, Uncracked; (f) Beam 5, e=+52mm, Cracked

post-tensioning strand configuration promotes crack closure in the bottom fibre, namely Beam 1, 3 and 5. It is clear from Figure 7.8, that once a

threshold value of post-tensioning force is reached, the cracked beams cease to vibrate as a series of different cracked entities and rather begin to vibrate as one monolithic beam specimen again. Once this occurs, there is a corresponding statistically significant increase in fundamental bending frequency, as shown in Figure 7.8.

It should be noted that despite Beams 2 & 4 also having post-tensioning strand eccentricities that promotes upward camber and crack closure in the bottom fibre, a similar trend to Beams 1,3 & 5 is not observable in the data for these beams. Such a trend is not observable in Beams 6-9 either, but since the post-tensioning strand eccentricity is such in these beams as to promote cracking in the bottom fibre, and subsequently open existing cracks further, this is consistent with what would be expected. In the case of Beams 2 & 4 the non-linear dynamic response due to cracking is observable at all levels of post-tensioning load, and the dominance of the first mode of vibration (linear response) does not return. The reason for this is suggested to be due to the high level of cracking and yielding of reinforcement. The beams were under reinforced meaning the steel is designed to yield first under flexural loading, and the beams were loaded to the point of yield under four point bending, as outlined in Figure 7.1 and the magnitude of the yield load for each beam is given in Table 7.2. It should be noted that Beam 4 was subjected to a much higher load before yielding, supporting the theory that the level of cracking and crack closure determines the value of the threshold value of post-tensioning force required for monolithic response. The factors affecting this are the eccentricity of the post-tensioning strand, the level of post-tensioning force, and the level of cracking initially applied to the structure. If, in some cases, the reinforcement has yielded in such a manner that the cracks are forced open and cannot be sufficiently closed to induce the monolithic response, the response would be expected to be as observed for Beams 2 & 4 and this is suggested to be the reason for these beams not displaying the same trends as observed for Beams 1,3 and 5 as shown in Figure 7.8.

7.4.2. Regression Analysis

Figures 7.12-7.14d show the first order linear regression model applied to the measured changes in fundamental bending frequency with increasing

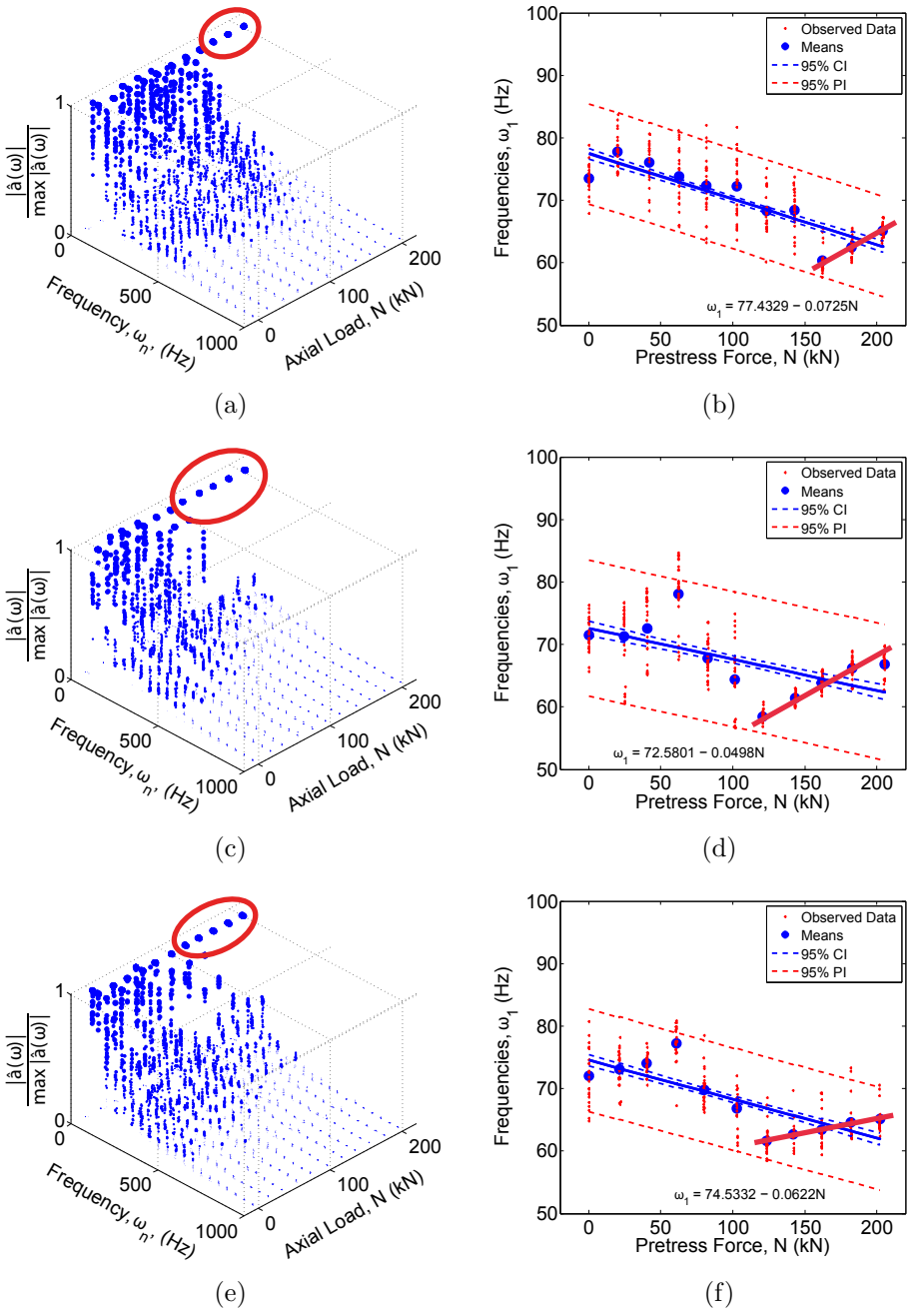

Figure 7.8.: Relationship between dominance of fundamental bending mode and a statistically significant increasing trend in natural frequency with increasing post-tensioning load for (a) & (b) - Beam 1; (c) & (d) - Beam 3, and (e) & (f) - Beam 3

post-tensioning force magnitude for the 9 cracked post-tensioned concrete beams. Whereas it is acknowledged that linear regression analysis is not strictly relevant for the case of cracked post-tensioned concrete beams, as the nature of opening and closing cracks is inherently non-linear, the purpose of the first order regression analysis is to compare the results obtained for the uncracked beam sections, and demonstrate that they are inherently, statistically significantly different to the results obtained for the same concrete sections following cracking. Figures 7.9-7.11d show the results obtained for the dynamic impact testing of the cracked beam sections, without the linear regression analysis applied, and the aforementioned trends mentioned in Section 7.4.1 are readily identifiable. The linear trend reappears once the cracks have been closed, as shown in Figure 7.8.

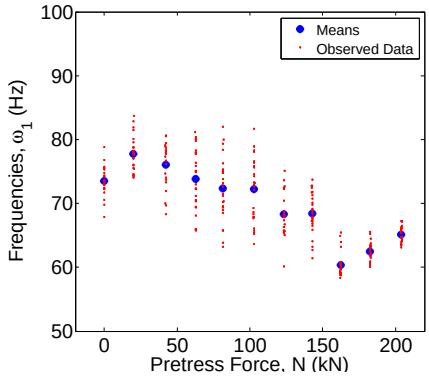

Figure 7.9.: Trends of ω_1 vs. N; Cracked Beam 1 (e=0mm)

In 7 of the 9 cracked post-tensioned concrete beams, a statistically significant decreasing trend in fundamental bending frequencies with increasing post-tensioning force magnitude has been found, as outlined in Figures 7.12-7.14d and in Table A.8. The statistically significant overall decreasing trend in fundamental bending frequency with increasing post-tensioning load magnitude may be considered counter-intuitive, however, the reason is hypothesised to be due to the presence of cracking and non-monolithic response. When the beam is fully cracked, it vibrates as a series of cracked entities. The accelerometer is located in the span of one of these cracked portions of the beam. In effect, the span length of vibration is shortened, and hence the measured natural frequency is increased. As the post-tensioning force is increased, these cracks begin to close and the beam approaches monolithic response. As the cracks are closed, the effective span length is increased, un-

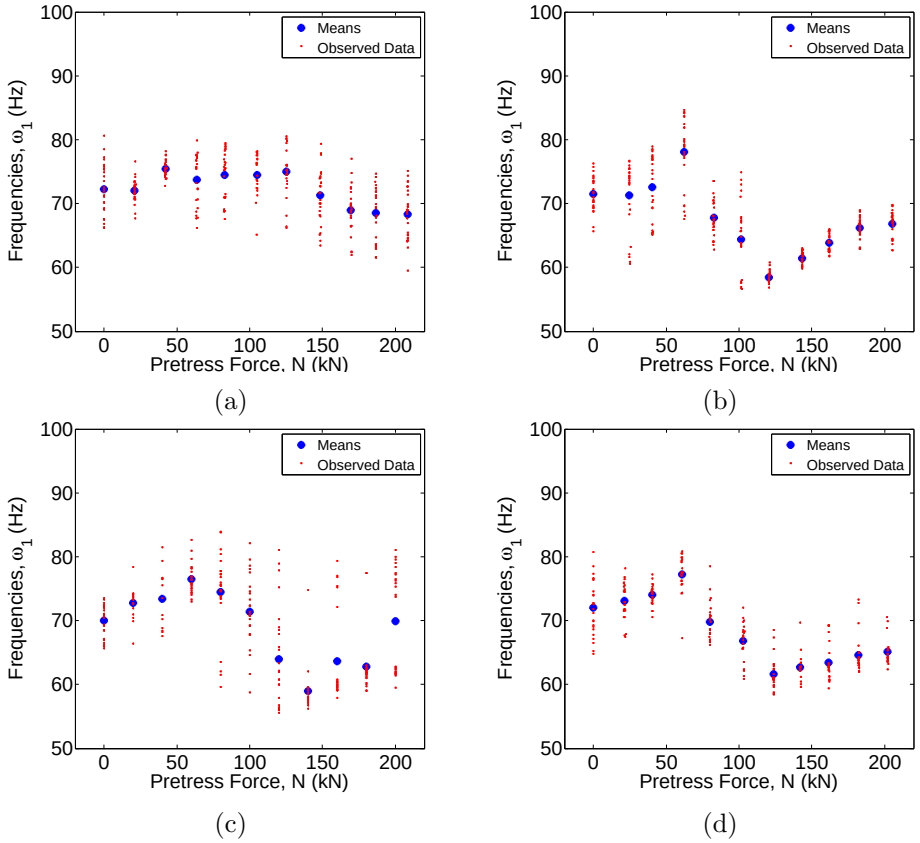

Figure 7.10.: Trends of ω_1 vs. N; (a) Beam 2 (e=+13mm); (b) Beam 3 (e=+26mm); (c) Beam 4 (e=+39mm); (d) Beam 5 (e=+52mm)

til it reaches a maximum at the point of monolithic response. This increase in span length is accompanied by a decrease in natural bending frequency that is evident in Figures 7.12-7.14d. At this point, the span length is returned to its maximum value, and the effect of the post-tensioning force is to increase the second moment of area through crack closure, and also to increase the Young's Modulus in a similar manner. Subsequently, from this value of post-tensioning force magnitude onward, a statistically significant increasing trend in the fundamental bending frequency is observed. The overall decreasing trend is attributed to an increase in effective span length due to crack closure.

Figure 7.15a and Figure 7.15b show regression analysis of fundamental frequency versus post-tensioning load for the same beam (Beam 1) in its uncracked and cracked states. From the regression analysis of the uncracked

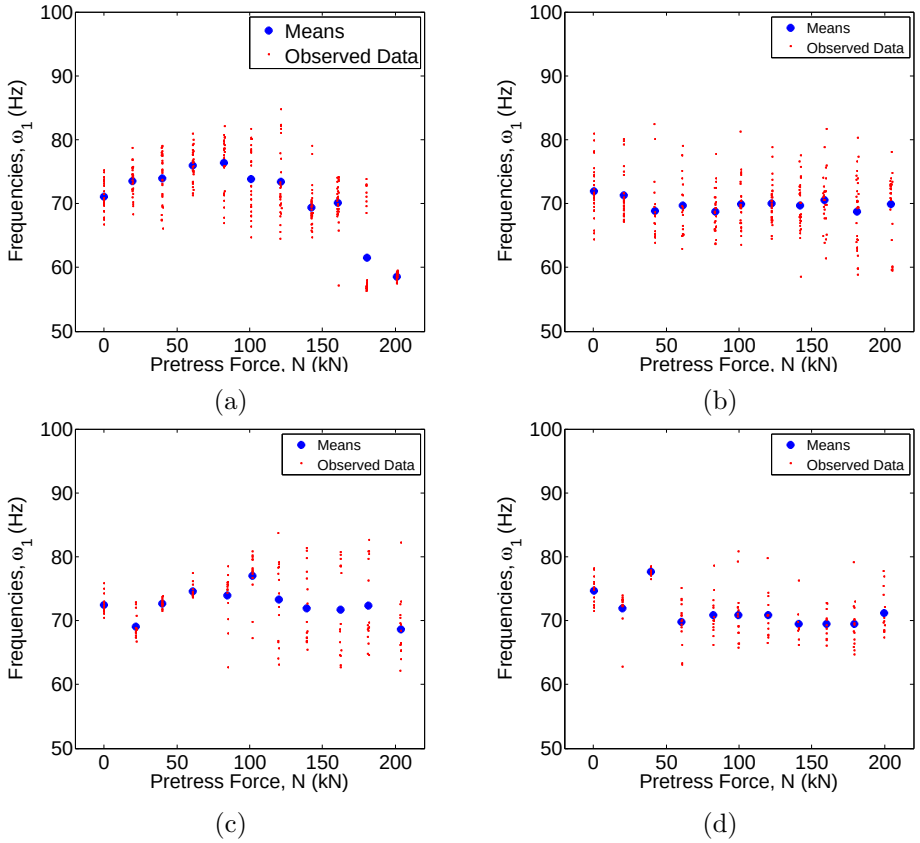

Figure 7.11.: Trends of ω_1 vs. N; (a) Beam 6 (e=-13mm); (b) Beam 7 (e=-26mm); (c) Beam 8 (e=-39mm); (d) Beam 9 (e=-52mm)

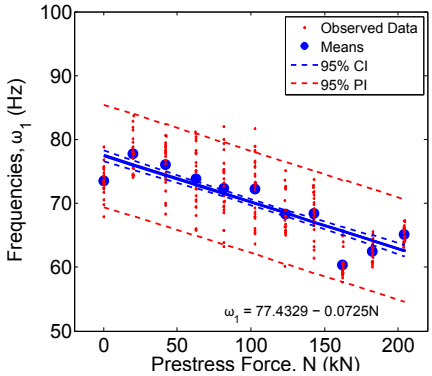

Figure 7.12.: Regression of ω_1 on N; Cracked Beam 1 (e=0mm)

case in Figure 7.15a, no statistically significant change in fundamental frequency with increasing post-tensioning force can be observed, as previously reported in Chapter 6. From first glance at the simple linear regression

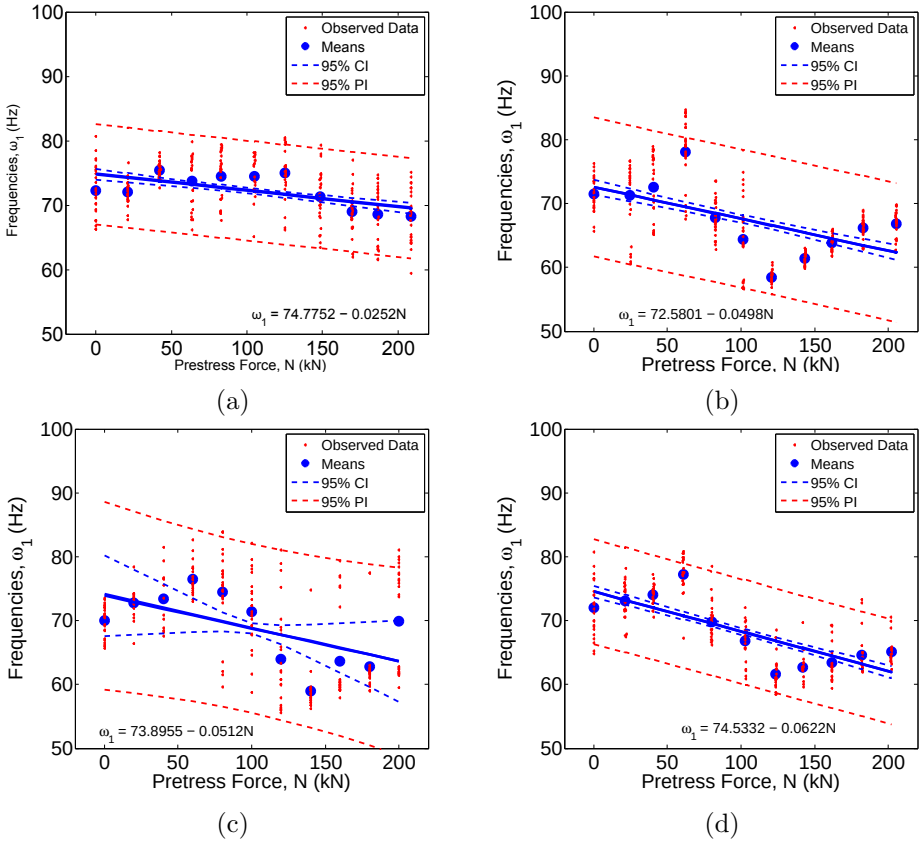

Figure 7.13.: Regression of ω_1 on N for cracked beams; (a) Beam 2 (e=+13mm); (b) Beam 3 (e=+26mm); (c) Beam 4 (e=+39mm); (d) Beam 5 (e=+52mm)

analysis of the cracked beam case, an overall decreasing trend in fundamental frequency versus post-tensioning load is observed. However, when analysed in conjunction with Figure 7.7b, it becomes apparent that there are two distinct trends in the data. For the non-fully post-tensioned case (0-160kN), the structural dynamic response is complex, the error in the estimation of the natural frequency is high, the structure behaves dynamically as a series of independent vibrating entities and a decreasing trend in fundamental frequency is observed. However, at a threshold post-tensioning load level and upward (160-200kN), the dominance of the first vibration mode returns, the error in the estimation of the fundamental frequency decreases, the structure begins to behave monolithically again, and an increasing trend can be observed for the final 3 data points. This increasing trend, has been widely reported for cracked beam sections (Saiidi et al., 1994; Williams and

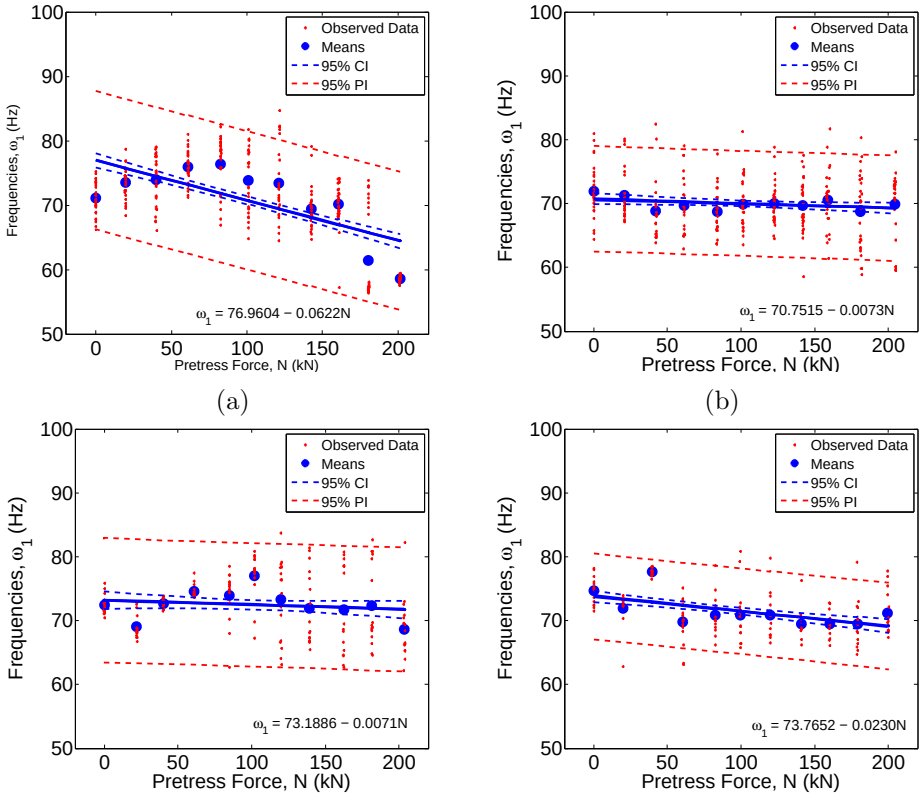

Figure 7.14.: Regression of ω_1 on N for cracked beams; (a) Beam 6 (e=-13mm); (b) Beam 7 (e=-26mm); (c) Beam 8 (e=-39mm); (d) Beam 9 (e=-52mm)

Falati, 1999; Grace and Ross, 1996; Unger et al., 2006; De Roeck, 2003; Hamed and Frostig, 2004; Pavic et al., 2001; Dall'Asta and Dezi, 1996), however, is not observed for uncracked beam sections (Hamed and Frostig, 2006; Dall'Asta and Dezi, 1996; Noble et al., 2014a). The stiffness of the section is increased by increasing the prestressing force due to crack closure, and the second moment of area moves from the cracked to the uncracked value.

7.4.3. Comparison of uncracked and cracked beams

Figures 7.16-7.18d show the comparison between the simple linear regression models for the cracked and uncracked beam cases. As discussed previously, this is not strictly a reasonable comparison as two different trends can be

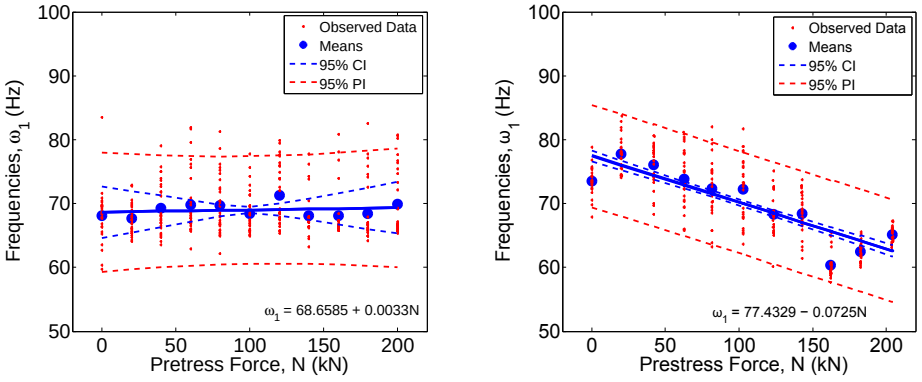

(a) (b)

Figure 7.15.: Regression analysis of fundamental frequency vs. post-tensioning load for Beam 1 (e=0mm); (a) Uncracked; (b) Cracked

observed in the cracked beam case. The initial fundamental frequencies for the cracked beams are higher to begin with, which is counter-intuitive. If it is considered that the beam in its damaged state behaves as a series of different vibrating cracked entities rather than as one monolithic structure, then the span length of each individual vibration entity is significantly reduced. Since the span length is a denominator in the equation for the prediction of natural frequency for simply supported beams, this explanation is consistent with what would be expected from theory. This span length increases as the post-tensioning force increases and more and more structural cracks are closed, meaning the measured frequency decreases. On the other hand, when the beam begins to vibrate again monolithically, the structural dynamic response becomes less complex and the fundamental mode dominates, an increasing trend is observed in the frequency with increasing post-tensioning force. At the threshold value of post-tensioning force, the span length reaches its original value. From this point onwards, as shown in Figure 7.12 an increasing trend in fundamental frequency is observed, and this is attributed to the gain in geometric stiffness due to crack closure, in accordance with previous research works (Saiidi et al., 1994; Williams and Falati, 1999; Grace and Ross, 1996; Unger et al., 2006; De Roeck, 2003; Hamed and Frostig, 2004; Pavic et al., 2001; Dall'Asta and Dezi, 1996). It should be noted that this also leads to the conclusion that at some second threshold value of post-tensioning force, the cracks in the beam will have

been fully closed, at which point the beam behaves just as the uncracked beam and there is no change in frequency with increasing post-tensioning force. This occurs up to the point where the post-tensioning force is such as to cause crushing in the concrete, at which point there exists another threshold value of post-tensioning force above which the frequency starts to decrease again due to the crushing in the concrete. However, it should be pointed out that this may not be practicable as the post-tensioning strands are rated to maximum forces much less than the crushing strength of the cross sections. Another issue with this model is that this does not take into account the effects that permanent, plastic deformation of the sections has on the ability of the post-tensioning force to close cracks. Concrete is a highly non-linear material, and when bonded to steel, as in reinforced concrete, the reinforcement steel may have reached its plastic limit and as such may never return to its original state, meaning that any benefit of crack closure from such state is limited by the second law of thermodynamics in which the deformation may not be recovered since the energy has already been dissipated through plastic deformation of the reinforcement.

It is evident from Figures 7.16-7.18d that the general trend for the uncracked beam is to favour a slight increase in fundamental frequency with increasing post-tensioning force magnitude, although, as pointed out in Chapter 6, this trend has not been found to be statistically significant in the majority of cases. However, when compared to the regression models for the case of the cracked beams, it can be seen that the majority of the cracked beams indicate a statistically significant decreasing trend in fundamental bending frequency with increasing post-tensioning load magnitude. The hypothesised reasons for this have been highlighted previously in this section and also in Section 7.4.2 previously. However, what is clear, is that the structural dynamic response and the relationship between post-tensioning force and fundamental bending frequency is significantly different for cracked and uncracked post-tensioned concrete beams.

Table 4.11 shows the statistical regression parameters - intercept parameter ($\alpha_{0,iuc/c}$), slope parameter ($\alpha_{1,iuc/c}$), standard error, t-values and 95% confidence intervals when regressing ω_1 on N for Beam 1, e=0 ($i = 1$) in its cracked (c) and uncracked (uc) case. The corresponding linear regression equations are obtained by substituting into Equation 7.1. Table 4.11 should

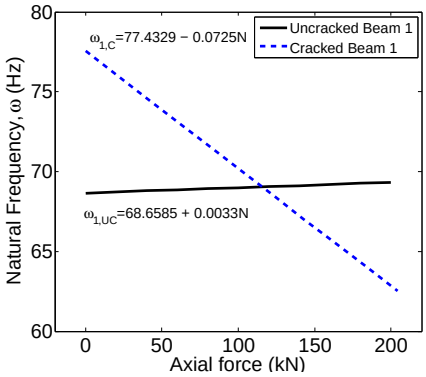

Figure 7.16.: Regression of ξ on N; Beam 1 (e=0mm)

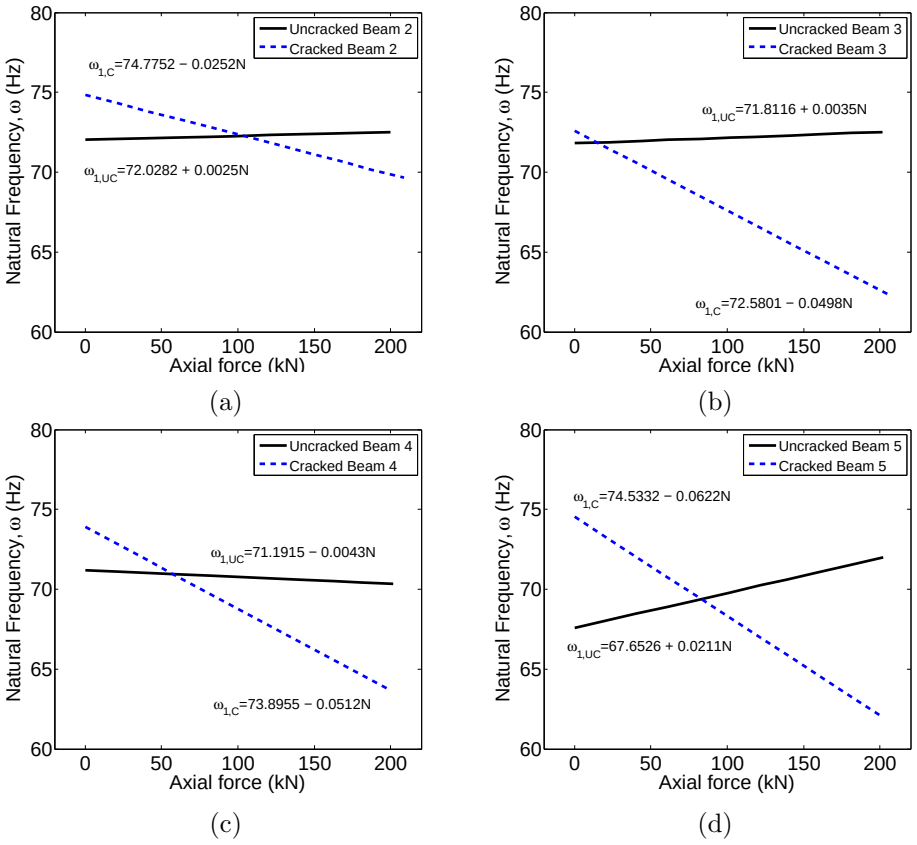

Figure 7.17.: Regression of ω_1 on N, comparing uncracked and cracked beams; (a) Beam 2 (e=+13mm); (b) Beam 3 (e=+26mm); (c) Beam 4 (e=+39mm); (d) Beam 5 (e=+52mm)

be read in conjunction with Figure 7.16 for completeness.

$$\omega_1 = \alpha_{0,i} + \alpha_{1,i} N \tag{7.1}$$

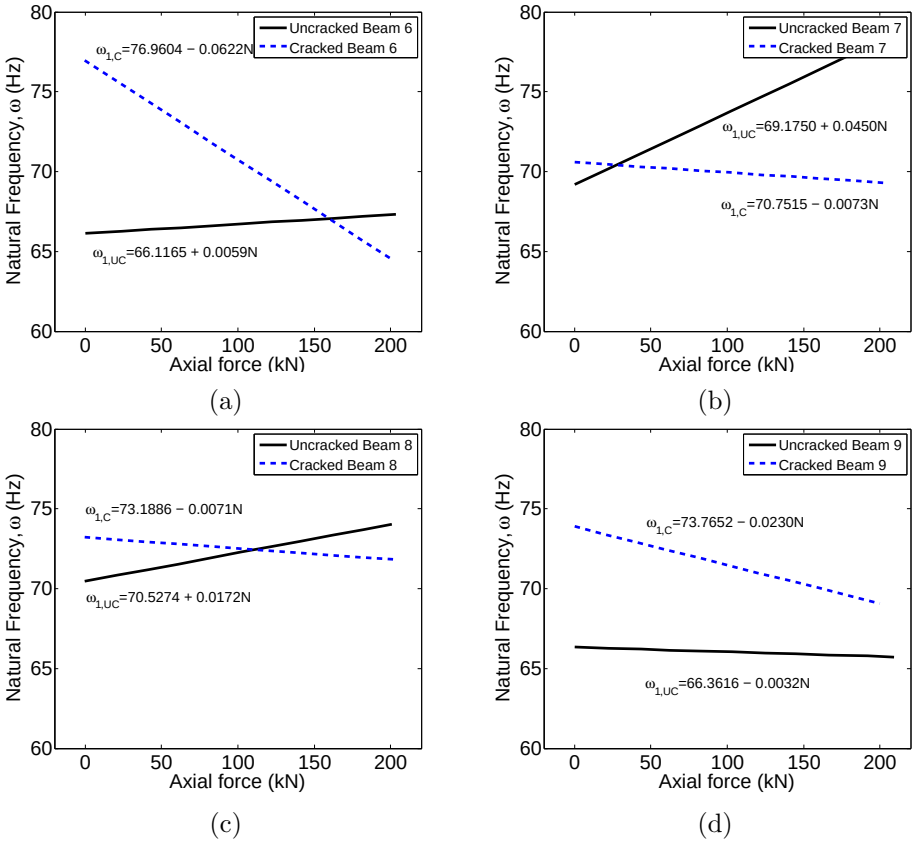

Figure 7.18.: Regression of ω_1 on N, comparing uncracked and cracked beams; (a) Beam 6 (e=-13mm); (b) Beam 7 (e=-26mm); (c) Beam 8 (e=-39mm); (d) Beam 9 (e=-52mm)

7.4.4. Damping Ratios

Figures 7.19-7.21d show the first order linear regression of damping ratios on post-tensioning load magnitude for the 9 uncracked post-tensioned concrete beams tested. Table A.9 outlines the statistical analysis on the regression intercept and slope parameters for Figures 7.19-7.21d. The damping ratios for the cracked post-tensioned concrete beam specimens were determined from the half-power bandwidth method, as outlined in Section 6.7.2, Chapter 6.

From the obtained results of changes in damping ratio with increasing post-tensioning force magnitude, no solid conclusions can be made, as 3 beams displayed a statistically significant increasing trend in damping ratio with increasing post-tensioning force magnitude, 2 beams displayed a

statistically significant decreasing trend in damping ratio with increasing post-tensioning force magnitude, and the remaining 4 beams displayed no statistical significant relationship between post-tensioning force magnitude and increasing post-tensioning load magnitude. As a result, no deterministic conclusions can be drawn on the changes in damping ratio with increasing post-tensioning load magnitude for the cracked post-tensioned concrete beams tested.

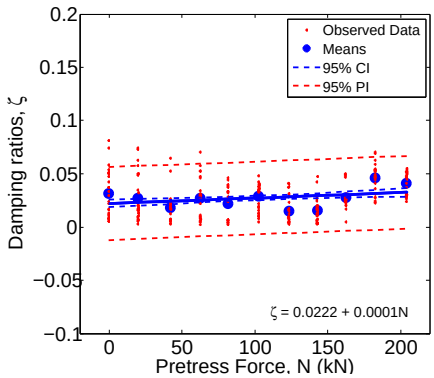

Figure 7.19.: Regression of ξ on N; Cracked Beam 1 (e=0mm)

7.5. Discussion of Accuracy of Experimental Results

In the case of the cracked beams, it was shown that a statistical significant increasing trend in fundamental bending frequency was identified with increasing post-tensioning load magnitude for the cracked beams, at a threshold value of post-tensioning load, once monolithic behaviour returned. Despite the aforementioned error/imprecision in the estimation of the fundamental bending frequency, trends are observable in the case of the cracked concrete beams. As outlined in Section 7.4, the increasing trend in frequency with increasing post-tensioning force, due to crack closure is observable over a certain threshold value of post-tensioning force. This threshold value has been determined to be the value of post-tensioning force above which the dominance of the first bending mode returns and the beam vibrates as a monolithic structure, rather than as a series of cracked entities. This indicates that, provided these trends exist, and despite the error/imprecision in the estimation of the frequency, the trends are observable

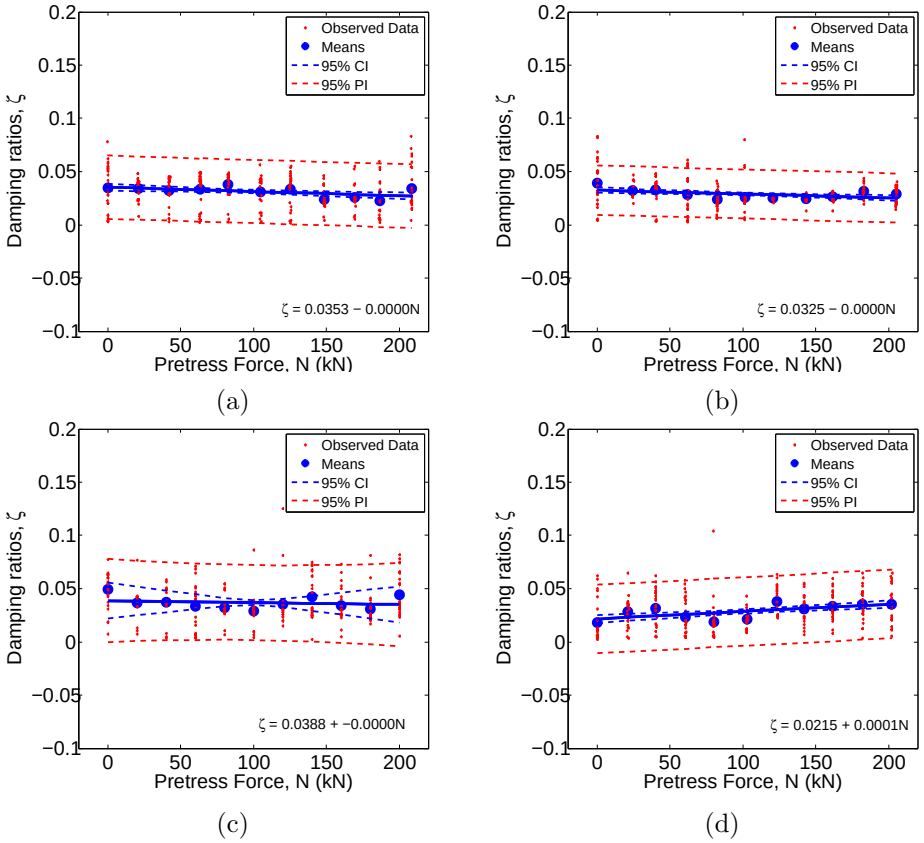

Figure 7.20.: Regression of ξ on N for cracked beams; (a) Beam 2 (e=+13mm); (b) Beam 3 (e=+26mm); (c) Beam 4 (e=+39mm); (d) Beam 5 (e=+52mm)

through this methodology. Therefore, it may be concluded that, in the case of the uncracked post-tensioned concrete beams, no relationship was found between natural frequency and post-tensioning load magnitude, however, in the case of the cracked post-tensioned concrete beams, over the aforementioned monolithic threshold, the effect of the post-tensioning force is to close the cracks and increase the bending frequency. The initial trend is a decreasing one due to the decreased effective span length due to cracking. This effective span length is increased as the cracks are closed until the point of monolithic response. From this point onwards, for Beams 1,3 & 5, as outlined in Chapter 7, Section 7.4, the increasing trend in frequency with increasing post-tensioning force, due to crack closure is observable. In all cases, the error in the estimation of the bending frequency may have been

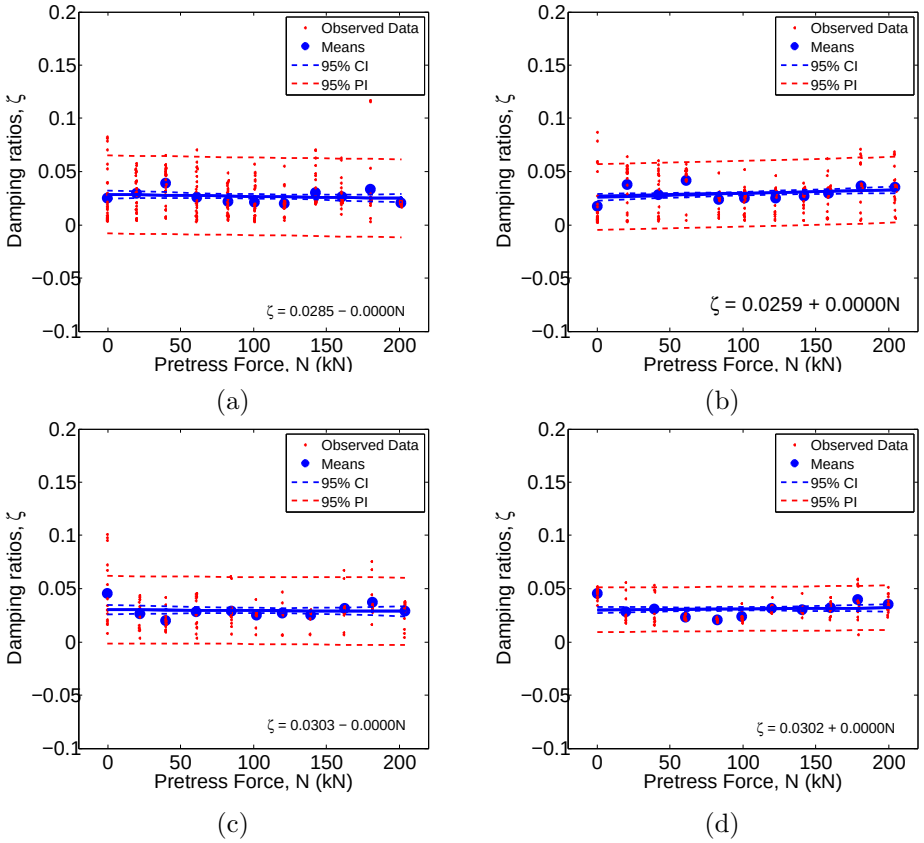

Figure 7.21.: Regression of ξ on N for cracked beams; (a) Beam 6 (e=-13mm); (b) Beam 7 (e=-26mm); (c) Beam 8 (e=-39mm); (d) Beam 9 (e=-52mm)

minimised by measuring the dynamic input force, increasing the number of excitation points, and increasing the number of response points. Furthermore, the points made in Section 4.10 regarding the "jumping" of the specimen from the supports and the resulting non-linear dynamic response and the effect of the span to depth ratio on the precision and accuracy of the estimation of the fundamental frequency also holds true for the cracked beam specimens. As before, the error in the estimation of the bending frequency may have been minimised by measuring the dynamic input force, increasing the number of excitation points, and increasing the number of response points.

7.6. Conclusions

Whereas there is significant disagreement among researchers as to the effect of prestress force magnitude on the natural vibration frequency of uncracked prestressed and post-tensioned concrete sections Quilligan et al. (2012), the effect of prestressing force on the bending frequency of cracked pre- and post-tensioned sections is more established. Researchers agree that, for cracked pre- and post-tensioned concrete beams, increasing the post-tensioning force acts as to close the cracks, increase the second moment of area of the cross section, resulting in an increase in the natural bending frequencies (Saiidi et al., 1994; Williams and Falati, 1999; Grace and Ross, 1996; Unger et al., 2006; De Roeck, 2003; Hamed and Frostig, 2004; Pavic et al., 2001; Dall'Asta and Dezi, 1996). The findings of these authors are based on the presumption of monolithic response of the cracked structure being tested. This is found to be the case in the experiments conducted and described in this chapter in that after the threshold level of post-tensioning force, at which the dominance of the first mode returns and the beam begins to vibrate monolithically again, the clear increasing trend is evident, specifically for Beams 1,3 & 5.

For the uncracked beam sections, the fundamental mode of vibration dominates the structural dynamic response and no statistically significant change in the fundamental vibration frequency can be observed. As such, for uncracked pre- and post-tensioned concrete beams, the prestressing force does not change the dynamic stiffness significantly. Pavic et al. (2001) concluded similar, stating that the dynamic properties are dependent on mass, stiffness and damping properties, on which prestressing does not have a major influence. It should also be noted that the error in the estimation of the frequency is high. Changes in frequency are affected by temperature effects, lack of ideal support conditions and material variability, which is reported to be in the order of 6-18% (Peeters and De Roeck, 2001; Cornwell et al., 1999), therefore any potential effect of prestressing force on dynamic properties is lost within this error.

For the cracked beam sections, the implications of prestressing force on dynamic properties is more apparent. For the cracked beam sections, it was found that the structural dynamic response was far more complex than for the uncracked beams. There is no clearly dominant vibration mode and the

response comprised of all modes of system. However, at threshold values of post-tensioning force there is evidence of dominance of the first vibration mode. This threshold post-tensioning load value is the load value at which the structure begins to vibrate monolithically again. The trend from this point onwards is easily identified. There is an increase in fundamental frequency with increasing post-tensioning force. This is attributed to crack closure and the subsequently increase the flexural stiffness of the member, as reported by previous authors (Saiidi et al., 1994; Williams and Falati, 1999; Grace and Ross, 1996; Unger et al., 2006; De Roeck, 2003; Hamed and Frostig, 2004; Pavic et al., 2001; Dall'Asta and Dezi, 1996).

The implications that this has for system identification, and structural health monitoring are profound. The above suggests that the identification of the existing prestressing force in uncracked prestressed concrete structures is not feasible through measurement of the natural frequency of the structure only, due to the confounding variables (temperature effects, support conditions, material properties). However, the existence of the relationship between the frequency and the level of cracking in the structure does allow for the calculation of the damage (cracking) state of the structure from the measurement of the natural frequency (De Roeck, 2003; Kim and Stubbs, 2002; Li et al., 2013) and application of the formula presented by Williams and Falati (1999).

The conclusions may be summarised as follows;

1. For the uncracked post-tensioned concrete beam sections, there is no statistically significant relationship between post-tensioning force magnitude and fundamental bending frequency evident from the data collected and presented in Chapter 6.

2. For the cracked post-tensioned concrete beam sections, there is a statistically significant change in the fundamental bending frequencies with increasing post-tensioning load magnitude.

3. There is an overall statistically significant decreasing trend in fundamental bending frequency with increasing post-tensioning load magnitude, as evident from Figures 7.12-7.14d.

4. This counter-intuitive decreasing trend is attributed to the increase in effective span length of the cracked beam. The beam in its fully

cracked state has an effective span length that is less that the actual span length due to the presence of cracking.

5. The overall structural dynamic response for the cracked post-tensioned concrete beams is complex. The fundamental bending mode does not dominate the structural response, as with the uncracked beam sections. The contribution of higher modes to the overall structural response is significant, and there is evidence of coupling of the modes. This is evident from Figures 7.4-7.6d.

6. There has been shown to be a threshold value of post-tensioning load at which the cracked post-tensioned concrete beams begin to vibrate monolithically again, in which the dominance of the first mode of vibration returns. This is evident from Figures 7.4-7.6d.

7. Once the beam begins to vibrate monolithically again, it is assumed that the effective span length returns to its maximum value. From this point onwards a statistically significant increasing trend in fundamental bending frequency is observed with increasing post-tensioning load magnitude, for beams that promote crack closure in the bottom fibre, as evident in Figure 7.8. It is acknowledged that once the cracks are fully closed the beam begins to behave as an uncracked beam, and no relationship between post-tensioning force and frequency is to be found. This is provided that the level of cracking is such that the plastic limit of the reinforcement in the under reinforced beams has not been reached. It is also acknowledged that the trend referred to is observable for Beams 1,3, & 5, however was not observed in the case of Beams 2 & 4, as outlined in Section 7.4.

The above findings, in conjunction with the findings outlined in the conclusions of Chapter 6 (Section 6.10) have profound implications in the fields of System Identification (SI) and Structural Health Monitoring (SHM). It has been suggested that, for post-tensioned concrete structures, the magnitude of the post-tensioning force may be deduced from knowledge of the modal properties of the structure, which can be obtained easily through non-destructive testing. The results obtained and reported in Chapter 6 indicate that there is no statistically significant relationship between post-tensioning load magnitude and fundamental bending frequency. Therefore,

the identification of the magnitude of the post-tensioning force based on the modal parameters is not deemed possible for uncracked concrete sections. The lack of correlation between post-tensioning force magnitude and modal properties may be attributed to the presence of confounding variables such as lack of ideal support conditions, temperature effects, and material variability of concrete.

However, in the case of the cracked post-tensioned concrete sections, a clear statistically significant relationship between post-tensioning force magnitude and fundamental bending frequency is evident, as outlined above. This clearly shows that the effect of post-tensioning force magnitude on the natural frequency of such beams is different depending on whether the beam is accompanied by originating cracks or not. This has implications in the field of Structural Health Monitoring (SHM), in which the fundamental frequency can be used not only as an indicator of damage and damage detection, but also as an indicator of the magnitude of the post-tensioning force for cracked post-tensioned concrete sections. This is in line with the findings of De Roeck (2003), who state that prestress loss results only in measurable changes in frequency if accompanied by originating cracks, Dall'Asta and Dezi (1996) who state it is possible to determine the prestressing force by measuring the natural frequency of a PSC structure in its cracked state only, and Rodríguez et al. (2010), who state that uncracked towers maintain their original stiffness and frequency, but once the towers are cracked and the cracks have been decompressed, any vibrations in the tower will mobilise smaller stiffness, which will be shown by the vibration frequencies.

8. Conclusions & Recommendations

This chapter outlines the main conclusions and recommendations arising from the modelling, analysis and results presented in Chapters 2-7, especially the conclusions from Chapter 2, which presents the current state of the art of the field to date, including a series of mathematical prediction models predicting changes in natural bending frequency with increasing post-tensioning force magnitude, Chapter 4, which presents the results of dynamic impact testing on steel rectangular sections for a series of different load cases, Chapter 5, which presents a simple new proposed linear mathematical model to predict changes in natural bending frequency with increasing post-tensioning force magnitude, Chapter 6, which presents the analysis and results of both static and dynamic testing of 9 uncracked post-tensioned concrete beams, and Chapter 7, which presents the analysis and results of dynamic testing of the same 9 post-tensioned concrete beams, following cracking by four-point bending.

The chapter is organised as follows; Section 8.1 presents a short introduction to the chapter and a recap of the objectives that were outlined in Chapter 1. Section 8.2 presents and summarises the main conclusions of the work carried out, and described throughout the course of the thesis. Section 8.3 summarises the work carried out and described throughout the course of the thesis and describes how the objectives presented in Chapter 1 and repeated in Section 8.1, have been achieved throughout the course of the work undertaken. Section 8.4 presents the main findings of the work conducted and outlines the main recommendations for future work in the field.

8.1. Review of Objectives

The main objectives of the study were previously outlined in Chapter 1 and are repeated below;

1. **Determine the validity of the *"compression-softening"* effect.** The "compression-softening" effect states that the natural frequency will decrease for an externally axially loaded slender section, as the section begins to soften. It is based on Euler buckling theory and it has been argued that this effect can be applied to pre- and post-tensioned concrete sections. The validity of this theory is put to the test, through dynamic testing of steel RHS sections.

2. **Determine whether *"compression-softening"* holds only for 'slender' members.** To determine the validity of the "compression-softening" effect for both slender and stocky sections, and to compare the dynamic response of the slender/stocky rectangular hollow sections.

3. **Determine how the dynamic properties of steel sections change with increasing axial force.** To determine the effect of both external axial load and post-tensioning force magnitude on the modal properties of rectangular steel hollow sections, and to compare both cases.

4. **To create a model to predict changes in natural frequency with increasing post-tensioning force magnitude.** To create a simple mathematical model that predicts changes in fundamental bending frequency with increasing post-tensioning force magnitude and varying post-tensioning strand eccentricity.

5. **Investigate how the dynamic properties of uncracked post-tensioned reinforced concrete sections change with increasing axial force.** To investigate how the modal properties, specifically damping ratio and fundamental frequency, of 9 uncracked post-tensioned concrete beams are affected by different post-tensioning load levels.

6. **Determine how the dynamic properties of uncracked post-tensioned reinforced concrete sections change with varying**

prestress force eccentricity. To determine how the modal properties of the post-tensioned concrete beams are affected by different straight-profiled post-tensioning strand eccentricities.

7. **Investigate how the dynamic properties of cracked post tensioned reinforced concrete sections change with increasing axial force.** To investigate how the modal properties of 9 cracked post-tensioned concrete beams are affected by different post-tensioning load levels.

8. **To compare the effect of changing post-tensioning force magnitude on the dynamic properties of cracked and uncracked post-tensioned concrete sections.** To compare the effect of post-tensioning force magnitude on both cracked and uncracked concrete beam sections and to compare the response of both type of sections.

9. **To compare the results of the generated model to the results obtained from dynamic testing.** A comparison of the simple mathematical model to the obtained experimental results in order to test the accuracy of the model.

8.2. Main conclusions of the work

The main conclusions of the work, as outlined in Chapters 4, 5, 6, 7, are outlined below;

Chapter 4

1. An externally axially loaded slender section displays good agreement with the *"compression-softening"* effect, as the obtained results have shown. A post-tensioned slender section deviates from what is expected from *"compression-softening"* theory, however, does display a decreasing trend in fundamental bending frequency, ω_1, with increasing post-tensioning load.

2. An externally axially loaded stocky section does not follow the trend predicted by *"compression-softening"* theory. A statistically significant increasing trend in ω_1 is observed with increasing axial load level.

A post-tensioned stocky section also deviates from *"compression-softening"* theory, however a statistically significant decreasing trend was observed.

3. Post-tension load is phenomenologically different to an external axial load and is not equivalent to an external axial load.

4. A post-tensioning load does not cause Euler buckling to occur.

5. *"Compression-softening"* is not valid for pre- or post-tensioned structures, therefore the use of Equation 2.1 is erroneous for post-tensioned concrete structures.

6. In all cases, a decrease in damping ratio, ξ, is observed with increasing axial load level.

7. The precision of prediction of the fundamental frequency is related to the complexity of dynamic response of the signal, and the proportion of dynamic response attributed to the fundamental mode.

Chapter 5

1. The proposed model presented in this chapter predicts an initial increase in natural bending frequencies, ω_n, of the modelled post-tensioned concrete beams with increasing post-tensioning load magnitude, N, over the range of post-tensioning force tested in the lab (0-200kN), as shown in Figure 5.31. However, when modelled over a greater range of post-tensioning force, the frequency is initially predicted to increase, and then drop off as the concrete begins to crush under post-tensioning force magnitude (Figure 5.32).

2. The proposed model predicts a greater initial increase in fundamental bending frequency than any of the existing models proposed by other authors (Saiidi et al., 1994; Kim et al., 2004; Miyamoto et al., 2000; Dall'Asta and Dezi, 1996; Zhang et al., 2012), as shown in Figure 5.33. As outlined in Section 5.8, modelling the changes in the parameters affecting natural frequency with varying post-tensioning force magnitude is a novel approach, and has not been conducted to date.

3. The proposed model is a linear kinematic model that accounts for small deflections only (i.e. Kirchoff's kinematic model) and models changes in Young's Modulus, second moment of area, span length, and mass per unit length with increasing post-tensioning force magnitude, i.e. $E(N)$, $I(N)$, $\ell(N)$, $m(N)$, as per Equation 5.1.

4. The effect of changing the Young's Modulus, $E(N)$, and second moment of area, $I(N)$, with increasing post-tensioning force magnitude are of similar importance with regard to the subsequent changes in bending frequency, and is much greater than the effect of changing span length, $\ell(N)$, and mass per unit length, $m(N)$, which can be considered negligible in comparison.

5. By taking non-linear kinematic effects into account, and allowing for large displacements and moderate rotations, Hamed and Frostig (2006) have proved that the final equation of motion for a post-tensioned concrete beam is independent of post-tensioning force magnitude, therefore there is no relationship between natural frequency and post-tensioning force magnitude.

Chapter 6

1. The "compression-softening" effect is not valid for post-tensioned concrete structures. From the static and dynamic tests conducted, no evidence of a decreasing trend in fundamental bending frequency with increasing post-tensioning force magnitude has been found.

2. From the obtained static data, the static-equivalent prediction of the fundamental bending frequency suggests that there is an increasing trend in fundamental bending frequency with increasing post-tensioning load magnitude.

3. However, from the obtained dynamic data, there is no indication of any relationship between post-tensioning load magnitude and fundamental bending frequency.

4. The dominance of the fundamental bending mode in the overall structural dynamic response of each of the 9 post-tensioned concrete beams is evident from the 3D graphs produced.

5. The results are inconclusive regarding the relationship between the change in critical damping ratio, ξ and the post-tensioning force magnitude, N.

6. Despite theory predicting that there should be a direct relationship between post-tensioning strand eccentricity and fundamental bending frequency, no such non-random systematic change could be identified from the analysis of the obtained data.

Chapter 7

1. For the uncracked post-tensioned concrete beam sections, there is no statistically significant relationship between post-tensioning force magnitude and fundamental bending frequency evident from the data collected and presented in Chapter 6.

2. For the cracked post-tensioned concrete beam sections, there is a statistically significant change in the fundamental bending frequencies with increasing post-tensioning load magnitude.

3. There is an overall statistically significant decreasing trend in fundamental bending frequency with increasing post-tensioning load magnitude, as evident from Figures 7.12-7.14d.

4. This counter-intuitive decreasing trend is attributed to the increase in effective span length of the cracked beam. The beam in its fully cracked state has an effective span length that is less that the actual span length due to the presence of cracking.

5. The overall structural dynamic response for the cracked post-tensioned concrete beams is complex. The fundamental bending mode does not dominate the structural response, as with the uncracked beam sections. The contribution of higher modes to the overall structural response is significant, and there is evidence of coupling of the modes. This is evident from Figures 7.4-7.6d.

6. There has been shown to be a threshold value of post-tensioning load at which the cracked post-tensioned concrete beams begin to vibrate monolithically again, in which the dominance of the first mode of vibration returns. This is evident from Figures 7.4-7.6d.

7. Once the beam begins to vibrate monolithically again, it is assumed that the effective span length returns to its maximum value. From this point onwards a statistically significant increasing trend in fundamental bending frequency is observed with increasing post-tensioning load magnitude, for beams that promote crack closure in the bottom fibre, as evident in Figure 7.8. It is acknowledged that once the cracks are fully closed the beam begins to behave as an uncracked beam, and no relationship between post-tensioning force and frequency is to be found. This is provided that the level of cracking is such that the plastic limit of the reinforcement in the under reinforced beams has not been reached. It is also acknowledged that the trend referred to is observable for Beams 1,3, & 5, however was not observed in the case of Beams 2 & 4, as outlined in Section 7.4.

8.3. Summary of Work and Fulfilment of Objectives

This thesis presented the methodology and results behind an experimental and numerical study conducted in order to determine if a statistically significant relationship between natural bending frequency and post-tensioning force magnitude is present for post-tensioned concrete structures. A thorough literature review was conducted on the current state of the art of the topic in the literature, and the current prediction models for changes in fundamental bending frequency with increasing post-tensioning load were compared and contrasted, highlighting some of their strengths and also some of their shortcomings.

Empirical testing was conducted on a series of rectangular hollow sections. These steel specimens were subjected to different axial load cases - an external axial load case, and a post-tensioned load case. The migration of the bending frequency with increasing axial load magnitude was determined through dynamic testing for both beam load cases, and for rectangular hollow sections with different slenderness ratios. A comparison was made between the migration of the frequency with increasing axial load magnitude for both beam load cases. As a result, conclusions could be made on the validity of the **"compression-softening"**, and its suitability

for application to pre- and post-tensioned concrete structures.

Subsequently, a simple, linear mathematical model was proposed predicting the changes in natural bending frequency with increasing post-tensioning force magnitude, for simply supported post-tensioned concrete beams with differing straight-profiled post-tensioning strand eccentricities. The model indicates a slight increase in natural frequency over practical ranges of post-tensioning force, however, does predict a theoretical peak, and a subsequent drop-off in frequency as the concrete begins to crush and lose strength under axial loading. Conclusions are drawn based on this model and it's suitability for application for both pre- and post-tensioned concrete structures.

Further static and dynamic testing was then conducted on 9 different simply-supported, uncracked post-tensioned concrete beams in the laboratory. Dynamic impact testing was conducted at increasing post-tensioning force magnitudes and a relationship between the post-tensioning force and the modal properties (fundamental bending frequency and damping ratio) was determined. The frequency was determined from peak-picking of the response signals in the frequency domain, and the damping ratio was determined via the half-power bandwidth method. Conclusions could hence be drawn about the relationship between post-tensioning force and the modal properties through a thorough statistical analysis of the data.

Following testing of the uncracked sections, the sections were cracked via four-point bending and the dynamic tests were repeated on the cracked post-tensioned concrete sections. Again, the fundamental frequency and damping ratio were determined as previously for increasing values of post-tensioning force for the cracked beam sections. The results for the uncracked and cracked post-tensioned concrete beams were compared and contrasted, and conclusions could be drawn regarding the different relationships between post-tensioning force magnitude and modal properties for both cracked and uncracked post-tensioned concrete sections.

Each of the objectives outlined previously in Chapter 1, and further outlined in Section 8.1, have been achieved, and the main conclusions are outlined in Section 8.4.

Section 8.4 summarises the main findings of the work to date, while Section 8.2 previously, summarised all of the conclusions drawn from Chapters 4, 5, 6, and 7.

8.4. Summary of Findings and Recommendations for Future Work

The main findings of the study are summarised in this section, and Section 8.4.1 outlines some suggestions for future research work following on from the work conducted and described throughout the course of this thesis.

Following the dynamic testing conducted on the steel sections, it was concluded that the "compression-softening" effect is only valid for externally axially loaded slender sections, and is not valid for stocky sections, nor is it valid for post-tensioned sections. The "compression-softening" effect is based on Euler buckling theory. Post-tensioning load cannot cause Euler buckling to occur as the post-tensioning strand is bounded by the extents of the cross section, and therefore the eccentricity of the axial force relative to the neutral axis is limited. Subsequently, Euler buckling does not occur, and the "compression-softening" effect is not valid for any type of pre- or post-tensioned structures. Furthermore, following steel testing, it was determined that the precision of prediction of the fundamental frequency is related to the complexity of dynamic response of the signal, and the proportion of dynamic response attributed to the fundamental mode. The greater the dominance of the fundamental mode, the more precise the measurement of the fundamental frequency through peak-picking.

From the simple linear mathematical model proposed, predicting changes in natural frequency with increasing post-tensioning force magnitude, it was concluded that over practical ranges of post-tensioning force, the natural frequency is predicted to increase slightly. However, as the range of post-tensioning force is extended into impractical regions (due to limits imposed by the strand tensile load capacity), a drop-off in frequency is predicted as the concrete crushes and loses strength. The proposed model predicts a greater initial increase in fundamental bending frequency than any of the existing models proposed by other authors (Saiidi et al., 1994; Kim et al., 2004; Miyamoto et al., 2000; Dall'Asta and Dezi, 1996; Zhang et al., 2012). However, it should be noted that by taking non-linear kinematic effects into account, and allowing for large displacements and moderate rotations, Hamed and Frostig (2006) have proven that the final equation of motion for a post-tensioned concrete beam is independent of post-tensioning force magnitude, therefore there is no relationship between natural frequency and

post-tensioning force magnitude.

Through the static and dynamic testing conducted on the 9 uncracked post-tensioned concrete beam sections, there were conflicting findings. From the obtained static data, the static-equivalent prediction of the fundamental bending frequency suggests that there is an increasing trend in fundamental bending frequency with increasing post-tensioning load magnitude, however, from the obtained dynamic data, there is no indication of any relationship between post-tensioning load magnitude and fundamental bending frequency. It was concluded, through dynamic testing, that for the uncracked post-tensioned concrete beams, post-tensioning force magnitude does not significantly affect the natural bending frequency, especially in the presence of confounding variables such as lack of ideal support conditions, temperature effect and material variability. Subsequently, it was concluded that non-destructive dynamic testing cannot be used as a system identification technique to determine the prestress loss for pre- and post-tensioned concrete structures. Furthermore, this implies that the prestress force magnitude need not be taken into account in design and analysis of pre- and post-tensioned concrete structures, and a simple linear beam-column analysis is sufficient to accurately describe post-tensioned concrete structures.

Finally, through dynamic testing conducted following cracking of the post-tensioned concrete sections, it was determined that there is a threshold value of post-tensioning load at which the cracked post-tensioned concrete beams begin to vibrate monolithically again, in which the dominance of the first mode of vibration returns. Once the beam begins to vibrate monolithically again, a statistically significant increasing trend in fundamental bending frequency is observed with increasing post-tensioning load magnitude, for beams that promote crack closure in the bottom fibre. As such, the effect of post-tensioning force is to close the cracks, increase the beam stiffness, and hence the natural bending frequency. This has implications in the field of damage detection/structural health monitoring, in which the correlation between crack closure, stiffness and fundamental frequency can be used in practice. Through conducting non-destructive dynamic testing on post-tensioned concrete structures that are accompanied by pre-existing cracks, the post-tensioning loss and the cracking level in the section can, theoretically be determined, from the degradation in the natural frequency over time.

In summary, *"compression-softening"* is not valid for pre- or post-tensioned concrete beams. There is only a relationship between post-tensioning force and natural frequency where the concrete section is cracked. In such cases, the effect of post-tensioning force is to close the cracks and increase the natural frequency. No such relationship exists between natural frequency and post-tensioning force for uncracked beam sections.

8.4.1. Recommendations for Future Work

There is plenty of scope for further research in this area. This section will outline some of the suggested possibilities for future investigation in this area;

Different span-to-depth ratios. Testing could be conducted on a series of different post-tensioned concrete sections, with varying span-to-depth ratios. As outlined in Section 6.9.1, the span-to-depth ratio of the tested sections was actually quite small in comparison to real pre- and post-tensioned concrete structures, consequently, the bending stiffness was high and the fundamental bending frequency was also high. It is postulated that the effect of post-tensioning force magnitude on the natural bending frequencies may in fact be significant for extremely slender structures, with very high span-to-depth ratios. Experimental modal analysis should be conducted on a variety of post-tensioned concrete beams, with differing span-to-depth ratios, at increasing post-tensioning force magnitudes, and comparison of the results should be made, to see the effect of the span-to-depth ratio on the results.

Different post-tensioning strand profiles. The 9 beams tested each had a different straight-profiled post-tensioning strand eccentricity. The effect of different strand profiles on the natural frequency of post-tensioned concrete structures should also be investigated. For example, parabolic strand profiles are also popular for simply-supported structures, as this profile maximises the eccentricity at mid-span, where the deflections are greatest. Other post-tensioning strand profiles are used, depending on the support conditions. For example, two-span pre- and post-tensioned structures tend to make use of triple-parabolic profiles, with maximum positive eccentricities

in the middle spans, and minimum negative eccentricity at the middle support, where hogging is induced. The effect of prestress force magnitude on different profiled sections should be investigated, to determine the effect of the profile on the dynamics of the sections.

Pre-stressed beams/Grouted post-tensioned concrete beams. The beams tested and described throughout the course of this thesis were ungrouted post-tensioned concrete beams. In practice, all forms of prestressing and the majority of post-tensioning makes use of grouting to bind the strand to the surrounding concrete. The effect of this bond, and it's relationship with the prestress/post-tensioning force magnitude should be investigated. The strand should be instrumented, and experimental modal testing should be conducted over time in order to measure the migration of frequency over time. The prestress force will decrease over time due to losses, and the relationship between prestress force and natural frequency can subsequently be determined.

Different reinforcement ratios. The reinforcement provided in the concrete beams tested was the minimum reinforcement in accordance with Eurocode 2 (British Standards Institute, 2004). Reinforcement was provided in order to prevent cracking from occurring under beam self-weight during lifting around the laboratory. The effect of the reinforcement ratio on the dynamics of the post-tensioned structures should be investigated. A series of post-tensioned concrete beams with different reinforcement ratios could be cast, and similar dynamic testing conducted at increasing post-tensioning load magnitudes to compare the effect of reinforcement ratios on the migration of natural bending frequency with increasing post-tensioning load magnitude.

Different concrete strengths/Young's Modulus. The concrete used to cast the test specimens was chosen as C30/37. The effect of concrete strength on the dynamic behaviour of the post-tensioned concrete beams should also be investigated. There is a direct correlation between concrete strength and Young's Modulus. The concrete strength also directly affects the cracking (tensile) strength of the concrete. A series of post-tensioned concrete beams should be cast with different concrete strengths, and the

testing outlined above should be repeated, determining the natural frequency at each post-tensioning load level for each of the different concrete strength beams, in order to determine the effect of concrete strength on the migration of the bending frequency with increasing post-tensioning force.

Different support conditions. The beams tested and described throughout the course of this thesis were simply supported, using pad foundations that allowed rotation to occur at the supports. They were not idealised simple 'knife-edge' supports. Further testing should be conducted on post-tensioned concrete beams with differing support conditions. For instance, the typical two span beam with an internal support, and triple parabolic tendon profile should be tested in a similar manner in order to determine if the presence of parasitic moments due to prestressing will effect the results obtained in any way. 'Parasitic' or 'secondary' moments arise in statically indeterminate post-tensioned concrete structures, where the post-tensioning force causes a moment due to the resistance of the internal support to the upward camber that would be induced in the supports absence.

Continuous monitoring of prestressed concrete structures. Practical non-destructive dynamic testing should be conducted on new pre- and post-tensioned concrete structures, such as post-tensioned concrete wind turbine tower, prestressed concrete bridge birders and pre- and post-tensioned concrete floor slabs. The strands should be instrumented from the time of construction and non-destructive dynamic testing conducted periodically over time, as the prestress force decreases. The purpose of this testing is to account for the in-situ behaviour of such structures and to account for the presence of the confounding variables such as the temperature effects and the lack of idealised support conditions. Ambient vibration testing may be carried out continuously to estimate the migration of the modal properties over time.

Expanded numerical model. The mathematical model proposed in Chapter 5 should be expanded to take into account all support conditions and all different strand profiles. The model, in its current guise is only applicable to simply-supported post-tensioned concrete beams with straight-profiled post-tensioning strand eccentricities - this should be expanded to

account for all section sizes, strand profiles and support conditions.

Analysis of potential interaction effects. An analysis of the potential interaction effects between post-tensioning force and eccentricity on the modal properties of such pre- and post-tensioned structures should be conducted. An analysis on such interaction effects was not conducted throughout the course of this study, as the results for such were inconclusive, and no evidence of such interaction effects was evident.

Analysis of the point of monolithic response of post-tensioned structures. An analysis of the point at which structures vibrate in a monolithic manner, and the factors affecting monolithic response for post-tensioned structures should be undertaken. For example, a simple laboratory experiment should be undertaken on a simple stacked masonry or wooden block structure, which is threaded with a post-tensioning strand/string to determine the post-tensioning force value at which the structure stops behaving as a series of stacked blocks, and begins vibrating as one monolithic structure.

Investigation of postulated "virtual effective length". The postulation for the observed initial increase in fundamental frequency of the tested sections when they were cracked as opposed to their uncracked state and the explanation of the increase in frequency in relation to a "virtual effective length" of the cracked section, as discussed in Section 7.4.3 is to be tested further, as it is acknowledged that this is merely a postulation for an effect observed during testing, and that this requires further proof/testing in order to be validated or discredited.

A. Appendices

A.2. Steel results

The statistical significance of the regression slope and intercept parameters for regressing both fundamental bending frequencies, ω_1 and Damping Ratios, ξ on applied axial load, N, for all beam and load case combinations for the steel rectangular hollow sections tested and outlined in Chapter 4 are given in Table A.1 and Table A.2. Statistical t-tests have been carried out to determine if the regression slope and intercept parameters are statistically significantly different from zero, or not.

Linear regression lines have been fitted to the data and the results are observed in Figures A.1 and A.3. The Normality of both the fundamental bending frequency and the damping ratios have been tested by plotting the results on a Normal Probability Paper, and the results are displayed in Figures A.2 and A.4.

A.2.1. Fundamental Bending Frequencies, ω_1

Table A.1 shows the calculated linear regression intercept parameter (α_0), and slope parameter (α_1) when regressing ω_1 on N for all four permutations of beam (i) and load cases (j). The corresponding linear regression equations are obtained by substituting into the following formula;

$$\omega_1 = \alpha_{0,ij} + \alpha_{1,ij} N \tag{A.1}$$

A.2.2. Damping Ratios, ξ

Table A.2 shows the calculated linear regression intercept parameter (β_0), and slope parameter (β_1) when regressing ξ_1 on N for all four permutations of beam (i) and load cases (j). The corresponding linear regression

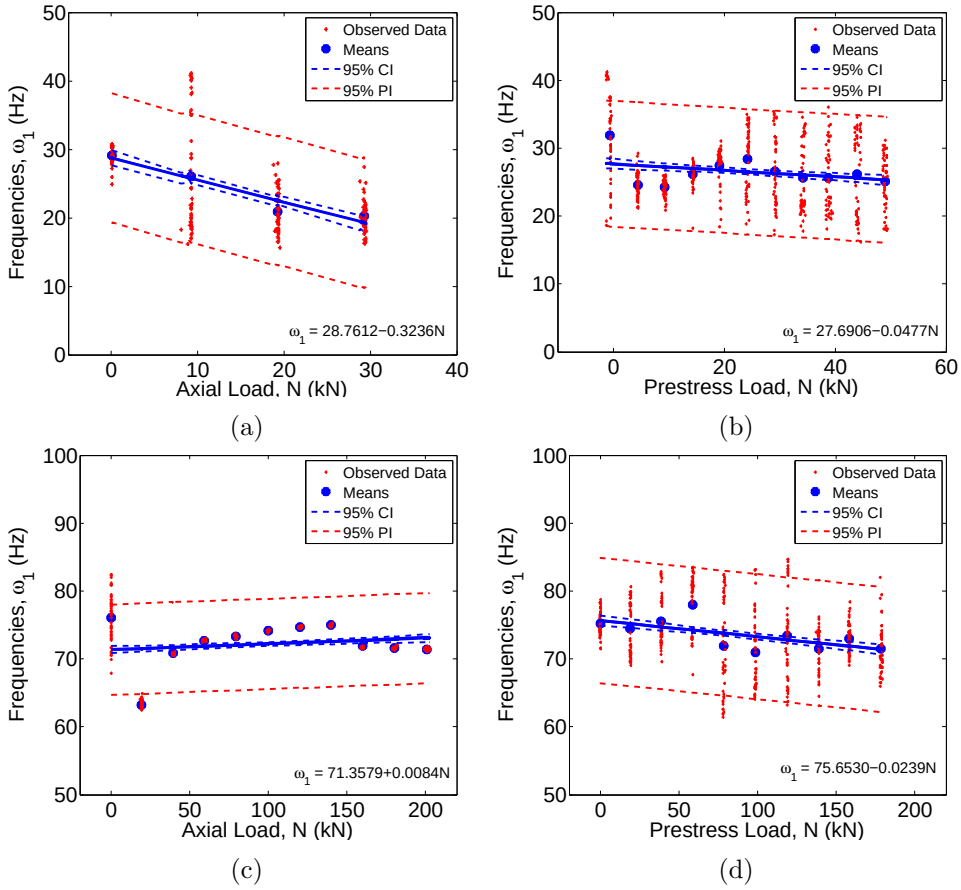

Figure A.1.: Regression analysis; ω_1 vs. N for different steel beams; (a) Beam 1, Case 1; (b) Beam 1, Case 2; (c) Beam 2, Case 1; (d) Beam 2, Case 2.

Table A.1.: Statistical analysis on regression parameters for ω_1 on N

B/C	Reg. P.	Value	SE	t-value	t-crit.	p	95% CI
B1 C1	$\alpha_{0,11}$	28.7612	0.5574	51.5969	1.9720	0.0000	(27.6620,29.8605)
	$\alpha_{1,11}$	-0.3236	0.0308	-10.5204	1.9720	0.0000	(-0.3842,-0.2629)
B1 C2	$\alpha_{0,12}$	27.6906	0.3709	74.6608	1.9643	0.0000	(26.9621,28.4192)
	$\alpha_{1,12}$	-0.0477	0.0130	-3.6845	1.9643	0.0003	(-0.0732,-0.0223)
B2 C1	$\alpha_{0,21}$	71.3579	0.2682	266.0298	1.9644	0.0000	(70.8310,71.8848)
	$\alpha_{1,21}$	0.0084	0.0023	3.5894	1.9644	0.0004	(0.0038,0.0130)
B2 C2	$\alpha_{0,22}$	75.6530	0.3855	196.2659	1.9647	0.0000	(74.8956,76.4103)
	$\alpha_{1,22}$	-0.0239	0.0037	-6.5195	1.9647	0.0000	(-0.0311,-0.0167)

equations are obtained by substituting into the following formula;

$$\xi_1 = \beta_{0,ij} + \beta_{1,ij} N \tag{A.2}$$

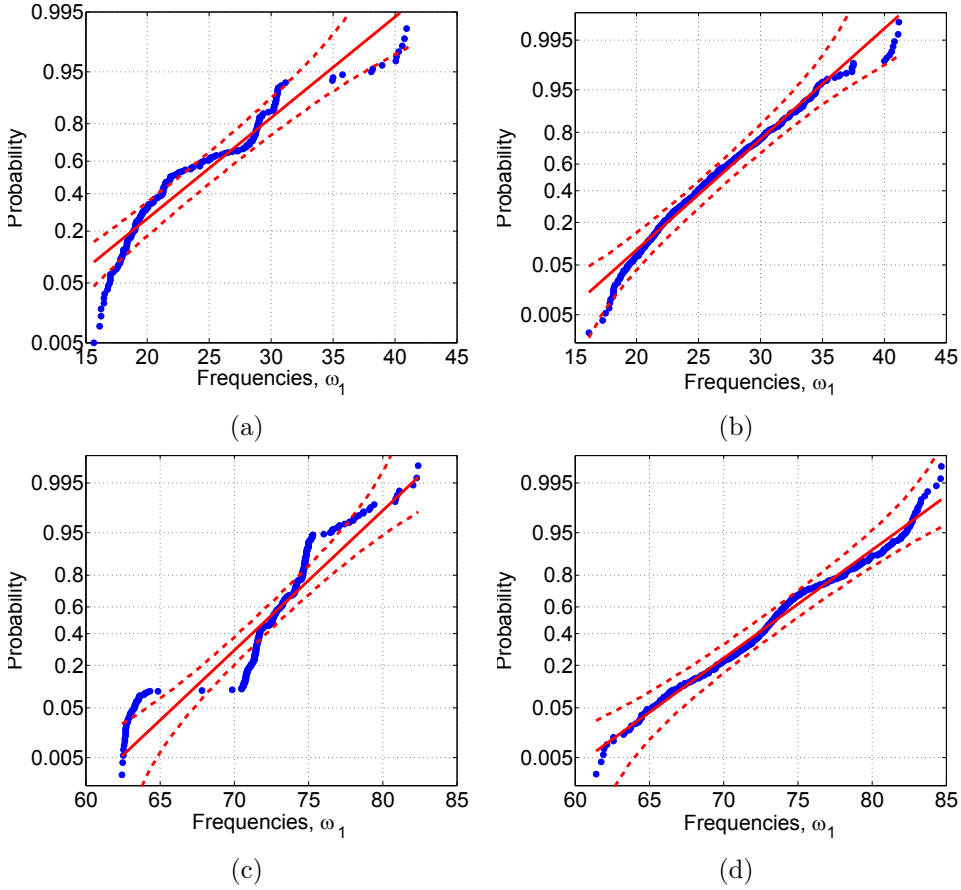

Figure A.2.: Normal Probability Plots of Fundamental Bending Frequency, ω_1 for each beam/load case combination; (a) Beam 1, Case 1; (b) Beam 1, Case 2; (c) Beam 2, Case 1; (d) Beam 2, Case 2.

Table A.2.: Statistical analysis on regression parameters for ξ_1 on N

B/C	Reg. P.	Value	SE	t-value	t-crit.	p	95% CI
B1 C1	$\beta_{0,11}$	0.0458	0.0032	14.2186	1.9720	0.0000	(0.0395,0.0522)
	$\beta_{1,11}$	-0.0010	0.0002	-5.3699	1.9720	0.0000	(-0.0013,-0.0006)
B1 C2	$\beta_{0,12}$	0.1371	0.0062	22.1801	1.9643	0.0000	(0.1249,0.1492)
	$\beta_{1,12}$	-0.0021	0.0002	-9.8760	1.9643	0.0000	(-0.0026,-0.0017)
B2 C1	$\beta_{0,21}$	0.0344	0.0010	35.8787	1.9644	0.0000	(0.0325,0.0363)
	$\beta_{1,21}$	-0.0002	0.0000	-19.4633	1.9644	0.0004	(-0.0002,-0.0001)
B2 C2	$\beta_{0,22}$	0.0714	0.0017	41.2609	1.9647	0.0000	(0.0680,0.0748)
	$\beta_{1,22}$	-0.0004	0.0000	-24.6953	1.9647	0.0000	(-0.0004,-0.0004)

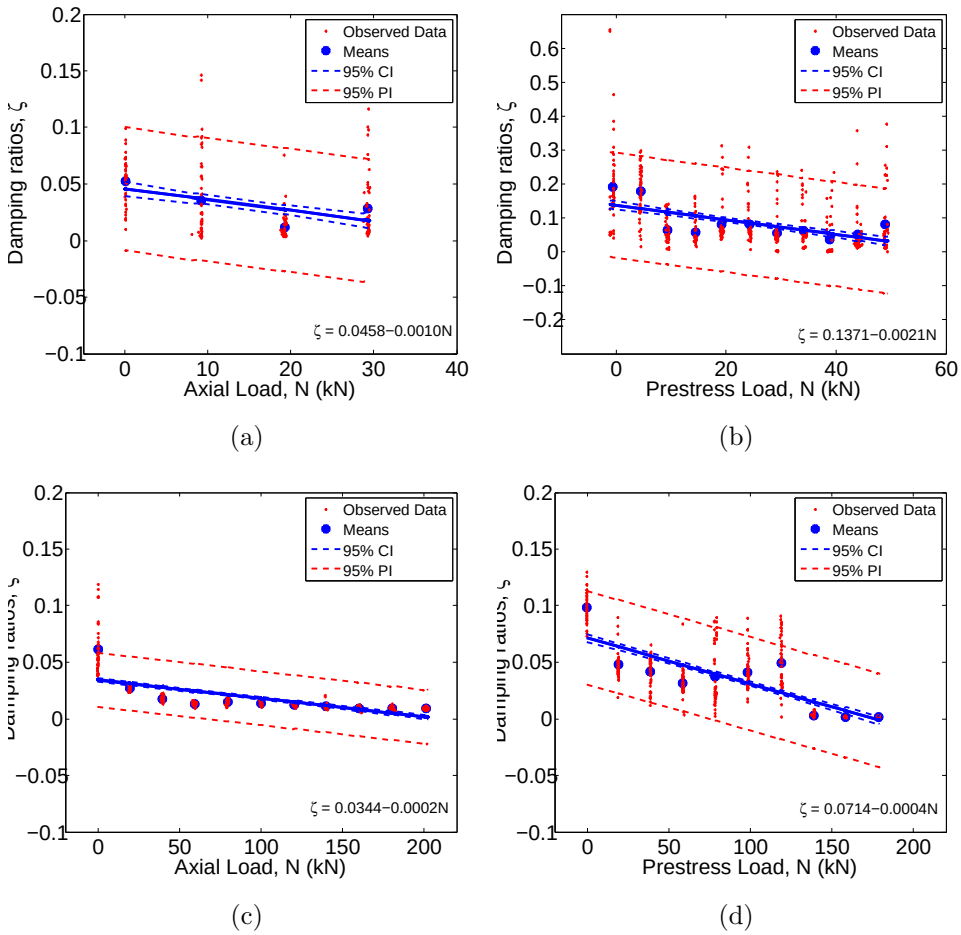

Figure A.3.: Regression analysis; ξ vs. N for different steel beams; (a) Beam 1, Case 1; (b) Beam 1, Case 2; (c) Beam 2, Case 1; (d) Beam 2, Case 2.

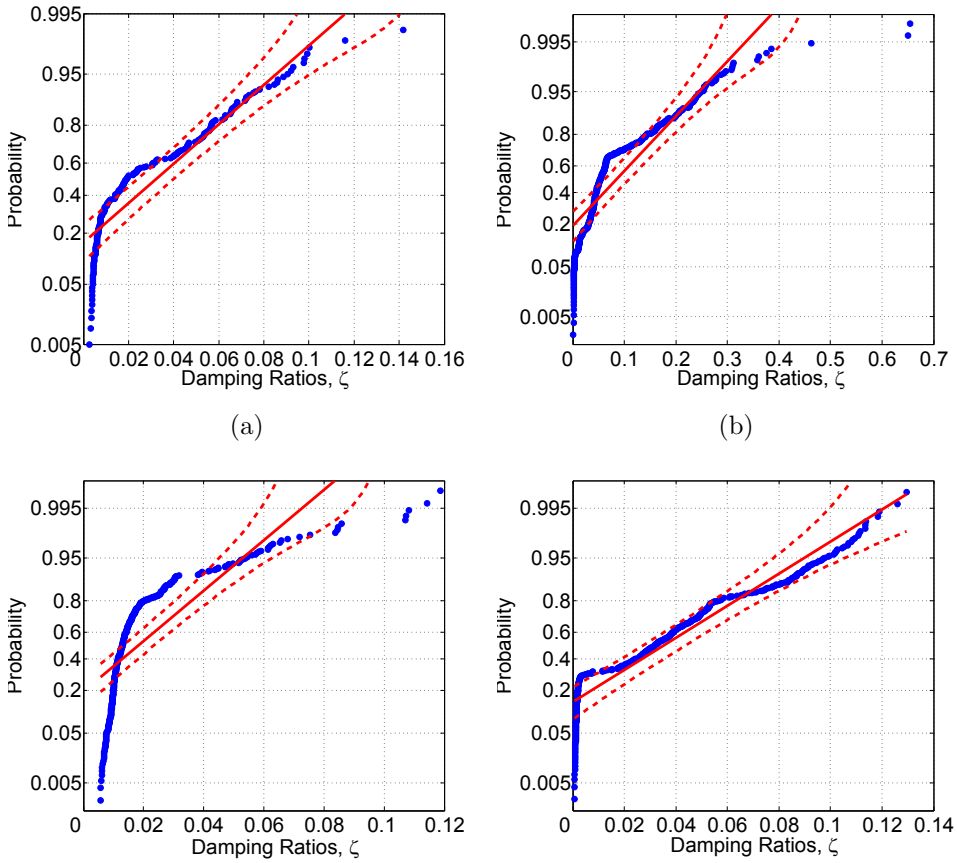

Figure A.4.: Normal Probability Plots of Damping Ratio, ξ for each beam/load case combination; (a) Beam 1, Case 1; (b) Beam 1, Case 2; (c) Beam 2, Case 1; (d) Beam 2, Case 2.

A.3. Uncracked Concrete Results

The results of the statistical analysis on the uncracked concrete sections, as described in Chapter 6 are outlined in this section. Section A.3.1 presents the statistical analysis of static equivalent fundamental frequencies at increasing post-tensioning load magnitude. Section A.3.2 presents the statistical analysis of the calculation of the dynamic frequency of the uncracked post-tensioned concrete beams, and Section A.3.2 presents the statistical analysis of the calculation of the damping ratio of the uncracked post-tensioned concrete beams.

A.3.1. Static Results, $\omega_{1,S1}$, $\omega_{1,S2}$

Table A.3 shows the results of the statistical analysis on the static equivalent of the fundamental frequency with increasing post-tensioning load magnitude for the uncracked concrete sections. Table A.3 provides supplemental information to that laid out in Chapter 6.

A.3.2. Dynamic Results

Table A.4 presents the statistical analysis on the regression parameters of regression natural frequency on post-tensioning load magnitude for the uncracked post-tensioned concrete sections, and Table A.5 indicates and summarises the general trends observed in accordance with the results and conclusions arising from Table A.4.

Frequencies, $\omega_{1,D}$

Table A.4 shows the calculated linear regression intercept parameter (α_0), and slope parameter (α_1) when regressing ω_1 on N for all nine number beams (i). The corresponding linear regression equations are obtained by substituting into the following formula;

$$\omega_1 = \alpha_{0,i} + \alpha_{1,i} N \tag{A.3}$$

Table A.3.: Statistical analysis on regression parameters for $\omega_{1,S1}$ and $\omega_{1,S2}$ on N

B#	Reg. P.	Value	SE	t-value	t-crit.	p	95% CI
B1	$\alpha_{0,1}$	59.7233	1.6972	35.19	2.2622	0.0000	(55.8840,63.5626)
	$\alpha_{1,1}$	0.1675	0.0142	11.76	2.2622	0.0000	(0.1353,0.1997)
	$\alpha_{0,1}$	58.7176	5.5784	10.53	2.2622	0.0000	(46.0984,71.3368)
	$\alpha_{1,1}$	0.2755	0.0468	5.88	2.2622	0.0002	(0.1696,0.3813)
B2	$\alpha_{0,2}$	47.7036	1.0101	47.22	2.0796	0.0000	(45.6029,49.8043)
	$\alpha_{1,2}$	0.0735	0.0087	8.44	2.0796	0.0000	(0.0553,0.0916)
	$\alpha_{0,2}$	41.7939	1.2572	33.24	2.0860	0.0000	(39.1716,44.4163)
	$\alpha_{1,2}$	0.0879	0.0105	8.36	2.0860	0.0000	(0.0660,0.1099)
B3	$\alpha_{0,3}$	74.0030	2.3010	32.16	2.0860	0.0000	(69.2032,78.8028)
	$\alpha_{1,3}$	0.2981	0.0193	15.48	2.0860	0.0000	(0.2579,0.3383)
	$\alpha_{0,3}$	60.2774	0.5241	115.01	2.0860	0.0000	(59.1841,61.3707)
	$\alpha_{1,3}$	0.0907	0.0044	20.69	2.0860	0.0000	(0.0816,0.0999)
B4	$\alpha_{0,4}$	66.8800	0.6230	107.35	2.0860	0.0000	(65.5804,68.1796)
	$\alpha_{1,4}$	0.1363	0.0052	26.04	2.0860	0.0000	(0.1253,0.1472)
	$\alpha_{0,4}$	64.1038	0.5541	115.70	2.0860	0.0000	(62.9481,65.2596)
	$\alpha_{1,4}$	0.1541	0.0047	33.06	2.0860	0.0000	(0.1444,0.1638)
B5	$\alpha_{0,5}$	66.5409	0.8758	75.98	2.0860	0.0000	(64.7140,68.3679)
	$\alpha_{1,5}$	0.1072	0.0073	14.67	2.0860	0.0000	(0.0919,0.1224)
	$\alpha_{0,5}$	63.8006	0.9855	64.74	2.0860	0.0000	(61.7448,65.8564)
	$\alpha_{1,5}$	0.1200	0.0082	14.64	2.0860	0.0000	(0.1029,0.1371)
B6	$\alpha_{1,6}$	61.3804	0.6625	92.65	2.0860	0.0000	(59.9984,62.7623)
	$\alpha_{1,6}$	0.0643	0.0055	11.61	2.0860	0.0000	(0.0528,0.0759)
	$\alpha_{1,6}$	58.8722	0.4548	129.46	2.0860	0.0000	(57.9237,59.8208)
	$\alpha_{1,6}$	0.0732	0.0038	19.22	2.0860	0.0000	(0.0653,0.0812)
B7	$\alpha_{0,8}$	66.7005	0.7977	83.62	2.0860	0.0000	(65.0366,68.3644)
	$\alpha_{1,8}$	-0.0005	0.0067	-0.07	2.0860	0.9462	(-0.0144,0.0135)
	$\alpha_{0,7}$	60.9159	0.4011	151.88	2.0860	0.0000	(60.0792,61.7525)
	$\alpha_{1,7}$	0.0189	0.0034	5.65	2.0860	0.0000	(0.0119,0.0259)
B8	$\alpha_{0,8}$	62.8552	0.4784	131.38	2.0860	0.0000	(61.8572,63.8532)
	$\alpha_{1,8}$	0.0073	0.0041	1.77	2.0860	0.9462	(-0.0013,0.0159)
	$\alpha_{0,8}$	57.7603	0.2238	258.10	2.0860	0.0000	(57.2935,58.2271)
	$\alpha_{1,8}$	0.0193	0.0019	10.31	2.0860	0.0000	(0.0154,0.0232)
B9	$\alpha_{0,9}$	63.1564	0.5440	116.10	2.0860	0.0000	(62.0216,64.2911)
	$\alpha_{1,9}$	-0.0012	0.0045	-0.27	2.0860	0.7921	(-0.0107,0.0083)
	$\alpha_{0,9}$	64.1017	0.9121	70.28	2.0860	0.0000	(62.1992,66.0043)
	$\alpha_{1,9}$	-0.0159	0.0077	-2.07	2.0860	0.0516	(-0.0319,0.0001)

Damping ratios, ξ

Table A.6 shows the calculated linear regression intercept parameter (β_0), and slope parameter (β_1) when regressing ξ on N for all nine number beams

Table A.4.: Statistical analysis on regression parameters for $\omega_{1,D}$ on N

B#	Reg. P.	Value	SE	t-value	t-crit.	p	95% CI
B1	$\alpha_{0,1}$	68.6585	2.0515	33.4680	1.9672	0.0000	(64.6228,72.6942)
	$\alpha_{1,1}$	0.0033	0.0204	0.1635	1.9672	0.8702	(-0.0368,0.0434)
B2	$\alpha_{0,2}$	72.0282	0.3415	210.9027	1.9672	0.0000	(71.3563,72.7000)
	$\alpha_{1,2}$	0.0025	0.0029	0.8589	1.9672	0.3910	(-0.0032,0.0082)
B3	$\alpha_{0,3}$	71.8116	0.4017	178.7481	1.9672	0.0000	(71.0213,72.6020)
	$\alpha_{1,3}$	0.0035	0.0034	1.0310	1.9672	0.3033	(-0.0031,0.0101)
B4	$\alpha_{0,4}$	71.1915	0.3728	190.9584	1.9672	0.0000	(70.4581,71.9249)
	$\alpha_{1,4}$	-0.0043	0.0031	-1.3659	1.9672	0.1729	(-0.0104,0.0019)
B5	$\alpha_{0,5}$	67.6526	0.5805	116.5487	1.9672	0.0000	(66.5107,68.7946)
	$\alpha_{1,5}$	0.0211	0.0049	4.2831	1.9672	0.0000	(0.0114,0.0307)
B6	$\alpha_{1,6}$	66.1165	0.4804	137.6213	1.9672	0.0000	(65.1714,67.0616)
	$\alpha_{1,6}$	0.0059	0.0040	1.4877	1.9672	0.1378	(-0.0019,0.0138)
B7	$\alpha_{0,7}$	69.6030	0.3444	202.1280	1.9677	0.0000	(68.9254,70.2806)
	$\alpha_{1,7}$	0.0445	0.0029	15.4322	1.9677	0.0000	(0.0388,0.0502)
B8	$\alpha_{0,8}$	70.6975	0.3820	185.0695	1.9684	0.0000	(69.9456,71.4494)
	$\alpha_{1,8}$	0.0453	0.0038	11.9044	1.9684	0.0000	(0.0378,0.0528)
B9	$\alpha_{0,9}$	66.3616	0.6663	99.5991	1.9672	0.0000	(65.0509,67.6724)
	$\alpha_{1,9}$	-0.0032	0.0054	-0.5856	1.9672	0.5586	(-0.0137,0.0074)

Table A.5.: Observed trends in uncracked beam data

B#	e (mm)	$\omega_1(N)$	$\xi(N)$
B1	0	-	-
B2	+13	-	↘
B3	+26	-	↗
B4	+39	-	-
B5	+52	↗	↗
B6	-13	-	-
B7	-26	↗	↗
B8	-39	↗	↘
B9	-52	-	↘

(i). The corresponding linear regression equations are obtained by substituting into the following formula;

$$\xi = \beta_{0,i} + \beta_{1,i} N \tag{A.4}$$

Table A.6.: Statistical analysis on regression parameters for ξ on N

B#	Reg. P.	Value	SE	t-value	t-crit.	p	95% CI
B1	$\beta_{0,1}$	0.0211	0.0096	2.2022	1.9672	0.0283	(0.0023,0.0400)
	$\beta_{1,1}$	0.0000	0.0001	0.1699	1.9672	0.8652	(-0.0002,0.0002)
B2	$\beta_{0,2}$	0.0370	0.0022	17.1074	1.9672	0.0000	(0.0327,0.0412)
	$\beta_{1,2}$	-0.0001	0.0000	-6.4672	1.9672	0.0000	(-0.0002,-0.0001)
B3	$\beta_{0,3}$	0.0056	0.0012	4.8365	1.9672	0.0000	(0.0033,0.0078)
	$\beta_{1,3}$	0.0000	0.0000	4.1999	1.9672	0.0000	(0.0000,0.0001)
B4	$\beta_{0,4}$	0.0338	0.0014	24.4342	1.9672	0.0000	(0.0311,0.0365)
	$\beta_{1,4}$	-0.0000	0.0000	-0.8902	1.9672	0.3740	(-0.0000,0.0000)
B5	$\beta_{0,5}$	0.0362	0.0021	16.9762	1.9672	0.0000	(0.0320,0.0404)
	$\beta_{1,5}$	0.0000	0.0000	2.5735	1.9672	0.0105	(0.0000,0.0001)
B6	$\beta_{1,6}$	0.0298	0.0013	22.4369	1.9672	0.0000	(0.0272,0.0324)
	$\beta_{1,6}$	-0.0000	0.0000	-0.0969	1.9672	0.9228	(-0.0000,0.0000)
B7	$\beta_{0,7}$	0.0366	0.0018	20.7348	1.9675	0.0000	(0.0332,0.0401)
	$\beta_{1,7}$	0.0001	0.0000	6.5090	1.9675	0.0000	(0.0001,0.0001)
B8	$\beta_{0,8}$	0.0469	0.0016	29.4815	1.9672	0.0000	(0.0438,0.0501)
	$\beta_{1,8}$	-0.0000	0.0000	-2.4571	1.9672	0.0145	(-0.0001,-0.0000)
B9	$\beta_{0,9}$	0.0420	0.0022	19.3577	1.9672	0.0000	(0.0377,0.0462)
	$\beta_{1,9}$	-0.0001	0.0000	-2.8821	1.9672	0.0042	(-0.0001,-0.0000)

Table A.7.: Observed trends in cracked beam data

B#	e (mm)	$\omega_1(N)$	$\xi(N)$
C1	0	$\searrow$	$\nearrow$
C2	+13	$\searrow$	$\searrow$
C3	+26	$\searrow$	$\searrow$
C4	+39	-	-
C5	+52	$\searrow$	$\nearrow$
C6	-13	$\searrow$	-
C7	-26	$\searrow$	$\nearrow$
C8	-39	-	-
C9	-52	$\searrow$	-

A.4. Cracked Concrete Results

Section A.4.1 outlines the statistical analysis conducted on the natural frequency values obtained from the testing described on the cracked post-tensioned concrete beam sections in Chapter 7, whereas Section A.4.2 outlines the statistical analysis conducted on the damping ratios calculated from the testing described on the cracked post-tensioned concrete beam sections in Chapter 7.

Table A.8 shows the statistical analysis on the regression parameters for regressing fundamental natural frequency on post-tensioning load magnitude for the uncracked post-tensioned concrete beams tested, while Table A.9 shows the statistical analysis on the regression parameters for regressing damping ratio on post-tensioning load magnitude for the uncracked post-tensioned concrete beams tested.

A.4.1. Fundamental Frequency, ω_1

Table A.8.: Statistical analysis on regression parameters for ω_1 on N

B#	Reg.P.	Value	SE	t-value	t-crit.	p	95% CI
C1	$\alpha_{0,1}$	77.4329	0.4465	173.4027	1.9680	0.0000	(76.5541,78.3117)
	$\alpha_{1,1}$	-0.0725	0.0038	-18.8934	1.9680	0.0000	(-0.0801,-0.0650)
C2	$\alpha_{0,2}$	74.7752	0.4102	182.2883	1.9677	0.0000	(73.9681,75.5824)
	$\alpha_{1,3}$	-0.0252	0.0034	-7.4582	1.9677	0.0000	(-0.0318,-0.0185)
C3	$\alpha_{0,3}$	72.5801	0.5957	121.8356	1.9677	0.0000	(71.4078,73.7523)
	$\alpha_{1,3}$	-0.0498	0.0049	-10.1514	1.9677	0.0000	(-0.0595,-0.0402)
C4	$\alpha_{0,4}$	73.8955	3.2289	22.8860	1.9687	0.0000	(67.5389,80.2521)
	$\alpha_{1,4}$	-0.0512	0.0320	-1.5981	1.9687	0.1112	(-0.1143,0.0119)
C5	$\alpha_{0,5}$	74.5332	0.4785	155.7534	1.9691	0.0000	(73.5909,75.4754)
	$\alpha_{1,5}$	-0.0622	0.0040	-15.5862	1.9691	0.0000	(-0.0700,-0.0543)
C6	$\alpha_{1,6}$	76.9604	0.5600	137.4217	1.9672	0.0000	(75.8587,78.0621)
	$\alpha_{1,6}$	-0.0622	0.0047	-13.1872	1.9672	0.0000	(-0.0715,-0.0529)
C7	$\alpha_{0,7}$	70.7515	0.4381	161.4799	1.9672	0.0000	(69.8896,71.6134)
	$\alpha_{1,7}$	-0.0073	0.0037	-1.9806	1.9672	0.0485	(-0.0145,-0.0000)
C8	$\alpha_{0,8}$	73.1886	0.6833	107.1066	1.9737	0.0000	(71.8399,74.5373)
	$\alpha_{1,8}$	-0.0071	0.0057	-1.2449	1.9737	0.2148	(-0.0185,0.0042)
C9	$\alpha_{0,9}$	73.7652	0.4917	150.0268	1.9746	0.0000	(72.7943,74.7361)
	$\alpha_{1,9}$	-0.0230	0.0048	-4.8378	1.9746	0.0000	(-0.0324,-0.0136)

A.4.2. Damping ratios, ξ

Table A.9.: Statistical analysis on regression parameters for ξ on N

B#	Reg.P.	Value	SE	t-value	t-crit.	p	95% CI
C1	$\beta_{0,1}$	0.0222	0.0019	11.6138	1.9680	0.0000	(0.0184,0.0259)
	$\beta_{1,1}$	0.0001	0.0000	3.0821	1.9680	0.0022	(0.0000,0.0001)
C2	$\beta_{0,2}$	0.0353	0.0016	22.4737	1.9677	0.0000	(0.0322,0.0384)
	$\beta_{1,2}$	-0.0000	0.0000	-3.1060	1.9677	0.0021	(-0.0001,-0.0000)
C3	$\beta_{0,3}$	0.0325	0.0013	25.5978	1.9677	0.0000	(0.0300,0.0350)
	$\beta_{1,3}$	-0.0000	0.0000	-3.4188	1.9677	0.0007	(-0.0001,-0.0000)
C4	$\beta_{0,4}$	0.0388	0.0086	4.5197	1.9687	0.0000	(0.0219,0.0557)
	$\beta_{1,4}$	-0.0000	0.0001	-0.2157	1.9687	0.8294	(-0.0002,0.0001)
C5	$\beta_{0,5}$	0.0215	0.0019	11.4405	1.9691	0.0000	(0.0178,0.0252)
	$\beta_{1,5}$	0.0001	0.0000	4.4532	1.9691	0.0000	(0.0000,0.0001)
C6	$\beta_{1,6}$	0.0285	0.0019	14.9605	1.9672	0.0000	(0.0248,0.0323)
	$\beta_{1,6}$	-0.0000	0.0000	-1.1019	1.9672	0.2713	(-0.0000,0.0000)
C7	$\beta_{0,7}$	0.0259	0.0016	15.7808	1.9672	0.0000	(0.0227,0.0292)
	$\beta_{1,7}$	0.0000	0.0000	2.4878	1.9672	0.0133	(0.0000,0.0001)
C8	$\beta_{0,8}$	0.0303	0.0022	13.5779	1.9737	0.0000	(0.0259,0.0347)
	$\beta_{1,8}$	-0.0000	0.0000	-0.4120	1.9737	0.6808	(-0.0000,0.0000)
C9	$\beta_{0,9}$	0.0302	0.0015	19.8011	1.9746	0.0000	(0.0272,0.0332)
	$\beta_{1,9}$	0.0000	0.0000	0.6187	1.9746	0.5370	(-0.0000,0.0000)

A.5. Conferences Attended

A list of the conferences attended so far are given in Table A.10;

Table A.10.: Conferences attended

Conference	**Date**	**Venue**	**Poster**	**Paper**	**Oral**
BCRI 2012	06-07/09/2012	DIT, TCD			
IStructE YRC 2013	14/03/2013	London			
DAMAS 2013	08-10/07/2013	TCD			
IStructE YRC 2014	05/03/2014	London	✓		
CERI 2014	28-29/08/2014	QUB		✓	✓
ACSMS 23	09-12/12/2014	Byron Bay, Australia		✓	✓
IStructE YRC 2015	14/04/2015	London		✓	✓
IOMAC 2015	10-14/05/2015	Gijón, Spain		✓	✓
DAMAS 2015	24-26/08/2015	Ghent, Belgium		✓	✓

A.6. List of Publications

A list of conference and journal publications stemming from the work conducted and described throughout this thesis is given in Sections A.6.1 and A.6.2 respectively.

A.6.1. Conference Papers

1. Noble, D., Nogal, M., O'Connor, A., and Pakrashi, V. (2014). Impact hammer testing on post-tensioned steel RHS sections; an investigation of the *"Compression Softening"* effect. In Proceedings of Civil Engineering Research in Ireland Conference, volume I, pages 427-432. Civil Engineering Research Association of Ireland.

2. Noble, D., Nogal, M., O'Connor, A., and Pakrashi, V. (2014). The effect of prestress force magnitude on the natural frequencies of prestressed concrete structures. In Proceedings of the 23rd Australasian Conference on the Mechanics of Structures and Materials (ACMSM23), volume I, pages 333-338. Southern Cross University.

3. Noble, D., Nogal, M., O'Connor, A., and Pakrashi, V. (2015). The effect of post-tensioning force magnitude and eccentricity on the natural bending frequency of cracked post-tensioned concrete beams. In Proceedings of 11th International Conference on Damage Assessment of Structures (DAMAS) 2015, pages xxx-xxx. 11th International Conference on Damage Assessment of Structures (DAMAS) 2015.

4. Noble, D., Nogal, M., O'Connor, A., and Pakrashi, V. (2015c). Output only investigation of the effect of post-tensioning force on natural frequencies of post-tensioned concrete beams. In Proceedings of International Operational Modal Analysis Conference (IOMAC), pages 197-204. International Operational Modal Analysis Conference (IOMAC).

A.6.2. Journal Papers

1. Noble, D., Nogal, M., O'Connor, A., and Pakrashi, V. (2015a). Dynamic impact testing on post-tensioned steel rectangular hollow sec-

tions; an investigation into the “compression-softening” effect. Journal of Sound and Vibration, 355:246-263.

2. Noble, D., Nogal, M., O’Connor, A., and Pakrashi, V. (2016). The effect of prestress force magnitude and eccentricity on the natural bending frequencies of uncracked prestressed concrete beams. Journal of Sound and Vibration, 365:22-44.

Nomenclature

$[\bar{C}]$	Modal damping matrix of given structure	
$[\bar{K}]$	Modal stiffness matrix of given structure	
$[\bar{M}]$	Modal mass matrix of given structure	
$[C]$	Damping matrix of given structure	
$[H(j\omega)]$	Frequency response function (FRF)	
$[K]$	Stiffness matrix of given structure	
$[M]$	Mass matrix of given structure	
β	Slenderness ratio, $\beta = \ell/r$	
ΔP_t	Change in tendon tension due to flexural vibration	N
ΔP_{tc}	Horizontal component of increase in prestressing force due to flexural vibration	N
ΔP_{ts}	Vertical component of increase in prestressing force due to flexural vibration	N
ℓ	Span length of the beam	m
ℓ_t	Length of tendon	m
ϵ_{xx}	Axial strain	
γ	Shear strain	
γ_i	Unit weight of the girder	kN/m^3
γ_{ss}	Beam shear rotation	
λ_b	Critical load parameter	

λ_f	Frequency parameter	
ν	Poisson's ratio for concrete	
ω_1	Fundamental bending frequency	rad/s
ω_n	n^{th} natural bending frequency	rad/s
$\phi(x)$	Eigenfunction describing modeshape of beam	
Φ_n	n^{th} fundamental bending mode shape	
ψ_x	Beam curvature	
ρ	Weight density of reinforced concrete,	kN/m^3
ρ_c	mass density of concrete	kg/m^3
ρ_s	mass density of prestressing steel	kg/m^3
θ_i	Initial angle of the post-tensioning tendons	
θ_s	Slope of FBD of beam in Figure 2.2	
ξ	Damping ratio	
$\{F(t)\}$	Time dependent force vector exciting the structure	
$\{x(t)\}$	Time dependent vector of displacements of the structure	
A	Cross sectional area,	mm^2
a	Distance from the support to the deviator	mm
A_b	Beam cross sectional area	m^2
A_i	Cross sectional area of girder cross section	mm^2
A_s	Cross sectional area of prestressing steel strand	m^2
A_t	Cross sectional area of tendon	mm^2
A_{cab}	Cable cross sectional area	m^2
A_{conc}	Cross sectional area of concrete section	m^2
b	Breadth of rectangular cross section,	mm

C, s	Arbitrary constants	
E	Young's Modulus of Elasticity	N/m^2
e	Eccentricity of the tendon from the centroid of the cross section	mm
E_b	Young's Modulus of beam	N/m^2
E_s	Young's Modulus of the steel girder	N/m^2
E_t	Young's Modulus of tendon	N/m^2
E_x	Young's Modulus in the axial direction	N/m^2
E_{cab}	Young's Modulus of cable	N/m^2
E_{conc}	Young's Modulus of concrete	N/m^2
EI	Flexural rigidity of cross section	$N - m^2$
f'_c	Characteristic concrete cube strength	MPa
f_t	Design tensile strength of concrete	MPa
G_{xz}	Transverse shear modulus in plane of vibration	
h	Height of rectangular cross section,	mm
I	Second moment of area of the beam cross section	m^4
I_e	Effective second moment of area of the cross section	m^4
I_r	Second moment of area of composite cross section	m^4
I_s	Second moment of area of prestress steel cross section	m^4
I_u	Uncracked second moment of area	m^4
I_{conc}	Second moment of area of concrete cross section	m^4
I_{cr}	Cracked second moment of area	m^4
I_{vs}	Second moment of area of steel girder	m^4
k	Shear factor for given cross section	N/m^2
L_r	Span length after axial shortening	m

M	Bending moment in beam	$N-m$
m	Mass per unit length of the beam	kg/m
M_a	Maximum gross moment	$N-m$
M_p	Bending moment due to the prestressing force	$N-m$
m_r	mass per unit length of the prestressed beam	kg/m
M_{cr}	Cracking moment	$N-m$
N	Magnitude of the external axial compressive load	N
n	n^{th} bending vibration mode	
P	Applied prestressing load	N
P_t	Magnitude of the prestressing force	N
P_{cr}	Critical Euler buckling load	N
P_{ext}	External axial load	
P_{ts}	Vertical component of the prestressing force	N
r	Radius of gyration	
T	Axial tensile force	N
t	Time variable	s
T_{KE}	Kinetic energy	
U	Strain energy	
u	Deflection of beam	m
V	Shear force in beam	N
W	Work done by external load, P	
w	Beam transverse displacement	
X	Axial load index; ratio of axial load to P_{cr}	
x	Horizontal Cartesian coordinate	

y	Vertical Cartesian coordinate	
y_{max}	Distance from neutral axis to extreme fibre	mm
Z	Sensitivity index of square of frequency to axial load index	

Bibliography

ACI Committee 318 (2008). *Building Code Requirements for Structural Concrete (ACI 318-05) and Commentary (ACI 318R-05)*. ACI report: American Concrete Institute. American Concrete Institute, Farmington Hills, MI.

American Concrete Institute (1989). Building Code Requirements for Concrete, ACI 318-89.

Attard, M. M. and Setunge, S. (1996). Stress-strain relationship of confined and unconfined concrete. *ACI Materials Journal*, 93(5):432–441.

Autodesk ROBOT Structural Analysis Professional 2012 - Student Evaluation Version (2012). *version 25.0.0.3774 (x64)*. Autodesk Inc., San Rafael, California, U.S.

Avitabile, P. (1998-2001b). *Modal Space - In our own little world*. Modal Analysis and Control Laboratory, University of Massachusetts, Lowell, One University Avenue, Lowell, Massachusetts 01854.

Avitabile, P. (2001a). Experimental modal analysis - a simple non-mathematical overview. *Sound and Vibration Magazine*.

Bartlett, F. (1987). Discussion of "Free Vibration Behavior of Prestressed Beams" by K. Kanaka Raju and G. Venkateswara Rao (February, 1986, Vol. 112, No. 2). *Journal of Structural Engineering*, 113(9):2085–2087.

Bažant, Z. and Cedolin, L. (1987). Discussion of "Free Vibration Behavior of Prestressed Beams" by K. Kanaka Raju and G. Venkateswara Rao (February, 1986, Vol. 112, No. 2). *Journal of Structural Engineering*, 113(9):2087–2087.

Bert, C. (1987). Discussion of "Free Vibration Behavior of Prestressed Beams" by K. Kanaka Raju and G. Venkateswara Rao (February, 1986, Vol. 112, No. 2). *Journal of Structural Engineering*, 113(9):2087–2088.

Bilošová, A. (2011). *Modal Testing*. VB-Technical University of Ostrava.

Blakeley, R., Park, R., and Shepherd, R. (1970). A review of the seismic resistance of prestressed concrete. *Bulletin*, pages 3–23.

Bourne, S. (2013). Prestressing: recovery of the lost art. *IStructE Journal: "The Structural Engineer, February 2013"*, 91(2).

British Standards Institute (2000). BS EN 12350-2:2000 Testing Fresh Concrete Part 2: Slump test.

British Standards Institute (2001). BS EN ISO 12390-3:2001 Testing Hardened Concrete Part 3: Compressive strength of test specimens.

British Standards Institute (2004). Eurocode 2: Design of concrete structures Part 1-1: General rules and rules for buildings.

British Standards Institute (2005). Eurocode 3: Design of steel structures Part 1-1: General rules and rules for buildings.

British Standards Institute (2006). PR EN 10138-3:2006 Prestressing Steels - Part 3: Strand.

British Standards Institute (2009). BS EN ISO 6892-1:2009 Metallic materials Tensile testing Part 1: Method of test at ambient temperature.

British Standards Institute (2013). BS EN 12390-13:2013 Testing Hardened Concrete Part 13: Determination of secant modulus of elasticity in compression.

Bruggi, M., Caprioli, A., Vanali, M., and Venini, P. (2008). Investigation of the pre-stress loss in the dynamical behaviour of concrete beams. In *Conference: 2008 IMAC-XXVI: Conference & Exposition on Structural Dynamics*. Society for Experimental Mechanics (SEM).

Butterworth, S. (1930). On the theory of filter amplifiers. *Experimental Wireless & the Wireless Engineer*, 7:536–541.

Chan, T. and Yung, T. (2000). A theoretical study of force identification using prestressed concrete bridges. *Engineering Structures*, 22(11):1529 – 1537.

Chopra, A. (2012). *Dynamics of Structures: Theory and Applications to Earthquake Engineering*. Civil Engineering and Engineering Mechanics Series. Prentice Hall.

Clough, R. and Penzien, J. (1993). *Dynamics of Structures*. Civil Engineering Series. McGraw-Hill.

Cooley, J. W. and Tukey, J. W. (1965). An algorithm for the machine calculation of complex fourier series. *Mathematics of Computation*, 19(90):pp. 297–301.

Cornwell, P., Farrar, C., Doebling, S., and Sohn, H. (1999). Environmental variability of modal properties. *Experimental Techniques*, 23(6):45–48.

Dai, K. and Chen, S. (2007). Vibration of spun-cast prestressed concrete poles. In *Conference Proceedings of the Society for Experimental Mechanics Series*.

Dall'Asta, A. and Dezi, L. (1996). Discussion of "Prestress Force Effect on Vibration Frequency of Concrete Bridges" by M. Saiidi, B. Douglas, and S. Feng. *Journal of Structural Engineering*, 122(4):458–458.

Dall'Asta, A. and Leoni, G. (1999). Vibrations of beams prestressed by internal frictionless cables. *Journal of Sound and Vibration*, 222(1):1 – 18.

De Roeck, G. (2003). The state-of-the-art of damage detection by vibration monitoring: The simces experience. *Journal of Structural Control*, 10(2):127–134.

Deák, G. (1996). Discussion of "Prestress Force Effect on Vibration Frequency of Concrete Bridge" by M. Saiidi, B. Douglas, and S. Feng. *Journal of Structural Engineering*, 122(4):458–459.

Ewins, D. (2000). *Modal testing: theory, practice, and application*. Mechanical engineering research studies: Engineering dynamics series. Research Studies Press.

Foti, D., Gattulli, V., and Potenza, F. (2014). Output-only identification and model updating by dynamic testing in unfavorable conditions of a

seismically damaged building. *Computer-Aided Civil and Infrastructure Engineering*, 29(9):659–675.

Grace, N. and Ross, B. (1996). Dynamic characteristics of post-tensioned girders with web openings. *Journal of Structural Engineering*, 122(6):643–650.

Hamed, E. and Frostig, Y. (2004). Free vibrations of cracked prestressed concrete beams. *Engineering Structures*, 26(11):1611–1621.

Hamed, E. and Frostig, Y. (2006). Natural frequencies of bonded and unbonded prestressed beams - prestress force effects. *Journal of Sound and Vibration*, 295(1-2):28 – 39.

Ho, D., Kim, J., Stubbs, N., and Park, W. (2012). Prestress-force estimation in PSC girder using modal parameters and system identification. *Advances in Structural Engineering*, 15(6):997–1012.

Hop, T. (1991). The effect of degree of prestressing and age of concrete beams on frequency and damping of their free vibration. *Materials and Structures*, 24:210–220.

Jain, S. and Goel, S. (1996). Discussion of "Prestress Force Effect on Vibration Frequency of Concrete Bridges" by M. Saiidi, B. Douglas, and S. Feng. *Journal of Structural Engineering*, 122(4):459–460.

Kato, M. and Shimada, S. (1986). Vibration of pc bridge during failure process. *Journal of Structural Engineering*, 112(7):1692–1703.

Kerr, A. (1976). On the dynamic response of a prestressed beam. *Journal of Sound and Vibration*, 49(4):569–573.

Kim, J.-T. and Stubbs, N. (2002). Improved damage identification method based on modal information. *Journal of Sound and Vibration*, 252(2):223 – 238.

Kim, J.-T., Yun, C.-B., Ryu, Y.-S., and Cho, H.-M. (2004). Identification of prestress-loss in PSC beams using modal information. *Structural Engineering and Mechanics*, 17(3 - 4):467–482.

Kong, F. and Evans, R. (1987). *Reinforced and Prestressed Concrete, Third Edition*. Taylor & Francis.

Law, S. and Lu, Z. (2005). Time domain responses of a prestressed beam and prestress identification. *Journal of Sound and Vibration*, 288(4-5):1011–1025.

Li, J., Law, S., and Hao, H. (2013). Improved damage identification in bridge structures subject to moving loads: Numerical and experimental studies. *International Journal of Mechanical Sciences*, 74(0):99 – 111.

Lu, Z. and Law, S. (2006). Identification of prestress force from measured structural responses. *Mechanical Systems and Signal Processing*, 20(8):2186–2199.

Mander, J., Priestley, M., and Park, R. (1988). Theoretical stress strain model for confined concrete. *Journal of Structural Engineering*, 114(8):1804–1826.

MATLAB (2014). *version 8.3.0 (R2014a)*. The MathWorks Inc., Natick, Massachusetts.

Miyamoto, A., Tei, K., Nakamura, H., and Bull, J. (2000). Behavior of prestressed beam strengthened with external tendons. *Journal of Structural Engineering*, 126(9):1033–1044.

Noble, D., Nogal, M., O'Connor, A., and Pakrashi, V. (2014a). The effect of prestress force magnitude on the natural frequencies of prestressed concrete structures. In *Proceedings of the* 23^{rd} *Australasian Conference on the Mechanics of Structures and Materials (ACMSM23)*, volume I, pages 333–338. Southern Cross University.

Noble, D., Nogal, M., O'Connor, A., and Pakrashi, V. (2014b). Impact hammer testing on post-tensioned steel RHS sections; an investigation of the "Compression Softening" effect. In *Proceedings of Civil Engineering Research in Ireland Conference*, volume I, pages 427–432. Civil Engineering Research Association of Ireland.

Noble, D., Nogal, M., O'Connor, A., and Pakrashi, V. (2015a). Dynamic impact testing on post-tensioned steel rectangular hollow sections; an investigation into the "compression-softening" effect. *Journal of Sound and Vibration*, 355:246 – 263.

Noble, D., Nogal, M., O'Connor, A., and Pakrashi, V. (2015b). The effect of post-tensioning force magnitude and eccentricity on the natural bending frequency of cracked post-tensioned concrete beams. In *Proceedings of 11th International Conference on Damage Assessment of Structures DAMAS 2015*, pages 197–204. 11th International Conference on Damage Assessment of Structures DAMAS 2015.

Noble, D., Nogal, M., O'Connor, A., and Pakrashi, V. (2015c). Output only investigation of the effect of post-tensioning force on natural frequencies of post-tensioned concrete beams. In *Proceedings of International Operational Modal Analysis Conference IOMAC*, pages 197–204. International Operational Modal Analysis Conference IOMAC.

Noble, D., Nogal, M., O'Connor, A., and Pakrashi, V. (2016). The effect of prestress force magnitude and eccentricity on the natural bending frequencies of uncracked prestressed concrete beams. *Journal of Sound and Vibration*, 365:22–44.

Oppenheim, A. V., Schafer, R. W., and Buck, J. R. (1999). *Discrete-Time Signal Processing*. Prentice Hall, Upper Saddle River, NJ, 2 edition.

Pauw, A. (1960). Static modulus of elasticity of concrete as affected by density. *Journal Proceedings of the American Concrete Institute ACI*, 57(6):679–687.

Pavic, A., Reynolds, P., Waldron, P., and Bennett, K. (2001). Dynamic modelling of post-tensioned concrete floors using finite element analysis. *Finite elements in analysis and design*, 37(4):305–323.

Peeters, B. and De Roeck, G. (2001). One-year monitoring of the z24-bridge: Environmental effectsversus damage events. *Earthquake Engineering and Structural Dynamics*, 30(2):149–171.

Quilligan, A., O'Connor, A., and Pakrashi, V. (2012). Fragility analysis of steel and concrete wind turbine towers. *Engineering Structures*, 36:270 – 282.

Raju, K. K. and Rao, G. V. (1986). Free vibration behavior of prestressed beams. *Journal of Structural Engineering*, 112:433–437.

Rodríguez, J., Martí, J., and Martínez, F. (2010). Post-cracking behaviour of a wind turbine concrete tower. In *Proceedings of SIMULIA Customer Conference*, pages 632–646, Providence, Rhode Island.

Saiidi, M., Douglas, B., and Feng, S. (1994). Prestress force effect on vibration frequency of concrete bridges. *Journal of Structural Engineering*, 120(7):2233–2241.

Saiidi, M., Shields, J., O'Connor, D., and Hutchens, E. (1996). Variation of Prestress Force in a Prestressed Concrete Bridge During the First 30 Months. *PCI Journal*, 96.

Stoer, J. and Bulirsch, R. (2010). *Introduction to Numerical Analysis (Texts in Applied Mathematics)*. Springer.

Tata Steel Europe Limited (2013). *Tata Steel - Blue Book*. Tata Steel Europe Limited.

Tse, F., Morse, I., and Hinkle, R. (1978). *Mechanical vibrations: theory and applications*. Allyn and Bacon series in mechanical engineering and applied mechanics. Allyn and Bacon.

Unger, J. F., Teughels, A., and De Roeck, G. (2006). System identification and damage detection of a prestressed concrete beam. *Journal of structural engineering*, 132(11):1691–1698.

Wikipedia (2015a). Butterworth filter — wikipedia, the free encyclopedia. [Online; accessed 31-March-2015].

Wikipedia (2015b). Damping — wikipedia, the free encyclopedia. [Online; accessed 18-May-2015].

Williams, M. S. and Falati, S. (1999). Modal testing of a post-tensioned concrete model floor slab. volume 1, pages 14–20.

Wu, B. (2014). A correction of the half-power bandwidth method for estimating damping. *Archive of Applied Mechanics*, pages 1–6.

Zhang, Y. and Li, R. (2007). Natural frequency of full-prestressed concrete beam. *Transactions of Tianjin University*, 13(5):354–359.

Zhang, Y., Zheng, Y., and Li, H. (2012). A dynamic test of fully prestressed concrete beams. *Advanced Materials Research*, 368 - 373:2483–2490.